Title
Electronic and magnetic structures in low dimensional systems

Permalink
https://escholarship.org/uc/item/5ff3h7kz

Author
Hejazi, Kasra

Publication Date
2021

UNIVERSITY of CALIFORNIA
Santa Barbara

Electronic and magnetic structures in low dimensional systems

A dissertation submitted in partial satisfaction of the
requirements for the degree of

Doctor of Philosophy

in

Physics

by

Kasra Hejazi

Committee in charge:

Professor Leon Balents, Chair

Professor Mark Sherwin

Professor Matthew Fisher

December 2021

The dissertation of Kasra Hejazi is approved.

Professor Mark Sherwin

Professor Matthew Fisher

Professor Leon Balents, Chair

December 2021

To my wife,
and my mother and my father,
and my sister and my brother,
for all their support and love,

and to the memory of my grandmother,
whose voice still soothes me in my darkest moments.

Acknowledgements

There are many people to whom I am indebted for the journey I had during my graduate school. First, I should thank my great adviser, Leon Balents, for his guidance and immense support during the past five years. He took me and my thoughts seriously when nobody else did. He was always available for discussions in which he would patiently listen to me and provide significant fruitful advice. His deep encyclopedic knowledge and his original ideas have always been a source of inspiration for me. Thank you for all that.

I should also thank my other committee members Matthew Fisher and Mark Sherwin; conversations with both of you have been always really inspiring.

I am also deeply grateful to my other mentors and collaborators at UCSB. Bela Bauer has undoubtedly played the role of a second advisor for me; he is energetic, full of ideas and supportive. Thank you for the great collaborations we had together. I should thank Hassan Shapourian for his great guidance; I learnt a lot about random matrices, quantum chaos and quantum information from our numerous long discussions. I should thank Xiao Chen, from whom I learnt a lot about doing numerics in a systematic way. I am also grateful to Jianpeng Liu for my collaborations with him early in my PhD. Thank you Zhu-Xi Luo for our numerous discussions on moiré magnets. I would also like to thank Tim Hsieh for the great discussuions we have had.

I have learnt a lot from the great professors at UCSB, in particular I am thankful for having the opportunity of learning from Matthew Fisher, Chetan Nayak, Andreas Ludwig, Mark Srednicki, Cenke Xu, Andrea Young and Ken Goodearl.

I would also like to show my appreciation to past and present local researchers Urban Seifert, Anna Keselman, Chaoming Jian, Lucile Savary, Tianci Zhou, Mengxing Ye, Dave Aasen, Gregory Polshyn and local students Mark Arildsen, Taka Park, Chaitanya Murthy, Aleksei Khindanov, Amber Cai, Misha Lipatov, Yichen Xu, Xiao-Chuan Wu, Zhitao Chen, Farzan Vafa, Charles Tschirhart, Marec Serlin, Christina Knapp, Teddy Parker, Alex Miller, Dominic Else, Alex Meiburg, Sergio Hernandez Cuenca, Zach Porter, Yaodong Li for the great discussions and friendship we have had. I would especially like to thank Chunxiao Liu for the nice collaborations we had and his friendship.

I would like to thank my Iranian friends at Santa Barbara with whom I spent enjoyable time; In particular, I would like to thank Shariar Shadkhoo (who is a great friend and spent a lot of time with me discussing physics), and our great neighbors MJ and Mahnaz, and Farnaz and Farnood.

I would also like to thank my other physicist friends Yahya Alavirad, Ali Lavasani and Amir Tajdini for the great time we have had together both online and in person. You are amazing friends. I have had many inspriing physics discussion with Yahya for which I am really grateful to him.

I am thankful to my long-time friend Reza Kaviany, who has always been on my side and has cheered me up in all these years.

I would like to thank my amazing family, Parvin, Ali, Pouya and Sanaz for all their support and encouragement and their unconditional love. I have been away for a few years now, but my heart is warm with your love. I should also thank my late grandmother who always loved and soothed me unconditionally. I would also like to pay tribute to my late father, Masoud, from whom I do not have lots of memories but he is always in my heart.

I would also like to say thank you to my mother-in-law, father-in-law, my sister-in-law and brothers-in-law for their constant love and encouragement.

And my dearest Razieh, my greatest friend and companion, all you gave me in these years was support and understanding and love. You are the light of my life. Thank you for accompanying me in this journey. You have also taught me a lot about quantum information; whenever I did not understand something in quantum information, I directly came to you. Thank you for all this.

Curriculum Vitæ

Kasra Hejazi

Education

2021	Ph.D. in Physics (expected), University of California, Santa Barbara
2018	M.A in Physics, University of California, Santa Barbara
2015	M.Sc. in Physics, Sharif University of Technology, Tehran
2013	B.Sc. in Physics, Sharif University of Technology, Tehran

Professional Experience

2017-2021	Graduate student researcher, University of California, Santa Barbara

Select Publications

K. Hejazi, Z.-X. Luo, and L. Balents. *Heterobilayer moir magnets: Moir skyrmions and commensurate-incommensurate transitions.* Physical Review B 104.10 (2021): L100406 (2021).

K. Hejazi, X. Chen, and L. Balents. *Hybrid Wannier Chern bands in magic angle twisted bilayer graphene and the quantized anomalous Hall effect.* Physical Review Research 3.1: 013242 (2021).

K. Hejazi, Z.-X. Luo, and L. Balents. *Noncollinear phases in moiré magnets.* Proceedings of the National Academy of Sciences 117.20: 10721-10726 (2020).

K. Hejazi, C. Liu, and L. Balents. *Landau levels in twisted bilayer graphene and semiclassical orbits.* Physical Review B 100.3: 035115 (2019).

K. Hejazi, J. Liu, and L. Balents. *Floquet spin and spin-orbital Hamiltonians and doublon-holon generations in periodically driven Mott insulators.* Physical Review B 99.20: 205111 (2019)

K. Hejazi, C. Liu, H. Shapourian, X. Chen, and L. Balents. *Multiple topological transitions in twisted bilayer graphene near the first magic angle.* Physical Review B, 99.3: 035111 (2019).

J. Liu, K. Hejazi, L. Balents. *Floquet engineering of multi-orbital Mott insulators: applications to orthorhombic titanates.* Physical Review Letters 121.10: 107201 (2018).

Preprint:

K. Hejazi, and H. Shapourian. *Symmetry protected entanglement in random mixed states.* arXiv preprint arXiv:2112.00032 (2021).

Abstract

Electronic and magnetic structures in low dimensional systems

by

Kasra Hejazi

Studying the physics of low dimensional systems has been a fruitful branch of condensed matter physics. A high level of control in experiments and the existence of numerous powerful analytical and numerical techniques for investigating these systems have made experimental and theoretical study of this subject accessible and rich.

A large portion of this thesis is devoted to the theoretical study of a class of two dimensional systems, the so-called moiré structures: these are structures made by stacking incommensurate layered materials, where e.g. a twist or a lattice mismatch between layers results in the formation of a large scale spatial pattern called the moiré pattern.

Different aspects of moiré systems are discussed; starting with the case of twisted bilayer graphene (TBG), first, the effects of an external magnetic field on TBG are studied. Hofstadter spectra and semiclassical analyses are carried out and it is shown that the rich band structure of TBG near its magic angle results in a nontrivial Landau level structure even at the noninteracting level that is different from naive

expectations. Next, the quantized anomalous Hall effect (QAHE) that is observed experimentally in TBG is considered; through extensive Hartree-Fock computations, the regimes in which the QAHE is expected are obtained.

Another moiré platform which is considered in this thesis is moiré structures made of intrinsic Van der Waals magnets. A general methodology for studying them theoretically is introduced and it is utilized to analyze various cases of such moiré magnets; first, twisted bilayers of antiferromagnets and ferromagnets are considered and it is shown that a rich phase diagram exists for such systems when different parameters in the system are tuned. Considering next the case of heterobilayer moiré magnets made of ferromagnetic and antiferromagnetic layers, we show that more interesting magnetic textures such as skyrmion lattices could potentially be realized.

The last topic that is covered in this thesis is numerical computation in low dimensional many body systems. It has been known that many body computational methods in the continuum experience difficulty compared to lattice models. Having this in mind, we propose a method using the wavelet basis for many body computations in the continuum; in order to tackle the difficulty mentioned above, a fine graining procedure is introduced which is general and can be used in combination with classical or quantum variational approaches; ultimately, we use tensor network computations to exhibit the usefulness of this procedure.

Contents

Chapter 1

Introduction

The physics of low dimensional many body systems has been an interesting subject of study for a long time. It has been a very rich topic of research for several reasons: on the experimental front, many remarkable phenomena such as the Luttinger liquid behavior in one dimension and the quantum Hall effect in two dimensions have been realized in practice in such systems. On the theory front, although studying many body system in general is a formidable task, a wealth of different analytical and numerical techniques in lower dimensions has made progress in theoretical understanding of lower dimensional phenomena possible. Often elegant theories developed for understanding these phenomena opened new paths to exciting new fields of research.

A particularly interesting recent addition to the array of low dimensional systems was the realization of single and multilayer Van der Waals (VdW) materials; these are systems that allow a high level of tunability and control which enables the observation of many interesting phenomena. Single layer VdW materials exhibit a variety of different behaviors such as insulating, semi-metallic (as in graphene), metallic, intrinsic magnetic, topological insulating, etc. Even the more exotic spin liquid behavior is believed to occur in a material like α-RuCl$_3$ [62].

Adding different VdW layers each having an interesting intrinsic behavior on its own and studying the resulting interplay has been very fruitful. Of the most interesting platforms in this family are moiré multilayer systems, where a large scale pattern called the moiré pattern is formed due to e.g. a lattice constant mismatch between layers or a twist in the layers with respect to each other. A variety of different moiré systems are realized wherein remarkable phenomena were observed by taking advantage of the vast range of possibilities for such structures.

A paradigmatic instance of moiré systems is the twisted bilayer graphene (TBG), which consists of two layers of graphene stacked with a twist. At the so-called magic twist angle between the two graphene layers, i.e. 1.1°, it is expected that the effect of electron-electron interactions are enhanced [15]. Indeed, experimental findings revealed that a plethora of interesting phenomena in this system emerge at the magic angle that were unprecedented in graphene-based systems, such as correlated insulating behavior[25], superconducting states [26, 137, 79] and the quantized anomalous Hall effect (QAHE) [110, 111].

Various aspects of moiré systems are discussed in this thesis; starting with the TBG system, the effect of an external magnetic field on the system is studied in chapter 2 and then an extensive theoretical investigation of the QAHE in TBG is presented in chapter 3. Another direction that is discussed next is moiré structures made out of intrinsic VdW magnets; a general methodology is introduced and is applied to several cases of twisted homobilayer of VdW magnets in chapter 4. The case of heterobilayer moiré magnets is furthermore analyzed in chapter 5. More information about all of these studies can be found later in the present chapter.

One of the main goals in moiré systems is to use the high level of tunability and engineer novel behaviors, which as mentioned above has been a very successful endeavor. The above chapters on the physics of moiré systems lie within this program where either an effect observed in moiré systems is studied (chapters 2 and 3) or some predictions for potentially interesting phenomena (chapters 4 and 5) are made.

Another topic that is covered in this thesis is computational many body physics in low dimensional systems; it is well known that a variety of different computational methods exist for low dimensional systems, most prominent of which are tensor network algorithms. Most of these computational methods are usually used with lattice models; however, for many applications (including the physics of moiré systems) a continuum description can be favorable. In cahpter 6, we introduce and study a computational method that provides an efficient means to analyze many body physics in the continuum. The method can be used along with different types of variational approaches, in particular tensor network methods and quantum algorithms. We give further introductory details on this study also later in the present chapter.

1.1 Moiré graphene systems

The study of moiré graphene systems has been very fruitful both experimentally and theoretically. On the experimental side, the existence of multiple tuning mechanisms for such systems and also a variety of different measurement techniques such as transport measurements has led to discovery of plenty of remarkable phenomena.

Historically, one of the most important discoveries that led to many of the coming progress was the formulation of a continuum model for TBG. In a seminal work [15], Bistritzer and MacDonald came up with a low energy continuum model which effectively describes the system in terms of an emergent periodic problem. This model works best for small twist angles, where the two graphene layers are almost aligned locally at every point. However, as is shown in Fig. 1.1, a closer look at local patches reveals that the bilayer *locally* resembles different types of stacking orders; the local stacking order is determined based on the position and as can be seen in Fig. 1.1, it modulates periodically in real space forming an effective periodic pattern called the moiré pattern. For small angles, the periodicity of the pattern becomes large, in fact, it scales as $\sim \frac{1}{\theta}$ for small angles. This local stacking order determines the local tunneling between the two graphene layers and as a result the tunneling between the two layers follows the same periodicity as that of the moiré pattern. This means that an effective periodic Hamiltonian is capable of describing the TBG system.

Having this periodic Hamiltonian for the system at hand, Bistritzer and MacDonald went on to find the corresponding Bloch bands. As the periodicity is much larger

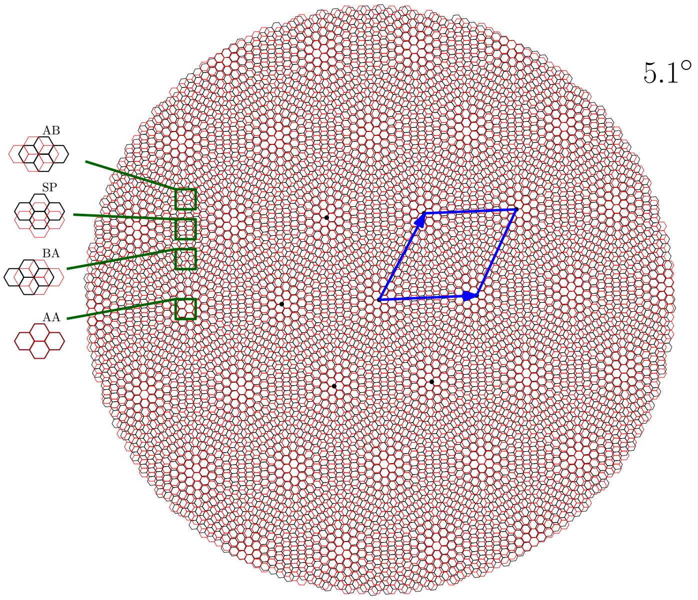

Figure 1.1: Twisted bilayer graphene with a twist angle of 5.1°. Different stacking orders are realized locally in different regions of the bilayer. The unit cell corresponding to the emergent periodicity is also shown.

than the graphene unit cell length, the effective *moiré* Brillouin zone is much smaller than that of the monolayer graphene. As a result, the moiré bands are called mini-bands. Interestingly, Bistritzer and MacDonald found out that at the magic angle 1.1°, two bands (per each spin and valley flavor) close to charge neutrality show exceptional flatness. They anticipated that provided samples with twist angles around the magic value are created, since the bands are very flat, the electronic coulomb interactions will be relatively enhanced and potentially interesting correlation induced behavior could be seen.

The corresponding experimental research on TBG followed. A first milestone was realizing moiré "band insulators" in experiments; it was shown experimentally that for a sample with the twist angle of 1.8° (which is away from the magic angle), *band* insulating states could be obtained as a result of full filling the mini-bands discussed above [24]. More precisely, we note that there is one mini-band above and one mini-band below the charge neutrality point for each spin and valley species, and thus there is in total $4 = 2 \times 2$ spin-valley flavors for each mini-band (we call these eight mini-bands the *active* bands); as a result of this, one needs addition or depletion of 4 electrons per moiré unit cell to completely fill or empty these bands and have a band insulator as a result; this was indeed in great agreement with the experimental findings of [24], validating the continuum model of TBG. Note that in the above experiment, electron addition/depletion was done simply by applying a gate voltage; because the moiré length scale is large, the required change in density to reach the band insulating states is small and in fact achievable by an applied gate voltage.

Before we continue, we introduce a notation, showing the number of electrons added or depleted per moiré unit cell from the charge neutrality point by the filling factor ν. For example in the above experiments, band insulators were observed for $\nu = \pm 4$.

With enhancement of fabrication techniques, later experiments were able to reduce the twist angle of the samples to smaller values, in particular samples with twist angles close to the magic angle were fabricated. With the magic angle samples at hand, experiments focused on partial fillings of the active bands, i.e. $-4 < \nu < +4$ resulting in remarkable findings: in particular, it was found by several different groups that for different integer values of ν between -4 and $+4$ the TBG system exhibits an insulating behavior [25, 137, 79]. Since for such fillings, active bands are partially filled in a noninteracting picture, the origin of the insulating behavior should be electron-electron interactions. Furthermore, probing the system at multiple different ranges of ν close to integers revealed that the system becomes superconducting in those ranges [26, 137, 79]. The mechanism for this superconductivity is still a matter of debate [**?**].

Another remarkable discovery was the observation of QAHE in TBG at $\nu = +3$ [110, 111]. Interestingly, a single sample has shown a Hall conductivity close to %99 of the quantized value under suitable conditions without any applied magnetic field. More details on this discovery will be presented in subsection 1.1.2.

Below, we focus on two interesting observations in TBG systems whose theoretical study is presented in later chapters of this thesis.

1.1.1 Landau fan diagram

One useful experimental probe of electronic degrees of freedom of a two-dimensional system is to observe its quantum oscillations in an applied magnetic field. The experiment goes as follows: the longitudinal and the Hall conductivities of a sample are measured when the external perpendicular magnetic field and total density of electrons are varied from a reference point. The density in the case of graphene systems, for example, is varied by an applied gate voltage. Considering a two dimensional color map of either the Hall conductivity or the longitudinal conductivity whose vertical axis shows the applied B field and its horizontal axis shows the density n, the Hall and the longitudinal conductivities show maxima and minima respectively along certain straight lines. Usually classes of such lines can be found that emanate from a common point in the diagram as shown in Fig. 1.2; due to the special structure and shape of these lines, the plot is called a *Landau fan diagram*. Note that the common point of the Landau fan lines, which lies on the $B = 0$ axis corresponds e.g. to an edge of a band where an insulating or semimetallic behavior in the system occurs.

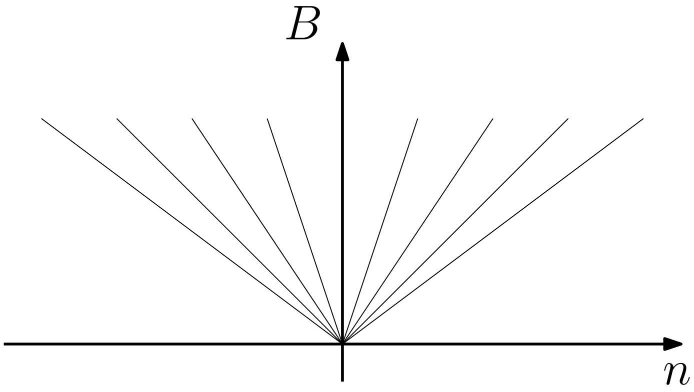

Figure 1.2: A schematic Landau fan diagram. In a color map with the magnetic field and density as axes, the Hall and the longitudinal conductivities show maxima and minima respectively along certain straight lines shown schematically above.

Interestingly, the straight lines along which the Hall (longitudinal) conductivity shows maxima (minima) correspond to having filled Landau levels; as a result, the inverses of the slopes of such lines have a definite relation given by:

$$N_e \frac{e}{h} = \frac{n}{B}, \tag{1.1}$$

N_e denotes the the multiplicity number of filled Landau levels, and it depends crucially on the number of species of electrons. Note that along each of these lines the Hall conductivity is given by $\sigma_H = N_e \frac{e^2}{h}$.

As an example the Landau Fan diagram for monolayer graphene around the charge neutrality point can be derived where the sequence of possible values of N_e in the above relation reads $\pm 2, \pm 6, \pm 10, \ldots$ [93]. The reason for the above sequence is that monolayer graphene near its charge neutrality can be well described as consisting of a Dirac point per spin and valley flavor of its electrons. Dirac electrons unlike electrons with a quadratic dispersion have a zero Landau level, and in fact, at charge neutrality under external magnetic fields partially fill a Landau level; this results in a Hall conductivity sequence of $\pm\frac{1}{2}, \pm\frac{3}{2}, \pm\frac{5}{2}, \ldots$ for a single Dirac point. When a total number of 4 flavors taking spin and valley into account are considered the above sequence of $\pm 2, \pm 6, \pm 10, \ldots$ is reproduced; this is also in agreement with experiments on monolayer graphene (see Fig. 1.3).

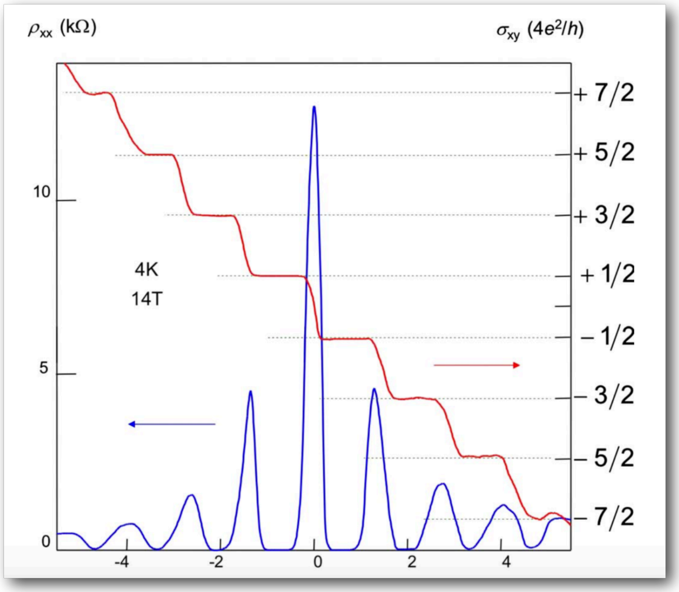

Figure 1.3: Hall conductivity and longitudinal resistivity of graphene that are experimentally found. The results agree very well with the picture of Landau levels of a total of four Dirac points. The plot is taken from [93].

In TBG systems, on the other hand, since the number of layers is 2, one naively expects a Landau fan slope sequence (or equivalently a Hall conductivity sequence) of $2 \times 2 \times 2 \times (\pm\frac{1}{2}, \pm\frac{3}{2}, \pm\frac{5}{2}, \dots)$ at charge neutrality, which results in the sequence $\pm 4, \pm 12, \pm 20, \dots$. This is indeed in agreement with the sequences found in TBG for twist angles that are considerably larger than the magic anlge, like for example $1.8°$ [24]. However, samples at the magic angle showed a differing sequence at charge neutrality i.e. $\pm 4, \pm 8, \pm 12, \dots$ [26, 137]. Some authors have argued that this happens due to interactions or some kind of symmetry breaking [102].

In Chapter 2, we study the TBG system under an external magnetic field at a noninteracting level; we obtain Hofstadter butterfly plots and carry out semiclassical analysis (that match with each other when expected). We show that the noninteracting physics is rich enough so that the above naive sequence is not achieved around the magic angle even at the noninteracting level. In other words and using a semiclassical reasoning, it is shown that the TBG band structure around the magic angle shows plenty of details and as a result the naive expectation of Dirac-like Landau levels does not hold.

The reader can see further details of this study in chapter 2.

1.1.2 Quantized anomalous Hall effect

Another interesting observation in magic angle TBG is the QAHE [110, 111], in which the system exhibits a quantized Hall conductivity and zero longitudinal conductivity without an external magnetic field. The system also shows a magnetization, mainly due to orbital effects. The QAHE happens at the filling factor of $\nu = +3$ and is an electronic interaction induced effect; as a consequence of a time reversal symmetry breaking, a valley polarization occurs leading to the orbital magnetization and the QAHE.

In order to study the effect theoretically, we take the following points into account: close to the magic angle, the set of the eight active bands show small bandwidth and are well separated from other bands. As a result, an active-bands-only model could be a minimal model into which the electronic interactions can be introduced. Since the electronic interactions are not long range due to several screening effects and in fact are local, it is best to come up with a local representation of the active bands subspace. This is usually done through a Wannier transformation of a set of bands; in such an approach, one ends up with a set of *localized* Wannier functions instead of the original *extended* Bloch functions.

However, it is well known that there are obstructions to forming symmetric Wannier functions in TBG; in particular, it is not possible to form maximally localized Wannier functions out of the active bands of each valley-spin flavor provided that a crucial symmetry of the system, i.e. a composition of time reversal and inversion $C_2\mathcal{T}$, is manifestly preserved [2, 102].

In chapter 3, a way out of this problem is considered which amounts to making a compromise in locality and working with *hybrid* Wannier functions (HWF), that

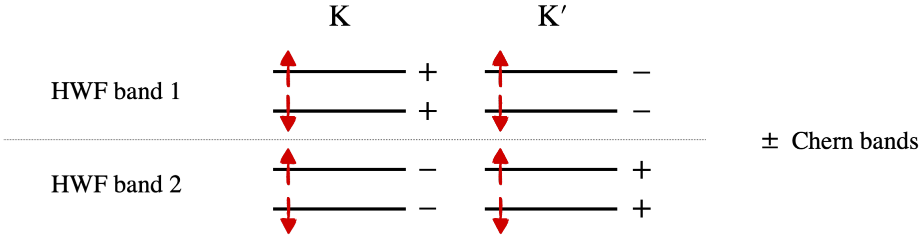

Figure 1.4: The set of eight active bands in the basis of maximally localized HWF states. There are a total of four bands with Chern number +1 and a total of four bands with Chern number −1.

are basically two-dimensional functions that are obtained by performing a Wannier transformation only in one dimension on the sets of Bloch functions; in other words, HWFs are localized Wannier-like in one direction and extended Bloch-like in the other. The one dimensional Wannier transform is performed separately for each valley-spin flavor of electrons and thus for each spin and valley flavor, we end up with two separate HWF bands, note that this results in a total of eight bands which is consistent; we choose to work with *maximally localized* HWF states within each spin-valley flavor. As is argued in detail in chapter 3, the maximally localized HWF bands when formed have nontrivial Chern number, i.e. ±1 values.

In this construction, one ends up with a total of four Chern +1 and four Chern −1 bands. Their composition is shown in Fig. 1.4. Within this basis, an extensive Hartree-Fock calculation is done for the fillings $\nu = \pm 3$, and different regimes where a QAHE is possible are characterized. Interestingly, for these two fillings, the QAHE is manifested as a fully filled spin-valley polarized HWF band of holes for $\nu = +3$ or of electrons for $\nu = -3$. Note that the state manifestly harbors QAHE as the HWF bands carry a Chern number.

The reader can see further details of this study in chapter 3.

1.2 Moiré magnets

A class of VdW materials showing very interesting behaviors are the VdW intrinsic magnets. Diverse magnetic orders have been observed in these materials such as honeycomb lattice antiferromagnetic (e.g. in $MnPS_3$ and $MnPSe_3$), zig-zag antiferromagnetic (e.g. in $FePS_3$ and $NiPS_3$), ferromagnetic (e.g. in CrI_3 and $CrCl_3$), etc.

In chapter 4, a new platform for moiré physics, i.e. moiré structures made out of VdW intrinsic magnets is introduced. A general methodology for considering these systems is also presented there, which relies on the existence of a large moiré length in a similar fashion to the continuum model of TBG [15].

A natural case to consider is a twisted bilayer of such 2D magnets. Here we consider a twisted bilayer of honeycomb antiferromagnets to demonstrate our approach. Such a construction is shown schematically in Fig. 1.5. Red and blue lattice points on the two layers show the two sublattices of the honeycomb lattices. This means that in a single antiferromagnetic layer, a spin on a red site has opposite orientation to a spin lying on a blue site. The behavior of the interlayer coupling in such a structure plays a crucial role in the study; to exhibit its effects we consider different regions in the system separately; first, considering the center of the figure, we see that if we take a blue site on the top layer in this region, its nearest site in the bottom layer is also a blue site. The same holds for a red site in this region as well. This means

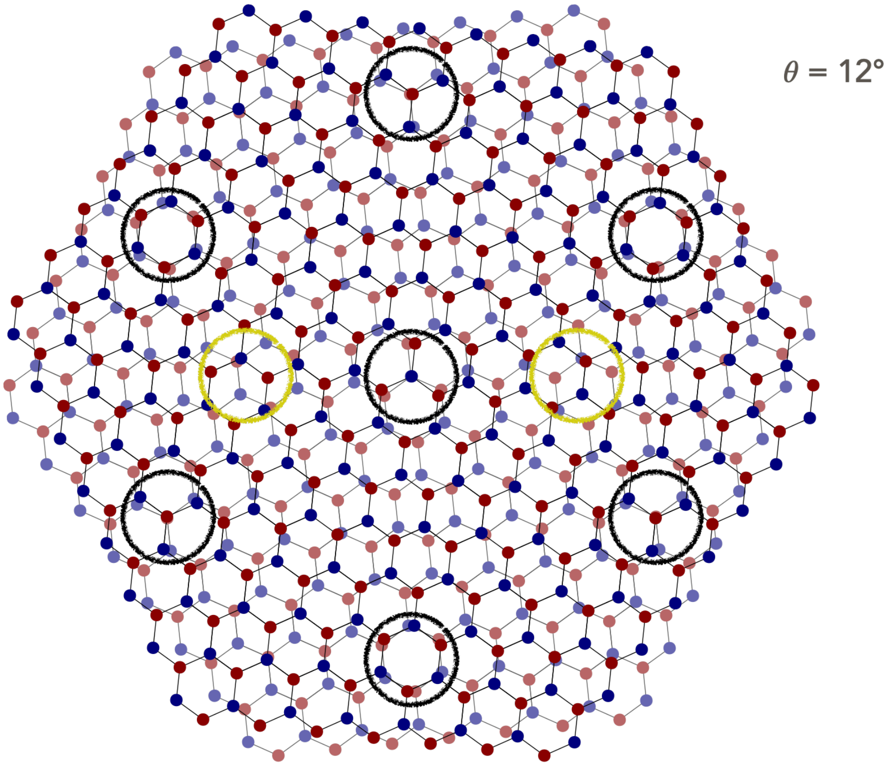

Figure 1.5: A twisted bilayer of antiferromagnets. The two sublattices on both of the layers are shown by blue and red colored sites.

that like sublattices of the two layers are interlayer nearest neighbors in this region. There are more regions with the same property that are also shown by black circles in Fig. 1.5.

However, there are also regions where opposite sublattices on the two layers are interlayer nearest neighbors; some of these regions are shown with yellow circles in Fig. 1.5. This means that assuming a Heisenberg interlayer coupling (Heisenberg interaction between spins of the two layers), the two layers cannot be both in their ground states and satisfy the interlayer coupling everywhere; in such a setting, the nearest neighbor interlayer bonds will be dissatisfied either in black regions or in yellow regions of Fig. 1.5. As a result, one expects that for strong enough interlayer coupling, the system will prefer to realize a noncollinear phase in which each layer is not in its ground state but the interlayer bonds are satisfied everywhere, in both black and yellow regions in particular. Indeed, the methodology used in chapter 4 shows that this is true when the interlayer coupling is strong enough, or as we will see equivalently when the moiré length is large enough; rich phase diagrams with noncollinear phases are obtianed for twisted bilayers where the two layers have simple antiferromagnetic order or zig-zag order.

1.2.1 Twisted bilayers of ferromagnets

With the above perspective, twisted bilayer of ferromagnets seem to be boring as naively all the spins in both of the layer will be aligned or anti-aligned based on the interlayer coupling and the fact that the two sublattices for a ferromagnetic honeycomb lattice do not have opposite spins. However, the situation is more interesting as for example in the material CrI_3, and cosidering a non-twisted bilayer, it has been shown that the interlayer coupling depends on the stacking order of the bilayer [83, 113, 124, 55, 112, 115, 58]. In particular, it has been shown that even the sign of the interlayer coupling can change based on the stacking order.

Since in a twisted bilayer all possible local stacking orders are realized, one can argue that if both of the layers are in their ground states, i.e. a collinear configuration, there will again be regions where the interlayer coupling is dissatisfied. This frustration, if large enough, can render noncollinear configurations energetically favorable similar to the antiferromagnetic case. In chapter 4, it is shown that such configurations again occur for large enough interlayer coupling or large enough moiré length.

Interestingly, this prediction has also been observed in experiments. In a recent experiment [135], twisted bilayers of the ferromagnetic material CrI_3 were fabricated. The experiments showed, by e.g. measuring the magnetization as a function of the magnetic field, that noncollinear phases occur for a twist angle of 1.2°. This is in agreement with the predictions and results presented in chapter 4.

1.2.2 Heterobilayer moiré magnets

Another interesting setup of moiré magnets considered in this thesis is heterobilayer moiré magnets. In such structures, the moiré pattern is formed due to a lattice mismatch between the two layers which are different materials and have different lattice constants.

In chapter 5, a structure in this class is considered, i.e. a bilayer consisting of a honeycomb ferromagnetic layer and a honeycomb antiferromagnetic layer. A moiré pattern is formed due to the lattice mismatch between the two layers. In Fig. 1.6 a schematic figure of such a structure is drawn, where the two sublattices of the antoferromagnetic layer are shown with red and blue colors and the ferromagnetic layer sites are shown by green. A closer look reveals that the spins in the ferromagnetic layer

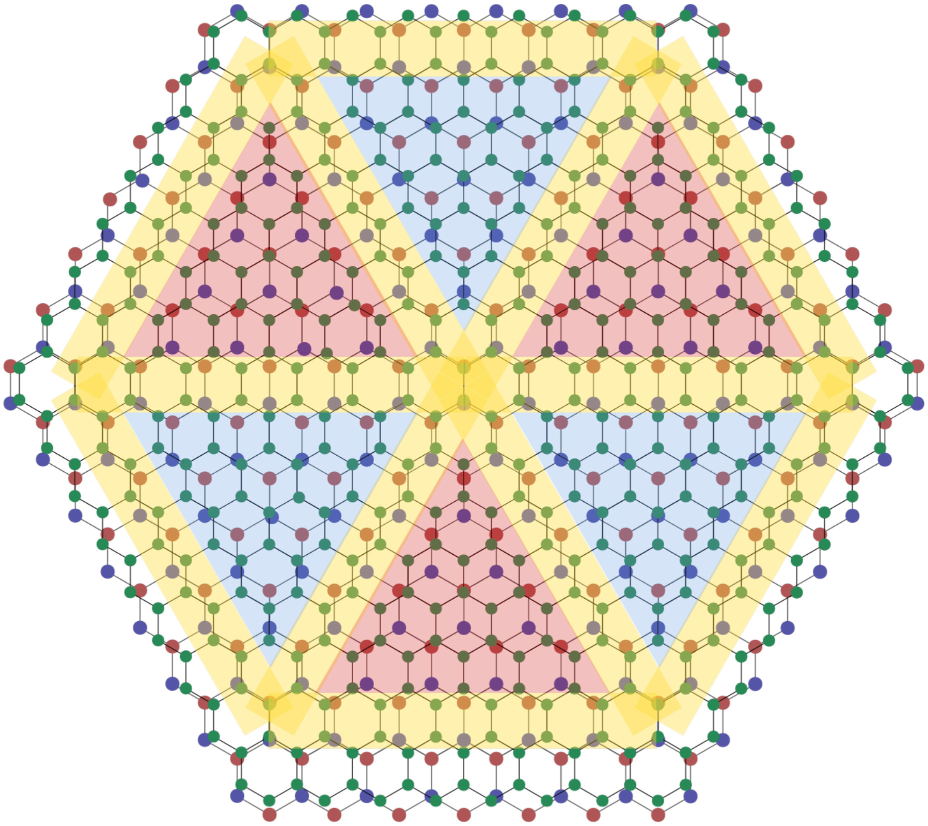

Figure 1.6: A hetrobilayer consisting of a ferromagnetic layer and an antiferromagnetic layer. The blue and red sites show the two sublattices of the antiferromagnetic layer and the green sites correspond to the sites on the ferromagnetic layer.

experience different environments based on their positions; in areas that are shaded red (or blue), the closest sites of the antiferromagnetic layer to the ferromagnetic sites belong to the red (or blue) sublattice. This means that if one supposes that the antiferromagnetic layer is in its ground state, the ferromagnetic layer experiences opposite effective external fields in the blue and red shaded regions. This, in other word, implies that a moiré scale external field is sensed by the ferromagnetic layer.

Such a possibility is considered in chapter 5, where also a dzyaloshinskii-moriya (DM) interaction is introduced into the ferromagnetic layer. The presence of the DM interaction is known to result in topologically nontrivial magnetic textures in materials, in particular skyrmion lattices in ferromagnetic materials. However, there is usually a need for an external magnetic field to stabilize a skyrmion lattice in the system. The DM interaction and skyrmion lattices have been observed in VdW materials [123, 101, 33] which makes considering a ferromagnetic layer with DM interaction in a moiré structure justifiable.

It is shown in chapter 5 that in a heterobilayer structure as detailed above different phases with the moiré periodicity can be stable, among which there is a skyrmion lattice phase; interestingly for this phase, there is no need for an external magnetic field. The reader can see further details of this study in chapter 5.

1.3 Efficient many body physics in the continuum

Studying many body physics computationally in the continuum has been challenging for several reasons. One of the main reasons is the following fact: supposing one uses a lattice discretization of the continuum and perform computations on the resulting effective lattice; if a very fine discretization is used, one ends up with a high number of sites in the effective lattice describing the system. However, when a particle number preserving Hamiltonian is at hand, one needs to find solutions with fixed total numbers of particles. With a very fine lattice which results in a high number of sites, and given some total number of particles, the effective model becomes that of a very dilute lattice system; it is known that variational many body approaches such as the density matrix renormalization group (DMRG) experience difficulties in dilute lattice systems [35]; this is due to the fact that a local variational approach, such as DMRG, optimizes solutions locally and as a result it is more difficult in dilute systems to obtain the large scale structures. This is not specific to DMRG though and it is expected that other variational approaches including quantum variational algorithms experience such difficulty in continuum many body systems.

In chapter 6, a solution to this difficulty is discussed which will be briefly reviewed in the following: instead of the usual way of lattice discretizing the continuum, in chapter 6, the *wavelet* basis is used for the discretization.

The wavelet basis is an *orthonormal* basis for real square integrable functions on the real axis, that consists of basis elements which we show as $\chi_n(x)$ that are wave packets localized in both real and momentum space. An interesting property of the wavelets is their multiresolution property: each wavelet basis element $\chi_n(x)$ can be associated with a given spatial scale. This means that expanding a real function in the wavelet basis, i.e. an expansion such as $f(x) = \sum_n c_n \chi_n(x)$, can decompose it into different scales: the structure at each scale can be determined based on the expansion coefficients c_n for the basis elements corresponding to that scale.

This multiresolution property of the basis allows one to modify a variational many body algorithm of choice, and supplement it with a fine graining procedure, so that the solution is found in a step by step fashion: first, the variational algorithm is employed at a coarse scale where the resulting effective lattice model has a low number of total sites and as a result the effective system is not dilute; as a result, the solution which describes large scale structures, is found simply. The second step consists of finding the solution at a little bit finer scale; to this end it is desirable to use the first step solution as a seed for the second step variational computation. However, the Hilbert space bases for these two steps are different, and as a result an *exact* fine graining transformation is employed to translate the solution of the first step from the first step basis into that of the second step. This transformation is performed as a quantum circuit which only involves two-qubit unitaries acting on nearest neighbors. The steps are continued until convergence is achieved.

The above fine graining procedure and the fine graining quantum circuit is a general approach that can be used in combination with classical variational algorithms such as tensor networks or quantum variational algorithms such as the variational quantum eigensolver to speed up the computation.

Furthermore, the above fine graining procedure is used in chapter 6 along with the DMRG algorithm and it is shown that finding the solution in a step by step fashion as discussed above leads to considerable speedup over a computation at the finest scale from the beginning.

Chapter 2

Landau levels in twisted bilayer graphene and semiclassical orbits

Twisted bilayer graphene has been argued theoretically to host exceptionally flat bands when the angle between the two layers falls within a *magic* range near 1.1°. This is now strongly supported by experiment, which furthermore reveals dramatic correlation effects in the magic range due to the relative dominance of interactions when the bandwidth is suppressed. Experimentally, quantum oscillations exhibit different Landau level degeneracies when the angles fall in or outside the magic range; these observations can contain crucial information about the low energy physics. In this chapter, we report a thorough theoretical study of the Landau level structure of the non-interacting continuum model for twisted bilayer graphene as the magnetic field and the twist angle are tuned. We first show that a discernible difference exists in the butterfly spectra when twist angle falls in and outside the magic range. Next, we carry out semiclassical analysis in detail, which quantitatively determines the origin of the low energy Landau levels from the zero field band structure. We find that the Landau level degeneracy predicted in the above analyses is capable of partially explaining features of the quantum oscillation experiments in a natural way. Finally, topological aspects, validity, and other subtle points of the model are discussed.

This chapter is based on Ref. [51].

2.1 Introduction

Twisted bilayer graphene (TBG) has attracted immense attention from physicists, following the observation of superconductivity and correlation-induced insulators when the layers are twisted relative to one another close to the "magic" angle ($\sim 1.1^\circ$)[25, 26]. These results have since been confirmed and extended by many independent groups[137, 111, 79, 103, 27, 78, 30]. While there are now many experiments and some results are limited to specific samples at specific angles and densities, so far all indications of correlated behavior have been limited to the density range corresponding to partial fillings of the two low energy bands closest to charge neutrality point (CNP); these two *active* bands are theoretically predicted to show exceptional flatness when the twist angle is tuned to lie within the magic range [15].

At the present stage, there is no consensus on the explanation of these effects, despite the many theoretical efforts[134, 60, 65, 102, 139, 34, 133, 71, 132, 57, 20].

A key issue is that the same physics which leads to anomalous narrowing of the low energy bands near the magic angle also makes those bands very sensitive to small details of the model in this regime. It would be desirable to put direct constraints on the theoretical model from experiment.

An effective way to obtain an understanding of the low energy degrees of freedom in a two-dimensional system is to probe it with perpendicular magnetic field and study the quantum oscillations; local minima of longitudinal resistivity form straight lines in the plane of carrier density and magnetic field, a fact that can be seen in Landau fan diagrams. Previous experimental results[24] at the angle 1.8° exhibited Landau level (LL) filling factors $\nu = \pm 4, \pm 12, \pm 20, \ldots$ at the CNP (we define $\nu = n\Phi_0/\Phi$, where n is the 2d density measured from charge neutrality, $\Phi_0 = h/e$ is the flux quantum, and $\Phi = B\mathcal{A}$ is the flux per unit cell of the moiré pattern, with unit cell area $\mathcal{A}$); note that these numbers double those of monolayer graphene. This can be understood by noting that there are two *renormalized* Dirac points in the moiré Brillouin Zone (BZ) where the two active bands touch as predicted by the continuum model [15, 37] (CM) of TBG, and that furthermore one needs to consider $4 = 2 \times 2$ copies of the model due to spin and valley degrees of freedom of the electrons. However, study of quantum oscillations in the magic range [137, 26] revealed a different sequence near CNP, namely $\nu = \pm 4, \pm 8, \pm 12, \ldots$. Some authors have argued that this happens due to interactions or some kind of symmetry breaking[102].

While certainly the interaction effects are of primary interest, without a firm foundation for the free electron moiré physics it is impossible to disambiguate subtle band effects from correlation ones. Here, inspired by the above observation, we study the effect of perpendicular magnetic field without interactions. We start with the CM, and incorporate the magnetic field into it; to this end, we use the method introduced in Ref. [14] with some modifications. In particular, we have considered the effects of lattice corrugation phenomenologically by differentiating between the tunneling amplitude at AA and AB/BA regions of the moiré superlattice [65].

We start by first studying angles larger than the magic value, and then restrict our attention to the magic range. We indeed observe that at larger angles, the same sequence mentioned above, $4\times(\pm 1, \pm 3, \pm 5, \ldots)$, can be seen; however, as the twist angle is reduced into the magic range, we first observe a sequence of $4 \times (\pm 1, \pm 2, \pm 3, \ldots)$, and then a sequence of $4 \times (\pm 1, \pm 4, \ldots)$ upon further decrease of the angle. The former happens close to the twist angle where the Γ point (the highest symmetry point) of the BZ becomes gapless in a quadratic band touching and the nonmagnetic active bands become most flat, while the latter happens upon the formation of three-fold local minima (maxima) in the upper (lower) active band. Finally we present a semiclassical study at small enough magnetic fields that associates the above results to certain regions in the BZ.

The rest of the chapter is organized as follows. In Sec. 3.2, we introduce the magnetic model used here; the details of the model are presented in App. A.1. Then in Sec. 2.3 the numerical solution of the magnetic model is presented and discussed

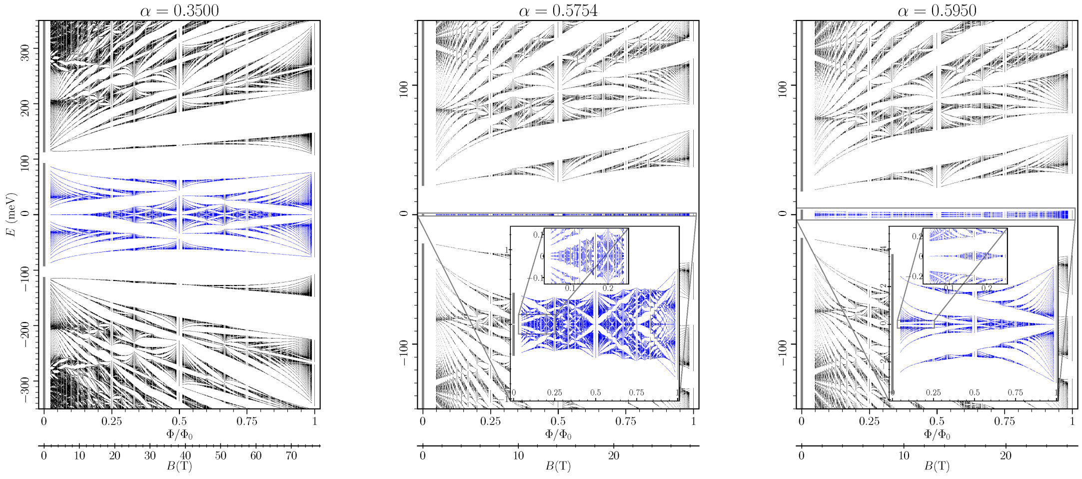

(a)

(b)

(c)

Figure 2.1: Magnetic energy levels as a function of flux per moiré cell (the butterfly plot) for (a) $\alpha = 0.35$ ($\theta \approx 1.82°$), (b) $\alpha = 0.5754$ ($\theta \approx 1.11°$), and (c) $\alpha = 0.595$ ($\theta \approx 1.07°$). The first α lies outside of and the other two lie within the magic range. The nonmagnetic bands in each case are also plotted on the far left with solid grey lines. The insets in (b) and (c) show magnified versions of the magnetic energy levels for the two active bands.

outside and within the magic range; in particular, relatively small field regime and LL filling factors therein are studied. Furthermore, comparison with results derived from a semiclassical analysis is presented. Finally, in Sec. 2.4 these discussions are summarized and also some further results regarding the intermediate and large field regimes, inclusion of particle-hole symmetry breaking terms, etc. are discussed. Further details of these discussions are presented in the Appendix.

2.2 The model

We start with the following model Hamiltonian for zero magnetic field [52]:

$$\begin{aligned} H(\boldsymbol{x}) = &-i\left(\boldsymbol{\nabla} - i\tau^z\frac{\boldsymbol{q}_0}{2} + i\boldsymbol{q}_{\mathrm{h}}\right)\cdot\left(\mathbf{S}_\theta\,\boldsymbol{\sigma}\right) \\ &+ \alpha\,\tau^+\left[\eta\,\beta_0(\boldsymbol{x}) + \beta_1(\boldsymbol{x})\sigma^+ + \beta_2(\boldsymbol{x})\sigma^-\right] + \text{h.c.}, \end{aligned} \tag{2.1}$$

where $\boldsymbol{x}$ and the Hamiltonian are made dimensionless by dividing by the moiré length scale $\frac{1}{k_\theta} = \frac{3\sqrt{3}a}{4\pi\,\theta}$ and the energy scale $\hbar v_{\rm F} k_\theta$. The Pauli matrices τ^z, σ^z are used to address the layer and sublattice degrees of freedom, and their ± 1 eigenvalues denote top/bottom layer and A/B sublattice respectively. The constant vectors $\boldsymbol{q}_{\rm h} = \left(\frac{\sqrt{3}}{2}, 0\right)$, and $\boldsymbol{q}_0 = (0, -1)$ define the center of BZ and the tunneling term is defined using the functions $\beta_n(\boldsymbol{x}) = \sum_{j=0}^{2} e^{-i\boldsymbol{Q}_j\cdot\boldsymbol{x}}\zeta^{nj}$, with $\zeta = e^{2\pi i/3}$. Also, $\boldsymbol{Q}_0 = 0$ and $\boldsymbol{Q}_1 = \sqrt{3}\left(-\frac{1}{2}, \frac{\sqrt{3}}{2}\right)$ and $\boldsymbol{Q}_2 = \sqrt{3}\left(\frac{1}{2}, \frac{\sqrt{3}}{2}\right)$ are the reciprocal moiré lattice vectors. The model has two parameters, one is $\alpha = \frac{w}{v_{\rm F} k_\theta} \sim \frac{w}{\theta}$, which shows the combined effect of interlayer hopping and the twist angle and the other is η which is responsible for incorporating the effect of corrugation [65]. This model concentrates on a single valley of graphene and a single spin, and so in order to take the complete physical system into account, four copies of H should be introduced. The sublattice matrices of the two layers are rotated in opposite directions, this is reflected in the use of the rotation matrix $\mathbf{S}_\theta = \hat{P}_+\mathbf{R}_{+\theta/2} + \hat{P}_-\mathbf{R}_{-\theta/2}$ above, where $\hat{P}_\pm$ is the projector onto top/bottom layer. Upon neglecting the rotation of σ matrices above, the effects of which are small for small θ, one recovers a particle-hole symmetry as defined in Ref. [52]. We will use this approximation unless otherwise stated.

Interestingly, there are two Dirac points (DPs) for all values of α at the K and K$'$ points of the BZ. At the Γ point, on the other hand, the top and bottom active bands reach their maximum and minimum respectively, except for a range of α around $\alpha_1 = 0.57544$ (for $\eta \approx 0.82$); at α_1, the Γ point becomes gapless with a quadratic band touching, and the bands show exceptional flatness. This transition happenning at α_1 is one of the series of topological transitions happening in the magic range ($\theta \approx 1.1^\circ$).

We then incorporate the magnetic field in the same way as is done in Ref. [14] (see App. A.1 for a self-contained derivation), i.e. we start by working in a basis of bare LLs of the two graphene sheets and take the effect of the tunneling term into account by finding its matrix elements in this basis. To solve the model, one is required to impose a commensurability condition for the magnetic flux and the moiré lattice, which validates the notion of a magnetic Brillouin zone (MBZ):

$$\frac{\Phi}{\Phi_0} = \frac{B\mathcal{A}}{\Phi_0} = \frac{1}{2}\frac{q}{p}, \tag{2.2}$$

where $\mathcal{A} = \frac{8\pi^2}{3\sqrt{3}k_\theta^2}$ is the moiré pattern unit cell area, and p and q are co-prime integers. [1] This results in the relation $B(\mathrm{T}) \approx \frac{12(\theta^\circ)^2}{p/q} \approx \frac{1}{\alpha^2}\frac{4.7}{p/q}$ between the magnetic field and the integers p and q. Also, the Zeeman energy is neglected here (we will comment on the possible effect of Zeeman energy in Sec. 2.4). We only consider one of the valleys, and therefore considering the spin degeneracy also, the physical filling factor is 4 times that of the magnetic model introduced above. We will report the model filling factor unless otherwise stated.

---

[1] Note that the commensurability condition chosen here is different from the one in Ref. [14], because of the difference in the convention for the moiré potential (see App. A.1).

2.3 Numerical solution and semiclassical analysis

In order to carry out numerical calculations, we need a cutoff for the number of LLs of the monolayer graphene sheets; we choose this cutoff by the criterion that the energies and the gaps found in the energy range of interest ($|E| \lessapprox 100\text{meV}$) remain approximately constant with further increase of the cutoff. To achieve this condition, we find that the cutoff needs to be taken about ten times larger than the one introduced in Ref. [14]. Generically, larger cutoffs are needed for smaller magnetic fields.

We work with $\eta \approx 0.82$ after Ref. [65], and carry out the analysis for different values of α. As α increases (i.e. θ decreases) we find three regimes, the energy spectrum of each one differs from the other two in a sense that will be discussed below; the comparative study of the three regimes is the main goal of this section. Below we start at larger angles than those in the magic range and discuss the results in depth, then using the same methods we specialize to the two regimes in the magic range.

The large angle regime. The first α value we consider is $\alpha = 0.35$, which corresponds to $\theta = 1.8°$. The energy spectrum as a function of the magnetic flux per unit cell (we will refer to such plots as butterfly plots) is shown in Fig. 2.1a. Note that the magnetic energies change continuously and form *magnetic bands* as the magnetic Bloch momentum is varied within MBZ. Each magnetic band when full corresponds to a density of electrons equal to $\frac{1}{\mathcal{A}}\frac{1}{2p}$, we call this quantity the weight[125] of that magnetic band (see App. A.1).

One first observation from the above plot is as follows: for small enough magnetic fields, there are magnetic energy levels within the range of nonmagnetic active bands and nonmagnetic remote bands, but there is no magnetic energy level in the gap between them. This can be seen in Fig. 2.1a, by noting that the nonmagnetic energy bands are shown on the far left of the plot. The observation holds true for all α values where there is a gap in the nonmagnetic band structure, a range starting around $\alpha = 0.25$ and continuing up to around $\alpha = 0.65$. When this observation holds, by inspection in several cases, the total number of magnetic bands in this active range of energy turns out to be $4p$; thus the corresponding total weight is equal to exactly two states per moiré supercell, which coincides with the density given by the active bands when full. In other words, for small enough magnetic field the energy levels shown in blue in Fig. 2.1 are confined within the range of energy given by the two active bands; their total weight is equal to the total weight of two nonmagnetic active bands. We will be mostly studying the magnetic bands within this active energy range.

There are in principle gaps between each two adjacent magnetic bands, however, there are wider gaps between certain *groups* of multiple bands. Such groups of bands can clearly be seen in the middle and at the edges of the active range of energy for small enough magnetic fields. The energy levels in the middle of the active range correspond to being close to CNP, and the ones at its edge are located close to the superlattice induced gaps. By inspection of the data shown in Fig. 2.1a (see

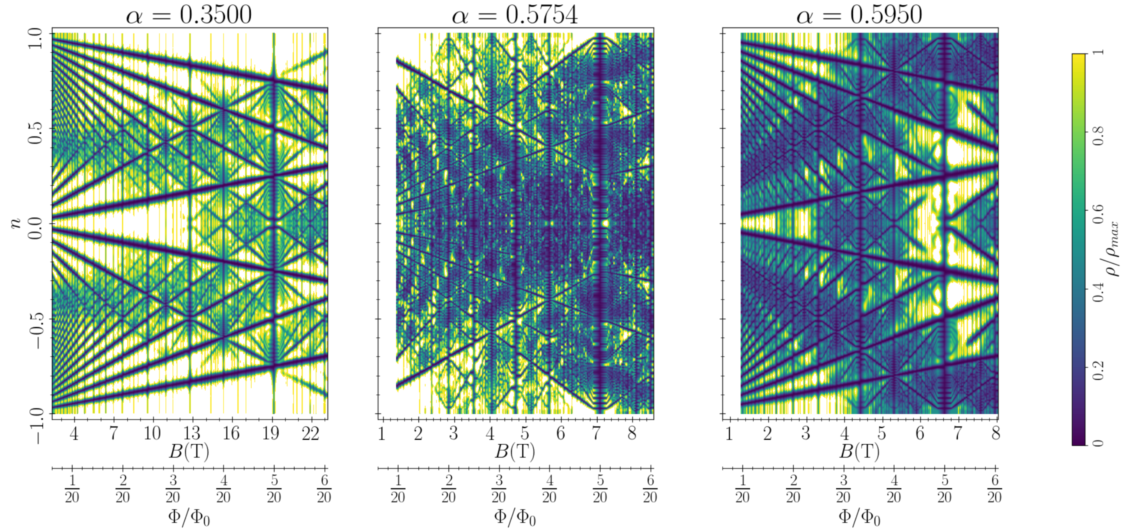

(a) (b) (c)

Figure 2.2: Wannier plots for (a) $\alpha = 0.35$, (b) $\alpha = 0.5754$, and (c) $\alpha = 0.595$ (see App. A.3 for more information regarding these plots). The vertical axes show the carrier density in the unit of one per moiré cell. The colors correspond to rescaled density of states ρ/ρ_{max}. The dark straight lines correspond to gaps and thus full LLs; the LL filling factors can be deduced using the slopes of these lines. A filling factor of 2 for the zero energy LLs can be inferred by noting that at CNP there are dark lines with slopes ± 1 in all of the plots, but no lines with slope 0. Furthermore, the filling factors of 2, 1 and 3 can be seen at CNP above the zero energy LL in the three plots respectively.

Figs. A.1 and A.2 in App. A.2 for a better illustration), the groups of bands at the edges comprise q bands each for a given p/q, while the groups of bands in the middle comprise $2q$ bands. Using the prescription above, it can be inferred that each of the former groups of bands carries a density of $\frac{1}{\mathcal{A}}\frac{q}{2p} = \frac{B}{\Phi_0}$ which is exactly the density of a full LL; likewise, the latter groups carry the total density of two LLs. Note that the wide gaps addressed here should correspond to experimentally seen gaps; they persist over a finite range of p/q and the weights above and below are continuous functions of the magnetic field.

Another way to visualize the weights discussed above is using a Wannier plot[125]; a Wannier plot records the density of states ρ as a function of carrier density n and magnetic field B. In order to calculate density of states we consider widening of each energy level found numerically by associating a Lorentzian density of states with it; its width parameter γ is chosen to ensure maximal resolution (see App. A.3). Such a plot for $\alpha = 0.35$ is presented in Fig. 2.2a. The energy gaps, corresponding to the minima in ρ, form straight lines; the LL filling factor can be inferred from the slopes of these lines. Consistent with the above, filling factors of 2 in the middle and 1 at the edges can be deduced from this plot. Following all the above observations, the filling factor seen in Landau fan diagrams at larger angles [24], can be understood by taking the above weights at CNP, resulting in the sequence $4 \times (\pm 1, \pm 3, \pm 5, \ldots)$ at the CNP (spin/valley degeneracy considered). Note that this coincides with the sequence found in Ref. [24].

The formation of groups of bands and their weights for sufficiently small B can be understood with a semiclassical analysis as well. In this method, in order to find the magnetic energy levels, one finds orbits of constant energy in k-space for a given band structure. Then one imposes the Bohr-Sommerfeld quantization condition[6, 29], which ultimately results in a quantization condition for the area in k-space enclosed by the orbits, denoted by A_k; the energy of such an orbit is obtained from the dispersion landscape. Concretely, quantized orbits formed around quadratic band edges satisfy the condition $A_k = 2\pi \frac{1}{\ell_{\mathrm{B}}^2} \left(N + \frac{1}{2}\right) = \Omega_{\mathrm{BZ}} \frac{\Phi}{\Phi_0} \left(N + \frac{1}{2}\right)$, and orbits enclosing a DP satisfy $A_k = 2\pi \frac{1}{\ell_\mathrm{B}^2}(N+1) = \Omega_\mathrm{BZ}\frac{\Phi}{\Phi_0}(N+1)$, where ℓ_B is the magnetic length, and $\Omega_\mathrm{BZ} = \frac{3\sqrt{3}}{2}k_\theta^2$ is the total BZ area. The difference between the above two cases is due to the π Berry phase accumulated when an orbit encloses a DP.

A plot of the nonmagnetic dispersion at $\alpha = 0.35$ in the top active band is presented in Fig. 2.3a; the two classes of groups of magnetic bands that are formed in the active range i.e. q-band groups at the edge and $2q$-band groups in the middle can be associated with the semiclassical orbits formed in this dispersion surface; each group in the former class can be identified as an orbit around the Γ point and each group in the latter class as the collection of two orbits each around one of the moiré Dirac cones (points K and K$'$). There is very good quantitative agreement between the energies found this way and the energies found in the butterfly plots for small enough fields (see App. A.4).

The magic regime I. We then specialize to the discussion of the magnetic bands in the magic range, i.e. where the active energy range becomes very narrow. The above scenario for the weights of groups of bands in the middle and the edges of the active range remains valid upon increasing α until α gets close to α_1 where the nonmagnetic active bands touch at the Γ point and show exceptional flatness. Noting that $\alpha_1 = 0.57544$, we present results at the close value of $\alpha = 0.5754$, but as discussed later there is in fact a range of α where this applies. A butterfly plot for $\alpha = 0.5754$ ($\theta \approx 1.1^\circ$) is presented in Fig. 2.1b. Still there are $2p$ bands in total in the active range that are shown in blue, corresponding to two electrons per moiré cell.

As before, groups of bands with wide gaps between them can be seen at the edges and in the middle of the active range. This time however, their group weights are different; each of the groups formed in the middle consists of q bands and each of the ones at the edges contains $3q$ bands. Since a q-band group corresponds to the weight of a LL, each of the middle groups carry the density of one LL and each of the edge groups carry the density of three LLs. The two zero energy LLs still have the same behavior. These weights are also exhibited in the Wannier plot shown in Fig. 2.2b; as a result, one expects a sequence $4 \times (\pm 1, \pm 2, \pm 3, \ldots)$ at CNP taking spin and valley degeneracy into account.

A dispersion plot of the top active band is shown in Fig. 2.3b for $\alpha = 0.5754$; note that there is a quadratic low energy dispersion at the Γ point. Remarkably, a semiclassical analysis shows that each of the middle groups of bands corresponds to a semiclassical orbit around the Γ point. Also, semiclassical analysis relates the groups with weights of three LLs at the edges to the orbits around the three inequivalent points $\mathrm{M}_1, \mathrm{M}_2, \mathrm{M}_3$ (which are C_3 related), where the highest (lowest) energy of the top (bottom) nonmagnetic band is reached with a quadratic dispersion (see App. A.4 for details). This set of LL filling factors can be seen in the α range 0.575–0.585, where there can be several DPs in the nonmagnetic active bands; we also observe several level crossings as the magnetic field is varied for small fields, but the sequence is unchanged away from the band crossing points.

The magic regime II. Finally, for slightly larger values of α, yet another different pattern for LL degeneracies emerges, as can be seen in Fig. 2.1c which shows results for $\alpha = 0.595$ ($\theta \approx 1.1^\circ$): a group of bands with a weight equal to three LLs appears in the middle of the active range, and groups of weight equal to a single LL appear at the edge. A semiclassical study (Fig. 2.3c) shows that the group of three LLs in the middle can be identified as the collection of the orbits that take place in the three low energy quadratic dispersions centered on high symmetry lines. On the other hand, the edge groups can be identified as the orbits enclosing the Γ point. The former results in the sequence $4 \times (\pm 1, \pm 4, \ldots)$ at CNP (Fig. 2.2c). This set of LL filling factors can be observed starting around $\alpha = 0.59$ up to $\alpha \approx 0.64$, where the nonmagnetic gap is closed and even beyond that.

It appears from the above results, and in particular the semiclassical analysis, that in the magic range, the low energy magnetic levels around CNP are not related to the dispersion around the two moiré DPs; in fact, one can get further insight using semiclassical analysis: one can identify the only contour in BZ that intersects itself as the saddle contour, which can play the role of separating different classes of orbits based on the orbit centers (shown as solid black contours in Fig. 2.3). In all the above cases, the saddle contours enclose the DPs and therefore limit the total area available to the orbits forming around K and K$'$; it is indeed the case at $\alpha = 0.5754$ and $\alpha = 0.595$ that the total area available around each DP is sufficient for an orbit to form only for very small magnetic fields, while orbits within other quadratic dispersion areas of the BZ begin to form at much larger fields. Concretely, the first orbits around

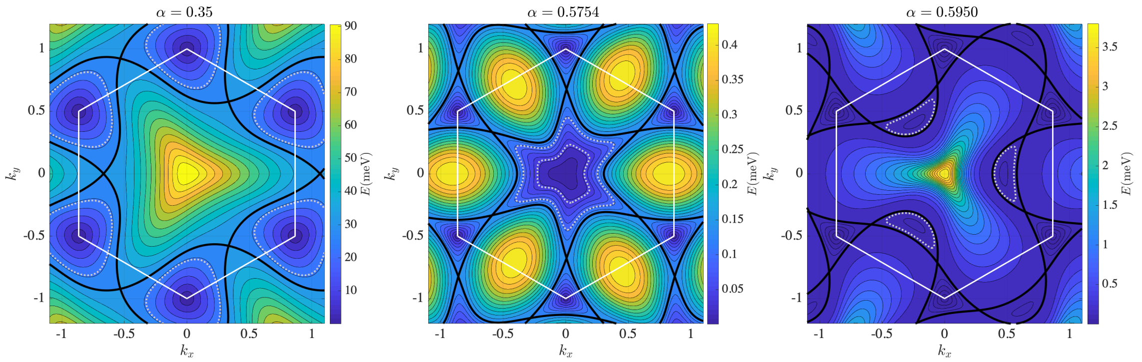

(a) (b) (c)

Figure 2.3: The nonmagnetic band structure in the BZ for three values of α. The BZ is shown as a white hexagon; there are two DPs located at its vertices K and K$'$ points and the Γ point is located at its center. It can be seen that in the magic range there are low energy regions in the BZ other than the vicinities of DPs (the two cases on the right). Some semiclassical orbits closest to CNP are shown in the three cases with dotted grey lines; the orbits are found at $\Phi/\Phi_0 = \frac{1}{10}$ for $\alpha = 0.35$, and $\alpha = 0.5754$, at $\Phi/\Phi_0 = \frac{1}{25}$ for $\alpha = 0.595$.

the DPs only form at $\frac{\Phi}{\Phi_0} \approx \frac{1}{25}$ ($B \approx 1$T) in the first case and at $\frac{\Phi}{\Phi_0} \approx \frac{1}{30}$ in the second case.

2.4 Discussion and Conclusion

We have considered the non-interacting continuum model of twisted bilayer graphene at twist angles above and within the magic range ($\approx 1^\circ$) when subject to a perpendicular magnetic field. The magnetic energy levels are found by imposing magnetic commensurabilty with the moiré superlattice, resulting in butterfly plots. By careful inspection we have derived three different sequences for the LL filling fractions at CNP as the twist angle is changed, i.e. $\nu = \pm4, \pm12, \pm20, \ldots$, for angles larger than the magic angle, and $\nu = \pm4, \pm8, \pm12, \ldots$ and $\nu = \pm4, \pm16, \ldots$ within the magic range with spin and valley degeneracies considered; we have presented these results concretely at the three α values of 0.35, 0.5754, and 0.595 respectively. We note that the second of these sequences seems to correspond to that which is observed experimentally by several groups. However, in the present model this sequence occurs only for a narrow range of α parameter. It is possible that the range in which this behavior occurs is enhanced by interaction effects, not included here, for example self-energy corrections. It is also possible that the observed sequence has an entirely different origin. We do not resolve this here but believe our results provide useful input to the issue.

We explained the above results by a semiclassical analysis of the energies at small magnetic fields. We found that in the magic angle range there is not enough area for even the first semiclassical orbit to form around the moiré DPs (the K and K$'$ points at the BZ corners), unless the magnetic field is very small ($\lessapprox$ 1T). This shows that in the magic range other areas of the BZ are responsible for the low energy LLs around CNP; as discussed above, the Γ point for $\alpha = 0.5754$ and three local minima appearing on high symmetry lines for $\alpha = 0.595$ play this role.

We have neglected the effect of Zeeman energy in this work; this approximation is indeed justified by an experimental result in Ref. [137] where it is argued, by a comparison between observed landau fan diagrams with a perpendicular field and a titled field, that the main sequence seen in Landau fan diagrams is not caused by spin splitting. However, taking the Zeeman effect into account will be also interesting.

Although we have been mostly concerned with relatively small magnetic fields in this work, the formalism also works for large fields. In particular, we have studied how the transition from the previously discussed small B regime to large B regime happens when there is a gap between active and remote nonmagnetic bands (see App. A.2). Deep in the small field limit, as discussed above we see a total density equal to two electrons per moiré cell confined within the active range of energy; the two gaps above and below this range evolve continuously as the magnetic flux is increased. In the large field limit on the other hand, one expects to recover the bare LLs of the monolayer graphene sheets, each widened due to the effect of the moiré lattice. The interpolation between the above two limits happens at intermediate field range; at a generic η (we have been using $\eta = 0.82$ as an example) one can see two different behaviors as α is varied: either i) the zeroth LLs of the two moiré DPs (small B) are adiabatically connected to the bare zeroth LLs of monolayer sheets (large B), which happens for smaller gaps, or ii) the total weight of two nonmagnetic bands (active range) at small B is adiabatically continued into the large B limit also, which occurs when the gap becomes larger (see Figs. A.1 and A.2 in App. A.2 for these cases). This observation is consistent with the results presented in Ref. [72], especially those where there is a gap[2].

As stated above, one expects to recover bare LLs of monolayer graphene sheets in the infinite magnetic field limit; the two bare zeroth LLs are infinitely far apart

---

[2] The result was reported differently in an earlier version of Ref. [72]: it was stated that the small field gap between the magnetic bands confined within the active range and higher bands is always closed with a sharp transition around $\Phi/\Phi_0 = 1$, for all α values. This was attributed to the "fragile topology" of the active bands in TBG.

in energy from other LLs, and so in this limit a low energy description of the model can be obtained through projection onto these two LLs. Remarkably, by looking at the detailed structure of the projected Hamiltonian, we find a duality between the description of these zeroth LLs at infinite magnetic flux limit, and a tight binding honeycomb model (i.e. the honeycomb Hofstadter butterfly[104]) at small magnetic flux limit (see App. A.6 for detail), with the layer index for the two zeroth LLs $s = 1, 2$ in the former theory playing the rule of honeycomb sublattice index in the latter. Sharing the same band structure and density of states, the latter theory which has been studied extensively can shed some light on the expected properties of former (see Appendices A.6 and A.7 for details).

It is worthwhile to discuss also the particle-hole symmetry we have considered here; restoring the sublattice pseudospin rotation in both the magnetic and nonmagnetic Hamiltonians will result in breaking of the particle-hole symmetry of both spectra. In the magnetic model, we have checked that (see App. A.5 for details) the relatively small field results and in particular the filling factors do not change except when one is close to α_1, where some level crossings can occur at small magnetic fields in the middle of the active range (see Fig. A.5 in App. A.5). These level crossings can be understood by noting that there are α values at which both of the non-magnetic active bands have a minimum (or a maximum) at the Γ point; as a result, an orbit forming around the Γ point in the top layer can have an energy smaller than that of the zeroth LLs of the DPs for small magnetic fields (see Fig. A.4 in App. A.5).

It is natural to expect that the LL degeneracy of 3 (not taking spin/valley degeneracy into account) that is seen at the edge of the active range at $\alpha = 0.5754$ and in particular at CNP at $\alpha = 0.595$ can be lifted when other effects are taken into account to make the study more realistic. The following three are the most obvious effects to consider: i) the effect of symmetry breaking terms at the level of noninteracting physics which can be induced by the effects of the environment, such as the hBN substrate; ii) the effect of disorder, which is not taken into account here and can have very nontrivial impact on Dirac dispersions[94, 9]; iii) and finally the effect of electron-phonon and electron-electron interactions which are neglected here. It would be an interesting further step to explore how taking these effects into account can affect the results presented here.

Chapter 3

Hybrid Wannier Chern bands in magic angle twisted bilayer graphene and the quantized anomalous Hall effect

In this chapter, we propose a method for studying the strong interaction regimes in twisted bilayer graphene using hybrid Wannier functions, that are Wannier-like in one direction and Bloch-like in the other. We focus on the active bands as given by the continuum model proposed by Bistritzer and MacDonald, and discuss the properties of corresponding hybrid Wannier functions. We then employ the method for a study of the fillings of ±3 electrons per moiré cell using the Hartree-Fock method. We discuss at length different regimes under which a quantized anomalous Hall effect is seen in these two fillings.

This chapter is based on Ref. [50].

3.1 Introduction

Heterostructures containing moiré patterns due to incommensurations in multilayers containing graphene and other two dimensional crystals have proven to be very tunable and promising platforms for observing interesting phases that are unprecedented in commensurate graphene systems[25, 26, 137, 79, 111, 110]. Twisted bilayer graphene (TBG) as the most prominent member has attracted much attention and also has given rise to numerous theoretical studies; however, still many of the different correlation induced phenomena in this system have eluded satisfactory theoretical understanding.

The most important theoretical discovery, probably, was the realization that a low energy theory, a continuum model (CM), could be effectively employed to study the single particle electronic properties of TBG at small twist angles [15]; in fact, an analysis based on this CM resulted in the prediction of the possibility of strong correlation physics at the magic angle in the first place. Specifically in this CM, the smallness of the twist angle leads to an emergent periodicity in the system – the so called *moiré* lattice, which has a unit cell length growing like $\sim \frac{1}{\theta}$; such large periodicity in turn leads to formation of Bloch *minibands*. Interestingly, around the magic angle, the bands closest to the charge neutrality point (CNP) show exceptional flatness and are well separated from other bands. Further including spin and valley degrees of freedom results in eight such bands in total. Since these bands are flat, the correlation between them can play an important role and give rise to interesting correlated phases and thus should be taken into account properly. A possible theoretical approach to this end, is to consider an interacting model consisting of these *active* bands only, treating the *remote* bands as inert; we will be taking this route in this work and introduce a basis for the study of strong interactions.

Experimental observations of correlation induced insulating states have been reported in commensurate fillings of these active bands, along with superconducting behavior for fillings close to these commensurate values[25, 26, 137, 79, 111, 110, 108, 116]. Motivated by these experimental observations, here we pursue a theoretical model consisting of the subspace of the active bands only, in which electronic interactions are also projected onto this subspace; these interactions are local and thus working with local representations of the subspace spanned by active bands is desirable. However, as is well known, a faithful representation preserving manifest symmetries of the active bands using fully localized Wannier functions is difficult[2, 102]. Having this in mind, in this work, we work with Hybrid Wannier Functions (HWFs) which are Bloch-like in one direction and localized and Wannier-like in the other. Using this basis is a compromise between locality and symmetry/topology, noting that the wave functions are only localized in one direction, however, as is elaborated later, this ensures that important symmetries like valley and $C_2\mathcal{T}$ (the intravalley symmetry that protects the moiré Dirac points) remain manifest (when not broken at the non-interacting level). Furthermore, one ends up with a quasi-one-dimensional model, with local interactions in one direction, which can be suitable for numerical methods like DMRG[61].

As we show later, remarkably, full bands of these HWFs when maximally localized automatically exhibit a nonzero Chern number; this means that indeed a suitable collection of full bands of such states can display quantized anomalous Hall effect (QAHE), a phenomenon that has been reported in TBG[111, 110] at the filling factor of $\nu = +3$ (we define the filling factor ν to show the number of electrons per moiré cell measured from CNP). This makes the present *maximally localized* HWFs a natural basis for a corresponding theoretical study. To analyze the effect of the interaction, which is evidently required for stabilizing a full band polarization in the HWF basis, we employ the self-consistent Hartree-Fock (HF) method at the two fillings $\nu = \pm 3$; these are the fillings where single fully occupied HWF bands of holes or electrons can be candidate many body states respectively.

We perform two separate studies of the effect of electron-electron interaction; first, we examine how the locality (in one direction only) of the HWFs makes full HWF bands advantageous for the interaction energy penalty when compared with other many body states at the same filling. Specifically, we check if full HWF bands turn out to be solutions of the HF equations when interaction is considered; this ensures that such HWF band polarized states have (at least local) minimal interaction energy compared with other candidate many body states. Second, we study the stability of similar many body states in a model obtained by projection of the full Hamiltonian onto the active bands. We present numerical results on the stability of QAHE in these two settings in a wide range of parameter choices of the models.

There have been other HF studies of the continuum model at various integer filling factors, with the analysis carried out completely using the basis of original Bloch states[77, 75, 133, 21]; in a subset of these works the remote bands are also kept in the analysis. The present study has the advantage of working directly with a faithful semi-localized representation of the active bands, while providing a continuous description of the QAHE with and without the $C_2\mathcal{T}$ symmetry of TBG. Moreover, in the present analysis, the QAHE appears naturally as polarized bands in the HWF basis and this could provide some more insight into the nature of the Chern bands responsible for this effect. A comparison between these prior HF studies and our results is presented in Appendix B.5.

The chapter is organized as follows: first, in Sec. 3.2, we demonstrate how the maximally localized HWFs are constructed and derive their topological properties. Then, in Sec. 3.3, we present the HF study of the interacting model at the fillings ±3, and the stability of QAHE by varying various parameters is examined. We conclude our results in Sec. 3.4.

3.2 Hybrid Wannier functions

We will be working with the continuum model introduced in Ref. [15]. To take into account the two valleys, two parallel copies of the CM are considered; in each copy, we will focus on the two *active* bands, closest to CNP. Details of the non-interacting Hamiltonian are presented in Appendix B.1. The CM has two free parameters in it: i) $\alpha \sim \frac{1}{\theta} w_{\mathrm{AB}}$, which accounts for the collective effect of interlayer hopping w_{AB} and the twist angle θ, and ii) $\eta = \frac{w_{\mathrm{AA}}}{w_{\mathrm{AB}}}$, the ratio of the interlayer tunneling strength in AA and AB regions of the moiré lattice, which encodes how much corrugation is present in the system. We will also consider adding a sublattice symmetry breaking term $\Delta\,\sigma^z$ to the non-interacting Hamiltonian, where the Pauli matrix σ^z is used to address sublattice degrees of freedom; this could account for the effect of aligned hexagonal Boron Nitride (hBN) substrates on the two sides of the TBG sample. [1] We will also be using an approximation[52, 114] which renders a particle-hole symmetry to the CM; this approximation becomes better at small angles, see Appendix B.1 for details.

Equipped with the full non-interacting content of the model, one can find the Bloch states lying in the middle two active bands for each valley. We take the active bands to be well separated from the remote bands, and thus develop an active-bands-only model. Following the notation and methods introduced in Refs. [82, 81] we will Wannier transform properly chosen Bloch states in only one direction to obtain the

---

[1] More relevant to experiments is a setup with different subalttice potentials on the two layers, but here for simplicity we take the potential to be identical on both layers.

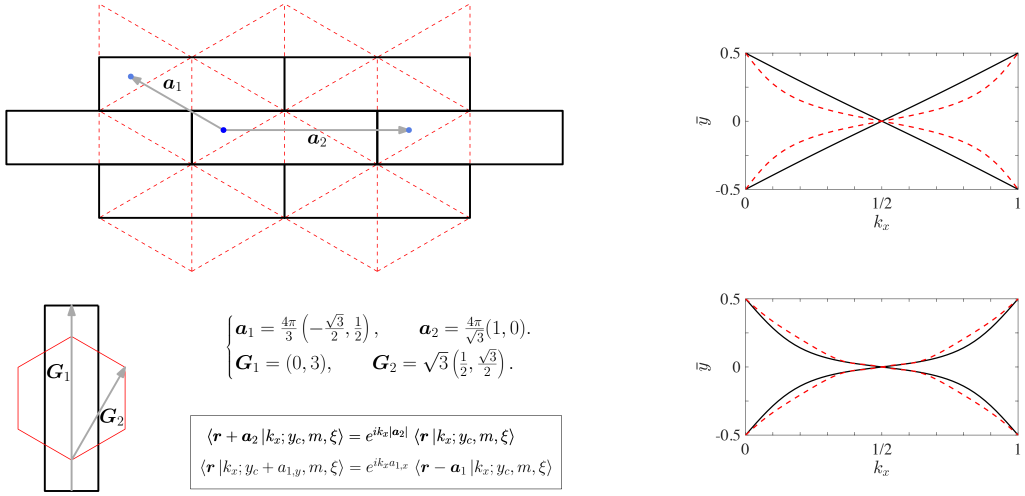

(a)

(b)

Figure 3.1: (a) The moiré lattice in real space and the corresponding BZ. A rectangular BZ is chosen $-\frac{\sqrt{3}}{4} < k_x < \frac{\sqrt{3}}{4}$, $-\frac{3}{2} < k_y < \frac{3}{2}$; note that this is contrary to the usual hexagonal choice so that the top and bottom of the BZ are identified, note that this is crucial for the usual properties of the one-dimensional Wannier transform in the y direction to hold. The equations governing the translational properties of the HWFs are also presented. (b) WCC positions (solid black lines) and single band Berry phases in the original Bloch bases (dashed red lines) of the two active bands. The top plot corresponds to the chiral limit, i.e. $\eta = 0$ and the bottom one corresponds to the physical value of $\eta = 0.8$. A small sublattice potential is added, $\Delta = 0.19$meV. The configuration of the dashed lines and the solid lines mean that the two bands carry $+1$ and -1 Chern numbers in the original Bloch representation and the parallel transport representation respectively. This is a robust feature present in a wide range of parameter choices. Note that k_x is rescaled and instead of plotting the interval $[-0.5, 0.5)$, equivalently $[0, 1)$ is drawn.

maximally localized HWF basis as follows:

$$\begin{aligned} |k_x; y_c, m, \xi\rangle &= \frac{1}{N_y} \sum_{k_y} e^{-ik_y y_c} \left|\tilde{\psi}_{\boldsymbol{k};m,\xi}\right\rangle , \\ \left|\tilde{\psi}_{\boldsymbol{k};m,\xi}\right\rangle &= \sum_{y_c} e^{ik_y y_c} |k_x; y_c, m, \xi\rangle , \end{aligned} \tag{3.1}$$

where $|k_x; y_c, m, \xi\rangle$ stands for a Hybrid Wannier state, with the indices y_c, m, ξ denoting the real space position in the localized direction, the band (orbital), and the valley respectively. The states on the right hand side are linear combinations of the

Bloch eigenstates of the non-interacting Hamiltonian at each $\boldsymbol{k}$:

$$\left|\tilde{\psi}_{\boldsymbol{k};m,\xi}\right\rangle = \sum_{n} \left|\psi_{\boldsymbol{k};n,\xi}\right\rangle U^{\boldsymbol{k},\xi}_{nm}. \tag{3.2}$$

The unitary (in the band basis) matrices U are chosen at each $\boldsymbol{k}$ to ensure that maximal localization is achieved in the y direction ultimately and the procedure is detailed below. Here, a rectangular BZ is chosen as shown in Fig. 3.1a so that the k_y sum needed for a one dimensional Wannier transform in (3.1) is performed at each k_x. The spin index trivially doubles all manipulations here and thus is suppressed. With the above convention, the allowed values of y_c form a one dimensional lattice with lattice spacing equal to half a moiré length ($\frac{1}{2}a_M = a_{1,y}$), i.e. $y_c = j\frac{a_M}{2}$ where j is an integer. Note that we take this lattice to be identical for different values of k_x, and so the above y_c values are different from but close to the actual locations of Wannier charge centers (WCC) of HWF states (see below for more information). The transformation of the HWFs under moiré lattice translations is depicted in Fig. 3.1a.

In order to obtain maximal localization, one needs to choose the matrices U in (3.2) properly: to this end, we will use the procedure discussed in Ref. [82] to form the *parallel transport* basis for the Bloch functions, an approach that is suitable for maximal localization of one dimensional Wannier functions, and in the present study should be carried out for each strip with a definite k_x separately. We will use a discretization which will lead to a Bloch momenta lattice with lattice spacings b_x, b_y, and with N_x, N_y total points along the two directions. According to this prescription, at each $\boldsymbol{k}$, the overlap matrices

$$\mathcal{M}_{mn}^{k_x,k_y,\xi} = \left\langle u_{k_x,k_y;m,\xi} \middle| u_{k_x,k_y+b_y;n,\xi} \right\rangle , \tag{3.3}$$

are calculated, where as usual $|u_{\boldsymbol{k};n,\xi}\rangle$ shows the unit cell periodic part of an original Bloch function; notice that there is a small displacement in the k_y direction in the ket state. Next, redefinitions of Bloch functions are made as shown in (3.2), with U matrices chosen in a way that the updated $\mathcal{M}$ matrix for all k_x, k_y, ξ attains a form as $K^{k_x,k_y,\xi}\ \gamma^{k_x,\xi}$, where K is Hermitian and γ is diagonal, unitary and independent of k_y. This, as discussed in Appendix B.2, ensures maximal localization in the y direction.

The path ordered product of all $\mathcal{M}$ matrices along a strip with a given k_x defines its Wilson loop, whose eigenvalues are invariant under a $\boldsymbol{k}$ dependent basis change such as the one in (3.2). One can show that the K matrices as defined above are equal to the identity matrix to first order in b_y and thus, the eigenvalues of each $\gamma^{k_x,\xi}$ matrix above are directly related to the Wannier charge center positions, i.e. Wilson loop eigenvalues, in the strip given by k_x. Using this fact, WCCs of HWFs as functions of k_x could be found with examples drawn in Fig. 3.1b. It could be seen by inspection that, regardless of the set of parameters chosen, there is a $+1$ winding and a -1 winding of the WCCs for the two HWF bands as k_x traverses the BZ.[76, 114] Noting, based on the above observations, that in the parallel transport basis, the single band Berry phases along each strip with a given k_x are equal to the WCC values, leads us to an important implication for the parallel transport basis: given how WCCs behave as functions of k_x shown in Fig. 3.1b, the two Bloch bands in the parallel transport basis have Chern numbers +1 and −1. This, in other words, means that a fully filled band of maximally localized HWFs exhibits a quantized Hall response. As a result, when addressing the *maximally localized* HWFs, the terms band, orbital and Chern number could be used interchangeably.

In some special cases, the parallel transport basis can be found explicitly. For instance, when $\Delta = 0$, there is a $C_2\mathcal{T} = \sigma^x\mathcal{K}$ symmetry of the Hamiltonian, where $\mathcal{K}$ is the complex conjugation operator; as shown in Appendix B.2, the combinations $\frac{e^{\pm i\phi_{\boldsymbol{k},\xi}}}{\sqrt{2}}\left(|\psi_{\boldsymbol{k};1,\xi}\rangle \pm i\,|\psi_{\boldsymbol{k};2,\xi}\rangle\right)$, with the phases $\phi_{\boldsymbol{k},\xi}$ appropriately chosen, form the parallel transport Bloch basis at $\boldsymbol{k}$, where states $|\psi_{\boldsymbol{k};m,\xi}\rangle$ show $C_2\mathcal{T}$ symmetric Bloch eigenstates. In particular, if one now sets $\eta = 0$ to obtain the chiral limit, since the two $C_2\mathcal{T}$ symmetric bands are related[117] by $|\psi_{\boldsymbol{k};1,\xi}\rangle = i\sigma^z\,|\psi_{\boldsymbol{k};2,\xi}\rangle$, the parallel transport basis consists of sublattice polarized states; remarkably, even with $\Delta \neq 0$ while keeping $\eta = 0$ this result holds, i.e. the parallel transport basis consists of sublattice polarized states. By numerical inspection, one can show that each of the two bands in the parallel transport basis is more concentrated on one of the sublattices to a high degree in a one-to-one fashion, even away from the chiral limit. It is worthwhile to mention that the $U(4) \times U(4)$ symmetry discussed in Ref. [21] (which states that the interaction term of the Hamiltonian is invariant under rotations of the bands with equal Chern numbers into each other) could be seen readily in the above construction of the parallel transport basis. This along with other symmetries of the CM as seen in the HWF basis are discussed in length in Appendix B.3.

The HWF basis naturally defines the problem in the geometry of a cylinder. The HWFs form ring shaped wires around the cylinder, since these wave functions are localized in one direction and extended in the other. Each wire is identified with a y_c, and is composed of states with different values for their k_x, band number, valley number and spin (see Eq. (3.1)). At the non-interacting level, hopping occurs between states in separate wires if they have identical k_x, valley number and spin (See Appendix B.3 for details). This hopping decays as the distance between wires along the cylinder is increased. Based on this HWF construction, in the next section we will present a HF study of a model consisting of active bands only with a total Hamiltonian of the form:

$$H = H_{\text{kin}} + H_{\text{int}} + H_{\text{MF},0}. \tag{3.4}$$

H_{kin} contains the single particle terms in the Hamiltonian induced by the CM, i.e. the hoppings between different wires as mentioned above. The remaining two terms represent effects of interactions: they are both proportional to e^2/ϵ, where e is the electron charge and ϵ is the dielectric constant, and thus vanish in the non-interacting limit. $H_{\text{MF},0}$, which is quadratic in fermion operators, is responsible for two separate effects: it takes the effect of filled remote bands into account at a mean field level and it also serves to avoid a double counting of HF terms that are already taken into account in H_{kin}[77, 21] (see the discussion at beginning of the next section for more details). Turning to the interaction term H_{int}, we have chosen the electron-electron potential to have a screened coulomb form as $V_{\text{int}}(\boldsymbol{r}) = \frac{e^2}{4\pi\epsilon}\frac{e^{-|\boldsymbol{r}|/\ell_\xi}}{|\boldsymbol{r}|}$, which is further projected onto the active bands. The interaction retains its *normal-ordered* density-density form with respect to spin, sublattice, layer and valley indices (more details are presented in Appendix B.3). Note that due to the locality of HWFs, the electron-electron interaction between the wires drops as the distance between them is increased, and thus the total Hamiltonian is local in the direction along the cylinder.

We conclude this section by some remarks regarding the parameter values and conventions used: via dividing the energies and lengths by $\hbar v_F k_\theta$ and $\frac{1}{k_\theta}$ respectively, we have made them dimensionless, where $k_\theta = \frac{4\pi}{3}\frac{1}{a_M}$. In this notation, we define the dimensionless interaction strength parameter $g_{\text{int}} = \frac{e^2}{2\epsilon}\frac{1}{\hbar v_F k_\theta^2 \mathcal{A}}$, where $\mathcal{A}$ is the area of a moiré unit cell. Numerically $g_{\text{int}} = 1.01\frac{\epsilon_0}{\epsilon}$, and thus, a choice of $\epsilon = 7\epsilon_0$ results in $g_{\text{int}} = 0.14$ as an example.

The model introduced above comprises bands (in the parallel transport basis) that carry nonzero ±1 Chern numbers; thus a quantized Hall signal can be observed at integer filling factors if with some interaction induced effect, a suitable valley and band polarization in the system occurs. As a result, it is natural to utilize the present model to study the physics of quantized anomalous Hall effect (QAHE) seen in some samples of twisted bilayer graphene[111, 110]. We will do so in the following section for the two fillings $\nu = \pm 3$.

3.3 Quantized anomalous Hall effect in twisted bilayer graphene

In this section, we present two separate HF studies in which different choices of $H_{\mathrm{MF},0}$ are utilized. We focus on the filling $\nu = \pm 3$ and explore the stability of QAHE phase in these two different schemes. Before we go into the detail, we first discuss how the HF procedure is carried out in general.

The HF procedure is implemented as follows: we fix the filling and seek a Slater determinant many body state, composed of single particle states $|\psi_l\rangle = \sum_\alpha \psi_{l,\alpha} |\alpha\rangle$, that minimizes the expectation value of the Hamiltonian (3.4), where $\alpha, \beta, \ldots$ denote the HWF basis indices k_x, y, ξ, m, s (the states $|\alpha\rangle$ will be normalized in this section). One seeks $|\psi_l\rangle$ states by transforming the Hamiltonian (3.4) written in the form

$$\begin{aligned} H = &\sum_{\alpha\beta} H_{0,\alpha\beta}\; c^\dagger_\alpha c_\beta \\ &+ \frac{1}{2} \sum_{\alpha\beta\,\alpha'\beta'} V_{\alpha,\beta,\beta'\alpha'}\; c^\dagger_\alpha c^\dagger_\beta c_{\beta'} c_{\alpha'}, \end{aligned} \tag{3.5}$$

into a single particle *HF Hamiltonian*, wherein the interaction term is transformed into

$$\begin{aligned} H^{\mathrm{HF}}_{\mathrm{int}} = &\sum_{k_1 k_2, aa'bb'} c^\dagger_{k_2 b} c_{k_2 b'}\, P(k_1)_{aa'} \\ &\left[V_{k_1 a, k_2 b, k_2 b', k_1 a'} - V_{k_1 a, k_2 b, k_1 a', k_2 b'}\right]. \end{aligned} \tag{3.6}$$

In the above, $a, b, \ldots$ (contrary to $\alpha, \beta, \ldots$) show the HWF indices except k_x. Notice that we have dropped the x subscript from k_x and will do so from now on; the k dependent matrices P have the form $P(k)_{aa'} = \sum_l \psi^*_{l,ka}\, \psi_{l,ka'}$. It has, furthermore, been assumed that the translational symmetry around the cylinder is not broken.

The above HF Hamiltonian depends on its own eigenstates and thus we aim to obtain them iteratively: starting from a well chosen initial many body state, at each iteration step, P matrices are updated using the eigenstates found in the previous step; a ν dependent number of these eigenstates with lowest eigenvalues participate in forming the P matrices. The resulting HF Hamiltonian is then diagonalized to yield the updated set of eigenvalues and eigenstates. This procedure is continued until convergence is achieved. We obtain the sought HF many body state as a slater determinant of the converged eigenstates with lowest HF eigenvalues. Moreover, the nearby eigenvalues above and below the “Fermi energy” could be used to give estimates of the actual energies needed for adding or removing an electron at this filling (Koopmans’ theorem[97]) [2].

The two approaches mentioned at the beginning of this section are taken into account by two different choices for $H_{\mathrm{MF},0}$ in the Hamiltonian (3.4). In the first study, Sec. 3.3.1, we examine the motivation with which the HWF basis was introduced: the interaction energy of different many body states are compared with $H_{\mathrm{MF},0} = 0$. In particular, the energy of the state that is described as a full band of electrons ($\nu = +3$) or holes ($\nu = -3$) in the HWF basis is compared with other HF many body states. Note that this choice of $H_{\mathrm{MF},0} = 0$ results in a competition between the interaction

---

[2] Koopmans’ theorem yields the change in energy if an electron or a hole is added to an N-particle HF state, while assuming that the N electrons’ states are unaltered. This is not necessarily a good approximation even in the HF approach. However, we mostly use a gap in the HF eigenvalues to determine whether QAHE is stabilized or not as detailed in the main text.

energies and the band structure energies as given by the CM; the latter, which could also be viewed as the hopping term in the HWF basis, is kept in the analysis so that one attains a measure for defining strong and weak interaction regimes.

In the second study, in Sec. 3.3.2, on the other hand, we take[3]

$$H_{\mathrm{MF},0} = -\sum_{\alpha\alpha'} \left[{\sum_{\beta\beta'}}' \left(V_{\alpha,\beta,\beta',\alpha'} - V_{\alpha,\beta,\alpha',\beta'} \right) \right] c^\dagger_\alpha c_{\alpha'} \tag{3.7}$$

where the α, α' summation is done over *all* states in the active bands, but the *partial* summation over β, β' (indicated by the prime on the sum) ranges *only* over those states in the active bands that are below the CNP of the CM. Note that the latter states when written in terms of the HWF basis will not be band diagonal. By taking $H_{\mathrm{MF},0}$ to have the form in Eq. (3.7), we are taking two separate effects into account: first, a mean field potential induced by the filled remote bands. The second effect, instead, has to do with the fact that within HF, the electron/hole dispersion will only agree (at best) at one filling with the dispersion given by the term H_{kin}. We take that point to be the CNP of the CM bands in the second study, i.e. we assume that the CNP dispersion given by the CM, describing single electron or single hole excitation energies on top of the CNP, is unaltered by HF (see Appendix B.3 for discussion). In order for this to be true, a HF effect of all filled bands (including remote and active bands) at the CNP is subtracted. The combination of these two effects results in a cancellation of the mean field effect of the filled remote bands and thus one ends up with the form in (3.7) with only the mean field effect of active filled bands subtracted.

---

[3] This choice is similar to the one in Ref. [77].

In the next two subsections, we present our numerical results corresponding to these two studies.

3.3.1 First study

In this subsection, we consider a model in which $H_{\mathrm{MF},0} = 0$, wherein a competition between electron-electron interactions and the noninteracting hopping in the HWF basis enables us to tune the model into and out of the strong coupling regime. Previous studies, working on generic models similar to the one used in this subsection, have shown analytically that in strong coupling limits, valley polarization in these two filling factors is expected[5, 105]. Here, we present a more thorough HF study of the Hamiltonian, trying to identify different regimes in which QAHE could be achieved.

In a given setting, we say that the QAHE is stabilized through HF if two requirements are met: i) if we initialize the HF iterative process with a fully spin-valley-band-polarized state, the HF iterations lead to a final HF state that is only achieved through smooth deformation of the spin-valley-band-polarized state (see below for further discussion of this notion of smooth deformation), and ii) the final HF solution properties in large enough systems do not change considerably as the system size is varied.

This means that the QAHE state is at least a minimum of energy; we have also tried perturbing the final HF state in different ways to examine the stability of the HF solutions and we have observed that the final many body states generally show a high

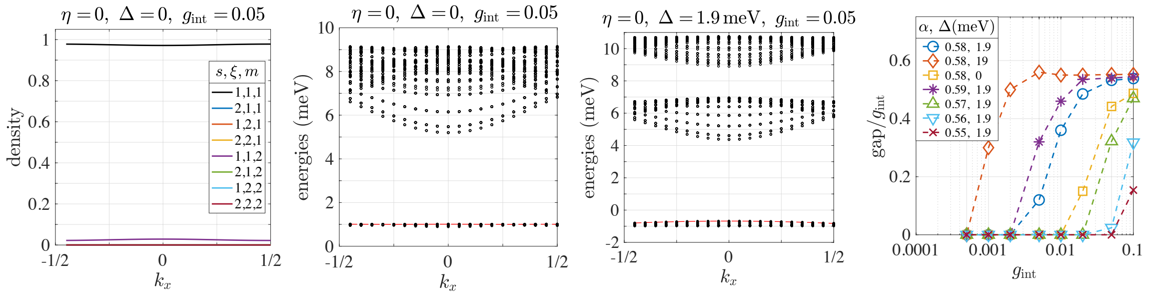

(a) (b) (c) (d)

Figure 3.2: The filling $\nu = -3$, $\eta = 0$, and $\ell_\xi = 0.17a_M$ plots within the first study, the angles are chosen around the magic value ($\alpha_0 = 0.586$ corresponding to $\theta = 1.05°$) (a) Density of electrons (number of electron per unit length of the cylinder) vs k_x (momentum across the cylinder) for different flavors where s, ξ, m stand for spin, valley, and band. $\alpha = 0.58$, $\Delta = 0$ and furthermore $g_{\rm int} = 0.05$ have been chosen here, this value for the latter corresponds to being close to strong interaction limit since the band width is very small. Almost full polarization is seen here. (b) The HF eigenvalues (energies), with the same parameters as described in (a). The Fermi surface is shown with the dashed red line, one can observe a HF gap which will be used as a criterion for determining whether QAHE has been stabilized under HF iterations or not. (c) The same plot as in (b) with $\Delta = 1.9$meV. One can observe a second gap that is formed above the interacting one, due to the relatively large Δ chosen; it separates the states belonging to the opposite sublattices. (d) The HF gap divided by $g_{\rm int}$ as a function of $g_{\rm int}$ for several parameter choices. It can be inferred that approaching the magic angle and making Δ larger makes the QAHE more HF stable.

level of stability (see the discussion right above Sec. 3.3.2 for more on other possible HF solutions). In each setting we start with strong interactions first and see if the QAHE state is stabilized, and then continue to lower the interaction strength. We will, furthermore, use periodic boundary conditions along the cylinder. For the numerical results presented in this chapter, the system is chosen to have $N_x = N_y = 20$.

$\eta = 0$, short range interaction

We now start to present our numerical HF results. We construct the basis of HWFs by forming the parallel transport basis on a finite lattice in k-space as discussed in Appendix B.2, and then make a Wannier transform along y for each k_x.

The chiral model, i.e. when $\eta = 0$, is first considered, in which absolutely flat bands are achieved at the magic angle. We start with the small ℓ_ξ limit so that the electron-electron interaction $V_{\text{int}}(\boldsymbol{r})$ is very short ranged. More realistic longer range interaction is considered later. Moreover, we also take the twist angle different from but close to the magic value so that the bands exhibit a nonzero small width.

In the first setting outlined above, or concretely with the choices $\eta = 0$ and $\ell_\xi = 0.17a_M$, numerical analysis shows that the QAHE is generically stabilized at $\nu = -3$ at large interaction strength, see Fig. 3.2(a,b), where the density of different flavors along with HF eigenvalues (energies) are shown for an instance where the interaction plays the dominant role. Note that because of the nature of the HWF basis, this is a $C_2\mathcal{T}$ broken many body state, despite the fact that this symmetry is present at the noninteracting level. We define a HF gap as the lowest unoccupied HF eigenvalue minus the highest occupied eigenvalue, this quantity when divided by the interaction strength g_{int} serves as a good qualitative measure of whether and to what extent the polarized state is stabilized under HF.

Note that in Fig. 3.2(a), although the many body state has components in both HWF bands in a single valley and spin sector, and the two bands have opposite Chern numbers, the Hall conductivity signal resulting from such state will be quantized; to see why this is in fact true, let us consider this HF many body state as defining an effective *filled* band. For a spin-valley-band polarized state which is achieved at large interaction strength, the filled band coincides with one of the HWF bands and thus has manifestly a nonzero Chern number; we can then consider a HF solution for smaller interaction strength, where the single particle states belonging to the effective filled band at each Bloch momentum could be written as linear combinations of the two HWF bands within a single valley; since the Chern number of a band is a topological property, one expects it to be invariant under smooth deformations of the band; starting from a spin-valley-band polarized state and decreasing the interaction strength, we expect that as long as the HF gap introduced above is not closed, the Chern number is intact and QAHE is expected.

A plot of such gaps as functions of interaction strength for several parameter choices is shown in Fig. 3.2d. Note that the polarized state continues to exhibit HF stability as the interaction is lowered but becomes unstable when the interaction energy per particle becomes roughly comparable to the band width. Moreover, we consider a range of Δ from small to large values (always smaller than the noninteracting gap to remote bands); as shown in Fig. 3.2d, regardless of the value of Δ, large interaction strength stabilizes the QAHE, while in the range of small interaction strength, larger Δ results in a more stable polarization. In addition, at intermediate interaction strength, a second gap between HF eigenvalues, apart from the one induced by the interaction, is visible due to the large sublattice potential and scales with Δ (see Fig. 3.2c); obviously, we will keep track of the former to study stability of QAHE. Also, as is expected and also shown in Fig. 3.2d, tuning the twist angle away from the magic value results in weaker stabilization of QAHE and generally larger interaction is needed to stabilize the QAHE.

At the filling of +3, on the other hand, starting from large values of interaction strength, with the present settings, the QAHE state is not stabilized. However, upon decreasing the interaction strength, interestingly, when the interaction energy per particle becomes comparable to the band width, a narrow interval of interaction strength allows for the QAHE to be stabilized although it gets unstable again for smaller interactions (see Fig. 3.3a). This observation holds true irrespective of the value of Δ.

The above discrepancy between the two filling factors indicates that there is a particle-hole *asymmetry* in the system with the current choice of the Hamiltonian, although the non-interacting Hamiltonian is chiral and thus particle-hole symmetric with and without Δ. This asymmetry could be understood by noting the following fact within the active-bands-only model we have chosen to work with here, i.e. the choice of $H_{\mathrm{MF},0} = 0$: starting from the extreme cases, there is a difference between a single electron at $\nu = -4$ and a single hole at $\nu = +4$, in that, the hole senses an additional potential due to the presence of eight full bands of electrons. In the same fashion, a single hole senses an additional k-dependent potential at $\nu = +3$ when compared with an electron at $\nu = -3$, and thus some k values in the hole bands could be preferred over others; more details can be found in Appendix B.4. This single hole potential is interaction induced and thus becomes stronger as the interaction is raised. One can argue that destabilization of QAHE in the strong interaction limit of the filling +3 presented above happens exactly due to this potential; holes prefer to occupy some momenta more than others. As we will see below, using a longer range interaction could weaken this asymmetry.

Let us mention two important points regarding the particle hole transformation of the many body state here before moving on: our choice of $H_{\mathrm{MF},0} = 0$ here means that single electron excitations on top of $\nu = -4$, receive no HF correction in their dispersion. Had we chosen another form for $H_{\mathrm{MF},0}$, so that the holes at $\nu = +4$ experienced no change in dispersion from the CM, we would have gotten the same theory but with electrons replaced with holes; in other words, using this prescription for $H_{\mathrm{MF},0}$ will yield the particle hole transformed version of the present model with $H_{\mathrm{MF},0} = 0$. Additionally here we only discussed the model at $\eta = 0$, where there is a chiral symmetry in the model, while for generic η, there is an approximate particle hole symmetry in the CM which plays a similar role. With this particle hole symmetry one can repeat the above considerations for nonzero η as well, i.e. show that the symmetry between holes and electron at the two fillings ±3 is broken within the present model and also that in a particle hole transformed version of the model, holes will play the role of electrons (see Appendix B.4 for details).

$\eta = 0$, longer range interaction

Upon using longer range interactions, which are more realistic, some of the results presented above are altered: a longer range interaction does not change the picture at $\nu = -3$ much, i.e. with the use of longer range interactions, the QAHE is still stabilized at large interaction and stability is lost at small enough interaction strength

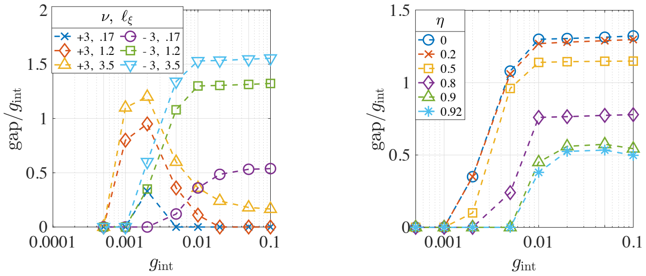

(a) (b)

Figure 3.3: Normalized gaps as functions of g_{int} with longer range interaction and nonzero η in the first study. $\alpha = 0.58$, and $\Delta = 1.9$meV have been chosen. (a) Here both of the fillings are considered still in the chiral limit ($\eta = 0$). The QAHE is more stable at larger screening length; interestingly, it is stabilized even for $\nu = +3$ for large interaction, if large enough screening length is chosen. Note that this feature is lost for larger η values and in particular $\eta_{\mathrm{phys}} = 0.8$, as discussed in the main text. (b) Gaps are drawn for $\nu = -3$ with $\ell_\xi = 1.2a_M$ here, as η is increased. Increasing η makes QAHE less stable until it is not stabilized at all even at large g_{int} at $\eta \approx 0.9 - 0.95$.

(see Fig. 3.3a). However at the filling +3 the effect is more remarkable: the narrow range of the polarized states is made wider. As can be seen in Fig. 3.3a, above some intermediate screening length, even at large interaction the QAHE state is stabilized. Generally, we have observed that increasing ℓ_ξ makes QAHE more stable.

$\eta \neq 0$, away from the chiral limit

We take another step toward making the model more realistic by choosing η to be nonzero and increasing it to the physical value $\eta_{\mathrm{phys}} \approx 0.8$[65]; the physics at $\nu = -3$ stays similar to a high extent even up to η_{phys}. However, at larger η, i.e. $\eta \approx 0.9-0.95$, one starts to observe that the HF iterations do not stabilize the QAHE at this filling even with largest interactions. This means that the spin-valley polarized state ceases to be a local minimum in energy (among Slater determinant states) even when the interaction plays the dominant role. As can be observed in Fig. 3.3b the HF gap becomes smaller as η is increased. For the filling of +3, on the other hand, we observed that although large interaction of long enough range stabilizes QAHE at small η, for larger η and in particular for the physical value this ceases to be true no matter how long range the interaction is chosen.

symmetry transformed states

Before closing the discussion of our first study, we would like to comment on other QAHE states that are obtained by symmetry transformations on the nearly spin-valley-band polarized ones. We start by considering the chiral limit, as was mentioned earlier a U(4)×U(4) symmetry of separate transformations of the two Chern sectors is seen in the interaction part of the Hamiltonian[21]; as is discussed in Appendix B.3, when the kinetic terms are also considered in the chiral limit, the symmetry of the total Hamiltonian reduces to U(4); this is due to the fact that the unitaries acting in the two Chern sectors cannot be chosen independently (see Appendix B.3). Apart from nearly polarized states in our numerics, we also observe states obtained by acting with such transformions on the nearly polarized states. The above intra-Chern-sector symmetry does not survive moving away from the chiral limit. It is also worthwhile to mention that apart from the ones discussed above, we did not obtain any other solution to our unrestricted HF calculations.

Next, we turn our attention to a second study with a projected Hamiltonian.

3.3.2 Second study

In this subsection we work with a Hamiltonian that is obtained by projecting an interacting Hamiltonian onto the subspace of active bands, and the zero point of the HF approach is chosen to be at the CNP of the moiré bands, i.e. we will use Eq. (3.7). Unlike the previous case, this choice results in a particle hole symmetry between the many body states at the two filling factors $+\nu$ and $-\nu$ (see Appendix B.4 for details), and therefore we will focus on $\nu = -3$ only in this study. Note that this particle hole symmetry is present regardless of the value of η and is reflected in the HF spectrum. As an illustration, we present two sets of converged HF energies shown in Fig. 3.4a with $\eta = 0$ and $\eta = 0.8$. The HF energies at $\nu = +3$ and $\nu = -3$ are related by the particle hole transformation which in particular involves a $k_x \to -k_x$ transformation. Notice that for $\eta = 0$, these two sets of HF energies are also related by the chiral symmetry.

Fig. 3.4b shows the HF gap as a function of interaction strength for several parameter choices. We observe that for large interaction strength at small η, QAHE is stabilized under HF iterations but this does not happen for larger η. In particular, the QAHE phase is HF stable at $\eta_{\text{phys}} = 0.8$ for a small windows of parameter choices and is absent when $\eta = 0.5$. We generically see a bump in the rescaled gap as shown in Fig. 3.4b when interaction strength is comparable to the noninteracting energies. This occurs due to a partial cancellation between quadratic terms of the Hamiltonian that arise from H_{kin} and $H_{\text{MF},0}$; it is indeed this same effect that gives rise to

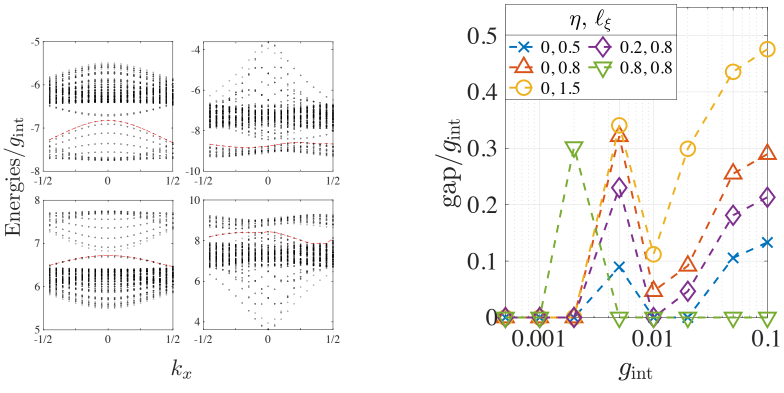

(a) (b)

Figure 3.4: The HF results obtained within the projected model, i.e. the model used in our second study. (a) The converged HF energies normalized by $g_{\rm int}$ vs k_x. The plots on the left and right columns correspond to $\eta = 0$ and $\eta = 0.8$ respectively, while, plots on the first and second rows correspond to $\nu = -3$ and $\nu = +3$ respectively. In all these four subplots, we take $\alpha = 0.58, \Delta = 0, \ell_\xi = 0.5a_M$. The interaction strength is chosen as $g_{\rm int} = 0.05$ and 0.002 for the left and right columns respectively. Note that plots in each column have the same parameter values except for the filling factor. It can be seen that the HF energies at the two fillings $\nu = \pm 3$ can be transformed into each other by the particle hole symmetry of the CM, which in particular needs $k_x \to -k_x$. It can be seen that for $\eta = 0$, the two sets of HF energies are also related by the chiral symmetry of the CM. (b) The gaps as functions of $g_{\rm int}$. $\alpha = 0.58, \Delta = 0$ are chosen for this plot and η and ℓ_ξ are varied.

the narrow window exhibiting QAHE at $\eta_{\rm phys}$. Furthermore, the destabilization of the QAHE at larger η values for large $g_{\rm int}$ is attributed to the fact that $H_{\rm MF,0}$ has quadratic terms that scale with $g_{\rm int}$, and these terms prefer states with particular k_x values over others.

The above results have focused on the $\Delta = 0$ limit. One can also consider finite Δ or even the large Δ limit. The latter limit is defined by requiring that the noninteracting gap due to Δ is not closed by the interaction induced effects, hence schematically $g_{\rm int} \lessapprox \Delta$. But this limit also results in similar behavior of the HF stability to the present model and we will not present these numerical results here.

Discussion

We have considered two different models with different $H_{\mathrm{MF},0}$, in a manner that the HF zero point is chosen at $\nu = -4$ and $\nu = 0$ (CNP) respectively. The former case, as is discussed in Appendix B.4, is actually also related to a model with HF zero point choice of $\nu = +4$, by a particle hole transformation. More specifically, the many body states at the filling factor ν that are obtained using the HF zero point of $\nu = -4$, with an appropriate replacement of electrons with holes, are equivalent to states at filling factor $-\nu$, if the HF zero point is moved to $\nu = +4$. On the contrary, the choice of $\nu = 0$ as the zero point, i.e. the case in the second study, is always particle-hole symmetric.

We would like to emphasize that the particle hole symmetry discussed above is expected to be broken even at the noninteracting level when actual physical effects like lattice relaxation are taken into account. However, we should bear in mind that if the particle hole symmetry is not broken at the noninteracting level, the interactions will also keep it intact. On the other hand, the current experiments exhibiting QAHE[110, 111] only observe the effect at $\nu = +3$, and not at $\nu = -3$, which is an indication of particle hole symmetry breaking. On a phenomenological level, this makes us speculate that among the three different cases discussed above, the HF zero point choice of $\nu = +4$ is probably most relevant to the physics seen in the samples exhibiting QAHE. Let us mention that ultimately within the framework of this chapter, we cannot argue in favor of any of the above three choices. However we note that a definitive answer to this issue needs further study of several other effects that are neglected here; in particular, consideration of the particle hole symmetry breaking effects (such as lattice relaxation as mentioned above) and also more careful treatment of the effects of the filled remote bands could play decisive roles in determining which of the above choices (if any) could serve as a consistent physical model describing the relevant physics.

3.4 Conclusion

To summarize, we introduce the hybrid Wannier basis in the continuum model of TBG and study the strong interaction effect by using the self consistent Hartree Fock approximation. We focus on the filling factors ±3 and investigate the stability of QAHE phases at these two fillings. Interestingly, we observe that stability of the QAHE depends crucially on the zero point choice of the HF dispersion. In the range of physically relevant parameter choices we see that the QAHE is most robustly stabilized at large interaction strength under HF for the zero point choices of ±4, and the corresponding filling factors of $\nu = \pm 3$. We note that the QAHE is observed in experiments on magic angle TBG at $\nu = +3$. Moreover, we numerically observe that reducing the sublattice potential, reducing the screening length and tuning away from the magic angle, generically make the QAHE less stable. In particular, the weakened stability by reducing the sublattice potential is consistent with experiments [110, 111], which have observed the effect in TBG samples with aligned hexagonal Boron Nitride substrates, which is believed to induce a sublattice potential.

Further development of the present method can be envisioned. The HWF basis we introduced in this chapter might be used to find possible fractional phases at non-integer fillings and other interesting phases at integer filling factors. Another possible application, for which HWFs are particularly well suited, is to address situations containing spatially varying configurations such as domain walls between different symmetry broken states or states with one-dimensional “stripey” translational symmetry breaking. We leave these directions for the future study.

Chapter 4

Noncollinear phases in moiré magnets

In this chapter, we introduce a general framework to study moiré structures of two-dimensional Van der Waals magnets using continuum field theory. The formalism eliminates quasiperiodicity and allows a full understanding of magnetic structures and their excitations. In particular, we analyze in detail twisted bilayers of Néel antiferromagnets on the honeycomb lattice. A rich phase diagram with non-collinear twisted phases is obtained, and spin waves are further calculated. Direct extensions to zig-zag antiferromagnets and ferromagnets are also presented. We anticipate the results and formalism demonstrated to lead to a broad range of applications to both fundamental research and experiments.

This chapter is based on Ref. [53].

4.1 Introduction

The wealth of new phenomena revealed in incommensurate layered structures of graphene and other two dimensional semi-conductors and semi-metals have sparked major efforts in the study of electronic physics atop moiré patterns. The materials from which these structures are made, Van der Waals (VdW) solids, come in many varieties, inspiring a nascent field going well beyond graphene [95]. In particular, a growing family of VdW *magnets* are being explored both for their magnetism directly as well as for the interplay of that magnetism with electronics [22]. Two dimensional magnets are of particular interest for the fluctuation effects inherent to them. For example, the Mermin-Wagner theorem [84] proves that a strictly two-dimensional magnet with Heisenberg or XY symmetry cannot show long-range order at any non-zero temperature. Exotic quantum phases of magnets, e.g. quantum spin liquids, are widely expected to be more prevalent in two dimensions[109].

In this chapter, we introduce a framework to study moiré structures of two dimensional magnets, under assumptions which are widely applicable and achievable in VdW systems. We present a general methodology to derive continuum models for incommensurate/twisted/strained multilayers including the effects of interlayer coupling, obviating the need to consider thousands or tens of thousands of lattice sites/spins with complicated local environments. We illustrate the method with detailed calculations for the case of a twisted bilayer of two-sublattice Néel antiferromagnets on the honeycomb lattice, a situation realized in $MnPS_3$ [99, 69, 66], $MnPSe_3$

[69], and also discuss applications to honeycomb lattice antiferromagnets with zig-zag magnetic order (as in $\mathrm{FePS_3}$ [66], $\mathrm{CoPS_3}$ [99], $\mathrm{NiPS_3}$ [98], see [18] for a review) and to the honeycomb lattice *ferromagnet* $\mathrm{CrI_3}$ [56]. We show that twisting these magnets leads to controllable emergent non-collinear spin textures (despite the fact that the parent materials all exhibit collinear ordering), and a rich spectrum of magnonic subbands.

4.2 The method, twisted antiferromagnets

Now we turn to the exposition of the problem and approach, which we illustrate as we go for the simplest case of a two-sublattice Néel order on the honeycomb lattice. First we detail the assumptions under which a continuum description is possible. We consider structures built from two dimensional magnets with long range magnetic order at zero temperature, and assume that the inter-layer exchange interactions $\sim J'$ are weak compared to the intra-layer exchange J, i.e. $J' \ll J$. Additionally, we assume that the lattice in each layer may be regarded as a deformed version of a parent structure shared by all layers. Each layer l is described by a displacement field $\boldsymbol{u}_l(\boldsymbol{x})$ in Eulerian coordinates:

$$\boldsymbol{u}_l(\boldsymbol{x}_l) = \boldsymbol{x}_l - \boldsymbol{x}_l^{(0)}, \tag{4.1}$$

where $\boldsymbol{x}_l$ and $\boldsymbol{x}_l^{(0)}$ are the deformed and original positions, respectively, of points in layer l. The displacement field of each layer need not be uniform or small but its gradients should be small, i.e. $|\partial_\mu u_{l,\nu}| \ll 1$. For uniform layers, this allows any long-period moiré structure, i.e. for which the period of the moiré pattern is large compared to the magnetic unit cell. For two identical but twisted layers, it corresponds to the case of a small twist angle, $\theta \ll \pi$. This construction is directly analogous to the procedure to build the continuum model of twisted bilayer graphene [15] following the recent derivation in Ref. [8] which is valid under nearly identical assumptions.

In this situation the interlayer couplings and the displacement gradients are small perturbations on the intrinsic magnetism of the layers, and therefore have signficant effects only at low energies. This allows a continuum representation of the magnetism of each layer in terms of its low energy modes: space-time fluctuations of the order parameters. The order parameter of the two sublattice antiferromagnet is a Néel vector $\boldsymbol{N}_l$ with fixed length $|\boldsymbol{N}_l| = 1$, and its low energy dynamics for an isolated undeformed layer is described by the non-linear sigma model with the Lagrange density

$$\mathcal{L}_0[\boldsymbol{N}_l] = \frac{\rho}{2v^2}\left(\partial_t \boldsymbol{N}_l\right)^2 - \frac{\rho}{2}\left(\nabla \boldsymbol{N}_l\right)^2 + d\left(N_l^z\right)^2, \tag{4.2}$$

where $\rho \sim J$ is the spin stiffness, v is the spin-wave velocity, and d is a uniaxial anisotropy with $d > 0$ signifying Ising-like and $d < 0$ XY-like anti-ferromagnetism. For MnPS$_3$, there is weak Ising-like anisotropy [129] so $0 < d \ll J/A_{\text{u.c.}}$ ($A_{\text{u.c.}}$ is the area of the 2d unit cell). Such smallness (but not the sign) of the anisotropy is common for third row transition metal magnets.

Next we consider the first-order effects of displacement gradients upon the intralayer terms in (4.2). As in Ref. [8], such terms arise from pure geometry – i.e. carrying out the coordinate transformation from $\boldsymbol{x}_l^{(0)}$ to $\boldsymbol{x}_l$ defined in (4.1) – and from strain-induced changes in energetics. Taking them together, the leading corrections to (4.2) are

$$\begin{aligned}\mathcal{L}_1[\boldsymbol{N}_l,\boldsymbol{u}_l] =&\rho(\varepsilon_{l,xx}+\varepsilon_{l,yy})\left[\frac{\delta_1}{v^2}\left(\partial_t\boldsymbol{N}_l\right)^2-\delta_2\left(\nabla\boldsymbol{N}_l\right)^2\right]\\&+\delta_3\varepsilon_{l,\mu\nu}\partial_\mu\boldsymbol{N}_l\cdot\partial_\nu\boldsymbol{N}_l,\end{aligned}\tag{4.3}$$

where $\delta_{1,2,3}$ are dimensionless $O(1)$ constants and $\varepsilon_{l,\mu\nu}=(\partial_\mu u_{l,\nu}+\partial_\nu u_{l,\mu})/2$ is the strain field in layer l. For simplicity we assumed that spin-orbit effects (e.g. anisotropy d) are small and hence that deformation terms in (4.3) are SU(2) invariant: anisotropic deformation terms must be small in both spin-orbit coupling and in displacement gradients, and hence are neglected.

Next we turn to the inter-layer coupling terms. By locality and translational symmetry, it is generally of the form

$$\mathcal{L}_2[\boldsymbol{N}_1,\boldsymbol{N}_2,\boldsymbol{u}_1-\boldsymbol{u}_2]=J'[\boldsymbol{u}_1-\boldsymbol{u}_2]\boldsymbol{N}_1\cdot\boldsymbol{N}_2,\tag{4.4}$$

where $J'[\boldsymbol{u}]$ is a function with the periodicity of the undeformed Bravais lattice. Due to the smallness of J', we neglect corrections proportional to displacement gradients in (4.4). Generally $J'[\boldsymbol{u}]$ can be expanded in a Fourier series, and well-approximated by a small number of harmonics. We obtain a specific form by considering local coupling of the spin densities in the two layers. Using the symmetries of the honeycomb lattice, the minimal Fourier expansion of the spin density $\boldsymbol{\mathcal{S}}_l$ of a single layer contains the three minimal reciprocal lattice vectors $\boldsymbol{b}_a$,

$$\boldsymbol{\mathcal{S}}_l(\boldsymbol{x})=n_0\boldsymbol{N}_l\sum_{a=1}^{3}\sin(\boldsymbol{b}_a\cdot\boldsymbol{x}^{(0)})=n_0\boldsymbol{N}_l\sum_{a=1}^{3}\sin[\boldsymbol{b}_a\cdot(\boldsymbol{x}-\boldsymbol{u}_l)],\tag{4.5}$$

where n_0 measures the size of the ordered moment, and we define the origin $\boldsymbol{x}=\boldsymbol{0}$

at the center of a hexagon. Taking the product $\mathcal{S}_1 \cdot \mathcal{S}_2$ and applying trigonometric identities to extract the terms which vary slowly on the lattice scale (rapidly varying components do not contribute at low energy) gives the form of (4.4), with

$$J'[\boldsymbol{u}] = J' \sum_{a=1}^{3} \cos(\boldsymbol{b}_a \cdot \boldsymbol{u}), \tag{4.6}$$

where the constant J' is proportional to the inter-layer exchange and n_0^2. Physically, (4.6) captures the fact that e.g. for intrinsically ferromagnetic exchange $J' > 0$, the preferred relative orientation of the A sublattice spins of the two layers is parallel for AA stacking but anti-parallel for AB and BA stackings.

The full Lagrange density $\mathcal{L} = \sum_{l=1,2}(\mathcal{L}_0[\boldsymbol{N}_l] + \mathcal{L}_1[\boldsymbol{N}_l, \boldsymbol{u}_l]) + \mathcal{L}_2[\boldsymbol{N}_1, \boldsymbol{N}_2, \boldsymbol{u}_1 - \boldsymbol{u}_2]$ captures the low energy physics of a bilayer with arbitrary deformations of the two layers. We now specialize to the case of a rigid twist of the two layers by a relative angle θ: $\boldsymbol{u}_1 = -\boldsymbol{u}_2 = \frac{\theta}{2}\hat{\boldsymbol{z}} \times \boldsymbol{x}$. In this case the strain vanishes, and one finds the full Lagrangian is

$$\mathcal{L} = \sum_l \frac{\rho}{2v^2} \left(\partial_t \boldsymbol{N}_l\right)^2 - \mathcal{H}_{\text{cl}}, \tag{4.7}$$

where

$$\mathcal{H}_{\text{cl}} = \sum_l \left[\frac{\rho}{2} \left(\nabla \boldsymbol{N}_l\right)^2 - d \left(N_l^z\right)^2\right] - J'\Phi(\boldsymbol{x}) \boldsymbol{N}_1 \cdot \boldsymbol{N}_2, \tag{4.8}$$

is the classical energy density. Here the coupling function

$$\Phi(\boldsymbol{x}) = \sum_{a=1}^{3} \cos(\boldsymbol{q}_a \cdot \boldsymbol{x}), \tag{4.9}$$

and $\boldsymbol{q}_a = \theta \hat{\boldsymbol{z}} \times \boldsymbol{b}_a$ are the reciprocal lattice vectors *of the moiré superlattice.*

Equations (4.7)-(4.9) form the basis for an analysis of the magnetic structure on the moiré scale, as well as for the magnon excitations above them. The magnetic ground state is obtained as the variational minimum of $\mathcal{H}_{\rm cl}[\boldsymbol{N}_1, \boldsymbol{N}_2]$. Owing to the sign change of $\Phi(\boldsymbol{x})$, the problem is frustrated: the Néel vectors of the two layers wish to be parallel in some regions and antiparallel in others, forcing them to develop gradients within the plane – the representation in the continuum of incompletely satisfied in-plane bonds. We find that the optimal classical solution is coplanar but not necessarily collinear (see appendix C for a complete weak coupling analysis), and without loss of generality we can take the spins to lie in the x-z plane: $\boldsymbol{N}_l^{\rm cl} = \sin\phi_l \hat{\boldsymbol{x}} + \cos\phi_l \hat{\boldsymbol{z}}$. The formulae are simplified by forming symmetric and antisymmetric combinations, $\phi_s = \phi_1 + \phi_2$, $\phi_a = \phi_1 - \phi_2$, and adopting dimensionless coordinates $\mathsf{x} = q_m \boldsymbol{x}$, with $q_m = |\boldsymbol{q}_a|$ the moiré wavevector. Then the dimensionless energy density $\mathsf{H}_{\rm cl} = \mathcal{H}_{\rm cl}/(\frac{1}{2}\rho q_m^2)$ becomes, up to an additive constant

$$\mathsf{H}_{\rm cl} = \frac{1}{2}\left(|\boldsymbol{\nabla}_{\mathsf{x}}\phi_s|^2 + |\boldsymbol{\nabla}_{\mathsf{x}}\phi_a|^2\right) - (\alpha\hat{\Phi}(\mathsf{x}) + \beta\cos\phi_{\mathsf{s}})\cos\phi_{\mathsf{a}}. \tag{4.10}$$

Here we have introduced the dimensionless parameters

$$\alpha = \frac{2J'}{\rho q_m^2}, \qquad \beta = \frac{2d}{\rho q_m^2}, \tag{4.11}$$

and $\hat{\Phi}(\mathsf{x}) = \sum_{a=1}^{3}\cos(\hat{\boldsymbol{q}}_a \cdot \mathsf{x})$, where $\hat{\boldsymbol{q}}_a = \boldsymbol{q}_a/q_m$ are unit vectors. We can obtain partial differential equations for the phase angles by applying calculus of variations to (4.10):

$$\nabla_{\mathsf{x}}^2\phi_s = \beta\cos\phi_a\sin\phi_s, \tag{4.12}$$

$$\nabla_{\mathsf{x}}^2\phi_a = \left(\beta\cos\phi_s + \alpha\hat{\Phi}(\mathsf{x})\right)\sin\phi_a. \tag{4.13}$$

We must find the solutions of the saddle point equations which minimize the integral of H_{cl}. There is always a trivial solution with $\phi_s = \phi_a = 0, \pi$, which corresponds to the Ising limit of aligned or counter-aligned spins. Nontrivial solutions with potentially lower energies will be discussed in different limits below. We first focus on the case of $\beta > 0$, i.e., the Ising-like anisotropy.

For $\alpha, \beta \ll 1$, corresponding to large angles, the gradient terms in the Hamiltonian dominate and the solution is nearly constant. Perturbation theory with fixed $\delta = \beta/\alpha^2$ gives a nontrivial solution

$$\begin{aligned} &\phi_s = \pi, \\ &\phi_a = \phi_a^{(0)} - \alpha \sin\phi_a^{(0)} \left(\hat{\Phi}(\mathsf{x}) - \Phi_0\right) + O(\alpha^2, \beta), \end{aligned} \tag{4.14}$$

with $\cos\phi_a^{(0)} = -\frac{2}{3}\,\delta$, and where Φ_0 is a constant given in Sec. C of appendix C. In this *twisted* solution, $\cos\phi_a$ tends to imitate the sign of $\hat{\Phi}(\mathsf{x})$, to gain energy from the potential term. This change of ϕ_a, however, will need to be balanced against the energy penalty due to the kinetic term. Comparing the energy of the twisted solution with that of the trivial one, we see that the former has a lower energy for $\delta < \frac{3}{2}$, i.e., whenever it exists. In this limit, at $\delta = \frac{3}{2}$, the system undergoes a continuous transition to the collinear phase. More details can be found in the appendix C.

For small twist angles, on the other hand, $\alpha \gg 1$; in this limit, we first consider small values of β; the potential term $\alpha\hat{\Phi}(\mathsf{x})$ in (4.10) dominates and the energy is minimized by choosing $\phi_a = 0$ or π almost everywhere, such that $\cos\phi_a = \mathrm{sign}[\hat{\Phi}(\mathsf{x})]$, which means the order parameter vectors in the two layers are locally parallel or antiparallel. At small values of β, ϕ_s prefers to take a constant value and, since the total area with negative $\hat{\Phi}(\mathsf{x})$ is larger than the positive area, $\phi_s = \pi$ is chosen; this solution lies in the same phase as that of the twisted solution found for $\alpha \ll 1$ above, that also showed the property $\phi_s = \pi$; we call this phase *twisted-s*. The twisted-s solution obviously breaks the U(1) symmetry of spin rotations about the z axis of spin space, but it retains an Ising symmetry under interchanging layers and reflecting spin $N^z \to -N^z$. One may check that $\varphi = \phi_s - \pi$ is odd under this symmetry.

Interestingly, however, one can further check that in the same limit of $\alpha \gg 1$, above some order-one value of β, another twisted solution becomes more energetically favored. It belongs to what we call a *twisted-a* phase, where ϕ_s is no longer constant and actually shows a twisted pattern similar to that of ϕ_a, such that $\cos\phi_s$ exhibits spatial variations following those of $\hat{\Phi}(\mathsf{x})$ (see the appendix C for details). This implies a non-zero value for φ so that the twisted-a phase spontaneously breaks the aforementioned Ising symmetry. The value of $\varphi \neq 0$ increases smoothly from zero on entering the twisted-a phase from the twisted-s one, consistent with the expected continuous behavior of an Ising transition (treated at mean-field level by the saddle point analysis).

Finally, we study the $\alpha, \beta \gg 1$ limit, where the twisted-a solution is the lowest energy nontrivial solution. It requires ϕ_s to take the values 0 or π almost everywhere along with ϕ_a, such that $\cos\phi_s$ matches the sign of $\hat{\Phi}(\mathsf{x})$; this means simply that the vectors $\boldsymbol{N}_l$ align or counter-align along the $\pm\hat{\boldsymbol{z}}$ axis almost everywhere. The order parameter rotations occur in a narrow domain wall centered on the zeros of $\hat{\Phi}(\mathsf{x})$, i.e. forming a closed almost circular loop in the middle of the unit cell. This domain wall costs an energy proportional to its length; as a result of this energy penalty, the twisted-a phase gives way to the collinear phase when the energy gain from the twist is exceeded by the domain wall energy. In order to study this competition, we assume that such transition occurs when $\beta \gg \alpha$, which we later check is self-consistent. The widths w_a and w_s (in dimensionless distance normal to the domain wall) over which ϕ_a and ϕ_s wind are determined by the balance of the gradient terms and the corresponding potential terms. This gives $\mathsf{w}_{a/s} \sim 1/\sqrt{\beta}$ in this limit and an energy cost per unit length of the wall of $\mathsf{E} \sim \sqrt{\beta}$. Now the bulk energy gain of the twisted state is simply proportional to α, so we obtain the result that the twist collapses when $\sqrt{\beta} \gtrsim \alpha$. This treatment is valid since under these conditions $\beta/\alpha \gtrsim \alpha \gg 1$ (we did not determine the multiplicative order one constant in this inequality). Note that the transition between the collinear and twisted-a phase is a "level crossing" between two distinct and disconnected saddle points; consequently it corresponds to a *first order* transition, and the first derivatives of the energy are discontinuous across this boundary. A tricritical point separates the two continuous transitions from this first order one.

To summarize, we find three different phases for $\beta > 0$, two of which correspond to twisted configurations. The transition between the two twisted phases happens at some β of order 1, when the phase boundary is crossed in the large α limit; the twisted phases collapse on the other hand when $\beta > \frac{3}{2}\alpha^2$ in the $\alpha, \beta \ll 1$ limit

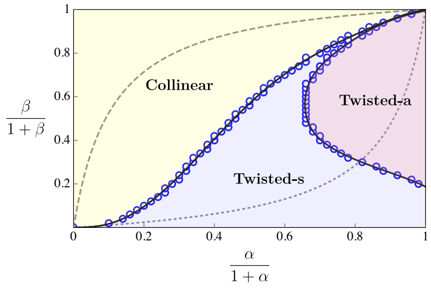

Figure 4.1: The phase diagram with respect to the normalized dimensionless parameters $\alpha/(1+\alpha)$ and $\beta/(1+\beta)$, respectively. In the collinear phase, the Néel vectors of the two layers are constant and either aligned or counter-aligned. The characteristics of the twisted phases are most obvious when the potential term plays the dominant role: in the twisted-s phase, $\phi_s = \pi$ while the sign of $\cos\phi_a$ exhibits modulations resembling those of $\hat{\Phi}(\mathsf{x})$ (see Fig. 4.2a). In the twisted-a phase, on the other hand, the signs of both $\cos\phi_s$ and $\cos\phi_a$ follow that of $\hat{\Phi}(\mathsf{x})$. The twisted-s phase terminates at $(0.88, 0.94)$ near the right top corner of the diagram. The dashed line shows $\beta = 10\alpha$ while the dotted line corresponds to $\beta = 0.1\alpha$. For $\beta = \alpha$, the corresponding line would be the diagonal one connecting the left bottom and right top corners.

(twisted-s to Ising transition) and when $\beta \gtrsim \alpha^2$ in the $\alpha, \beta \gg 1$ limit (twisted-a to Ising transition). We sketch a phase diagram in Fig. 4.1 based on the numerical solutions to (4.12), (4.13), which is consistent with and in fact interpolates between the perturbative and strong-coupling analyses above. The dashed and dotted lines in the figure show examples of paths with a fixed ratio $\beta/\alpha = d/J'$; this ratio is determined by the material, but one can tune the twisting angle θ to move along the lines, and consequently enter/leave different phases. Remarkably, for a fixed d/J', *the twisted-a state is always stabilized for sufficiently small* θ; this can be understood by noting that β/α is invariant when θ changes as mentioned above, and thus decreasing the twist angle, increases α linearly with β forming a straight line in the $\alpha - \beta$ plane (different from the axes in Fig. 4.1), but the twisted-a phase, when $\alpha, \beta \gg 1$, is separated from the collinear phase by a $\beta \sim \alpha^2$ relation and from the twisted-s phase by $\beta \sim$ const.; thus the above mentioned straight line lies between these two phase

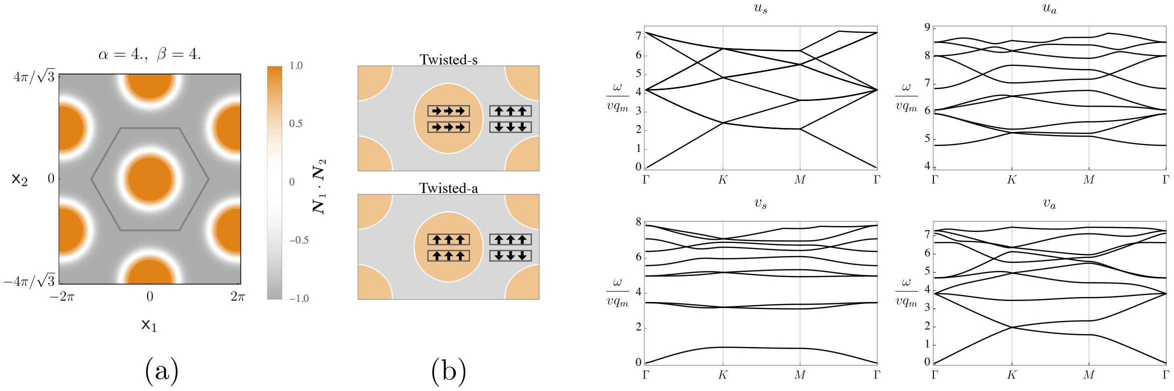

(a) (b) (c)

Figure 4.2: Real space configurations and spin wave plots in twisted antiferromagnets. (a) Spatial configurations of $\boldsymbol{N}_1 \cdot \boldsymbol{N}_2 = \cos\phi_a$. It can be seen that $\cos\phi_a$ is either $+1$ or -1 almost everywhere, based on the sign of $\hat{\Phi}(\mathsf{x})$; indeed, the choice of $\alpha = 4, \beta = 4$ corresponds to a solution in which the potential term plays the dominant role and that lies in the twisted-a phase; the same quantity, i.e. $\cos\phi_a$ looks very similar if β is lowered even into the twisted-s phase while keeping α fixed. (b) A schematic diagram of the spatial dependence of the orientation of the Néel vectors (not actual spins) in the two layers in the strong coupling limit, a vertical (horizontal) arrow denotes out-of-plane (in-plane) orientation; the brown and gray areas show regions with positive and negative values for $\hat{\Phi}(\mathsf{x})$. The main difference is that in the brown region, the twisted-s phase shows in plane orientation and the twisted-a phase shows out-of-plane orientation. (c) The lowest ten magnon bands at $\alpha = 2$ for the four branches, in the isotropic case ($d = 0$) of two coupled two-sublattice antiferromagnets.

boundaries at sufficiently small θ. Plots of the real space configurations of the ground states in the two twisted solutions are presented in Figures 4.2a and 4.2b.

Once the minimum energy saddle point is obtained, the full Lagrangian allows for calculation of the magnon spectrum. We define

$$\boldsymbol{N}_l = \sqrt{1 - u_l^2 - v_l^2}\,\boldsymbol{N}_l^{\mathrm{cl}}(\mathsf{x}) + u_l \boldsymbol{u}_l(\mathsf{x}) + v_l \boldsymbol{v}_l(\mathsf{x}), \tag{4.15}$$

where $\boldsymbol{u}_l = \cos\phi_l(\mathsf{x})\hat{\boldsymbol{x}} - \sin\phi_l(\mathsf{x})\hat{\boldsymbol{z}}$ and $\boldsymbol{v}_l = \hat{\boldsymbol{y}}$ complete a *spatially dependent* orthonormal basis such that $\hat{\boldsymbol{u}} \times \hat{\boldsymbol{v}} = \boldsymbol{N}_l^{\mathrm{cl}}$ at every $\boldsymbol{x}$. The fluctuations about the classical solution are described by space-time dependent fields $u_l(\mathsf{x}, t), v_l(\mathsf{x}, t)$. Inserting (4.15) into the (4.7), expanding to quadratic order in the fluctuations and finding the Euler-Lagrange equations for $u_{s/a} = u_1 \pm u_2, v_{s/a} = v_1 \pm v_2$, one obtains linear wave equations for four branches of excitations. For simplicity, we present the results for $d = \beta = 0$ (see appendix C for the general result), in which case the four modes decouple immediately

$$-\partial_t^2 u_{s/a} = v^2 q_m^2 \hat{\mathsf{D}}_{u,s/a} u_{s,a}, \qquad -\partial_t^2 v_{s/a} = v^2 q_m^2 \hat{\mathsf{D}}_{v,s/a} v_{s,a}, \tag{4.16}$$

with the linear operators

$$\begin{aligned}
\hat{\mathsf{D}}_{u,s} &= -\nabla_{\mathsf{x}}^2, \qquad\qquad (4.17)\\
\hat{\mathsf{D}}_{u,a} &= -\nabla_{\mathsf{x}}^2 + \alpha\hat{\Phi}(\mathsf{x})\cos\phi_a,\\
\hat{\mathsf{D}}_{v,s} &= -\nabla_{\mathsf{x}}^2 - \frac{1}{4}|\boldsymbol{\nabla}_{\mathsf{x}}\phi_a|^2 - \frac{\alpha}{2}\hat{\Phi}(\mathsf{x})\left(1-\cos\phi_a\right),\\
\hat{\mathsf{D}}_{v,a} &= -\nabla_{\mathsf{x}}^2 - \frac{1}{4}|\boldsymbol{\nabla}_{\mathsf{x}}\phi_a|^2 + \frac{\alpha}{2}\hat{\Phi}(\mathsf{x})\left(1+\cos\phi_a\right).
\end{aligned}$$

Taking $u_{s/a}(\mathsf{x},t) = e^{i\omega t}u_{s/a}(\mathsf{x})$, we obtain eigenvalue problems such that the magnon frequencies are (vq_m multiplied by) the square roots of the eigenvalues of the $\hat{\mathsf{D}}$ operators. These eigenvalue problems have the form of continuum non-relativistic Schrödinger-Bloch problems and therefore can be solved using the Bloch ansatz to find an infinite series of magnon bands. When α is large, the potential terms in the above equations become alternated deep wells and hard walls, which confine the magnons to either of the two domains. This leads to the flattening of magnon bands in branches u_a and v_s. Fig. 4.2c shows the lowest magnon bands when α is at intermediate value. There are three gapless Goldstone modes in the u_s, v_s and v_a branches, which correspond to the three generators of the $O(3)$ group.

Finally, we comment on the case of $d < 0$ in brief, where the anisotropy term favors the spins to lie in the XY-plane. The corresponding equations of motion resemble those of the isotropic case, i.e., ϕ_s tends to be uniform everywhere, while $\cos\phi_a$ imitates the sign of $\hat{\Phi}(\mathsf{x})$ due to the interlayer exchange, leading to twisted configurations. More details can be found in appendix C.

4.3 Zig-zag antiferromagnets

Having described the case of the Néel antiferromagnet in detail, we give further results more succinctly for other types of 2d magnets. The materials $FePS_3$, $CoPS_3$, and $NiPS_3$ all have the same lattice structure as $MnPS_3$ but exhibit "zig-zag" magnetic order. It is a collinear magnetic order which doubles the unit cell. There are three possible ordering wavevectors: the M points at the centers of the edges of the moiré Brillouin zone, which are half reciprocal lattice vectors, $\boldsymbol{b}_a/2$, with $a = 1, 2, 3$. The spin density (analogous to (4.5)) therefore contains three order parameter "flavors", $\boldsymbol{N}_a$:

$$\mathcal{S}_l(\boldsymbol{x}) = n_0 \sum_{a=1,2,3} \boldsymbol{N}_{l,a} \sin\left[\frac{1}{2}\boldsymbol{b}_a \cdot (\boldsymbol{x} - \boldsymbol{u}_l)\right]. \tag{4.18}$$

Here in a zig-zag state, just a single one of the three $\boldsymbol{N}_a$ vectors is non-zero: this describes three possible spatial orientations of the zig-zag chains of aligned spins.

Proceeding as before, we obtain the effective classical Hamiltonian in the form

$$\mathcal{H}_{\text{cl}}^{\text{zig-zag}} = \sum_{a,l} \left[\frac{\rho}{2} (\boldsymbol{\nabla} \boldsymbol{N}_{a,l})^2 + \frac{\tilde{\rho}}{2} (\hat{\boldsymbol{q}}_a \cdot \boldsymbol{\nabla} \boldsymbol{N}_{a,l})^2 \right] \tag{4.19}$$

$$+ \sum_l V[\boldsymbol{N}_{1,l}, \boldsymbol{N}_{2,l}, \boldsymbol{N}_{3,l}] - \frac{J'}{2} \sum_a \boldsymbol{N}_{a,1} \cdot \boldsymbol{N}_{a,2} \cos\left(\frac{\boldsymbol{q}_a \cdot \boldsymbol{x}}{2} \right).$$

Here $\rho, \tilde{\rho}$ are two stiffness constants, and V is a potential which may be taken in the form

$$V[\boldsymbol{N}_1, \boldsymbol{N}_2, \boldsymbol{N}_3] = u(\sum_a |N_a|^2 - 1)^2 + v \sum_{a>b} |N_a|^2 |N_b|^2 - d \sum_a (N_a^z)^2, \tag{4.20}$$

with $u, v > 0$ to model the energetic preference for a single non-zero stripe orientation, and d as before to tune anisotropy.

(4.19) gives a continuum model to determine the magnetic ordering texture for arbitrary twist angles. The most important difference from the two-sublattice antiferromagnet is that here each spatial harmonic couples to a single "flavor", while in the former case, (4.18), the single flavor of order parameter couples to the sum of harmonics. While we do not present a general solution, we note immediate consequences in the strong coupling limit, $J' \gg \rho q_m^2, \tilde{\rho} q_m^2$. In this situation, for each $\boldsymbol{x}$ we must choose the *largest* harmonic, i.e. the a which maximizes $|\cos\left(\frac{\boldsymbol{q}_a \cdot \boldsymbol{x}}{2}\right)|$, and then take $\boldsymbol{N}_{a,1} = \text{sign}[J' \cos\left(\frac{\boldsymbol{q}_a \cdot \boldsymbol{x}}{2}\right)] \boldsymbol{N}_{a,2}$ and $\boldsymbol{N}_{a',l} = 0$ for $a' \neq a$. Remarkably, the result is a tiling of six possible zig-zag domains which evokes a "dice lattice", as shown in Fig. 4.3. Narrow domain walls separate these regions.

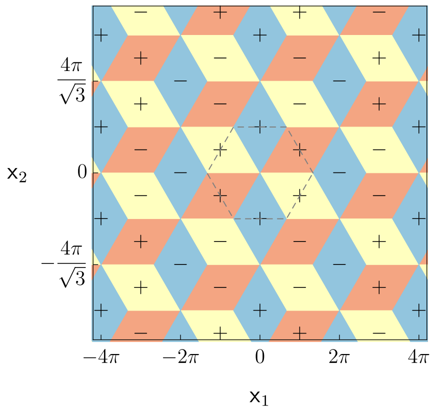

Figure 4.3: The real space tiling with six possible domains which appear in a twisted bilayer of zig-zag antiferromagnets in the strong coupling (small angle) limit. The colors show which flavor of the order parameter is nonzero in each domain, while the ± signs label the relative sign between the order parameter in the two layers. The dashed hexagon shows a moiré structural unit cell.

4.4 Twisted ferromagnets

Naïvely, twisting a homo-bilayer of ferromagnets is relatively innocuous. However, experiments and theory [83, 113, 124, 55, 112, 115, 58] for CrI_3 have indicated that the interlayer exchange has a strength and sign that depends upon the displacement between neighboring layers. This can be directly incorporated into a continuum model following our methodology.

To this end, for a general twisted bilayer of a ferromagnetic material with the above property, one can use the energy functional shown in (4.8) with minimal modifications: *i*) the Néel vectors $\boldsymbol{N}_l$ should be everywhere replaced by the uniform magnetization $\boldsymbol{M}_l$, since in fact each layer is ferromagnetic within itself and *ii*) the function $\Phi(\boldsymbol{u}_1 - \boldsymbol{u}_2)$ takes a more complicated form. Assuming a small twist angle, the latter may be determined from the dependence of the interlayer exchange of untwisted layers on a uniform interlayer displacement. For the case of CrI_3, we have extracted the stacking dependent interlayer exchange data from the first principle calculations in Ref. [112]. Similar to the case of twisted antiferromagnets, a variational analysis of (4.8) can be performed, which leads to the same set of Euler-Lagrange equations, i.e. (4.12) and (4.13). In order to simplify the analysis, we will only consider an infinitesimal β here; its effect is to fix the value of $\phi_s = 0$ for CrI_3 as discussed in appendix C. The effects of non-zero β can also be studied in a way similar to the previous case. The mathematical problem is then to obtain the functional form of $\phi_a(\boldsymbol{x})$ and its dependence upon α. In the ferromagnetic case, the Fourier expansion of $\hat{\Phi}(\mathsf{x})$ generally has a nonzero constant term, which dominates the solution at small α. In the case of CrI_3, the constant term is small and ferromagnetic, thus $\phi_a = 0$ is chosen for small α. However, if other harmonics of $\hat{\Phi}(\mathsf{x})$ are strong enough, a *twisted* solution starts to appear at a finite value of α with a lower energy. As in the antiferromagnetic case, $\cos\phi_a$ shows spatial modulations imitating the changes of $\hat{\Phi}(\mathsf{x})$ in this twisted solution. This property of the twisted solution is most visible in the large α limit, where the kinetic energy penalty is least important: one observes then domains with $\cos\phi_a = \mathrm{sign}\left[\hat{\Phi}(\mathsf{x})\right]$, separated by narrow domain walls. For a detailed analysis of the above statements in the case of CrI_3, see appendix C. A plot of the average magnetization in the system is shown in Fig. 4.4a with a transition form collinear to twisted phase at finite α. Unlike the antiferromagnets discussed above, there is a finite interval of twist angles where the collinear phase exists even with infinitesimal anisotropy parameter β. Also a plot of the spatial configuration of

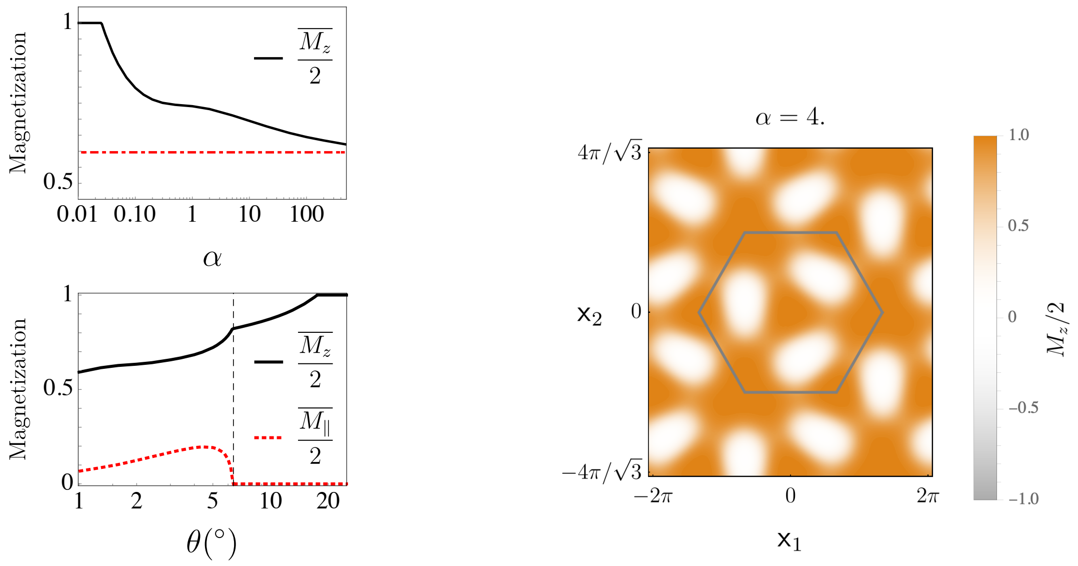

(a)

(b)

Figure 4.4: Phase diagrams and a real space configuration plot in twisted bilayers of the ferromagnet CrI_3. (a) Top: the average value of the z component of the sum of the two layers' spins for CrI_3, when the anisotropy parameter is taken to be positive and infinitesimal. A continuous transition from the collinear phase to the twisted phase occurs at $\alpha = 0.025$. This phase is analogous to the twisted-s phase discussed previously. The total area in which $\hat{\Phi}(\mathsf{x}) > 0$ is shown with a dashed red line here as the limiting value of $\frac{\overline{M_z}}{2}$ for very large α. Bottom: the average value of the z and in-plane components of the total magnetization calculated with physical parameters chosen as discussed in the main text for CrI_3; in particular, the anisotropy is nonzero here. At $\theta = 17.5°$, a transition from collinear to twisted-s phase occurs at which point $\overline{M_z}$ starts to be nonzero. Moreover, a transition to the twisted-a phase occurs at $\theta = 6.4°$, which exhibits itself in $\overline{M_\parallel}$ starting to be nonzero for smaller angles. (b) Spatial profile of local magnetization $\frac{M_z}{2} = \frac{1}{2}(M_{1,z} + M_{2,z})$ for a twisted solution in CrI_3. The anisotropy parameter is taken to be positive and infinitesimal. There are large regions in real space with a net magnetization, while other regions have vanishingly small net magnetization.

a twisted solution is presented in Fig. 4.4b; it shows that there are large regions in real space with maximal magnetization while at the same time there are also other regions exhibiting close to zero magnetization.

4.5 Conclusion

In this work, we have considered moiré two dimensional magnets and in particular the twisted bilayers of Van der Waals magnetic materials. We have developed a low energy formalism in the continuum and studied in detail three different examples of twisted bilayers: antiferromagnetic, zig-zag antiferromagnetic and ferromagnetic. Remarkably, a rich phase diagram is obtained as one varies the twist angle and material parameters; there are interesting *twisted* ground state solutions comprising long-wavelength non-collinear magnetic textures. Such spatial patterns can potentially be observed in experiments, where the twist angle control adds to the tunability of the system. Furthermore, at small twist angles in the non-collinear phases, certain spin waves also exhibit interesting features such as flattening dispersion curves.

Material-wise, $\mathrm{MnPS_3}$ has $\beta \approx 4.54\alpha$, and the system is in the collinear phase for generic twist angles. The ratio can be derived using $d = \Delta^2/(12JA_{\text{u.c.}})$ and $J' = J'_{\text{exp}}S^2/(2A_{\text{u.c.}})$, where the intralayer exchange J, interlayer coupling J'_{exp} and the magnon gap Δ are extracted from [129]. On the other hand, for $\mathrm{CrI_3}$, we have derived $\beta \approx 0.62\alpha$ using the intralayer exchange and anisotropy parameter as given in Ref. [31], and the interlayer exchange data as given in Ref. [112]. A plot of average magnetization for $\mathrm{CrI_3}$ in the perpendicular and parallel directions for which the above parameters are used is presented in Fig. 4.4a in the bottom panel; it can be seen that at large angles, the system is in the collinear phase, but the twisted-s phase ($\phi_s = 0$) starts to be preferred at $\theta = 17.5°$; upon further decreasing the angle, starting at

$\theta = 6.4^\circ$, the twisted-a phase becomes the ground state (see the caption for details). This shows that in a twisted bilayer of CrI_3, it is reasonable to expect both of the twisted phases to be realized in experimentally accessible settings.

The present methodology can be utilized with minimal modifications in further analyses of other moiré systems in the vast collection of possible bilayer magnetic materials. For example, here we have mainly presented the examples of homobilayers, but interesting phenomena can also arise for heterobilayers of VdW magnets, such as the stacking of ferromagnets on antiferromagnets [120]. The magnetic properties of general moiré systems as well as their interplay with the electronic/transport properties could be the subject of future studies. Given the extremely fruitful research done in the field of moiré electronic systems, one can anticipate that the magnetic moiré systems could play the role of a new platform where novel exciting physics could be pursued.

Chapter 5

Heterobilayer moiré magnets: Moiré skyrmions and commensurate-incommensurate transitions

In this chapter, we study untwisted heterobilayers of ferromagnetic and antiferromagnetic van der Waals materials, with in particular a Dzyaloshinskii-Moriya interaction in the ferromagnetic layer. A continuum low energy field theory is utilized to study such systems. We develop a phase diagram as a function of the strength of inter-layer exchange and Dzyaloshinskii-Moriya interactions, combining perturbative and strong coupling analyses with numerical simulations using Landau-Lifshitz-

Gilbert equations. Various moiré-periodic commensurate phases are found, and the commensurate-incommensurate transition is discussed. Among the commensurate phases, we observe an interesting skyrmion lattice phase wherein each moiré unit cell hosts one skyrmion.

This chapter is based on Ref. [54].

5.1 Introduction

Magnetic skyrmions are long-lived, topologically protected spin-textures that were predicted to exist in chiral magnets [17, 16, 106], and experimentally observed in cubic, non-centrosymmetric materials such as MnSi [88], $\mathrm{Fe}_{1-x}\mathrm{Co}_x\mathrm{Si}$ [89, 141] and FeGe [140]. Non-collinear spin configurations occur in these materials due to the antisymmetric Dzyaloshinskii-Moriya (DM) interactions [38, 87]. In three-dimensional bulk magnets, skyrmion lattices are stabilized by thermal fluctuations above the helical state [88]. Interestingly, in the thin-film, two-dimensional limit, the skyrmion lattice is stable over a wide range of the phase diagram [138, 47, 70].

A new class of two-dimensional crystals, magnetic van der Walls (vdW) materials, has opened up numerous possibilities for both theoretical and experimental physics [100, 23]. All three fundamental spin Hamiltonians have been reported in these materials: the two-dimensional Heisenberg, Ising, and XY models [59, 130]. Furthermore, novel quantum phases are expected to appear in the heterostructures of these materials [53]. Recently, skyrmion crystals have been observed in the single-layered ferromagnetic vdW material Fe_3GeTe_2 [123, 101, 33], predicted to exist in CrI_3 [13] and Janus magnets [142], all attributed to the DM interaction, motivating us to study the moiré physics of such vdW systems.

We will focus on a nontwisted heterobilayer of ferromagnetic (harboring a DM interaction) and antiferromagnetic vdW materials. A similar construction was explored in [120], where dipolar interactions along with an external field were added to the moiré structure in contrast to the DM interaction of the present work. We show that a wealth of different phases featuring magnetic textures on the moiré scale and in particular a skyrmion lattice phase could form.

We will use the continuum formalism introduced in [53], which obviates the need to consider numerous lattice sites with complicated local environments. First, we review this continuum formalism and derive the Hamiltonian that we will focus on, followed by a perturbative analysis. The competition between the DM interaction and the moiré potential induces a commensurate-incommensurate transition that will further be analyzed in the weak-coupling regime. Then different types of commensurate phases are introduced, supplemented furthermore by a numerical ground-state phase diagram, obtained from a Landau-Lifshitz-Gilbert analysis. Finally, we discuss the possible extensions and experimental relevance of the work. Details of the weak-coupling analysis will be presented in appendix D.

5.2 Setup of the problem

We study a heterobilayer system of honeycomb ferromagnetic and honeycomb antiferromagnetic vdW materials. This setting is similar to that in [120]. Both layers are assumed to exhibit long-range order, so a local description in terms of the order parameters $\boldsymbol{M}$, $\boldsymbol{N}$ for the ferromagnetic and the Néel antiferromagnetic layers will be employed, where $|\boldsymbol{M}| = |\boldsymbol{N}| = 1$. After [53], we will develop a continuum model to provide a low energy description of the system. When the interlayer coupling and the displacement gradients act as small perturbations on the intrinsic magnetism of the two layers, a continuum treatment is justified. Since we will only be concerned with ground state configurations (and possible other nearby states) in this work, it suffices to analyze the classical Hamiltonians only. This consists of intralayer and interlayer terms; we take the former as

$$\begin{aligned} \mathcal{H}_{\text{intra}} = &\frac{\rho_1}{2}(\nabla \boldsymbol{M})^2 + \frac{\rho_2}{2}(\nabla \boldsymbol{N})^2 \\ &+ D\, \boldsymbol{M} \cdot (\nabla \times \boldsymbol{M}) - C\,(N_z)^2, \end{aligned} \tag{5.1}$$

where a single-ion anisotropy for the antiferromagnetic layer and a DM interaction for the ferromagnetic layer are assumed; the latter is predicted to be present in families of Janus magnets in particular [142]. We have utilized a Bloch-type DM interaction in this work, however the same results hold for a Neél-type DM interaction as well appendix D. The anisotropy term is neglected in the ferromagnetic layer.

We now turn to the interlayer coupling: the spin densities of the two layers are parametrized as: $\boldsymbol{\mathcal{S}}_1 = m_0 \boldsymbol{M} \left[f_0 - \sum_a \cos(\boldsymbol{b}_a \cdot \boldsymbol{r})\right]$ and $\boldsymbol{\mathcal{S}}_2 = n_0 \boldsymbol{N} \sum_a \sin(\boldsymbol{c}_a \cdot \boldsymbol{r})$, where $\boldsymbol{b}_a, \boldsymbol{c}_a$ denote the reciprocal lattice vectors of the microscopic lattices in the two layers. Furthermore, m_0 and n_0 are proportional to the ordered moments in the two layers, and the zeroth Fourier component f_0 is undetermined; its value will not matter for the low-energy physics. Taking a minimal Fourier expansion, we limit the summation over $\boldsymbol{c}_a$ and $\boldsymbol{b}_a$ to the three smallest reciprocal lattice vectors. Assuming a local interlayer exchange of the form $H' = -J' \boldsymbol{\mathcal{S}}_1 \cdot \boldsymbol{\mathcal{S}}_2$ and that $|\boldsymbol{b}_a| - |\boldsymbol{c}_b| \ll |\boldsymbol{b}_a|,\ |\boldsymbol{c}_b|$, one arrives at the following interlayer interaction: $\mathcal{H}' = J' \boldsymbol{M} \cdot \boldsymbol{N} \sum_a \sin(\boldsymbol{d}_a \cdot \boldsymbol{r})$, where the three vectors $\boldsymbol{d}_a = \boldsymbol{b}_a - \boldsymbol{c}_a$ represent the reciprocal vectors of an emergent moiré lattice, and the fast-oscillating terms have been omitted. We would also like to mention in passing that considering a triangular lattice ferromagnet also leads to the same interlayer coupling.

$\mathcal{H} = \mathcal{H}_{\text{intra}} + \mathcal{H}'$ describes the system in the general setting described above. However, for simplicity, in the remainder of this work we make the assumption that spin stiffness and anisotropy parameters of the antiferromagnetic layer are large enough to render it essentially nondynamical; this results in a uniform Néel vector in the $\pm\hat{\boldsymbol{z}}$ directions; we choose $\boldsymbol{N} = +\hat{\boldsymbol{z}}$. With these assumptions, the Hamiltonian reduces to an effective single-layer one, which, up to a constant rescaling, has the form:

$$\mathcal{H} = \frac{1}{2}(\nabla \boldsymbol{M})^2 + \beta\, \boldsymbol{M} \cdot (\nabla \times \boldsymbol{M}) + \alpha\, M_z\, \Phi(\boldsymbol{x}). \tag{5.2}$$

We have introduced the dimensionless parameters $\alpha = \frac{J'}{\rho_1 d^2}$, $\beta = \frac{D}{\rho_1 d}$ with $d = |\boldsymbol{d}_a|$, and adopted the dimensionless coordinates $\boldsymbol{x} = d\, \boldsymbol{r}$ and defined $\Phi(\boldsymbol{x}) = \sum_\alpha \sin(\hat{\boldsymbol{d}}_\alpha \cdot \boldsymbol{x})$.

When $\alpha = 0$, ground states of the system consist of spirals with wavenumber

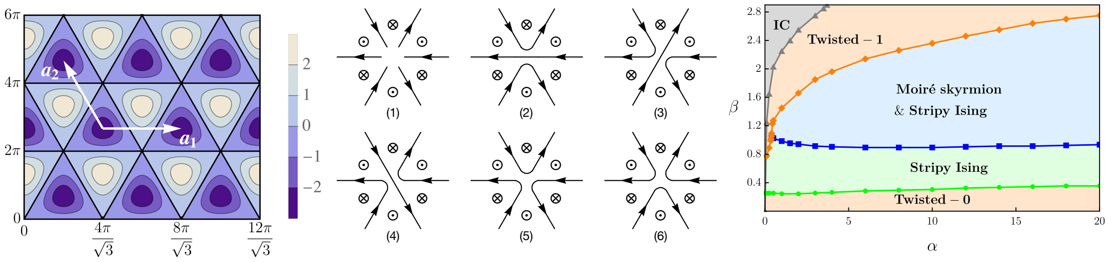

(a) (b) (c)

Figure 5.1: (a) The moiré potential $\Phi(\boldsymbol{x})$. $\boldsymbol{a}_1$ and $\boldsymbol{a}_2$ form a basis for the emergent moiré lattice. (b) (1) An avoided vertex at large α and β. The magnetization vectors on the domain walls point along them. (2-4) The 3-state clock vertex. (5-6) The Ising vertex. (c) The ground-state phase diagram obtained from LLG equations. IC stands for incommensurate phases which can include states of various periodicities. In the blue region of intermediate β, the moiré skyrmion and the stripy Ising states are degenerate in energy. Different commensurate phases are separated by first-order transitions.

β (period $2\pi/\beta$). Generically, $\boldsymbol{M} = (\hat{\boldsymbol{q}} \times \hat{\boldsymbol{z}} \sin[\boldsymbol{q} \cdot \boldsymbol{x}], \cos[\boldsymbol{q} \cdot \boldsymbol{x}])$ describes a spiral propagating in the $\hat{\boldsymbol{q}}$-direction for $\beta > 0$ (and $|q| = \beta$). In the strong-coupling limit when α is large and β is zero, the energy is minimized by a coplanar solution, where domains with $\boldsymbol{M}$ close to $(0, 0, \pm 1)$ form, separated by narrow domain walls. Each domain is identified as a region in which $\Phi(\mathbf{x})$ has a definite sign, resulting in the opposite sign for M_z. In Fig. 5.1a, we plot the structure of $\Phi(\mathbf{x})$, which forms a triangular lattice; $\Phi(\mathbf{x})$ has a positive or negative sign in each of the faces of the triangles.

5.3 Weak-coupling Analysis

In the small α and β regime, two possibilities can arise: when the α term is dominant over β, a *twisted* solution forms, where in each face of the triangular lattice the magnetization tends to bend towards $-\text{sign}[\Phi(\boldsymbol{x})]\hat{\boldsymbol{z}}$; nonzero β causes distortions in the $\beta = 0$ coplanar solution. We call the phase containing these solutions as twisted-0 for a reason that will be explained later. Alternatively when the β term dominates, one expects a spiral configuration perturbed by the moiré potential. Since the spiral can have a period that is different from that of the moiré lattice, we call this the incommensurate phase. A commensurate-incommensurate (CI) transition can occur between these two phases. Below we perform a perturbative solution in the commensurate case, and then extend the analysis to the incommensurate phase and also the transition between the two phases.

We will use a polar coordinates parametrization $\boldsymbol{M} = (\sin\theta\cos\phi, \sin\theta\sin\phi, \cos\theta)$ for the minimization of the classical Hamiltonian (5.2). To zeroth order in β, the solution to the Euler-Lagrange equation (see appendix D for a complete discussion) yields a constant value for ϕ: $\phi(\boldsymbol{x}) = \phi^{(0)} + O(\beta\alpha)$. The simplified Euler-Lagrange equation for θ then reads $\nabla^2\theta + \alpha\sin\theta\,\Phi(\boldsymbol{x}) = 0$, with the solution to zeroth order in β taking the form $\theta(\boldsymbol{x}) = \frac{\pi}{2} + \alpha\,\Phi(\boldsymbol{x}) + O(\alpha^3, \beta^2\alpha)$; this solution requires a definite mean value for θ, i.e. $\bar{\theta} = \pi/2$. It furthermore predicts that in the twisted-0 phase, fluctuations of θ from $\pi/2$ are captured by $\Phi(\boldsymbol{x})$ and hence triangular domains form in which spins prefer either up or down directions. We have checked numerically that the solution even with infinitesimal β, prefers only three values for $\phi^{(0)}$, i.e. $e^{i\phi^{(0)}} = \left[\hat{d}_y - i\hat{d}_x\right]^n$, with $n = 1, 2, 3$.

We now turn to a perturbative study of the incommensurate phase and the CI transition; we will focus on the incommensurate solutions close to the CI transition line. If α plays a subdominant role, the solution resembles a spiral with a period close to $\frac{2\pi}{\beta}$; this period increases as β is lowered towards the CI transition. Close to the transition point, locally the configuration looks similar to a commensurate one but small-width discommensurations (or solitons) can form with large separations. It is this separation distance that diverges at the CI transition [28]. We exploit this key information to find incommensurate solutions close to the transition by considering configurations that are locally very close to being commensurate but their local properties could change appreciably if a distance close to the long incommensurate periodicity is taken.

To this end, we make use of the commensurate solution found above, in which θ has the mean value $\bar{\theta} = \pi/2$; we now allow this mean value to fluctuate slowly as the position is varied. As a result, we work with a modified Euler-Lagrange equation $\nabla^2\theta + \alpha \sin\theta\, \Phi(x) = \lambda$, where λ is a Lagrange multiplier. This equation can be solved, and one finds the energy density per unit cell of such a periodic solution to have the form $-\frac{3}{4}\alpha^2 \sin^2\bar{\theta}$; note that this is minimized for $\bar{\theta} = \pi/2$. Letting $\bar{\theta}$ fluctuate over long distances will result in an energy penalty; we require this energy penalty to be compensated by the DM interaction energy gain in the incommensurate solutions. In fact an effective one-dimensional Hamiltonian of the form $\mathcal{H}^{\text{eff}} = \frac{1}{2}\left(\partial_y\bar{\theta}\right)^2 - \frac{3}{4}\alpha^2 \sin^2\bar{\theta} - \beta\, \partial_y\bar{\theta}$, can be exploited to study this competition. This sine-Gordon Hamiltonian has been extensively studied, see e.g. [28], and is known to have a continuous CI transition at $\beta_c = \frac{\sqrt{6}}{\pi}\alpha$. This means that the phase separation line between the commensurate and the incommensurate phases has a linear form for small α and β. For $\beta \gtrsim \beta_c$, the ordering wavevectors deviate from the moiré ones (including the vanishing wavevector) with the asymptotic behavior $\delta k \sim \frac{\sqrt{3}\alpha}{2}\, 1/\log\left(\alpha^2 \frac{1}{\beta-\beta_c}\right)$; the direction of this incommensurate wavevector correction is not fixed at this order of perturbation theory.

5.4 Possible Commensurate Phases

We now turn to the large-α regime where the properties of different commensurate phases are in most contrast. In this regime, triangular domains of spins mostly pointing in the $\pm\hat{\boldsymbol{z}}$ directions form. These domains correspond to those in Fig. 5.1(a) with $\text{sign}[\Phi(x)] = \mp 1$, respectively The widths of the domain walls (in dimensionless units) decrease as α increases, resulting from the competition of the kinetic and moiré potential terms. On the domain walls $\Phi(x) \approx 0$, thus the magnetization is not constrained by the α term. It is actually the different configurations that the magnetization could take on these domain walls that distinguish the different commensurate phases. Starting at $\beta = 0$, the energy is minimized by a coplanar configuration wherein for all points, the in-plane magnetization can take any direction, i.e. there is an $SO(2)$ rotational symmetry.

Next we consider the effect of nonzero β. The DM term, up to integration by parts, can be written as $-2\beta\, \boldsymbol{M} \cdot (\hat{\boldsymbol{z}} \times \boldsymbol{\nabla} M_z)$. Namely, $\boldsymbol{M}$ prefers to be perpendicular to the gradient of M_z, which lies normal to the domain walls. When β is not large, it does not affect configurations deep inside the triangular domains, but drives the magnetization vectors on the triangles' edges to point along them in the direction preferred by the DM interaction, as shown in Fig. 5.1b(1).

However, the configurations close to the vertices are frustrated, i.e., the three directions of magnetization vectors along the edges of the triangles cannot be satisfied at the same time, and hence different vertex configurations could arise. One possibility is that the vertex magnetization follows one of the three directions on the edges, breaking the $SO(2)$ symmetry down to C_3, as shown in Figs. 5.1b(2-4); we name this a 3-state clock vertex. Interestingly, a solution consisting of the same vertex configuration everywhere has the same symmetries as those of the twisted-0 solution discussed above. We call the phase containing this solution twisted-1 for reasons explained below.

Another possibility of the vertex configuration is Ising-like, i.e. spins pointing along $+\hat{\boldsymbol{z}}$ or $-\hat{\boldsymbol{z}}$ as in Figs. 5.1b(5) and 5.1b(6), enabling the possibility of skyrmions: if all the vertices choose the same configuration, say 5.1b(6), a skyrmion lattice of moiré scale is formed: triangular domains with up spin constitute a lattice of skyrmions in a down-spin sea (see also Fig. 5.2).

The skyrmion lattice phase can be viewed as stabilized due to an effective ferromagnetic interaction between neighboring Ising-type vertices, however it could happen that this interaction becomes antiferromagnetic, making a translational-symmetry-broken phase possible: Our numerical results (see below) indicate that one of such phases is possible, where the Ising vertices all point in the same direction along the direction specified by one of the moiré lattice unit vectors, while along the directions of other independent unit vectors, the Ising vertices alternatively point up and down (see Fig. 5.2). We name it as the Ising stripy phase.

Symmetries of these solutions are discussed in appendix D. We go through the full Hamiltonian minimization next and determine the energetically favored solution for different parameter choices.

5.5 Numerical minimization

To minimize the energy functional in (5.2), we work with the Landau-Lifshitz-Gilbert (LLG) equations [68, 45]. The variation of the Hamiltonian with respect to the magnetization vector is treated as an effective external field, $\boldsymbol{B}^{\text{eff}} = -\delta H/\delta \boldsymbol{M}$, which results in the LLG equations: $\frac{d\boldsymbol{M}}{dt} = -g\,\boldsymbol{M} \times \boldsymbol{B}^{\text{eff}} + \eta\,\boldsymbol{M} \times \frac{d\boldsymbol{M}}{dt}$. Here g is the gyromagnetic ratio, which is not important since we are only interested in the late-time static configurations, and η is the Gilbert damping coefficient. Releasing from various trial configurations and comparing the energies of the final configurations, one can find the ground state with of the Hamiltonian. Fig. 5.1c shows the numerical phase diagram obtained from LLG equations using the *ubermag* and *OOMMF* packages [11, 12, 36]. Different periodic boundary conditions compatible with moiré lattice periodicities are imposed. More details on the numerics are presented in appendix D.

We find that apart from the incommensurate phases, the twisted-0, the twisted-1,

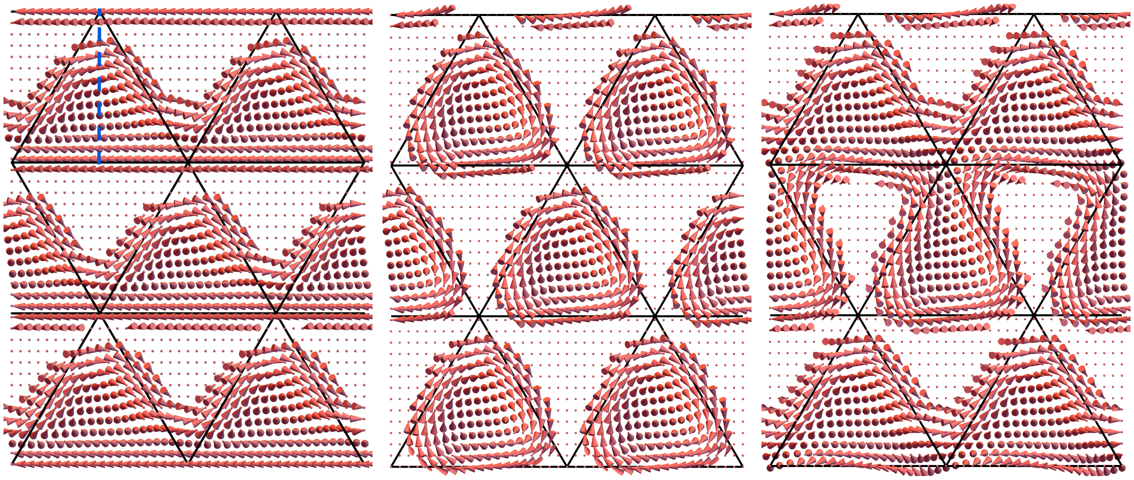

Figure 5.2: Top view of the twisted-1 (left), skyrmion lattice (middle) and the stripy Ising (right) configurations generated at $(\alpha, \beta) = (1.25, 1)$, $(1.25, 1)$ and $(2.5, 0.5)$, respectively. The background $-\hat{\boldsymbol{z}}$ pointing magnetization vectors are depicted as points. The vertices are of the type shown in Fig. 5.1b(2) for the twisted-1, of the Fig. 5.1b(6) type for the skyrmion lattice and of both 5.1b(5) and 5.1b(6) types for the Ising stripy. The solution on the left panel shows a nonzero winding in its magnetization as the dashed line is traversed (see the main text).

the moiré skyrmion and the Ising stripy phases introduced above constitute the main body of the phase diagram in the strong coupling regime. In Fig. 5.2, we present examples of steady-state configurations for these three phases (note that the shown configurations are not necessarily ground states for the chosen parameters). In the moiré skyrmion phase, interestingly, there is one skyrmion per moiré unit cell with skyrmion number ±1 and helicity $\pi/2$, i.e. $N_{sk} = \frac{1}{4\pi} \iint_{u.c.} d^2\boldsymbol{x}\, \boldsymbol{M} \cdot \left(\frac{\partial \boldsymbol{M}}{\partial x} \times \frac{\partial \boldsymbol{M}}{\partial y} \right) = \pm 1$; the sign is different for the two types of skyrmion lattices, i.e. it depends on the direction of magnetization ($+\hat{z}$ or $-\hat{z}$) at the centers of the skyrmions in each solution.

We see that the twisted-0 phase has the lowest energy for small β as expected. Upon increasing β, it is then replaced by the stripy Ising phase. Interestingly, at larger

β, the stripy Ising and the moiré skyrmion states, despite having different symmetries, become degenerate in energy. Note that these two states both have Ising-type vertices that are only spatially arranged differently. Then at higher values of β, the twisted-1 phase, that has vertex configuration 5.1b(2-4) everywhere, minimizes the energy. This phase has the same symmetries as the twisted-0 phase, but is different in the winding numbers along high symmetry lines: The magnetization vector rotates exactly by 2π in the $x - z$ plane along the dashed blue line segment specified in the left panel of Fig. 5.2. On the other hand, the net winding is zero in the twisted-0 phase (see appendix D for a strong coupling figure of the twisted-0 phase), hence the names twisted-0 and twisted-1. In principle, other winding numbers can also be be possible (similarly all other solutions can also have higher winding numbers as well). All transitions between these commensurate phases are first order, which can be observed by comparing the energies. More details can be found in appendix D.

In the upper left corner of the phase diagram, we have found different incommensurate phases, i.e., states incommensurate with the moiré potential. For example when $\alpha = 0$, the periodicity of the spirals is given by $2\pi/\beta$. In general, the competition between α and β can lead to configurations with various periods and symmetries, and even chaotic structures [7]. Since, in the LLG equations, we cannot exhaust all possible trial configurations and unit cells enlargements, and thus the extent of the incommensurate phases is underestimated; as a result, we take a cautious view and do not make definitive conclusions regarding the nature of this region or its phase boundary, except what can be extracted from the weak-coupling analysis presented above. In this weak-coupling regime, the prediction for the CI transition line is supported using numerics with large sample sizes, see appendix D.

5.6 Discussion

A considerable portion of the phase diagram Fig. 5.1c for $\alpha > 3$ is occupied by phases with the Ising type vertices. In this chapter, we have ignored the single-ion anisotropy for the ferromagnetic layer; such anisotropy, if Ising-like, further stabilizes Ising-type vertices. On the other hand, a perpendicular magnetic field will similarly stabilize the Ising vertices, and in particular favor the skyrmion lattice phase over the stripy Ising phase in the blue region of the phase diagram in Fig. 5.1c; this is consistent with the well-known fact that external fields can stabilize skyrmion lattice phases [17, 16, 138, 47, 70].

We have made the assumption that the spin-stiffness and anisotropy parameters of the antiferromagnetic layer are large, such that the antiferromagnetic layer is in the collinear phase. We expect this assumption to be valid in the regime where $C/(\rho_2 d^2) \gtrsim \alpha^2$ and $\rho_2/\rho_1 \gtrsim 1$, as analyzed in our previous work [53]. Relaxing this assumption could lead to ground state solutions requiring nontrivial textures in both layers resembling those in [53]. Furthermore, let us mention that a small twisting between the two layers effectively increases the magnitude of the wavevector d introduced above. In the dimensionless parametrization, this corresponds to a modification of the spatial structure of $\hat{\Phi}(\boldsymbol{x})$, and a decrease in α and β.

The material MnPS_3, having an antiferromagnetic Heisenberg Hamiltonian and an Ising-like anisotropy [59, 131, 96, 67], may be a good candidate for the antiferromagnetic layer. The family of Janus transition metal dichalcogenides [143] could be a promising candidate for the FM layer; these materials have small lattice mismatches compared with MnPS_3 and also exhibit the DM interaction [142].

Interesting phenomena such as the topological Hall effect could arise due to the effect of moiré skyrmions on the conduction electrons through the emergent electromagnetic field (see for example [91, 90]). We leave the full description of the related physics to future work.

Note added: During the preparation of this draft, we noticed [4] which has some overlap with our work. Their focus is mainly on the LLG simulation of commensurate phases, however, other strong-coupling commensurate phases, incommensurate phases and in particular the commensurate-incommensurate transition studied here are not captured. In particular, the Ising stripy phase which we found to be degenerate with the skyrmion phase is absent their treatment.

Chapter 6

Many-body physics in the continuum using wavelets

In this chapter, we introduce a methodology for studying many body physics in the continuum, in which instead of the usual approach of employing a finite differences lattice discretization, the wavelet basis is used. The main property of our interest that wavelets have is that they can provide a *multiresolution* basis for particles' wave functions; structures at different length scales can be distinguished within the wavelet basis. We use this multiresolution property to design a *fine graining quantum circuit* that can be used in combination with a variational many body method of choice to efficiently solve for the ground state of a continuum system; starting from a coarse scale the solution is found and fine grained into finer scales until the desired resolution is achieved. The method is general and can be utilized in combination with classical or quantum variational many body algorithms. We finally use the method in combination with density matrix renormalization group algorithm in one dimension and exhibit its power and efficiency.

This chapter is based on Ref. [49].

6.1 Introduction

Real particles live in the continuum. However, in the study of strongly correlated matter one usually resorts to lattice models. This is typically justified when considering the electronic degrees of freedom in a solid-state system, which experience a periodic potential due to the ions, and the ions can be treated as classical degrees of freedom within the Born-Oppenheimer approximation. Yet many different situations in solid state or cold atomic systems can be considered which benefit from a continuum description. This includes cases where a continuum description is more accurate than a lattice model formed from Wannier states, for example in very shallow periodic potentials, or cases where a set of (symmetric) localized Wannier states is unavailable due to topological obstructions [19, 81, 2]. Likewise, there are cases where the periodic potential is absent entirely, for example for ion or atomic traps, in quantum chemistry applications, or when treating mesoscopic systems within the effective-mass approximation.

Several numerical techniques are able to approach continuum problems directly. These include quantum Monte Carlo techniques such as variational or diffusion quantum Monte Carlo (QMC) [92, 10], which have been able to provide high-precision simulations in many cases. However, unbiased QMC techniques have limited applicability due to the fermionic sign problem. More recently, the overwhelming success of tensor network methods for studying the low-energy properties of lattice systems has inspired the development of tensor networks formulated directly in the continuum [122, 119, 121]. However, the main drawback here is the complicated minimization procedure without flexibility to use the body of previously developed tensor network methods.

Alternatively, one can choose to discretize the problem. A widely used approach is to introduce a finite-difference discretization of the continuum Hamiltonian, thus obtaining an effective lattice Hamiltonian which can be studied using standard techniques. However, such a discretization invariably leads to very dilute systems and wide discrepancies between UV and IR energy scales [35], which are very unfavorable for the convergence of tensor network approaches, requiring extra steps such as multi-grid approach to obtain reliable results [35, 46].

Another approach is to introduce a set of basis functions in which the wavefunctions are decomposed. This approach is widely used in quantum chemistry or *ab initio* electronic structure calculations. In this chapter, we pursue the latter approach using Daubechies wavelets [32, 63] as basis. These wavelets have several properties that make them appealing for this application: First, they have strictly compact support in real space, such that Hamiltonians that are local in real space will also be local when represented in the wavelet basis. Secondly, they are localized also in momentum space, and thereefore each wavelet can be associated with a spatial resolution. Thirdly, they can – along with their first and second derivatives – be computed exactly at dyadic points, thus yielding an efficient and accurate way of evaluating matrix elements. Finally, and most importantly, they form a *multiresolution analysis*: starting from a set of orthonormal *scaling* functions at some chosen resolution, one can systematically refine the basis by adding *wavelet* functions of higher resolution without compromising the orthonormality of the entire basis. This last step can be done globally or locally, if desired.

In this chapter, we will show how to take advantage of these properties within variational simulation techniques both on classical computers using tensor networks and on quantum computers using variational quantum eigensolvers. Our general approach will be to first solve the system at a coarse scale, where the large scale structure of the state is captured; this solution is then used for an *exact* transformation into a basis with higher resolution, where smaller length scale details will be found iteratively, and the process goes on until convergence is achieved. This transformation can be expressed as a local, finite-depth quantum circuit. To demonstrate the power of the approach, we use this quantum circuit in a DMRG calculation and show how this step-by-step algorithm makes the procedure to find the ground state considerably faster by reducing the number of the required DMRG sweeps.

Wavelets and other similar constructions have been used in combination with computational approaches for the study of electronic structure in several situations [39, 127, 128, 85].

The chapter is organized as follows: first, in Sec. 6.2 we present a concise introduction to the wavelet basis and in particular Daubechies wavelets. In Sec. 6.3, we discuss how we study many body physics in the continuum using the wavelet basis, and present some preliminary DMRG results. Then in Sec. 6.4, we go into details of the quantum circuit that implements the wavelet scale transformation discussed above and how the fine graining procedure should be carried out in general. After that in Sec. 6.4.1, we discuss how DMRG could be implemented using the wavelet basis, we furthermore show the fine graining circuit can be used for a step by step DMRG which adds significantly to the efficiency of the whole procedure.

6.2 The Daubechies wavelet basis

While wavelets were originally conceived to process time-domain signals both in time and frequency domains, they have found use far beyond those limits, including the simulation of quantum systems. In this work, we focus on *Daubechies* wavelets [32]. These form an *orthonormal* basis for square-integrable functions on the real axis [63, 107] (we denote the space of such functions as L^2). They have strictly compact support in real space, while also being localized in momentum space. As such, working in the wavelet basis will preserve the locality of the Hamiltonian under study while also lending an ability to assign each basis element to a spatial resolution that is

a_0	a_1	a_2	a_3	a_4	a_5	a_6	a_7
0.163	0.505	0.446	-0.020	-0.132	0.022	0.023	-0.007

Table 6.1: Recursive coefficients for Daubechies wavelet of order $K = 4$.

associated with the range of momenta that it is supported on.

Many classes of wavelets, including the Daubechies wavelets, can be obtained by starting from a single *scaling function* $\phi(x)$, which is recursively defined by

$$\phi(x) = 2 \sum_n a_n \, \phi(2x - n), \tag{6.1}$$

where the a_n are real coefficients that ultimately define the wavelet. Daubechies wavelets in fact form an entire family of wavelet bases, each of which is characterized by an integer K, often referred to as the *order* of the wavelet, which also denotes half the number of non-vanishing coefficients a_n. The choice of these coefficients determines the properties of the wavelets. As an example, we list the coefficients for $K = 4$ in Table 6.1, which in practice we will be mainly using in this work; the coefficients for other orders can be found in many references or software packages. By inspection of Eq. (6.1), we can confirm that the order-K Daubechies scaling function has compact support from 0 to $2K - 1$ and is strictly zero outside this range. Furthermore it can be shown, e.g. by direct computation, that the Fourier transform of the scaling function is peaked around zero momentum. Below, we will describe practical algorithms for computing $\phi(x)$ given the coefficients a_n; example scaling functions are shown in Fig. 6.1.

Next, we consider integer translations of the scaling function. One interesting property of the Daubechies scaling functions is that they are normalized and integer translations of the scaling function have zero overlap with the scaling function itself:

$$\int dx\, \phi(x)\, \phi(x-n) = \delta_{n0}, \tag{6.2}$$

for integer n. This means that the set of integer translations of the scaling function form an orthonormal basis for a subset of L^2. However, it is intuitively clear that it is not a complete basis: it is not able to capture functions with spatial features on a resolution finer than the feature size in the wavelet.

To improve on this situation, one can consider rescaled versions of the scaling function. To resolve features that are smaller than what the scaling function can resolve by some factor 2^{-j}, where j is an integer, consider the transformed scaling function

$$\phi_{jn}(x) = 2^{-\frac{j}{2}}\, \phi(2^{-j}x - n). \tag{6.3}$$

Note that j and n are integers that can take all possible positive and negative values. These functions inherit the features of the original scaling function, in particular all ϕ_{jn} for a given j are orthonormal. We denote the space they span by

$$V_j = \text{span of } \{\phi_{jn} | n \in \mathbb{Z}\}. \tag{6.4}$$

From Eq. (6.1), we note that we can always decompose a given ϕ_{jn} in terms of the $\phi_{(j-1)n}$, and therefore

$$V_j \subset V_{j-1}. \tag{6.5}$$

Furthermore, it can be shown that in the limit $j \to \infty$, the entire space of square-integrable functions is recovered, i.e. $\lim_{j \to -\infty} V_j \to L^2$.

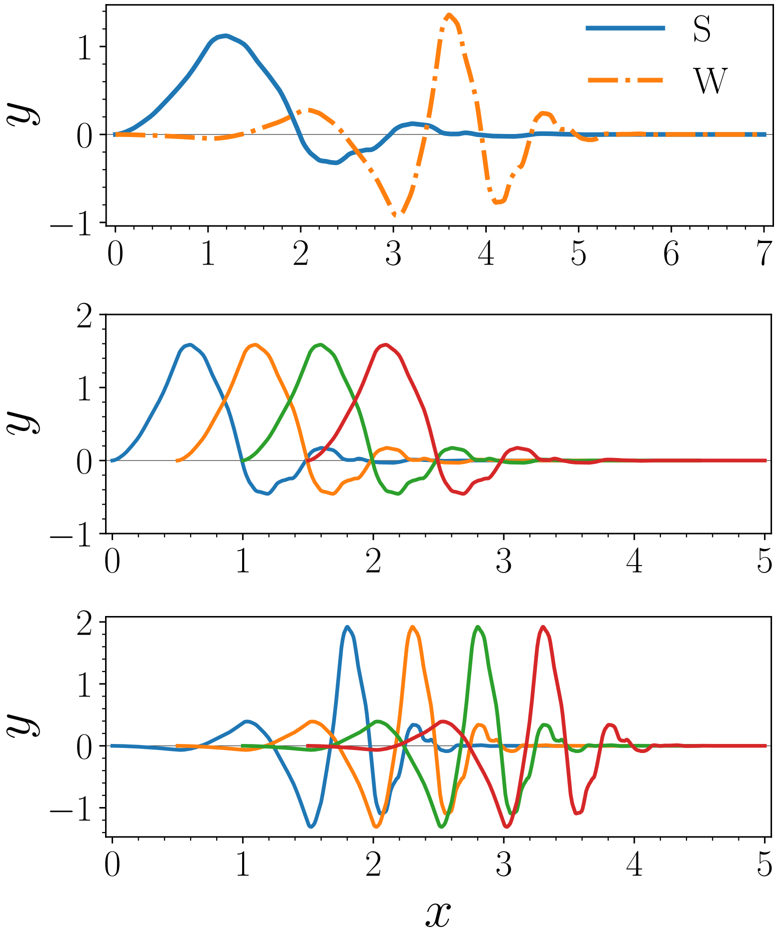

Figure 6.1: Scaling and wavelet functions of the Daubechies wavelet basis of order 4 are depicted here for illustration. We use the same order Daubechies wavelets in this work. Top: The main scaling function and the mother wavelet, i.e. $y = \phi(x)$ and $y = \psi(x)$ are plotted. Middle: scaling functions of level $j = -1$, i.e. the functions $\phi_{-1,0}, \phi_{-1,1}, \phi_{-1,2}, \phi_{-1,3}$ are plotted. Bottom: wavelet functions of level $j = -1$, i.e. the functions $\psi_{-1,0}, \psi_{-1,1}, \psi_{-1,2}, \psi_{-1,3}$ are plotted.

However, there is another way to refine the basis of scaling functions at some level of refinement, V_j. Instead of directly considering V_{j-1}, we can consider the space of functions that are missing to reach higher resolution, i.e. the space W_j that satisfies:

$$V_{j-1} = V_j \oplus W_j. \tag{6.6}$$

Remarkably, this space can be constructed in a similarly simple fashion as the space of scaling functions using a basis, called the wavelets, with similarly desirable properties!

The starting point is the definition of the *mother wavelet*

$$\psi(x) = 2\sum_n b_n\, \phi(2x - n), \tag{6.7}$$

where $b_n = (-1)^n a_{2K-1-n}$. The mother wavelet is again compactly supported on $[0, 2K-1]$, localized in Fourier space, and its integer translations are orthogonal to each other,

$$\int dx\; \psi(x)\psi(x-n) = \delta_{n0}. \tag{6.8}$$

To construct a basis for the space W_j, we consider the rescaled translations of the mother wavelet to recover wavelets at different scales:

$$\psi_{jn} = 2^{-\frac{j}{2}}\, \psi(2^{-j}x - n). \tag{6.9}$$

By construction, we have the desirable properties

$$\begin{aligned} &\int dx\; \psi_{jn}(x)\, \psi_{km}(x) = \delta_{jk}\delta_{nm}, \\ &\int dx\; \psi_{jn}(x)\, \phi_{km}(x) = 0, \qquad \text{for } j \leq k. \end{aligned} \tag{6.10}$$

The above orthogonality relations along with iterative use of Eq. (6.6) show that an orthonormal basis for L^2 can be constructed that consists of a single level of scaling functions and multiple levels of wavelet functions; such basis is capable of resolving structures at arbitrary scales. This so-called multiresolution property is a central feature of Daubechies wavelets and lends one great flexibility in constructing a basis that is numerically convenient. To reach a resolution on the order of 2^{-k} (with k a positive integer), one might work directly with the scaling functions V_{-k}, but one might also start with some V_j, $j > -k$, and then add wavelet basis functions from

W_m, $-k < m \leq j$, as convenient. For example, the additional basis states could be added throughout the sweeps of a variational algorithm to increase the resolution once the variational estimate has converged at a given resolution, or they might only be added locally if different spatial resolution is required in different parts of the system. We will illustrate applications of both of these ideas to quantum many-body systems in the remainder of this chpater.

6.3 Many-body physics in the wavelet basis

Having chosen some basis of Daubechies scaling and wavelet functions, we would like to obtain a discrete representation of fermionic field operators in the continuum. We will refer to the elements of the entire multiresolution basis as $\chi_\alpha(x)$, where α now enumerates all (scaled and shifted) scaling and wavelet functions that we use. Given an operator $c^\dagger_\sigma(x)$ of spin σ that creates a fermion of spin σ at position x, we will rewrite it as

$$c^\dagger_\sigma(x) \approx \sum_\alpha \chi_\alpha(x) c^\dagger_{\alpha\sigma}, \tag{6.11}$$

where now $c^\dagger_{\alpha\sigma}$ can be viewed as creating a fermion of spin σ in the basis state $\chi_\alpha(x)$. The relation becomes exact as the limit of infinite resolution of the basis is taken; in practice, we truncate the basis at a small enough resolution based on the problem in consideration.

Considering a single-particle Hamiltonian with a kinetic energy and a potential energy term,

$$H_{\mathrm{sp}} = \int dx\, c_\sigma^\dagger(x) \left[-\frac{1}{2} \frac{\partial^2}{\partial x^2} + V(x) \right] c_\sigma(x), \tag{6.12}$$

we can rewrite it in the wavelet basis as

$$H_{\mathrm{sp}} \approx \sum_{\alpha\beta\sigma} c_{\alpha\sigma}^\dagger h_{\alpha\beta} c_{\beta\sigma} \tag{6.13}$$

$$h_{\alpha\beta} = \int dx\ \chi_\alpha(x) \left[-\frac{1}{2} \frac{\partial^2}{\partial x^2} + V(x) \right] \chi_\beta(x). \tag{6.14}$$

Note that we have used the spin symmetry of the Hamiltonian, such that $h_{\alpha\beta}$ need not have spin indices; the generalization to Hamiltonians that include, e.g., spin-orbit coupling is straightforward. Since the basis functions are compactly supported, $h_{\alpha\beta}$ will be a banded matrix with the number of occupied diagonals increasing with the order K of the basis; it is thus desirable to keep K small.

However, for this procedure to be well-defined, it is important that the derivatives of the scaling and wavelet functions exist. As shown in Ref. [32], as the order K of the Daubechies basis is increased, more and more derivatives exist; for example, first derivatives exist for $K > 3$, while second derivatives exist for $K > 7$, and so on. To avoid having to use $K > 7$, one can rewrite the above integral using integration by parts,

$$\int dx\ \chi_\alpha(x)\ \partial_x^2\, \chi_\beta(x) = -\int dx\ \left[\partial_x\, \chi_\alpha(x)\right]\ \left[\partial_x\, \chi_\beta(x)\right]. \tag{6.15}$$

To evaluate these integrals in practice, we make use of the fact that Daubechies wavelets as well as their derivatives can be evaluated *exactly* and *efficiently* at dyadic rationals, i.e. for $x = \frac{m}{2^r}$ where m is an integer and r a non-negative integer [63, 74]. By choosing sufficiently large r such that $1/2^r$ is much smaller than the resolution of any basis state and rewriting the integrals as Riemann sums, the numerical error from these integrals becomes negligible. We describe the details of how to perform this calculation in App. E.1.

This approach is easily extended to interacting systems. We can, for example, consider a translationally invariant density-density interaction of the form

$$H_{\text{int}} = \frac{1}{2} \sum_{\sigma\sigma'} \int dx\, dx'\; c^\dagger_\sigma(x) c^\dagger_{\sigma'}(x')\, \mathcal{U}(x-x')\; c_{\sigma'}(x') c_\sigma(x). \tag{6.16}$$

In this chapter, we will set $\mathcal{U}(x-x') = U_0\, \delta(x-x')$ and thus obtain the wavelet-basis interaction Hamiltonian

$$\begin{aligned} H_{\text{int}} &\approx \sum_{\alpha,\beta,\beta',\alpha'} h_{\text{int},\, \alpha\beta\beta'\alpha'}\; c^\dagger_{\alpha\uparrow} c^\dagger_{\beta\downarrow} c_{\beta'\downarrow} c_{\alpha'\uparrow} && (6.17) \\ h_{\text{int},\, \alpha\beta\beta'\alpha'} &= U_0 \int dx\; \chi_\alpha(x)\, \chi_\beta(x)\, \chi_{\beta'}(x)\, \chi_{\alpha'}(x) && (6.18) \end{aligned}$$

In our numerical examples, we will consider finite-size systems, and thus need to restrict the physical states to finite intervals. Since truncating the basis states at the boundaries would break their orthogonality, we instead implement this by adding a very high potential barrier (denoted as V_b throughout) outside of the finite system. This ensures that the resulting wave functions will have a small spatial component beyond the interval of our interest, and also have a small overlap with those wavelet basis elements at the two spatial ends; such overlap will have a scaling as $\sim e^{-\sqrt{V_b}}$.

This is an important point to which we will come back later. In the construction of the wavelet basis, we consider all basis functions that overlap with the finite-size system.

We use scaling functions at a level denoted by j_0, which in principle is arbitrary and use wavelets between levels j_0 and j_{min} throughout the system. In order to capture all the relevant physics in a problem, we need to choose the level j_{min} such that $2^{j_{min}}$ (basis elements' length scale at level j_{min}) is small enough and in particular smaller than the smallest length scale in the problem. If a higher resolution is needed locally in some location, we use the multi-resolution property further and add more wavelet functions with $j < j_{min}$ to the vicinity of that location and address local details there.

A side note, which we would like to discuss here, is that we are working in units where $\hbar = m = 1$, and as a result only one dimension remains which we take to be the length dimension; every energy in particular will have the dimension $(\text{length})^{-2}$. Also, note that the wavelets have characteristic lengths. For example, the scaling and wavelet functions at level j have a spacing of 2^j in the above units.

6.3.1 DMRG simulations

At this point, we turn to performing DMRG with the wavelet basis. The wavelet basis states define an effective lattice on which the resulting DMRG solution, which is a matrix product state (MPS), lives. Different basis states, i.e. scaling and wavelet functions of different levels are sorted on this lattice based on their center of mass position. The DMRG is numerically performed using the ITensor package [40]. We benchmark the approach by considering the Gaudin-Yang model which is a model of 1 dimensional fermions with a δ function interaction and is exactly solvable by means of a nested Bethe ansatz[136, 43, 44]; the details of the benchmarking procedure is presented in appendix E.2.

We consider next the case of interacting particles in a binding potential that is a combination of parabolic and quartic; a situation that is usual in atomic and ion traps. The potential we consider here has the functionality

$$V(x) = \frac{V_b}{1+r}\left[\left(\frac{x}{L/2}\right)^2 + r\left(\frac{x}{L/2}\right)^4\right] \tag{6.19}$$

with the choice of $r = 5, L = 40, V_b = 1000$ which is depicted as the solid line in Fig. 6.2 right panel. The fermions interact through a δ-function potential with interaction strength $U_0 = +2$. Due to the theorem by Lieb and Mattis [73], the ground state lies in the sector with total spin eqaul to zero and thus we restrict the DMRG to lie within this subspace.

We use the multiresolution property of the wavelet basis here and, as shown in Fig. 6.2, use scaling and wavelet functions at the level $j = -1$ throughout the region that we expect the state to have a support; however, we add one more level of wavelets, i.e. $j = -2$, close to the center of the trap where a higher momentum cutoff is required. A total number of 20 fermions are considered in this potential.

If we start form the beginning with performing DMRG taking all of the basis elements into account, we end up with a very dilute effective lattice model, in which the DMRG algorithm experiences difficulties and a high number of sweeps can be needed for a converged solution [35]. In order to avoid this, we carry out the DMRG computation in multiple steps here: first the Hilbert space is restricted to the span of the scaling functions at the level $j = -1$ only, by adding a large chemical potential to all wavelet states, and the DMRG is performed. Note that DMRG sweeps are fast here. The solution is then used as a seed for DMRG calculation with only one level of wavelets, i.e. a Hilbert space consisting of scaling functions and wavelets at the level $j = -1$. Ultimately, the solution to the latter DMRG computation is used as the seed for DMRG with the complete Hilbert space, where DMRG sweep are slow; however, a few sweeps with this procedure suffice for convergence. Furthermore, the DMRG solutions at different steps are depicted in Fig. 6.2; one can see that as higher resolution solutions are considered, the spin density becomes more and more free from irregularities.

The above computation shows that with the wavelet basis, it would generally be desired to construct a multiresolution analysis and find the solution to a variational algorithm in a step by step fashion. This is indeed intended to circumvent the difficulty arising due to the slowness of variational algorithms in dilute fermionic systems. To put it another way, it would be beneficial if we utilize a multiresolution basis and start the variational process at the coarsest level of the basis finding the solution fairly fast there; one can then descend step by step into finer and finer details of

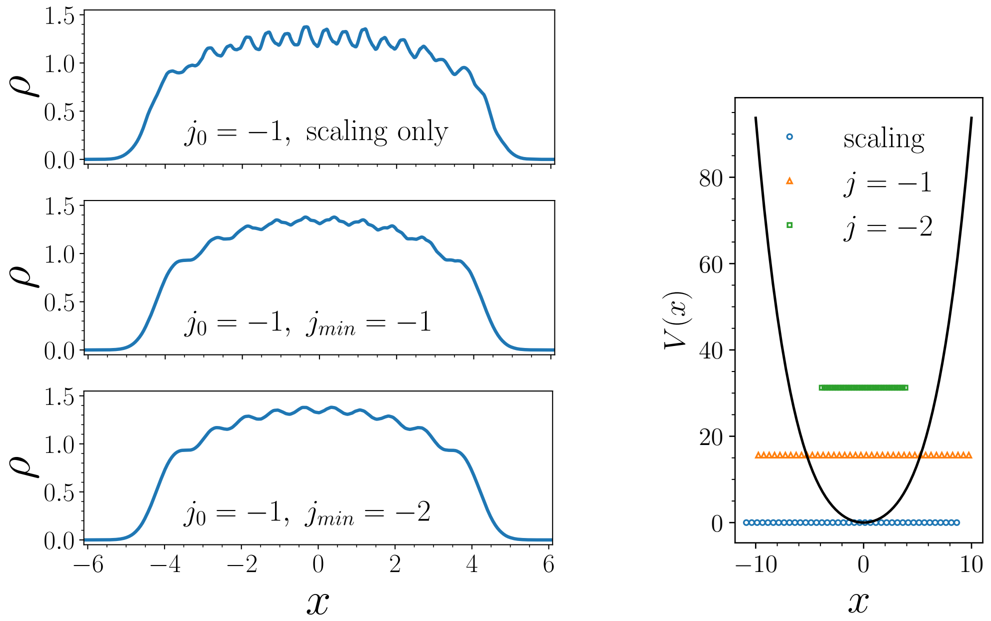

Figure 6.2: Left: The DMRG is performed step-by-step where the Hilbert space is truncated at a certain level of the wavelet basis. The solution of every step is used as the seed for the following step. Right: the potential considered in the main text that is a combination of quadratic and quartic (see main text for details). As the potetntial is deeper in the center of the trap, higher resolution is introduced there; the center of mass position of the basis states are denoted with different colors, it can be seen that wavelets of level -2 are only used closer to the center. Note that the y-coordinate of the center of mass positions does not indicate anything. All the solutions showed convergence with bond dimension equal to 100.

the problem, where the solution components on the higher resolution wavelet functions should be found. However, a problem that arises with this approach is that within a multiresolution basis, there are coarse scaling and wavelet functions of level j_0 with large supports (which capture the large scale properties of solutions) that have nonzero overlap with many finer wavelets; this reduces the sparsity of the interaction Hamiltonian considerably which slows down the whole procedure. Given this, we see that using a multiresolution basis can be very costly.

Along the same line, we have observed empirically that both the Hamiltonian MPO evaluations and DMRG sweeps are substantially faster when $j_0 = j_{min}$ is chosen which basically means that one level of scaling functions and one level of wavelets are chosen for the basis. This value of $j_0 = j_{min}$ should be chosen in a way that the fine details of the problem are captured. Note that this basis essentially spans the same state as the one spanned by a basis with larger values of j_0. The latter basis will be more beneficial for the step by step variational algorithm, but as discussed above adds considerably to the time that is needed for the computation.

This is not special to DMRG and other local variational methods including quantum algorithms can also suffer from this problem when a step by step modification of them is considered. However, there is a way out of this which will be detailed in the next section.

6.4 The fine graining circuit

We saw in the previous section that although there are motivations to perform DMRG with a multiresolution basis, the large bond dimension for the Hamiltonian MPO in this case makes working with such a multiresolution basis inefficient. We also saw that the Hamiltonian MPO construction is fastest when $j_0 = j_{min}$ is chosen as the number of overlapping basis states will be minimal in this case. Note that these observations hold true not only for the DMRG or tensor network algorithms as what causes these properties is the degree to which the interaction Hamiltonian is sparse. In this section, we discuss how it is possible to use the multiresolution property of the wavelet basis and still work with interaction Hamiltonians that are kept quite sparse.

We will work in general and will not have a particular variational method in mind for this section.

The method essentially goes as follows: the Hamiltonian is the most sparse and thus the variational procedure is fastest when $j_0 = j_{min}$, that is when one works with scaling functions and only wavelets at the same level. Noting this, we start by carrying out the variational procedure on a coarse basis which is populated by scaling functions and wavelets of some level j that is larger than our target j_{min} value; this results in a coarse solution which describes the large scale structure of the state but does not capture the fine details we are interested in. We note that the space that is spanned by the scaling functions and wavelets at this given level j is the same space as that spanned only by scaling functions at one finer level $j-1$, i.e. $V_j + W_j = V_{j-1}$. This allows us to continue the procedure in the second step by working on a basis that contains scaling functions and wavelets at the level $j-1$; there is an *exact* transformation, which we call the fine graining process, that allows us to rewrite the solution written in terms of the first step basis in terms of only scaling functions of the second step; this way, the solution found at the first step can be used as the seed for the variational procedure on the second step. The procedure can be continued until convergence is achieved. Put another way, with this approach at each step, the solution from the previous step determines the scaling functions components to a large extent and the variational procedure works out the wavelets components.

There is in general a shallow quantum circuit that can carry out the transformation discussed above from each step to the next, we call this circuit the fine graining circuit. We will detail it below.

For a given step n, we represent the elements of the basis i.e. scaling and wavelet functions, whose level we denote as j, as different sites of a given lattice of size N on which the computation is performed (see Fig. 6.3, top left); these lattice sites could correspond to e.g. qubits in a quantum computer, each of which represents a basis function with up or down spin using an encoding like Jordan-Wigner; another possibility for this lattice is the effective lattice on which the MPS solution of the DMRG is defined, etc. For simplicity, we assign odd sites on this lattice to the wavelets which we denote by w sites and assign even sites to scaling functions which we denote by s sites; the latter sites are the target sites for our fine graining procedure. The w sites will be empty at the end of the fine graining procedure; noting this fact, either by the construction of the variational procedure or by some auxiliary quantum circuit, we arrange for the scaling and wavelet functions of the previous step to be encoded in terms of the w sites of the lattice of the present step (see Fig. 6.3, middle left). Note here that since we are considering a finite interval, we have an equal number of w sites and s site on the lattice; this number, which is equal to $N/2$, is also the number of all scaling and wavelet functions of the previous step; this allows for the above encoding to be done.

Now one needs to perform the fine graining transformation on the lattice; if we write the state from the previous step in a second quantized language, every creation

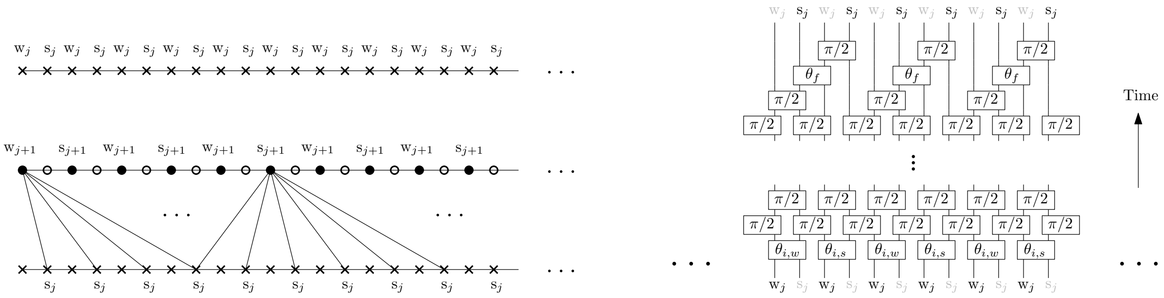

Figure 6.3: Left: on the top, the lattice used for step n is shown, which employs scaling and wavelet functions of level j. The solution of step $n-1$ (with scaling and wavelet functions of level $j+1$) is encoded on the w sites of the step n lattice. The fine graining transformation in this picture can be seen as a basis transformation on the lattice of step n. Right: the parallelized Givens circuit for the case of spinless fermions. θ values are determined at each step by requiring an element in the matrix $\tilde{u}$ to vanish. The depth of this circuit is around $8K$, where K is the order of the Daubechies basis. Details of the derivation of this circuit is presented in appendix E.3.

operator of basis elements at level $j+1$, i.e. operators like $c^{\dagger}_{\alpha_{j+1},\sigma}$ should be transformed into $\sum_{\beta_j} V_{\beta_j\alpha_{j+1}} c^{\dagger}_{\beta_j,\sigma}$ in the fine graining process. Note that the index α_{j+1} runs over both the scaling and wavelet function at level $j+1$ but β_j only denotes scaling functions at level j, and σ is a spin index. The transformation matrix V is defined as $V_{\beta_j\alpha_{j+1}} = \langle \psi_{\beta_j} | \psi_{\alpha_{j+1}} \rangle$ and is determined based on the Daubechies wavelet basis properties. We have added the level index to make the notation more clear.

Such transformation can be viewed as a basis transformation on the lattice at the beginning of step n, since we have encoded the solution from the previous step on the w sites and we want it transformed onto the s sites (see Fig. 6.3, bottom left); this transformation can be carried out using the approach presented in [64, 126], i.e. decomposing a basis transformation into a series of nearest neighbor two body gates via the use of Givens rotations on the basis transformation matrix. First we need to incorporate the above transformation matrix V into a basis transformation matrix u that acts on the combined lattice of step n, i.e. a transformation that does the following to the creation operators

$$c_a^\dagger \longrightarrow \sum_b u_{ba} c_b^\dagger \tag{6.20}$$

where a, b are indices on the lattice at step n and u is a unitary matrix. Note that spin is also encoded in the indices a, b. It is shown in Ref. [64] that such transformation of creation operators of a state is implemented if we act on the state by the following operator:

$$U(u) = \exp\left[\sum_{ab} \log(u)_{ba}\ c_b^\dagger c_a\right] \tag{6.21}$$

They furthermore show that this transformation can actually be implemented in a series of two-site unitaries such as the following

$$R_{pq} = \exp\left[\theta_{pq}\left(c_p^\dagger c_q - c_q^\dagger c_p\right)\right], \tag{6.22}$$

we take p and q to lie as nearest neighbors on the lattice we are considering, and thus in the case of encoding fermions on qubits, a Jordan-Wigner string is not needed to be considered here. It is shown in Ref. [64] that the unitary $U(u)$ can be written in terms of a number N_g of the above R matrices as: (see appendix E.3 for details)

$$U(u) = R_{p_1 q_1}(\theta_1)\, R_{p_2 q_2}(\theta_2)\, \ldots\, R_{p_{N_g} q_{N_g}}(\theta_{N_g}), \tag{6.23}$$

where the angles θ_j for the R matrices are determined through making the u matrix upper diagonal by means of acting sequentially with Givens rotations $r_{pq}(\theta)$ from the left on the matrix u. Each givens rotation is defined as (assuming $p < q$):

$$r_{pq}(\theta) = \begin{pmatrix} 1 & 0 & \dots & 0 & \dots & 0 & \dots & 0 \\ 0 & 1 & \dots & 0 & \dots & 0 & \dots & 0 \\ \vdots & \vdots & \ddots & \vdots & & \vdots & & \vdots \\ 0 & 0 & \dots & \cos\theta & \dots & -\sin\theta & \dots & 0 \\ \vdots & \vdots & & \vdots & \ddots & \vdots & & \vdots \\ 0 & 0 & \dots & \sin\theta & \dots & \cos\theta & \dots & 0 \\ \vdots & \vdots & & \vdots & & \vdots & \ddots & \vdots \\ 0 & 0 & \dots & 0 & \dots & 0 & \dots & 1 \end{pmatrix}, \tag{6.24}$$

where the only nontrivial rows are p, q rows. It is required that the matrix D, defined in the following way:

$$D = r_{p_{N_g} q_{N_g}}(\theta_{N_g}) \, \dots \, r_{p_2 q_2}(\theta_2) \, r_{p_1 q_1}(\theta_1) \, u, \tag{6.25}$$

is diagonal. In our case, we will be interested in a unitary matrix u which is real and thus D is the identity matrix. The order in which Givens rotations act on the matrix u and the rotation angles in Eq. (6.25) are discussed below after the matrix u is constructed, note that this order also determines the order in (6.23) to create $U(u)$.

Now, we turn to the question of what form the u matrix takes in our case. Due to a complication at the edges of the lattice, we first form an auxiliary matrix $\tilde{u}$ which is very close to our target matrix u. For the time being the reader may ignore their difference. For this, we note that the w sites at the beginning are partially occupied and they should be empty at the end of the fine graining procedure, while, the s sites are empty at the beginning and are partially occupied at the end; this means that in the matrix u, the only elements u_{ba} that matter for the fine graining transformation are those with the a index corresponding to a w (odd) site; these elements lie on the odd columns of u and also our auxiliary matrix $\tilde{u}$. We populate the odd columns of $\tilde{u}$ with elements of the V matrix in the following way: the column and row of $\tilde{u}$, to which an element $V_{\beta_j \alpha_{j+1}}$ is assigned, are determined respectively by the α_{j+1} and β_j indices, based on the encoding used for incorporating the previous step basis states into the lattice of step n. Note that this leaves the odd rows on the odd columns of u to have the value zero. Since the even sites at the beginning are unoccupied, even columns can simply be populated by all zeros except one element equal to 1 right above the diagonal. In other words, an even column a of $\tilde{u}$ is chosen to be a column vector with zeros everywhere except at its $a-1$ row, which will be equal to 1. This way odd sites are mapped to even sites and even sites (that are empty at the beginning) are mapped to the odd sites in a trivial way; this whole mapping ensures that the matrix $\tilde{u}$ is, in a colloquial language, *almost* unitary.

$\tilde{u}$ is not unitary due to a complication close to the edges of the lattice: the level $j+1$ basis and the level j basis, being truncated bases to represent finite intervals of interest, are not capable of representing all possible functionalities close to the edges. In particular, they are not able to faithfully represent each other close to the edges, a fact that is needed for u to be unitary. Nevertheless, this is not a problem for our variational procedure, since by construction we should make the basis long enough so that the solution has negligible overlap with basis functions at the end. Despite nonunitarity of $\tilde{u}$, we find the sequence of Givens rotations that upper triangularize it such as in Eq. (6.25); however, the resulting D matrix is not the identity matrix precisely due to the fact that $\tilde{u}$ is not unitary. Nevertheless, an important point is that if one subtracts the identity matrix from this D, the resulting matrix only acts nontrivially on the sites very close to the edges. Since, as discussed above the solution will have small overlap with these sites, we neglect the difference and replace D by the identity to get our desired u matrix: we define u to satisfy Eq. (6.25) with the same r matrices found for $\tilde{u}$, but with the left hand side equal to the identity matrix. This furthermore allows us to get the sequence of the two site unitaries R_{pq} in Eq.(6.22) to implement the fine graining procedure. The error caused by this approximation scales as $e^{-\sqrt{V_b}}$, where V_b is the potential penalty for particles outside of the spatial interval of interest (see Sec. 6.3).

Now, we can determine the specifics of the actual fine graining circuit; it can be obtained by starting from the lowest nonzero element in the first column of $\tilde{u}$ and eliminating it by a suitable Givens rotation involving this row and the one just above it. One can sequentially eliminate elements in the first column this way until one reaches the diagonal. Then, the same procedure is applied to the other columns of $\tilde{u}$ to make the matrix completely upper triangular. For concreteness, we consider now an encoding of the spinless fermions based on the one shown in Fig. 6.3 to show the number of required two-site unitaries. The spinful case is similar. Taking the aforementioned form of $\tilde{u}$, we note that only odd columns have elements below the diagonal; noting that odd sites correspond to wavelets and scaling functions at level $j+1$, we also note that the furthest overlapping scaling function at level j lies on a lattice site that is around $8K$ sites away. This is because the extent of each basis element at level $j+1$ is $(2K-1)2^{(j+1)}$, and thus on its right, it will have nonzero overlap with around $4K$ scaling function at level j (because their spacing is 2^j); there is another factor of 2, because on the lattice scaling functions of level j are separated by a w site. As a result of all this, the total number of two-site unitaries that are required is around $8K(N/2)$. Considering spinful fermions is similar and brings in another factor of 2 for the total number of unitaries needed.

We will show how this approach can be used in a DMRG calculation with wavelets in the next subsection. On the other hand, for the use of the fine graining procedure in a quantum variational algorithm, one needs to parallelize the two-site unitaries to make the whole circuit shallow. We can show that a circuit with a depth around $8K$ is able to implement the Givens circuit in practice. Such a circuit is shown in Fig. 6.3 and more details about it is presented in appendix E.3.

6.4.1 DMRG with the wavelet basis

In order to illustrate validity and usefulness of the fine graining algorithm presented above, we use it in this section in obtaining DMRG solutions in the continuum in a step by step fashion. The problem of interacting fermions in a periodic potential at half filling is considered and DMRG is performed in two ways: first, we consider the problem with a fine basis from the beginning and seek the solution in a definite number of sweeps with definite bond dimensions. Second, the step by step algorithm

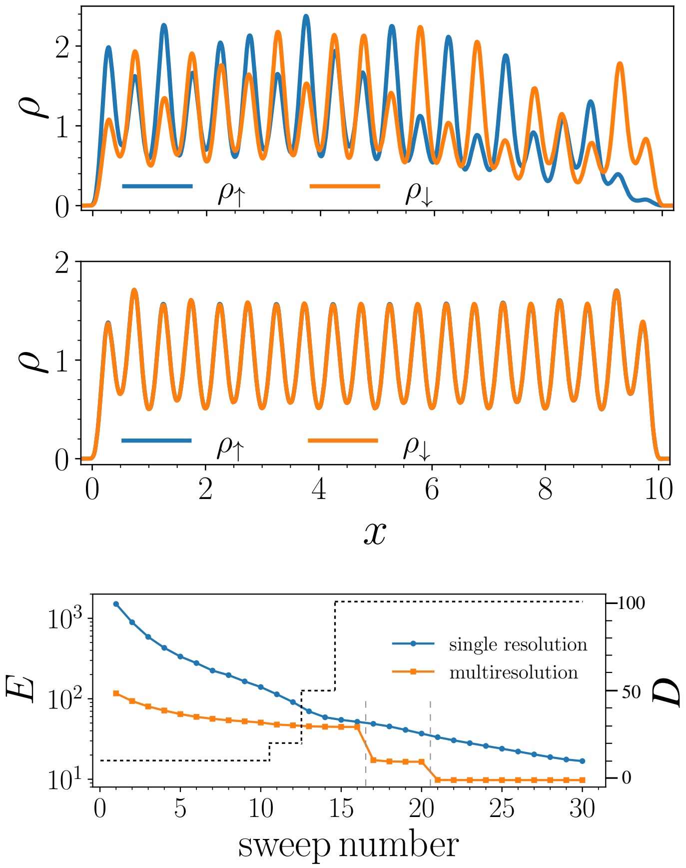

Figure 6.4: DMRG done with the wavelet basis with and without the fine graining procedure. The parameter values used for this particular computation are as follows: $L = 10$, potential period $= 0.5$, $U_0 = 3.$ (δ-function interaction strength), $V_0 = 20$. An external potential with strength equal to 1000 is imposed beyond the spatial limit of our strength i.e. for $x < 0$ or $x > 10$. Top: spin density for the single resolution algorithm with $j_0 = j_{min} = -3$ is plotted, the result is far from convergence. A total number of 176 basis elements (88 scaling and 88 wavelet functions) are used for discretization. Middle: spin density for the multiresolution algorithm that utilizes the fine-graining procedure. Bottom: Energy obtained in DMRG as function of the number of sweeps taken in both single resolution and multiresolution cases. The bond dimension is also plotted as the black dashed line whose vertical axis is shown on the right. Two vertical gray dashed lines are plotted to show the sweep numbers where the basis is made finer (from 44 basis elements to 88 elements and then to 176 elements) in the multi-resolution algorithm.

is employed with the exact same number of sweeps and bond dimensions as the first case but the basis also becomes finer as the sweeps are performed. We show that the latter works significantly better.

Concretely, we consider a Hamiltonian whose $V(x)$ is chosen to have the form

$V_0 \cos(4\pi x)$, note that the potential has a periodicity equal to $\frac{1}{2}$. A total length of 10 is considered and the system is solved with 20 fermions, this corresponds to the half-filling of the potential. The model at half filling is expected to become a Mott insulator; the strong coupling picture corresponds to having exactly one electron per potential minimum with electron spins ordering antiferromagnetically. We have chosen potential and interaction parameters in a way that the strong coupling picture is relevant to some extent. See the caption of Fig. 6.4 for the actual parameter values. Our target ultimate resolution for this problem is $j_{min} = -3$. As discussed above, we solve the problem with two approaches:

- From the beginning all the sweeps are performed with a basis that has the desired ultimate resolution $j_0 = j_{min} = -3$.
- First the problem is solved with a basis having $j_0 = j_{min} = -1$; the solution is used as the seed for DMRG with a basis having $j_0 = j_{min} = -2$; finally, the solution is found at the finest level $j_0 = j_{min} = -3$.

A typical instance of DMRG computation is considered below: starting from random initial states, the exact same number of sweeps and bond dimensions are used in the two cases, the bond dimensions used in DMRG sweeps are shown in the bottom panel of Fig. 6.4 as the black dashed line. In the second case, the basis is made finer before sweep 17 and finest before sweep 21. Spin densities in the two cases are plotted in the top and middle panels of Fig. 6.4; the energy as a function of number of sweeps of is also plotted on the bottom panel of Fig. 6.4. It can be seen that the multiresolution energy has reached convergence to a great extent; its spin density has also converged and shows antiferromagnetic order in the form of a many body singlet. The single resolution solution, on the contrary, is far from any convergence as is clear from the spin density and energies plots. This shows that the fine graining algorithm is effective in efficiently leading the DMRG solution towards the actual energy minimum.

Note that, apart from the above advantage, sweeps with coarser bases take significantly less time than with a fine basis and as a result, although the same numbers of sweeps and bond dimensions were used, the whole process for the second approach is faster. Furthermore, the reason for the choice of a periodic potential is that it contains many local minima in its energy landscape, and as a result, it illustrates the weakness point of DMRG with a dilute system more vividly.

6.5 Discussion

In conclusion, we have introduced a methodology for efficient computational study of many body problems in the continuum; the main benefit comes from the multiresolution property of the wavelet basis which is employed to devise a systematic scheme to fine grain a solution from coarse to fine scales. The fine graining procedure is performed using a general shallow quantum circuit consisting of nearest neighbor two-qubit unitaries; this makes the approach suitable for both classical and quantum variational algorithms. The method is furthermore used concretely in a DMRG calculation and the advantage of utilizing the fine-graining procedure over a single resolution approach is exhibited.

The prescription for performing the fine graining transformation can be modified to implement other general basis transformations as well. As an important instance of this, note that the solutions of the many body problems in our approach will be found in the wavelet basis; as a result, calculation of real space quantities, e.g. entanglement properties across a real space cut, can bring in some difficulty. However, one can use the Givens rotations prescription and design a shallow circuit consisting of two-site unitaries to transform the many body solution from the wavelet basis to a real space lattice basis, in which real space quantities can be accessed directly. General basis transformations can be dealt with in this fashion.

We expect the current work to open new paths to computationally studying many body physics in the continuum. In particular, the use of the methods introduced here along with tensor network algorithms or quantum algorithms to explore a variety of extensions will be interesting; to name a few, one can consider problems in higher dimensions, those regarding time evolution of many body states and the physics of excited states, those in disordered systems, etc. Furthermore, the methods can be adapted to other numerical techniques such as Hartree-Fock, etc.

Appendix A

Appendix for Chapter 2

A.1 The model

The Hamiltonian consists of two terms:

$$H = H_{\mathrm{LL}} + H_{\mathrm{tunneling}}. \tag{A.1}$$

We have made everything dimensionful here to keep track of the new parameters in terms of the magnetic field, however we will ultimately work with the dimensionless Hamiltonian $H/(\hbar v_{\mathrm{F}} k_\theta)$, as in the zero-field Hamiltonian (B.1).

- H_{LL} is the Hamiltonian corresponding to the bare LLs of each of the graphene sheets and can be written in the following form:

$$H_{\mathrm{LL}} = \hat{P}_+ \, h(-\theta/2) + \hat{P}_- \, h(\theta/2). \tag{A.2}$$

where $\hat{P}_{\pm} = \frac{1 \pm \tau^z}{2}$. The single layer Hamiltonian $h(\theta/2)$ is also defined as:

$$h(\theta/2) = \hbar v_{\mathrm{F}} \left[-i\boldsymbol{\nabla} + \frac{e\boldsymbol{A}}{\hbar} + \mathrm{sgn}(\theta)\frac{\boldsymbol{q}_0}{2} + \boldsymbol{q}_h \right] \cdot \left(\mathbf{R}_{\theta/2}\, \boldsymbol{\sigma} \right). \tag{A.3}$$

R is a rotation matrix:

$$\mathbf{R}_{\theta/2} = \begin{pmatrix} \cos\theta/2 & -\sin\theta/2 \\ \sin\theta/2 & \cos\theta/2 \end{pmatrix}.$$

The single layer Hamiltonian can finally be written as:

$$h(\theta/2) = \hbar v_{\mathrm{F}} \left[\sigma^+ e^{i\theta/2} \left(\sqrt{\frac{2eB}{\hbar}} O + i\, \mathrm{sgn}(\theta) \frac{|\boldsymbol{q}_0|}{2} \right) + \mathrm{h.c.} \right], \tag{A.4}$$

the operators O and $O^\dagger$ are defined as follows using the Landau gauge $\boldsymbol{A} = B\left(-y, 0\right)$:

$$\sqrt{\frac{2eB}{\hbar}} O = -\partial_y + k_x + |\boldsymbol{q}_h| - \frac{eBy}{\hbar}, \qquad \sqrt{\frac{2eB}{\hbar}} O^\dagger = \partial_y + k_x + |\boldsymbol{q}_h| - \frac{eBy}{\hbar}. \tag{A.5}$$

They are raising and lowering operators of LL index:

$$\left[O, O^\dagger\right] = 1. \tag{A.6}$$

The wave functions are extended in the x direction and harmonic-oscillator-like (localized) in the y direction.

- $H_{\text{tunneling}}$ can be found by computing the matrix elements of the tunneling terms in the LLs found above.

- The commensurability condition is taken as follows ($\ell_{\rm B} = \sqrt{\frac{\hbar}{eB}}$):

  $$\frac{3}{2}k_\theta \Delta = \frac{3\sqrt{3}}{4}k_\theta^2 \ell_{\rm B}^2 = 2\pi p/q, \tag{A.7}$$

  where Δ, the change in the guiding center induced by the tunneling term is given by:

  $$\Delta = \sqrt{3}\, k_\theta \ell_{\rm B}^2/2.$$

  Note furthermore that since we are working with a different but equivalent form of the tunneling, our commensurability condition is different. In terms of the moiré pattern unit cell area, the above condition can be written as:

  $$\frac{B\mathcal{A}}{\Phi_0} = \frac{1}{2}\frac{q}{p}. \tag{A.8}$$

- We will work with a basis of LL's as follows: $|\tau, n, \sigma, y_c\rangle$, where τ shows the layer, n shows LL index, σ shows sublattice and y_c is the guiding center coordinate. The guiding centers in a tunneling process can only change with the values $\pm\Delta$. Thus one can write y_c as $y_c = y_0 + (mq + j)\,\Delta$, with

  $$0 < y_0 = k_1 \ell_{\rm B}^2 < \Delta, \qquad 0 < j < q-1,$$

  and $j = j + q$. The parameter k_1 defines the x component of the magnetic Bloch momentum. Then we can do a Fourier transform on the parameter

m and work with the new basis:

$$|\tau, n, \sigma, y_0, j, k_2\rangle = \frac{1}{\sqrt{N}} \sum_m e^{ik_2(mq+j)\Delta} |\tau, n, \sigma, y_0 + (mq+j)\Delta\rangle. \tag{A.9}$$

The parameter k_2 defines the y component of the magnetic Bloch momentum.

- The tunneling term can be decomposed into three terms according to the different spatial dependences:

$$H_{\text{tunneling}} = (\mathcal{T}_0 + \mathcal{T}_1 + \mathcal{T}_2) + \text{h.c.}. \tag{A.10}$$

Each term in the above form $\mathcal{T}_n$ is given by

$$\frac{1}{\hbar v k_\theta} \mathcal{T}_n = \tau^+ \alpha \, e^{-i \boldsymbol{Q}_n \cdot \boldsymbol{x}} \, T_n, \tag{A.11}$$

where $\boldsymbol{Q}_0 = 0$, $\boldsymbol{Q}_1 = \sqrt{3}\, k_\theta \left(-\frac{1}{2}, \frac{\sqrt{3}}{2}\right)$ and $\boldsymbol{Q}_2 = \sqrt{3}\, k_\theta \left(\frac{1}{2}, \frac{\sqrt{3}}{2}\right)$ and the 2×2 matrices T_n are given by:

$$T_0 = \eta\, \sigma^0 + \sigma^x, \quad T_1 = \eta\, \sigma^0 + \zeta\, \sigma^+ + \zeta^*\, \sigma^-, \quad T_2 = \eta\, \sigma^0 + \zeta^*\, \sigma^+ + \zeta\, \sigma^-, \tag{A.12}$$

$$\left(\zeta = e^{2\pi i/3}\right),$$

- Now, each of the tunneling terms in the dimensionless form can be written as follows:

$$
\begin{aligned}
\frac{1}{\hbar v_{\mathrm{F}} k_\theta}\langle 1, n', \sigma', y_0', j', k_2'|\, \mathcal{T}_0\, |2, n, \sigma, y_0, j, k_2\rangle &= (\alpha)\ \delta_{y_0,y_0'}\, \delta_{jj'}\, \delta_{k_2,k_2'}\, \delta_{n',n} \\
&\qquad \langle 1, \sigma'|\, T_0\, |2, \sigma\rangle, \\
\frac{1}{\hbar v_{\mathrm{F}} k_\theta}\langle 1, n', \sigma', y_0', j', k_2'|\, \mathcal{T}_1\, |2, n, \sigma, y_0, j, k_2\rangle &= (\alpha)\ \delta_{y_0,y_0'}\, \delta_{(j+1)j'}\, \delta_{k_2,k_2'} \\
\times\ F_{n'n}(\widetilde{\boldsymbol{Q}}_1\, \ell_{\mathrm{B}}/\sqrt{2})\ e^{-\frac{3}{2}ik_\theta y_0}&\, e^{-i\, k_2 \Delta}\ e^{-i\frac{2\pi p}{q}\left(j+\frac{1}{2}\right)} \\
&\qquad \langle 1, \sigma'|\, T_1\, |2, \sigma\rangle\,, \\
\frac{1}{\hbar v_{\mathrm{F}} k_\theta}\langle 1, n', \sigma', y_0', j', k_2'|\, \mathcal{T}_2\, |2, n, \sigma, y_0, j, k_2\rangle &= (\alpha)\ \delta_{y_0,y_0'}\, \delta_{(j-1)j'}\, \delta_{k_2,k_2'} \\
\times\ F_{n'n}(\widetilde{\boldsymbol{Q}}_2\, \ell_{\mathrm{B}}/\sqrt{2})\ e^{-\frac{3}{2}ik_\theta y_0}&\, e^{i\, k_2 \Delta}\ e^{-i\frac{2\pi p}{q}\left(j-\frac{1}{2}\right)} \\
&\qquad \langle 1, \sigma'|\, T_2\, |2, \sigma\rangle\,.
\end{aligned}
\tag{A.13}
$$

Where in the above equations $\widetilde{\boldsymbol{Q}}_j = Q_{j,x} + i\, Q_{j,y}$.

- The function F reads:

$$
F_{n'n}(z) = \begin{cases} (-z^*)^{n'-n}\sqrt{\frac{n!}{n'!}}\, L_n^{n'-n}(zz^*)\, e^{-zz^*/2} & n' \geq n \\ (z)^{n-n'}\sqrt{\frac{n'!}{n!}}\, L_{n'}^{n-n'}(zz^*)\, e^{-zz^*/2} & n' < n \end{cases}. \tag{A.14}
$$

  L_a^b is the generalized Laguerre function.

- The magnetic BZ for the magnetic momentum $\boldsymbol{k} = (k_1, k_2)$ is a region given by:

$$
0 < k_1 k_\theta \ell_{\mathrm{B}}^2 = k_\theta y_0 < \frac{4\pi}{3}\frac{p}{q}, \qquad 0 < k_2 \Delta < \frac{2\pi}{q}. \tag{A.15}
$$

- Using the commensurability condition the dimensionless single layer term can also be written as:

$$
\frac{1}{\hbar v_{\mathrm{F}} k_\theta} h(\theta/2) = \sigma^+ e^{i\theta/2}\left(\sqrt{\frac{3\sqrt{3}}{4\pi}\,\frac{q}{p}}\ O + \frac{i\,\mathrm{sgn}(\theta)}{2}\right) + \mathrm{h.c.} \tag{A.16}
$$

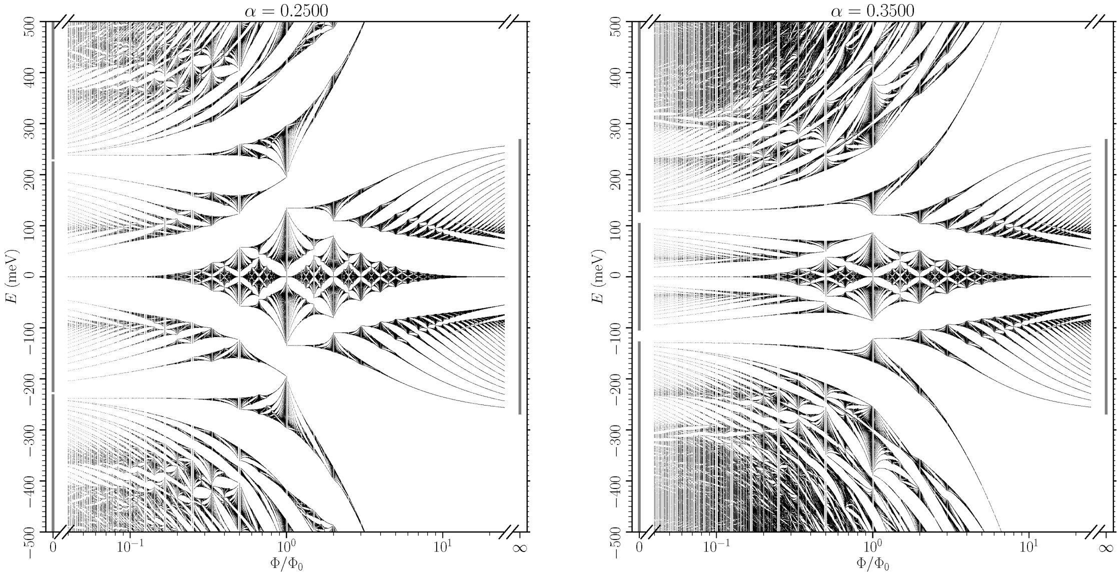

(a)

(b)

Figure A.1: Butterfly plots in the wide range of $\frac{1}{25} \leq \Phi/\Phi_0 \leq 25$ for (a) $\alpha = 0.25$ ($\theta = 2.5°$) and (b) $\alpha = 0.35$ ($\theta = 1.8°$). The horizontal axis uses log scale to reflect the duality between Φ/Φ_0 and Φ_0/Φ. The bands for the nonmagentic case and the infinite magnetic field case (see App. A.6) are also plotted with solid grey lines, on the far left and far right, respectively.

A.2 Small and large magnetic field correspondence in the butterfly plots

The butterfly plots in a large range of magnetic flux ($\frac{1}{25} \leq \Phi/\Phi_0 \leq 25$) for $\alpha = 0.25$ and $\alpha = 0.35$ are shown in Fig. A.1. The plots in the small magnetic regime qualitatively agree with the result of Moon et al. [86] which was obtained at nearby commensurate angles using a tight binding model. By comparing the low energy levels at a flux $\Phi/\Phi_0 = q/2p < 1$ and its reciprocal $\Phi/\Phi_0 = 2p/q > 1$ in Fig. A.1,

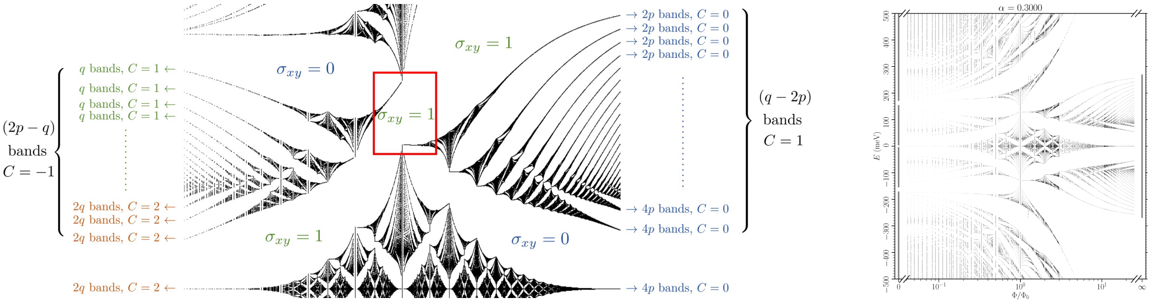

(a)

(b)

Figure A.2: (a) Magnetic bands and their Chern numbers of the butterfly plot at $\alpha = 0.25$. The integer Hall conductivity σ_{xy} in unit of e^2/h for the major gaps is given; the $\sigma_{xy} = 1$ gap persists adiabatically from small to large fields. Although not shown, the band Chern numbers of the butterfly plot at $\alpha = 0.35$ has the same pattern as labeled here, except for the persisting gap through $\Phi/\Phi_0 = 1$ (the gap inside the red box): for $\alpha = 0.35$ the $\sigma_{xy} = 1$ gap is closed while the $\sigma_{xy} = 0$ gap is adiabatically continued (as shown in Fig. A.1b). (b) Butterfly plot in a wide range of $1/25 \leq \Phi/\Phi_0 \leq 25$ for $\alpha = 0.30$. Notice that both the major $\sigma_{xy} = 0$ and $\sigma_{xy} = 1$ gaps are closed at $\Phi/\Phi_0 = 1$, one can declare that a transition from the former behavior ($\alpha = 0.25$) to the latter ($\alpha = 0.35$) happens at this value of α.

one notices a resemblance: the butterfly structure at flux $q/2p$ and its reciprocal flux value $2p/q$ look similar. One can establish the details of this correspondence by taking a close look at the low energy magnetic bands, shown in Fig. A.2: the low energy butterfly exhibits a left wing ($\Phi/\Phi_0 < 1$) and a right wing ($\Phi/\Phi_0 > 1$). Near the left (right) edge of the left (right) wing, the magnetic bands collapse to well-defined levels. Analyzing the weight of these levels was our major task, discussed in the main text. At the upper edge, the levels of the left (right) wing each contain q ($2p$) bands, while the levels at the lower edge (note that in the main text these levels are referred to as the LLs in the middle of the active range) of the left (right) wing each contain $2q$ ($4p$) bands.

In the main text we have commented on the two different behaviors for the adiabaticity of the band weights: either the weight of the zeroth LLs of the two moiré

DPs (consisting of $2q$ magnetic bands) or the weight of the two nonmagnetic bands (consisting of $4p$ magnetic bands) is adiabataically continued as flux is varied through $\Phi/\Phi_0 = 1$. The former behavior is found at $\alpha = 0.25$ (see Fig. A.2): the gap between the active $2q$ magnetic bands (zeroth LLs of the two moiré DPs) and higher bands persists at all flux values, while the gap between $4p$ magnetic bands in the active range and the the remote bands closes at $\Phi/\Phi_0 = 1$; the latter behavior is found at $\alpha = 0.35$, where the persisting gap and the closing gap are switched. Note that there is a gap at CNP (although the two bands above and below it can also touch at this point), which corresponds to having a vanishing Hall conductivity, $\sigma_{xy} = 0$; the Hall conductivity (in the units of e^2/h) for other gaps can then be obtained by suming over all the Chern numbers for the bands below this gap but above CNP.

In this way, we find that the gap above CNP persisting from small to large fields has a unit Hall conductivity, $\sigma_{xy} = 1$ for $\alpha = 0.25$, and $\sigma_{xy} = 0$ for $\alpha = 0.35$ (see Fig. A.2a). Furthermore, we found that a transition between these two behaviors happens at $\alpha \approx 0.30$, where both gaps are closed at $\Phi/\Phi_0 = 1$, see Fig. A.2b. The difference in the adiabaticity behavior found above may have observable effects in quantum Hall experiments.

Fig. A.2a shows the Chern numbers of the LLs lying between the two major gaps (the gap with $\sigma_{xy} = 0$ and the gap with $\sigma_{xy} = 1$). Notice that at small magnetic field limit, the total Chern number of magnetic bands within the active range vanishes, while for large magnetic field limit the total Chern number for the $2q$ bands is 2. The results are in accordance with a computation based on Streda's formula.

A.3 Wannier plot

In this section we give a prescription for extracting the weight information in the butterfly plot. The final result is the wannier plots shown in Fig. 2.2 in the main text.

The wannier plot is a density plot, which shows the density of states $\rho(n, B)$ as a function of carrier density n and magnetic field B. In principle it can be obtained by transcribing the energy spectrum (butterfly) plot according to the following method:

- The density of states are obtained by broadening the δ functions using a Lorentz distribution:

$$\rho(E) = \sum_i \delta(E - E_i) \to \sum_i \frac{1}{\pi} \frac{\gamma}{(E - E_i)^2 + \gamma^2}, \tag{A.17}$$

  where the parameter γ is an empirical parameter. This parameter is adjusted for each value of α to achieve optimal resolution for the Landau levels.

- The carrier density at energy E is obtained by integrating density of states from above:

$$n(E) = \sum_i \theta(E - E_i) \to \sum_i \frac{1}{\pi} \arctan\left(\frac{E - E_i}{\gamma}\right), \tag{A.18}$$

Due to the fact that the number of magnetic bands scales with p, where p and q are coprime numbers satisfying $\Phi/\Phi_0 = q/2p$ (and also noting the prescription for finding densities given in the main text), a normalization factor $\frac{1}{2p}$ has to be given to the expressions Eq. (A.17) and (A.18) when the density of a numerically found magnetic band is calculated. This guarantees that the active range corresponds to $n \in [-1, 1]$ in a Wannier plot.

As mentioned in Fig. 2.2, the colors therein in fact correspond to a rescaled density of states ρ/ρ_{max}, where ρ_{max} is a large value of density of states which sets the rightmost scale of the colorbar. The value of ρ_{max} is different for the three subplots; furthermore it may not be the actual largest density of states computed from the butterfly plot. ρ_{max} is chosen simply to obtain the best resolution of the LLs for the figures.

A.4 Semiclassical energies

In this section of the supplemental information, we compare the energies found using the semiclassical analysis and the energy levels in the butterfly plots at small (relevant to experiments) fields. The semiclassical energies are shown as red dashed lines on top of butterfly plots in Fig. A.3. Each semiclassical line is found by imposing the relevant quantization condition on the enclosed area in different areas of the BZ; the lines are continued until the energy reaches the saddle contour energy (see main text).

The agreement between the two sets of energies is best at $\alpha = 0.35$, however, within the magic range the agreement is less pronounced; at $\alpha = 0.5754$, the agreement of the edge levels is better while in the middle of the active range the LLs in

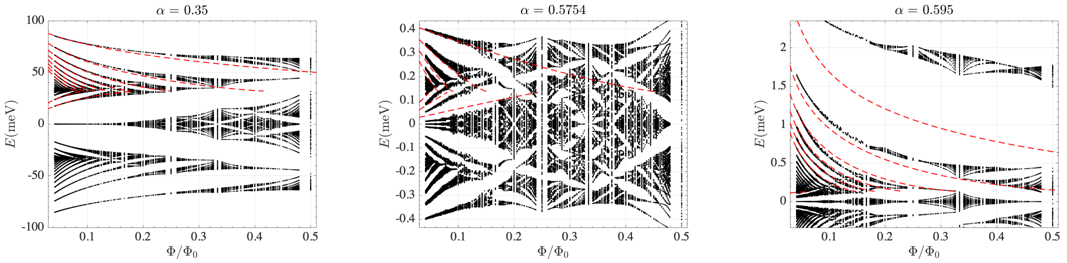

(a) (b) (c)

Figure A.3: A comparison between LLs found using semiclassical analysis and those in butterfly plots. The semiclassical energies are shown by red dashed lines on top of the butterfly plots.

the butterfly plot have a smaller energy than those found by semiclassical analysis. This discrepancy can be understood by noting that at this value of α the two active bands approach each other at the Γ point which can lead to interband mixing, and that we are neglecting this here. Still good qualitative agreement can be seen. At $\alpha = 0.595$ finally, the edge LLs found by the two methods show better agreement as one gets further from the edge; and in the middle of the active range, the only 3-fold degenerate LL found in the butterfly plot is acceptably close to the 3-fold LL found by semiclassical analysis.

A.5 Broken particle-hole symmetry

As is discussed in the main text, with the inclusion of sublattice rotation matrices $\mathbf{S}_\theta$ the particle-hole symmetry in the magnetic spectrum is broken. This does not have a major effect on the filling factor sequences discussed in the main text when the twist angle is outside the magic range. However, close to $\alpha = \alpha_1$ (where the two active bands have a quadratic band touching), the situation can be different; at α_1

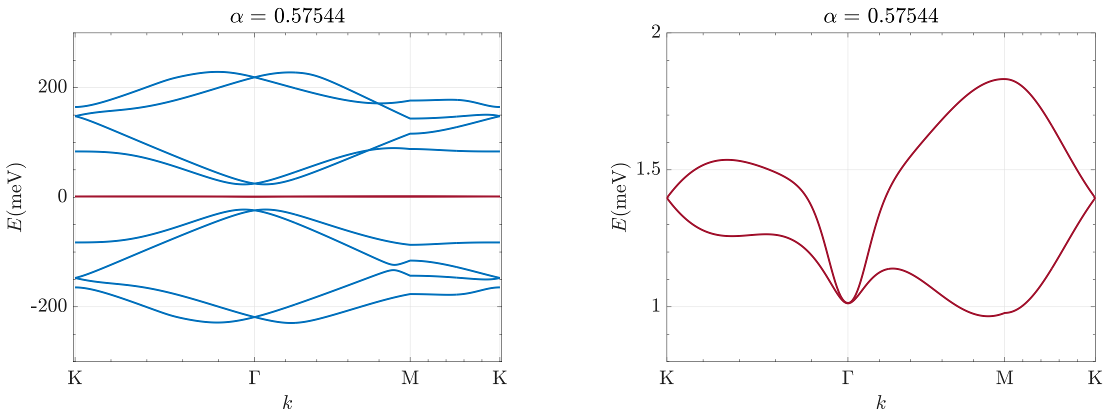

(a) (b)

Figure A.4: Nonmagnetic bands close to CNP, for $\eta = 0.82$ and $\alpha = \alpha_1$. The ten closest bands and the two active bands are shown in (a) and (b) respectively. At this value of α the active bands show a considerable asymmetry.

the nonmagnetic active bands touch each other below the energy of DPs as shown in Fig. A.4. As a result of this, the orbits formed in the top band around the Γ point can have lower energy than the zero energy LLs of moiré DPs, when α is close to α_1. As can be seen in Fig. A.5, for small magnetic field level crossings in the middle of the active range can occur which can potentially result in an abrupt change of the filling factor sequence.

A.6 Mapping the model in the infinite magnetic field limit to a zero field model

Although the magnetic model introduced in App. A.1 looks rather complicated, it can be simplified in the inifinte magnetic field limit $B \to \infty$. This is due to the decoupling of the bare LLs, which can be observed in the butterfly diagram: at infinite magnetic

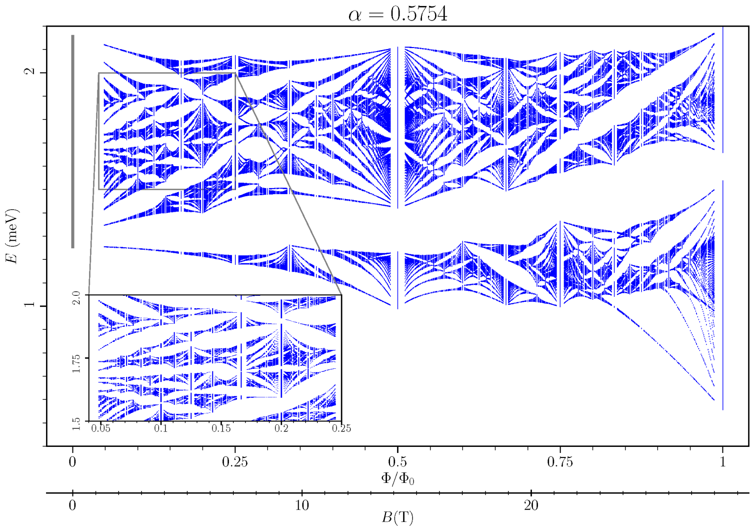

Figure A.5: Butterfly plot for the $(\eta, \mathbf{R}) = (0.82, \mathbf{S}_\theta)$ model (i.e. both lattice corrugation and sublattice pseudospin considered) at $\alpha = 0.5754$. The inset shows magnified version of the magnetic energy levels at small fields.

field limit $\Phi/\Phi_0 = q/2p \to \infty$, the low energy part of the butterfly spectrum consists of $2q$ magnetic bands, which are precisely the two zeroth LLs of the Dirac points of the two graphene sheets, i.e. the zero energy solution of the part H_{LL} which are widened due to moiré lattice. They are infinitely apart in energy from the other LLs. Furthermore, as magnetic field approaches infinity, the band width of each of the $2q$ magnetic bands tends to vanish, and eventually these $2q$ bands merge into one continuous band.

As discussed in App. A.2, the butterfly plot (see Fig. A.1) shows a kind of duality between small and large fluxes: $2q$ magnetic bands appear at charge neutrality point for small fields and eventually evolve (with the possibility for a gap closing) into the zeroth LLs at large fields; on the other hand, the $4p$ bands corresponding to the total weight of the two active bands at small fields also evolve (again with the possibility for a gap closing) and gradually converge to charge neutrality point at large fields. This spectral duality is reminiscent of the duality of the Harper's equation in the weak potential limit and the strong potential limit [118], where the flux quantization condition of one case is the inverse of the other.

These facts motivate us to look for a simple description of the $2q$ bands at large magnetic fields. Such a $2q$ by $2q$ Hamiltonian $\mathcal{H}_{2q\times 2q}$ can be easily obtained by projecting the Hamiltonian introduced in App. A.1 onto the $2q$-fold basis of the zeroth LLs. Crucially, $\mathcal{H}_{2q\times 2q}$ can be interpreted differently as a fictitious Hofstadter Hamiltonian obtained from a *tight binding model* on a honeycomb lattice subject to a commensurate *dual* magnetic field $\widetilde{B}$. Here the tight binding model and the dual magnetic field $\widetilde{B}$ are fictitious; the sublattice index $s = \widetilde{1}, \widetilde{2}$ of the fictitious honeycomb lattice in fact is dual to the zeroth LLs of layers 1 and 2, and the fictitious magnetic field $\widetilde{B}$ requires that the dual flux per honeycomb unit cell $\widetilde{\Phi}$ in this dual magnetic problem is the inverse of the physical flux per unit cell $\widetilde{\Phi}/\Phi_0 = \Phi_0/\Phi = 2p/q$. From now on we will refer to this fictitious theory as the dual theory for simplicity.

To be more precise, we introduce the fictitious honeycomb lattice in the dual theory by specifying the vectors $\boldsymbol{a}_{0,1,2}$ from a $\widetilde{1}$ sublattice site to its three nearest neighbor (NN) $\widetilde{2}$ sites:

$$\boldsymbol{a}_0 = (\widetilde{a}, 0), \qquad \boldsymbol{a}_1 = (-\widetilde{a}/2, \widetilde{b}), \quad \text{and} \quad \boldsymbol{a}_2 = (-\widetilde{a}/2, -\widetilde{b}), \tag{A.19}$$

where we defined

$$\widetilde{a} = k_\theta \ell_{\mathrm{B}}^2 \quad \text{and} \quad \widetilde{b} = \Delta. \tag{A.20}$$

Depending on the ratio between $\widetilde{a}$ and $\widetilde{b}$ the honeycomb may appear elongated or compressed but this will not affect the physics we study. The tight binding Hamiltonian we propose in the dual theory is the NN hopping Hamiltonian on the honeycomb lattice:

$$H = -t\sum_i \sum_{j=0,1,2} c^\dagger_{\boldsymbol{r}_i,\widetilde{1}} c_{\boldsymbol{r}_i+\boldsymbol{a}_j,\widetilde{2}} + \text{H.c.}, \tag{A.21}$$

where i runs over all $\widetilde{1}$ sublattice sites, and the hopping amplitude $t = \alpha\eta\hbar v_{\text{F}} k_\theta$. Let us define lattice translation vectors $\boldsymbol{t}_1 = (3\widetilde{a}/2, -\widetilde{b})$ and $\boldsymbol{t}_2 = (3\widetilde{a}/2, \widetilde{b})$ for the $\widetilde{1}$ sublattice.

Then, we apply the fictitious magnetic field $\widetilde{B}$ by using the Landau gauge $\widetilde{\boldsymbol{A}} = (-y\widetilde{B}, 0)$ (y is continuous here). The magnetic Hamiltonian $\widetilde{H}'$ can be obtained via a Peierl's substitution:

$$\widetilde{H}' = -t\sum_i e^{\frac{2\pi i}{\Phi_0}\widetilde{B}\widetilde{a}\widetilde{b}y_i} c^\dagger_{\boldsymbol{r}_i,\widetilde{1}} c_{\boldsymbol{r}_i+\boldsymbol{a}_0,\widetilde{2}} + e^{-\frac{2\pi i}{\Phi_0}\frac{\widetilde{B}\widetilde{a}\widetilde{b}}{2}(y_i+1/2)} c^\dagger_{\boldsymbol{r}_i,\widetilde{1}} c_{\boldsymbol{r}_i+\boldsymbol{a}_1,\widetilde{2}} + e^{-\frac{2\pi i}{\Phi_0}\frac{\widetilde{B}\widetilde{a}\widetilde{b}}{2}(y_i-1/2)} c^\dagger_{\boldsymbol{r}_i,\widetilde{1}} c_{\boldsymbol{r}_i+\boldsymbol{a}_2,\widetilde{2}} + \text{H.c.}, \tag{A.22}$$

note that y_i is an integer. Next, we perform a gauge transformation

$$c_{\boldsymbol{r}_i,\widetilde{1}} \to e^{\frac{\pi i}{\Phi_0}\widetilde{B}\widetilde{a}\widetilde{b}y_i} c_{\boldsymbol{r}_i,\widetilde{1}}, \qquad c_{\boldsymbol{r}_i+\boldsymbol{a}_0,\widetilde{2}} \to e^{-\frac{\pi i}{\Phi_0}\widetilde{B}\widetilde{a}\widetilde{b}y_i} c_{\boldsymbol{r}_i+\boldsymbol{a}_0,\widetilde{2}}, \tag{A.23}$$

under which the Hamiltonian transforms as $\widetilde{H}' \to \widetilde{H}$, where

$$\widetilde{H} = -t\sum_i c^\dagger_{\boldsymbol{r}_i,\widetilde{1}} c_{\boldsymbol{r}_i+\boldsymbol{a}_0,\widetilde{2}} + e^{-\frac{2\pi i}{\Phi_0}\frac{\widetilde{\Phi}}{2}(y_i+1/2)} c^\dagger_{\boldsymbol{r}_i,\widetilde{1}} c_{\boldsymbol{r}_i+\boldsymbol{a}_1,\widetilde{2}} + e^{-\frac{2\pi i}{\Phi_0}\frac{\widetilde{\Phi}}{2}(y_i-1/2)} c^\dagger_{\boldsymbol{r}_i,\widetilde{1}} c_{\boldsymbol{r}_i+\boldsymbol{a}_2,\widetilde{2}} + \text{H.c.}. \tag{A.24}$$

Note that we have defined flux per unit cell $\widetilde{\Phi} = \widetilde{B}\widetilde{\mathcal{A}}$, where $\widetilde{\mathcal{A}} = 3\widetilde{a}\widetilde{b}$ is the hexagonal unit cell area of the dual honeycomb lattice. Having the purpose of getting a dual theory to the initial model, we impose the following commensurate flux condition

$$\frac{\widetilde{\Phi}}{\Phi_0} = \frac{2p}{q}, \tag{A.25}$$

under this condition the Hamiltonian $\widetilde{H}$ has new translation symmetry along vectors $\widetilde{\boldsymbol{t}}_1 = (3\widetilde{a}/2, -q\widetilde{b})$, $\widetilde{\boldsymbol{t}}_2 = (3\widetilde{a}/2, q\widetilde{b})$ for odd q, or $\widetilde{\boldsymbol{t}}_1 = (3\widetilde{a}, 0)$, $\widetilde{\boldsymbol{t}}_2 = (0, q\widetilde{b})$ for even q. Next we turn to using the Fourier transformed operators $c_{\widetilde{\boldsymbol{k}},l_i,s}$ instead of $c_{\boldsymbol{r}_i,s}$, where $l_i \equiv y_i \bmod q$. $\widetilde{\boldsymbol{k}}$ belongs to the dual magnetic BZ (which is valid for q being both odd and even)

$$\widetilde{\boldsymbol{k}} = (\widetilde{k}_1, \widetilde{k}_2) \in \left[0, \frac{2\pi}{3\widetilde{a}}\right] \times \left[0, \frac{2\pi}{q\widetilde{b}}\right] = \left[0, \frac{2\pi}{3k_\theta \ell_{\mathrm{B}}^2}\right] \times \left[0, \frac{2\pi}{q\Delta}\right], \tag{A.26}$$

And the Hamiltonian becomes

$$\widetilde{H}(\widetilde{\boldsymbol{k}}) = -t \sum_{l=0}^{q-1} c^\dagger_{l,\widetilde{1}} c_{l,\widetilde{2}} + e^{-i\widetilde{\boldsymbol{k}}\cdot\boldsymbol{t}_1} e^{-2\pi i \frac{\widetilde{\Phi}}{\Phi_0}(l+\frac{1}{2})} c^\dagger_{l,\widetilde{1}} c_{l+1,\widetilde{2}} + e^{-i\widetilde{\boldsymbol{k}}\cdot\boldsymbol{t}_2} e^{-2\pi i \frac{\widetilde{\Phi}}{\Phi_0}(l-\frac{1}{2})} c^\dagger_{l,\widetilde{1}} c_{l-1,\widetilde{2}} + \mathrm{H.c.}, \tag{A.27}$$

this Hamiltonian, written in basis of $c_{l,\widetilde{1}/\widetilde{2}}$, will give a $2q$ by $2q$ hermitian matrix $\widetilde{\mathcal{H}}_{2q\times 2q}$. Comparing this with the matrix elements given in Eq. (A.13), we establish the following relations between the corresponding quantities in the original theory and the dual theory:

- $\widetilde{\mathcal{H}}_{2q\times 2q}$ is equal to $\mathcal{H}_{2q\times 2q}$, if one relates $\widetilde{k}$ to the magnetic momentum of the original magnetic theory by

$$\widetilde{k}_x = k_x \quad \text{and} \quad \widetilde{k}_y = -k_y; \tag{A.28}$$

- The dual magnetic flux is related to the original magnetic flux by

$$\frac{\widetilde{\Phi}}{\Phi_0} = \frac{\Phi_0}{\Phi} = \frac{2p}{q}; \tag{A.29}$$

- From Eq. (A.29), the magnetic fields of the original theory and the dual theory are actually equal:

$$B = \widetilde{B}. \tag{A.30}$$

  This implies that in the large magnetic field limit $B \propto q/p \to \infty$, the dual magnetic field $\widetilde{B}$ is also large. However the dual magnetic flux per unit cell, $\widetilde{\Phi}$, approaches zero in this limit, despite $\widetilde{B}$ being large. This is due to the fact that, by definition, the dual unit cell area $\widetilde{A} \propto (p/q)^2$, while $\widetilde{B} \propto q/p$.

Therefore, we have established a duality map between the model of App. A.1 in the large magnetic flux limit and a dual model describing "monolayer graphene" in small (fictitious) magnetic flux limit. A couple of observations immediately follow from this duality:

- The bandwidth of the two zeroth LLs at infinite magnetic field is equal to that of the tight binding model: $-3 \leq \frac{1}{t}E \leq 3$, in agreement with numerical results (see Fig. A.2).

- At large flux $\Phi/\Phi_0 \gg 1$, the butterfly plot of the $2q$ magnetic bands of the two zeroth LLs as a function of the inversed flux Φ_0/Φ should be similar to the Hofstadter butterfly plot of the honeycomb lattice [104], see Fig. A.6.

- Since the butterfly at extreme fields admits two physical pictures (in the original theory and dual theory), it is interesting to compute the band Chern numbers in both theories, and try to understand their relations. Regarding this the first claim is that the for the same band in the spectrum, band Chern number may not be equal in the two theories. As shown above, the Chern numbers of the group of bands near the lower or upper edges of the original model in the large magnetic field always vanish, while the fictitious Chern numbers of the bands calculated in the fictitious tight binding model near the upper and lower edges have the values 1 and 2 respectively [48, 1]. The correspondence between the Chern numbers in the two theories will be established in App. A.7.

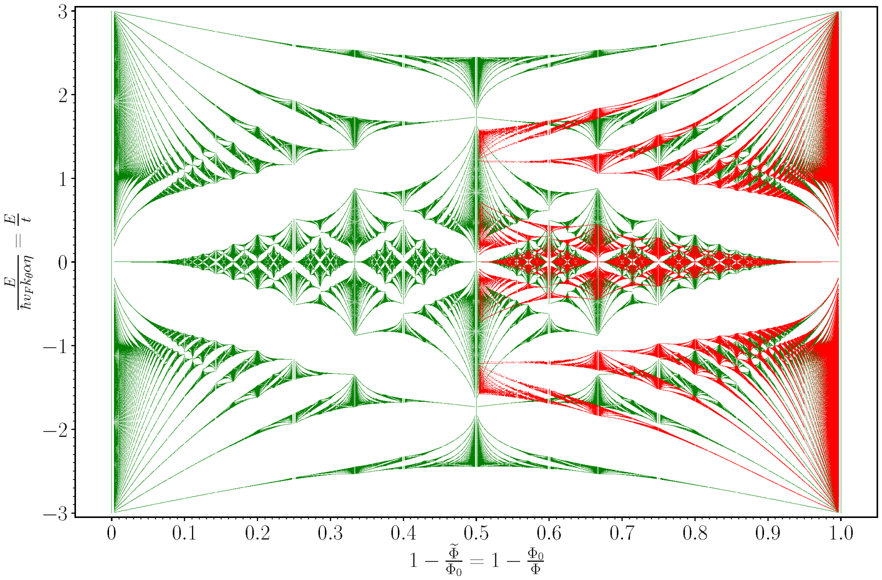

Figure A.6: Comparison of the butterfly plots obtained from the original theory and the dual theory. Red: the butterfly spectrum of the model in App. A.1 for $\alpha = 0.3$ in the flux range $\frac{1}{2} \leq 1 - \Phi_0/\Phi \leq 1$; Green: the butterfly spectrum of the dual model (see Eq. (A.27)) – honeycomb Hofstadter butterfly. Note that the green butterfly does not change if one uses $\widetilde{\Phi}/\Phi_0$ as the horizontal axis due to its mirror symmetry about $\widetilde{\Phi}/\Phi_0 = 1/2$. In the limit $\widetilde{\Phi}/\Phi_0 = \Phi_0/\Phi \to 0$ (i.e. the rightmost part of the plot), the spectra of the two models become identical.

A.7 Chern number

Quite often the quantized Hall conductivity (in units of e^2/h) in an energy gap can be determined algebraically by writing down the Diophantine's equation describing the gap and then applying Streda's formula. The Chern number for a group of bands can then be obtained by computing the quantized Hall conductivity at the energy gap above and below this group of bands, and then take the difference. An equally good method to determine Chern number for a group of bands is to make direct use of the band topology by computing the berry curvature numerically. In this method, care must be taken to make sure the numerically computed berry curvature is gauge invariant as required by definition. Such a method has been developed in Ref. [42], which applies to any Bloch Hamiltonian $H(\boldsymbol{k})$ which is periodic along the two directions of the (2D) Brillouin zone. The two methods have been shown to give identical results in several cases [3, 48].

The situation, however, is subtle for the magnetic model (see App. A.1) we are using here: the hermitian matrix corresponding to the Hamiltonian in the Landau level basis, $H(\boldsymbol{k})$, does not have the "expected" periodicity, that is being periodic with respect to the reciprocal vectors of the magnetic translation lattice (see Eq. A.15). The issue has to do with the fact that the Landau level basis we are using satisfies a *generalized* Bloch theorem[118] rather than the original Bloch theorem. Consequently, the numerical method for computing the Chern numbers mentioned above has to be modified.

To give the modified numerical method, let us first establish the correspondence between the magnetic model in App. A.1 and the standard problem of Bloch electrons moving in perpendicular magnetic field[118]. We first establish the correspondence between the Landau basis. Define $k_1 = y_0/\ell_{\mathrm{B}}^2$, the Landau level basis used in App. A.1 can be written in real space

$$\begin{aligned}\langle \boldsymbol{x}|\tau, n, \sigma, y_0, j, k_2\rangle &= \Gamma_{\tau,n,\sigma,j,\boldsymbol{k}}(\boldsymbol{x}) \\ &= \sum_{m=-\infty}^{\infty} e^{-ik_2(x-(m+\frac{j}{q})pa)} e^{i\frac{2\pi}{a}(mq+j)y} \phi_n\left(y - \left(\left[m + \frac{j}{q}\right] pb - \frac{p}{q}\frac{ab}{2\pi}k_1\right)\right),\end{aligned} \tag{A.31}$$

where we defined lengths along $\hat{x}$ and $\hat{y}$ direction, respectively,

$$a = \frac{4\pi}{\sqrt{3}k_\theta}, \qquad b = \frac{4\pi}{3k_\theta}.$$

This is essentially the same basis used in Ref. [118], with a change of definition $(p, q) \to (q, p)$ and axis $(\hat{x}, \hat{y}) \to (\hat{y}, \hat{x})$. The translation vector along $\hat{x}$ and $\hat{y}$ is then $a\hat{x}$ and $pb\hat{y}$; this essentially defines a rectangular magnetic BZ of size $2\mathcal{A}$:

$$(k_x, k_y) \in \left[0, \frac{2\pi}{a}\right] \times \left[0, \frac{2\pi}{pb}\right].$$

The Bloch function $|u(\boldsymbol{k})\rangle$ is then written as

$$|u_{\tau,\sigma}(\boldsymbol{k})\rangle = \sum_{j=0}^{q-1}\sum_{n=0}^{\infty} d_{\tau,\sigma,n,j}|\tau, n, \sigma, y_0, j, k_2\rangle.$$

The Bloch Hamiltonian $H(\boldsymbol{k})$ constructed in App. A.1 gives a Hermitian matrix in the basis $|\tau, n, \sigma, y_0, j, k_2\rangle$. One then diagonalizes this Hermitian matrix numerically to obtain the eigenvectors $\mathbf{d}(\boldsymbol{k})$, with entries $d_{\tau,\sigma,n,j}(\boldsymbol{k})$.

We now derive the modified numerical method to computing the correct band Chern number. Remember that in the original method of Ref. [42], the band Chern number is obtained by summing over berry curvature of this band (or multiple bands) in the BZ; the berry curvature $\mathcal{B}(\boldsymbol{k})$ is computed numerically from the eigenvectors $\mathbf{d}(\boldsymbol{k})$ using a discretized and gauge invariant version of the definition:

$$\mathcal{B}_{\text{numerical}}(\boldsymbol{k}) = i\epsilon_{ij} \left(\partial_{k_i}\mathbf{d}(\boldsymbol{k})\right)^\dagger \partial_{k_j}\mathbf{d}(\boldsymbol{k}), \tag{A.32}$$

where ϵ_{ij} is the 2D antisymmetric tensor and i and j are implicitly summed.

To remedy this, one must remember that here we are using Landau levels as the basis; thus the basis states are also functions of momentum, and may as well contribute to berry curvature. The complete Berry curvature is then computed as follows:

$$\begin{aligned}\mathcal{B}(\boldsymbol{k}) &= i\epsilon_{ij}\left(\partial_{k_i}\langle u(\boldsymbol{k})|\right)\partial_{k_j}|u_{\boldsymbol{k}}\rangle \\ &= i\epsilon_{ij}\left(\partial_{k_i}\mathbf{d}(\boldsymbol{k})\right)^\dagger \partial_{k_j}\mathbf{d}(\boldsymbol{k}) \\ &\quad + i\epsilon_{ij} \sum_{\tau,\tau',\sigma,\sigma',j,j',n,n'} d^*_{\tau,\sigma,n,j}(\boldsymbol{k}) d_{\tau',\sigma',n',j'}(\boldsymbol{k}) \left(\partial_{k_i}\langle \tau, n, \sigma, y_0, j, k_2|\right)\partial_{k_j}|\tau', n', \sigma', y_0', j', k_2'\rangle,\end{aligned} \tag{A.33}$$

note that the Berry curvature receives contribution from two parts, the first from the eigenvector $\mathbf{d}$ and the second from the LL basis Γ.

Now we integrate both sides over the BZ to obtain the Chern number C. Note that the integral of the second term can be calculated analytically, which gives a $-1/q$

contribution. Therefore we have

$$C = C_{\text{numerical}} - 1/q, \tag{A.34}$$

i.e. each LL contributes a fraction $1/q$ to the total Chern number. Note the second term in Eq. (A.33) does not contribute to Chern number if the Bloch Hamiltonian matrix is written under a plane wave or Wannier basis.

As an application of the formula, let us study the correspondence between the Chern numbers obtained in the original magnetic theory (App. A.1) at large flux and that obtained in the dual theory at small flux (see App. A.6). The Chern number of the dual theory (the honeycomb Hofstadter butterfly problem, i.e. Eq. (A.21)) has been obtained previously[48, 1]: each band at the edge contributes Chern number $C = 1$ and each band at the charge neutrality contributes $C = 2$. In fact the relation between the Chern number sequence $2, 2, ..., 1, 1$ of the honeycomb Hofstadter butterfly model and the vanishing of Chern number of our model in App. A.1 at large field can be understood using Eq. (A.33). Take the group of $4p$ bands at charge neutrality of our model at large field as an example: since $C = 0$, $C_{\text{numerical}} = 4p/q$. The dual theory has a dual magnetic BZ with an area that is equal to $q/2p$ times the MBZ area of the model in App. A.1. Since the Chern number for the dual magnetic model, C_{dual}, is evaluated on the dual magnetic BZ, and noting that the MBZ of the model in App. A.1 is p-fold degenerate (consisting of p identical segments along k_x direction when computing Berry curvature), we have

$$C_{\text{dual}} = \frac{q}{2p} \cdot C_{\text{numerical}} = 2, \tag{A.35}$$

this is exactly the Chern number for the zeorth Landau level of the magnetic honeycomb [48, 1]. Note the second term in Eq. (A.33) does not contribute to the Chern number of the dual theory, since the Hamiltonian is written in plane wave basis.

Using this line of argument, all Chern numbers in the original and the dual theory can be understood.

Appendix B

Appendix for Chapter 3

B.1 The model

In this Appendix, we briefly review the continuum model of Bistritzer and MacDonald, which is the starting point of this work. We take the Hamiltonian for the two valleys ($\xi = \pm 1$) as

$$\begin{aligned} H(\boldsymbol{x}) = -i \left(\boldsymbol{\nabla} + i\xi \left[-\tau^z \frac{\boldsymbol{q}_0}{2} + \boldsymbol{q}_\mathrm{h} \right] \right) \cdot (\xi\sigma^x, \sigma^y) \\ + \alpha\, \tau^+ \left[\eta\, \beta_0(\boldsymbol{x}) + \beta_1(\boldsymbol{x})\sigma^+ + \beta_2(\boldsymbol{x})\sigma^- \right] + \text{h.c.}. \end{aligned} \tag{B.1}$$

The Hamiltonian and the position are made dimensionless by dividing by $\hbar v_F k_\theta$ and $\frac{1}{k_\theta} = \frac{3a_M}{4\pi}$, where $a_M = \frac{\sqrt{3}a}{\theta}$ is the moiré unit length (a is the distance between adjacent carbon atoms in graphene). The Pauli matrices τ^z, σ^z denote the layer and sublattice degrees of freedom. There are two parameters in the above Hamiltonian: $\alpha = \frac{w_\mathrm{AB}}{\hbar v_F k_\theta} \sim \frac{w_\mathrm{AB}}{v_F \theta}$ and $\eta = \frac{w_\mathrm{AA}}{w_\mathrm{AB}}$. The moiré periodic funcitons $\beta_n(\boldsymbol{x}) = \sum_{j=0}^{2} e^{-i(\xi \boldsymbol{Q}_j)\cdot \boldsymbol{x}} \zeta^{\xi n j}$, are defined in terms of moiré reciprocal lattice vectors $\boldsymbol{Q}_0 = 0, \quad \boldsymbol{Q}_1 = \sqrt{3}\left(-\frac{1}{2}, \frac{\sqrt{3}}{2}\right), \boldsymbol{Q}_2 =$

$\sqrt{3}\left(\frac{1}{2},\frac{\sqrt{3}}{2}\right)$, and also with $\zeta = e^{2\pi i/3}$. Also, $\boldsymbol{q}_{\mathrm{h}} = \left(\frac{\sqrt{3}}{2},0\right)$, and $\boldsymbol{q}_0 = (0,-1)$. Notice that we have neglected the opposite rotation of sublattice matrices in the two layers in the Hamiltonian (B.1), which is a small effect (order θ) for small twist angles; this results in an approximate particle/hole symmetry which is detailed below along with some other symmetries of the CM.

The presence of a $C_2\mathcal{T}$ breaking sublattice potential is also considered in this work which is taken to be of the form $\Delta\,\sigma^z$.

Some symmetries of the CM:

- The neglect of the rotation of the sublattice matrices results in a particle-hole symmetry as defined in Ref. [52] (see also Ref. [114]), note that it is an intravalley transformation:

  $$U_{\mathrm{ph}}^{\dagger} H_{(-k_x,k_y)}\Big((-x,y)\Big)U_{\mathrm{ph}} = -H_{\boldsymbol{k}}(\boldsymbol{x}), \tag{B.2}$$

  where $U_{\mathrm{ph}} = \sigma^x\tau^z e^{2i(\xi\boldsymbol{q}_{\mathrm{h}})\cdot\boldsymbol{x}}$. This symmetry is preserved even if a sublattice symmetry breaking term is also present. One should have in mind that this particle-hole symmetry is different from the chiral symmetry of the Chiral model, since the latter keeps the Bloch momentum intact and the present particle-hole symmetry takes $(k_x,k_y)\to(-k_x,k_y)$ and also is present regardless of the value of η within the above approximation.

- The above form of the Hamiltonian (no sublattice potential) has a $C_2\mathcal{T}$ symmetry, which also acts within a single valley:

$$U_{C_2\mathcal{T}}^{\dagger} H_{\boldsymbol{k}}^{*}(-\boldsymbol{x}) U_{C_2\mathcal{T}} = H_{\boldsymbol{k}}(\boldsymbol{x}), \tag{B.3}$$

with $U_{C_2\mathcal{T}} = \sigma^x$. In the plane waves basis, it has the form $\sigma^x \mathcal{K}$, where $\mathcal{K}$ is the complex conjugation.

- There is another intravalley symmetry of our interest, which is a mirror symmetry with respect to y:

  $$U_{M_y}^{\dagger} H_{(k_x,-k_y)}\Big((x,-y)\Big) U_{M_y} = H_{\boldsymbol{k}}(\boldsymbol{x}), \tag{B.4}$$

  where $U_{M_y} = \sigma^x \tau^x$. This symmetry is also only present when $\Delta = 0$, and thus when $C_2\mathcal{T}$ is not broken.

- There is a time reversal symmetry that acts between the two valleys:

  $$H_{-\boldsymbol{k}}(\boldsymbol{x})\Big|_{\xi=-1}^{*} = H_{\boldsymbol{k}}(\boldsymbol{x})\Big|_{\xi=+1} \tag{B.5}$$

B.2 Maximally localized hybrid Wannier functions

As discussed in the main text the maximally localized HWFs are actually maximally localized one dimensional Wannier functions for each k_x that are derived using the method in Ref. [82]. In this Appendix a sketch of the procedure is presented, and also special cases are discussed in more length.

At each k_x, the spread function

$$\Omega_{k_x,\xi} = \sum_m \left[\left\langle y^2 \right\rangle_{m,k_x,\xi} - \langle y \rangle^2_{m,k_x,\xi} \right],$$

where the expectation values are calculated with respect to states $|k_x; y_c, m, \xi\rangle$, is minimized through suitable gauge transformations of the Bloch functions; the spread function consists of an invariant part Ω_{I}, which does not change under gauge transformation at all, and a contribution which can be minimized; the latter on its own comprises a band-diagonal part $\Omega_{\mathrm{D}} = \frac{1}{N_y} \sum_{k_y} \frac{1}{b^2} \sum_m \left(-\operatorname{Im} \log \mathcal{M}^{\boldsymbol{k},\xi}_{mm} - b_y \langle y \rangle_{m,k_x,\xi} \right)^2$ and a band-off-diagonal part $\Omega_{\mathrm{OD}} = \frac{1}{N_y} \sum_{k_y} \frac{1}{b^2} \sum_{m \neq m'} \left| \mathcal{M}^{\boldsymbol{k},\xi}_{mm'} \right|^2$. Here we give more details for the procedure discussed in the main text; starting from a smooth gauge for the original Bloch functions, suitable off-diagonal gauge transformations are made so that the $\mathcal{M}$ matrices are updated to be Hermitian. This is done by making use of the singular value decompositions (SVD) of the $\mathcal{M}$ matrices as follows (for every $\mathcal{M}$, one can define the SVD to have the form $\mathcal{M} = V \Sigma W^{\dagger}$, where V and W are unitary and Σ is diagonal with nonnegative entries): starting from a point in the BZ for every k_x, say $k_{y,0} = -\frac{3}{2}$ or in other words the left edge of the rectangular BZ, one can do series of gauge transformations separately along each constant k_x line, so that all (except for the last one completing the 1D loop) $\mathcal{M}$ matrices become Hermitian; this is done by the Gauge transformation

$$\left(\left| u_{k_x,k_y;1,\xi} \right\rangle, \left| u_{k_x,k_y;2,\xi} \right\rangle \right) \rightarrow \left(\left| u_{k_x,k_y;1,\xi} \right\rangle, \left| u_{k_x,k_y;2,\xi} \right\rangle \right) \cdot \left[\left(W V^{\dagger} \right)_{k_y - by} \cdots \left(W V^{\dagger} \right)_{k_{y,0}} \right], \tag{B.6}$$

where $\cdot$ denotes a matrix multiplication in the space of bands, and the k_x, ξ indices on W and V matrices are suppressed. In traversing the BZ in the y direction once, one is able to define the accumulated matrix

$$\Lambda_{k_x,\xi} = \left[\left(WV^\dagger \right)_{-k_{y,0}-by} \cdots \left(WV^\dagger \right)_{k_{y,0}} \right], \tag{B.7}$$

note that this matrix naively gives the prescription for a change of basis at $k_{y,0}$, the point one started with. However, we would like to end up with the state we started with so that a smooth Bloch basis is defined throughout the 1D Brillouin zone. One can achieve this if a series of actions are taken: at all k_y points, a unique basis change is made with the unitary matrix that diagonalizes $\Lambda_{k_x,\xi}$, i.e. the matrix V_λ, where $V_\lambda^\dagger \Lambda V_\lambda = \lambda$ with λ a diagonal matrix.

This last basis change updates all of the $\mathcal{M}$ matrices (except the last one at $-k_{y,0}-b_y$, more on this below) to have the form of a Hermitian matrix. The Hermitian matrices are proportional to unity to first order in b_y, and this ensures that Ω_{OD} shown above vanishes to first order in lattice spacings. However, there remains band-diagonal total Berry phases in this new basis which are invariant under single band gauge transformations; these are the inverses of the eigenvalues of the Λ matrix defined above and are at this stage accumulated in the last $\mathcal{M}$ matrix, i.e. at $-k_{y,0} - b_y$. One should make a band-diagonal gauge transformation (a phase redefinition) to ensure that this Berry phase is distributed evenly along the one-dimensional Brillouin Zone to make Ω_{D} vanish as well. This final (band diagonal) gauge transformation results in the final form $K\gamma$ for the $\mathcal{M}$ matrices, with a Hermitian K and a diagonal unitary

γ for the $\mathcal{M}$ matrices.

Note that an evenly distributed Berry phase means that $\gamma^{k_x,\xi}$ is independent of k_y and in fact equal to $\lambda^{-\frac{1}{N_y}}$. Furthermore, bear in mind that the matrix $\Lambda^\dagger$ is equal to the path ordered product of $\mathcal{M}$ matrices to first order in b_y for each k_x and thus is equal to the Wilson loop at k_x to this order. Noting that eigenvalues of the Wilson loop operators are related to the WCCs of the final bands means that eigenvalues of $\gamma^{k_x,\xi}$ take the form $e^{\frac{2\pi i}{N_y}\overline{y_{k_x,n}}}$, where $\overline{y_{k_x,n}}$ denotes the Wannier charge centers at k_x in units of $\frac{1}{2}a_M$.

The U matrices defined in Eq. (3.2), can be explicitly derived as:

$$U^{k_x,k_y;\xi} = \left[\left(WV^\dagger\right)_{k_y-by}\cdots\left(WV^\dagger\right)_{k_{y,0}}\right]\cdot V_\lambda\cdot(\lambda)^{-\frac{k_y-k_{y,0}}{2k_{y,0}}}\,, \tag{B.8}$$

where all right hand side matrices are evaluated at k_x,ξ.

Finally, we discuss further the special cases mentioned in the main text:

- In the case where $\Delta = 0$, due to the $C_2\mathcal{T}$ symmetry of the Hamiltonian, one can work with Bloch eigenstates of Hamiltonian that are $C_2\mathcal{T}$ symmetric. Any inner product of two $C_2\mathcal{T}$ eigenstates is real; this means that the $\mathcal{M}$ matrices have the form $\exp\left[i\mu^y m_{\boldsymbol{k},\xi}b_y\right]+\mathcal{O}(b_y^2)$, where μ^y acts in the two dimensional band space. Thus every SVD operator $VW^\dagger$ could be taken to be equal to $\mathcal{M} = \exp\left[i\mu^y m_{\boldsymbol{k},\xi}b_y\right]+\mathcal{O}(b_y^2)$ and furthermore V_λ could be taken to be the matrix that diagonalizes μ^y. Additionally, the integrals $\pm\int dk_y\ m_{\boldsymbol{k},\xi}$ yield the single band total Berry phases of the two bands in the parallel transport basis which should be distributed evenly along the strip with k_x. All this means that the states $\frac{e^{\pm i\phi_{\boldsymbol{k},\xi}}}{\sqrt{2}}\left(|\psi_{\boldsymbol{k};1,\xi}\rangle \pm i\,|\psi_{\boldsymbol{k};2,\xi}\rangle\right)$, with $C_2\mathcal{T}\,|\psi_{\boldsymbol{k};m,\xi}\rangle = |\psi_{\boldsymbol{k};m,\xi}\rangle$, form the parallel transport basis, if the phases are chosen properly to distribute the single band Berry phases evenly along the y direction.

- In the case of $\eta = 0$, regardless of the value of Δ, the sublattice polarized states form the parallel transport basis. One can argue for this as follows: starting from $\Delta = 0$, we note that states with opposite sublattice polarizations automatically have zero contribution to Ω_{OD}. Suitable single band gauge transformations are furthermore needed to minimize Ω_{D} as well. On the other hand, we know that the two bands in the chiral limit are related by[117]: $|\psi_{\boldsymbol{k},\xi,1}\rangle = i\,\sigma^z\,|\psi_{\boldsymbol{k},\xi,2}\rangle$. This means that adding the term $\sigma^z\Delta$ to the Hamiltonian does not change the subspace of active bands. And thus previously found sublattice polarized states still represent the active bands subspace, and with suitable single band phase redefinitions will form the parallel transport basis. It is important to note that addition of Δ does not change Wilson loop matrices for each k_x, and thus the phases chosen for $\Delta = 0$ in the parallel transport basis remain valid choices for nonzero Δ as well.

B.3 Hamiltonian in the HWF basis

In this section we describe how different terms of the Hamiltonian are derived in the HWF basis.

- **Kinetic term:**

H_{kin} could be written in different bases, we start by writing it in the basis of original Bloch eigenstates:

$$\begin{aligned} E^{\boldsymbol{k};\xi} &= \frac{1}{N_x N_y} \begin{pmatrix} \langle \psi_{\boldsymbol{k};1,\xi} | \\ \langle \psi_{\boldsymbol{k};2,\xi} | \end{pmatrix} \; H_{\text{kin}} \; \left(|\psi_{\boldsymbol{k};1,\xi}\rangle \, , |\psi_{\boldsymbol{k};2,\xi}\rangle \right) \\ &= \begin{pmatrix} E_1^{\boldsymbol{k};\xi} & 0 \\ 0 & E_2^{\boldsymbol{k};\xi} \end{pmatrix} . \end{aligned} \tag{B.9}$$

This defines the diagonal energy matrix $E^{\boldsymbol{k};\xi}$. The kinetic term in the HWF basis then reads:

$$\begin{aligned} t^{y'_c - y_c \, ; \, k'_x, k_x \, ; \, \xi', \xi} &= \frac{1}{N_x} \begin{pmatrix} \langle k'_x ; y'_c, 1, \xi' | \\ \langle k'_x ; y'_c, 2, \xi' | \end{pmatrix} \; H_{\text{kin}} \; \left(|k_x ; y_c, 1, \xi\rangle \, , |k_x ; y_c, 2, \xi\rangle \right) \\ &= \delta_{k'_x \, k_x} \delta_{\xi' \, \xi} \left\{ \frac{1}{N_y} \sum_{k_y} e^{i k_y (y'_c - y_c)} \left[\left(U^{\boldsymbol{k},\xi} \right)^{\dagger} \; E^{k_x, k_y ; \xi} \; U^{\boldsymbol{k},\xi} \right] \right\} \end{aligned} \tag{B.10}$$

and this defines the hopping matrix. As a result the kinetic term can be written as:

$$H_{\text{kin}} = \sum_{k_x, y'_c, y_c, m', m, \xi, s} |k_x ; y'_c, m', \xi, s\rangle \, \langle k_x ; y_c, m, \xi, s| \;\; t_{m'm}^{y'_c - y_c \, ; \, k_x \, ; \, \xi} \tag{B.11}$$

Where spin index has also been added trivially.

- **Interaction terms:**

The electron-electron interactions involve all electrons regardless of which moiré bands of the CM they belong to. However, here we are making an assumption that the gap between the active bands and the remote bands is large compared to the electron-electron interactions and thus it is legitimate to take the active bands as rigidly empty or full.

First, we discuss the four Fermi interaction Hamiltonian between the electrons in the active bands in the HWF basis; it takes the following form, the notation will be changed from y_c to y in HWF indices:

$$H_{\text{int}} = \frac{1}{2}\frac{1}{N_x^2} \sum_{[k_x]\,;\,[y]\,;\,[m]} \sum_{\xi,\xi',s,s'} \mathcal{I}_{[k_x]\,;\,[y]\,;\,[m],\xi,\xi'} \\ c^{\dagger}_{k_{x,1},y_1,m_1,\xi,s}\, c^{\dagger}_{k_{x,2},y_2,m_2,\xi',s'}\, c_{k_{x,3},y_3,m_3,\xi',s'}\, c_{k_{x,4},y_4,m_4,\xi,s}, \tag{B.12}$$

with the coefficients shown by $\mathcal{I}$ as follows:

$$\mathcal{I}_{[k_x]\,;\,[y]\,;\,[m],\xi,\xi'} = \frac{1}{N_y^2}\sum_{[k_y]} e^{i(k_{y,1}y_1+k_{y,2}y_2-k_{y,3}y_3-k_{y,4}y_4)} \\ \Bigg\{ \frac{1}{N_xN_y\mathcal{A}} \sum_{\boldsymbol{G}} \delta_{\boldsymbol{k}_1+\boldsymbol{k}_2-\boldsymbol{k}_3-\boldsymbol{k}_4,\boldsymbol{G}} \;\times \\ \left[\sum_{\Delta\boldsymbol{G}} \tilde{V}(\boldsymbol{k}_1-\boldsymbol{k}_4-\Delta\boldsymbol{G}) \quad \lambda_{m_1,m_4,\xi}\left(\boldsymbol{k}_1,\boldsymbol{k}_4,\Delta\boldsymbol{G}\right) \lambda^*_{m_3,m_2,\xi'}\left(\boldsymbol{k}_3,\boldsymbol{k}_2,\Delta\boldsymbol{G}-\boldsymbol{G}\right)\right] \Bigg\}. \tag{B.13}$$

In the above equation, we take the electron electron potential to have the form $\tilde{V}(\boldsymbol{q}) = \frac{e^2}{4\pi\epsilon}\frac{2\pi}{\sqrt{q^2+\mu^2}}$. Furthermore, the form factors are defined in terms of certain inner products of parallel transport basis:

$$\lambda_{m_1,m_4,\xi}\left(\boldsymbol{k}_1,\boldsymbol{k}_4,\Delta\boldsymbol{G}\right) = \sum_{\boldsymbol{G}_1}\sum_{\sigma\tau} \tilde{\phi}^*_{\boldsymbol{k}_1,m_1,\xi}(\boldsymbol{G}_1,\sigma\tau)\, \tilde{\phi}_{\boldsymbol{k}_4,m_4,\xi}(\boldsymbol{G}_1+\Delta\boldsymbol{G},\sigma\tau), \tag{B.14}$$

where, the $\tilde{\phi}$'s are coefficients for expansions of parallel transport Bloch states in terms of plane wave states, i.e. $\left|\tilde{\psi}_{\boldsymbol{k};m,\xi}\right\rangle = \sqrt{N_xN_y}\sum_{\boldsymbol{G},\sigma\tau}\tilde{\phi}_{\boldsymbol{k},m,\xi}(\boldsymbol{G},\sigma\tau)\left|\psi_{\boldsymbol{k}+\boldsymbol{G},\sigma\tau,\xi}\right\rangle$.

Second, we discuss the terms shown in the main text by $H_{\text{MF},0}$. Although remote bands are not treated as dynamical, a proper projection of the interacting Hamiltonian onto the active bands needs inclusion of an induced mean field potential due to the filled remote bands on the electrons in the active bands. This contribution will have the form:

$$H_{\text{MF, ind}} = \sum_{\alpha\alpha'} \left[\sum_{\beta\beta'} \left(V_{\alpha,\beta,\beta',\alpha'} - V_{\alpha,\beta,\alpha',\beta'} \right) \right] c_{\alpha}^{\dagger} c_{\alpha'}, \tag{B.15}$$

where α, α' run over active bands and β, β' run over remote bands below CNP.

In addition to that, as discussed in the main text, we have taken the zero point of the HF to be at the CNP of the moiré bands. This means that at CNP, the single electron/hole dispersions as given by the CM should be unaltered under HF. In order for this to be true, we subtract the HF effect of the moiré CNP noninteracting state from the Hamiltonian. The addition of these two effects will result in the form given in Eq. (3.7) in the main text for $H_{\text{MF},0}$.

There is a subtlety in the projection approach outlined above; with the above projected model at hand, we have considered changing the interaction strength in our study presented in the main text, this alters the coefficients of both H_{int} and $H_{\text{MF},0}$ (a change in the dielectric constant, for example, could result in this effect). However, such a change will result in a different single electron/hole potential according to (B.15); in particular, the single layer Fermi velocity v_F and the interlayer tunneling parameters $w_{\text{AA}}, w_{\text{AB}}$ will be renormalized, and other single particle terms will be induced or altered, these can include for example nonlinearities in the single layer dispersion in general, etc. . A change in $v_F, w_{\text{AA}}, w_{\text{AB}}$ parameters will tune the system away from the magic angle range. In this work, we have assumed that such change could be compensated by a change in the twist angle so that the system is tuned back to the new magic value for the twist angle as the interaction strength is altered. We have furthermore assumed that other induced effect (such as the monolayer nonlinear dispersion) could also be corrected by some means or are negligible and do not result in an appreciable effect. These assumptions allows us to also change the interaction strength in the terms correcting the zero point of our HF, and we will be left with the form in Eq. (3.7) with the interaction strength altered.

- **Symmetries:**
  - The $C_2\mathcal{T}$, when present, acts on the parallel transport basis as stated in the main text, transforms one band to the other with $\boldsymbol{k}$ unchanged:

    $$\left\langle \boldsymbol{r}, \sigma\tau \middle| \tilde{\psi}_{\boldsymbol{k},m,\xi} \right\rangle = \left\langle -\boldsymbol{r}, \bar{\sigma}\tau \middle| \tilde{\psi}_{\boldsymbol{k},\bar{m},\xi} \right\rangle^{*}. \tag{B.16}$$

    This in turn implies:

    $$\langle \boldsymbol{r}, \sigma\tau | k_x, y, m, \xi \rangle = \langle -\boldsymbol{r}, \bar{\sigma}\tau | k_x, -y, \bar{m}, \xi \rangle^{*} = \langle (2y\hat{\boldsymbol{y}} - \boldsymbol{r}), \bar{\sigma}\tau | k_x, y, \bar{m}, \xi \rangle^{*} \tag{B.17}$$

    Note that y is an integer times $\frac{a_M}{2}$ and we have used the translational properties shown in Fig. 3.1a.
  - The particle hole symmetry exchanges the two bands of the HWFs basis, taking k_x to $-k_x$. In the parallel transport basis the states can be related by this transformation as follows:

    $$\left\langle \boldsymbol{r}, \sigma\tau \middle| \tilde{\psi}_{\boldsymbol{k},m,\xi} \right\rangle = (-1)^{m}\, i \left\{ e^{-i(2\xi \boldsymbol{q}_{\mathrm{h}})\cdot\boldsymbol{r}}\, (-1)^{1+\tau} \left\langle (-x, y), \bar{\sigma}\tau \middle| \tilde{\psi}_{(-k_x,k_y),\bar{m},\xi} \right\rangle \right\}. \tag{B.18}$$

The factor $(-1)^m i$ in the above equation can be derived in the $C_2\mathcal{T}$ symmetric case explicitly; it furthermore can be maintained in the $\Delta \neq 0$ case as well by appropriate phase redefinitions. The above property, furthermore, results in the symmetry of WCC positions under $k_x \leftrightarrow -k_x$, as seen in Fig. 3.1b.

– The time reversal symmetry also relates the HWF states in the valleys in the following fashion:

$$\langle \boldsymbol{r}, \sigma\tau \, | k_x, y, m, \xi \rangle = \left\langle \boldsymbol{r}, \sigma\tau \, \middle| -k_x, y, m, \bar{\xi} \right\rangle^* . \tag{B.19}$$

This symmetry can also be viewed in the parallel transport basis as:

$$\left\langle \boldsymbol{r}, \sigma\tau \, \middle| \tilde{\psi}_{\boldsymbol{k},m,\xi} \right\rangle = \left\langle \boldsymbol{r}, \sigma\tau \, \middle| \tilde{\psi}_{-\boldsymbol{k},m,\bar{\xi}} \right\rangle^* . \tag{B.20}$$

- **Extra symmetry of the interaction term:**

Interestingly, when $C_2\mathcal{T}$ is present, the above equations show that under simultaneous action of the symmetries $C_2\mathcal{T}$, particle hole, time reversal and M_y (not exhibited above for the parallel transport basis) on a parallel transport band, one obtains the other band with the same Chern number, i.e. one with the parallel transport band number and valley number swapped; explicitly, it is straightforward to show that the wave functions in these two bands satisfy the following relation (we will use the parallel transport basis for the following argument and not the HWF basis):

$$\left\langle \boldsymbol{r}, \sigma\tau \left| \tilde{\psi}_{\boldsymbol{k},m,\xi} \right\rangle = (-1)^{\tau} e^{-i(2\xi \boldsymbol{q}_{\mathrm{h}} i)\cdot \boldsymbol{r}} \left[(-1)^{\bar{m}} \left\langle \boldsymbol{r}, \bar{\sigma}\bar{\tau} \left| \tilde{\psi}_{\boldsymbol{k},\bar{m},\bar{\xi}} \right\rangle \right] . \right. \right. \tag{B.21}$$

This means that if one acts with this intra-Chern-sector transformation on one creation and one annihilation operator with the same spin and valley indices in the interaction terms,

$$c^{\dagger}_{\boldsymbol{k}_1,m_1,\xi,s}\, c^{\dagger}_{\boldsymbol{k}_2,m_2,\xi',s'}\, c_{\boldsymbol{k}_3,m_3,\xi',s'}\, c_{\boldsymbol{k}_4,m_4,\xi,s}, \tag{B.22}$$

the matrix element of the interaction remains unchanged; this implies the existence of a symmetry of the interaction term of the Hamiltonian, which we discuss for the chiral limit and also away from the chiral limit separately below:

– $\eta = 0$, magic angle: in the chiral limit, since the parallel transport basis is sublattice polarized, the interaction in Eq. (B.22) becomes of density-density type in the band index as well as the spin and valley indices. This, along with the above observation of the invariance of interaction matrix elements, implies that the interaction terms could be grouped together so that only fermion bilinear terms $\begin{pmatrix} c^{\dagger}_{\boldsymbol{k}_1,1,K} & c^{\dagger}_{\boldsymbol{k}_1,2,K'} \end{pmatrix} \begin{pmatrix} c_{\boldsymbol{k}_4,1,K} \\ c_{\boldsymbol{k}_4,2,K'} \end{pmatrix}$ and $\begin{pmatrix} c^{\dagger}_{\boldsymbol{k}_1,2,K} & c^{\dagger}_{\boldsymbol{k}_1,1,K'} \end{pmatrix} \begin{pmatrix} c_{\boldsymbol{k}_4,2,K} \\ c_{\boldsymbol{k}_4,1,K'} \end{pmatrix}$ appear in the four Fermi terms of the interaction, where the spin indices are suppressed. This means that separate unitary transformations within each Chern sector keep the interaction intact. Upon further including the spin rotation symmetry as well, one recovers the two separate $U(4) \times U(4)$ symmetries of the two Chern sectors discussed in Ref. [21].

- $\eta = 0$, away from the magic angle: in the chiral limit, the non-interacting Hamiltonian can be written in the parallel transport basis as follows:

$$\begin{aligned} H_{\text{kin}} &= \epsilon_{\boldsymbol{k}} \left[c^\dagger_{\boldsymbol{k},1,K} \, c_{\boldsymbol{k},2,K} - c^\dagger_{\boldsymbol{k},2,K'} \, c_{\boldsymbol{k},1,K'} + \text{h.c.} \right] \\ &= \begin{pmatrix} c^\dagger_{\boldsymbol{k},1,K} & -c^\dagger_{\boldsymbol{k},2,K'} \end{pmatrix} \begin{pmatrix} c_{\boldsymbol{k},2,K} \\ c_{\boldsymbol{k},1,K'} \end{pmatrix} + \text{h.c.}, \end{aligned} \tag{B.23}$$

  suppressing the spin indices. The creation operators in the row vector correspond to one Chern sector and the annihilation operators in the column vector belong to the opposite Chern sector; this shows that the two unitary matrices acting on the two separate Chern sectors need to be related so that the kinetic term remains invariant as well. In other words, if, for example, the 2×2 unitary U is used for the $C = +1$ sector, $U\mu^z$ (μ^z is the Pauli matrix acting on the above doublets of fermion operators) should be used for the $C = -1$ sector. This reduces the symmetry group to U(4) when spin is also included.

- $\eta \neq 0$: away from the chiral limit, apart form the bilinears

$$\begin{pmatrix} c^\dagger_{\boldsymbol{k}_1,1,K} & c^\dagger_{\boldsymbol{k}_1,2,K'} \end{pmatrix} \begin{pmatrix} c_{\boldsymbol{k}_4,1,K} \\ \\ c_{\boldsymbol{k}_4,2,K'} \end{pmatrix} \text{ and } \begin{pmatrix} c^\dagger_{\boldsymbol{k}_1,2,K} & c^\dagger_{\boldsymbol{k}_1,1,K'} \end{pmatrix} \begin{pmatrix} c_{\boldsymbol{k}_4,2,K} \\ \\ c_{\boldsymbol{k}_4,1,K'} \end{pmatrix},$$

  other combinations also appear in the four Fermi interaction; these terms could be written as:

$$\begin{pmatrix} c^\dagger_{\boldsymbol{k}_1,1,K} & c^\dagger_{\boldsymbol{k}_1,2,K'} \end{pmatrix} \begin{pmatrix} c_{\boldsymbol{k}_4,2,K} \\ c_{\boldsymbol{k}_4,1,K'} \end{pmatrix} \text{ and } \begin{pmatrix} c^\dagger_{\boldsymbol{k}_1,2,K} & c^\dagger_{\boldsymbol{k}_1,1,K'} \end{pmatrix} \begin{pmatrix} c_{\boldsymbol{k}_4,1,K} \\ c_{\boldsymbol{k}_4,2,K'} \end{pmatrix}.$$

This again means that the unitaries in the two Chern sectors should be related, and in fact identical so that these new terms also remain invariant. This results in the symmetry group U(4) with spin included; this last symmetry of the interaction term away from the chiral limit does not survive when the noninteracting terms of the Hamiltonian are considered.

B.4 Particle-hole symmetry between $\nu = +3$ and $\nu = -3$

In this Appendix, we discuss how the particle hole symmetry of the CM is displayed in the way the many body states are transformed between the two fillings $\nu = \pm 3$. We should note that for general η, we have an approximate particle hole symmetry which needs a $k_x \to -k_x$ transformation as well. As was discussed in the main text, this particle hole symmetry is broken in our numerical results for the first study, i.e. when the HF zero point is taken at $\nu = -4$, or in other words when only the HWF basis hoppings along with the interaction between particles in the active bands are kept. It is broken even in the limit of $\eta = 0$, i.e. the chiral model regardless of the value of Δ. We will furthermore argue that had we started with a model where the zero point of the HF is at $\nu = +4$, we would have gotten the particle hole transformed version of the same model; in this model holes will play the role of electrons. Finally we will sketch how the particle hole symmetry is retained in the projected model of our second study.

We consider the model of our first study in the chiral limit for simplicity. The chiral symmetry of the model in this limit indicates that each state with an energy $E(\boldsymbol{k})$ has a counterpart with the same $\boldsymbol{k}$ value that but opposite energy $-E(\boldsymbol{k})$. Note again that this is different from the particle hole symmetry we discussed above (the latter is present with an approximation of neglecting the rotation of sublattice matrices); we only consider the chiral limit in the following but very similar reasoning can be done for the particle hole symmetry at general η. The two states with energies $\pm E(\boldsymbol{k})$ could be written in terms of each other as $|\psi_{\boldsymbol{k},1,\xi}\rangle = i\ \sigma^z\,|\psi_{\boldsymbol{k},2,\xi}\rangle$, where the indices $1,2$ correspond to states within the two active bands. Thus, it is easy to form sublattice polarized states:

$$\tilde{c}^{\dagger}_{\boldsymbol{k},m,\xi} = \frac{e^{i\phi_{k_x;k_y,m,\xi}}}{\sqrt{2}}\left[c^{\dagger}_{\boldsymbol{k},1,\xi} + (-1)^m i\ c^{\dagger}_{\boldsymbol{k},2,\xi}\right]. \tag{B.24}$$

It has been argued in the main text and the Appendix that the states in the parallel transport basis also have such a form and thus we take $\tilde{c}^{\dagger}_{\boldsymbol{k},\xi,m}$ to be the creation operator in the parallel transport basis. One can get the maximally localized HWFs by doing a Wannier transform:

$$c^{\dagger}_{k_x;y,m,\xi} = \frac{1}{N_y}\sum_{k_y} e^{-ik_y y}\,\tilde{c}^{\dagger}_{\boldsymbol{k},m,\xi}. \tag{B.25}$$

Note that on the left hand side, i.e. Fermi operators in the HWF basis we are not using $\tilde{\cdot}$ signs anymore. We will also drop the subscript of k_x. The kinetic term of the Hamiltonian in terms of these states reads:

$$\begin{aligned} H_{\text{kin}}|_{\Delta=0} &= \frac{1}{N_x N_y} \sum_{\xi,\boldsymbol{k}} \epsilon_{\boldsymbol{k},\xi} \left[e^{i\varphi_{k,k_y,\xi}} \; \tilde{c}^{\dagger}_{\boldsymbol{k},1,\xi} \, \tilde{c}_{\boldsymbol{k},2,\xi} + e^{-i\varphi_{k,k_y,\xi}} \; \tilde{c}^{\dagger}_{\boldsymbol{k},2,\xi} \, \tilde{c}_{\boldsymbol{k},1,\xi} \right] \\ &= \frac{1}{N_x} \sum_{\xi,k,yy'} \left[t^{\,y'-y,k,\xi} \; c^{\dagger}_{k,y',1,\xi} \, c_{k,y,2,\xi} + \left(t^{\,y'-y,k,\xi} \right)^{*} \; c^{\dagger}_{k,y,2,\xi} \, c_{k,y',1,\xi} \right], \end{aligned} \tag{B.26}$$

where $\varphi_{k,k_y,\xi} = \phi_{k,k_y,2,\xi} - \phi_{k,k_y,1,\xi}$, and the hopping parameter reads

$$t^{\,y'-y,k,\xi} = \frac{1}{N_y} \sum_{k_y} e^{ik_y(y'-y)} \left[\epsilon_{\boldsymbol{k},\xi} \; e^{i\varphi_{k,k_y,\xi}} \right],$$

and the subscript of k_x is not shown from here on. When the sublattice potential term is also present, we have argued above that since the term $\sigma^z \Delta$ keeps the active bands subspace intact at each $\boldsymbol{k}$, the states shown in (B.24) still form the HWF basis; it is straightforward to work out the sublattice potential form as well, since HWF basis is sublattice polarized:

$$H_{\Delta} = \frac{1}{N_x} \Delta \sum_{\xi,k,y} \left[\, c^{\dagger}_{k,y,1,\xi} \, c_{k,y,1,\xi} - c^{\dagger}_{k,y,2,\xi} \, c_{k,y,2,\xi} \right]. \tag{B.27}$$

We also note that $\phi_{k,k_y,2,\xi} = -\phi_{k,k_y,1,\xi}$, regardless of the value of Δ.

Now, it is straightforward to check that the terms in H_{kin}, including the Δ term, have the same form in terms of d operators as that in terms of c operators, where they are defined as in the following particle hole transformations:

$$c^{\dagger}_{k,y,1,\xi} = d_{k,-y,2,\xi}, \quad c^{\dagger}_{k,y,2,\xi} = -d_{k,-y,1,\xi}, \tag{B.28}$$

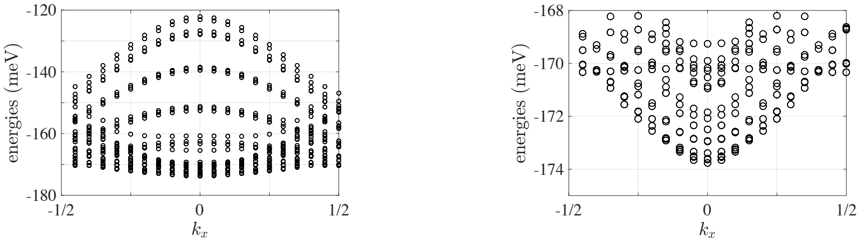

(a) (b)

Figure B.1: Eigenvalues of the single hole potential shown in (B.31). The following set of paramters has been used: $\eta = 0$, $\alpha = 0.58$, $\Delta = 1.9$meV, $\ell_\xi = 0.1 a_M$, $g_{\text{int}} = 0.1$. Lower energies are available for smaller k_x values. A magnified view of smallest energies is shown in panel (b).

This means that H_{kin} is particle hole symmetric with the above prescription. Spin indices could be trivially added to the above terms.

One should furthermore consider the interaction term; the interaction in general can be written as follows:

$$H_{\text{int}} = \frac{1}{2} \sum_{k\text{'s}, y\text{'s}} \sum_{\xi\xi' ss'} \sum_{mm'} V_{k_1 y_1 \xi m;\, k_2 y_2 \xi' m';\, k_3 y_3 \xi' m';\, k_4 y_4 \xi m} \left[c^\dagger_{k_1, y_1, m, \xi, s}\, c^\dagger_{k_2, y_2, m', \xi', s'}\, c_{k_3, y_3, m', \xi', s'}\, c_{k_4, y_4, m, \xi, s} \right] . \tag{B.29}$$

Since, $\langle \boldsymbol{r}, \sigma\tau \,| k_1 y_1 m \xi \rangle = \langle -\boldsymbol{r}, \bar{\sigma}\tau \,| k_1 (-y_1) \bar{m} \xi \rangle^*$, the interaction terms have the following relations between themselves:

$$V_{k_1 y_1 \xi m;\, k_2 y_2 \xi' m';\, k_3 y_3 \xi' m';\, k_4 y_4 \xi m} = V_{k_4 (-y_4) \xi \bar{m};\, k_3 (-y_3) \xi' \bar{m}';\, k_2 (-y_2) \xi' \bar{m}';\, k_1 (-y_1) \xi \bar{m}}.$$

The interaction thus takes the following form in terms of the d operators:

$$\begin{aligned} H_{\text{int}} =& \frac{1}{2}\sum_{1234} V_{1,2,3,4}\ d_1^\dagger\, d_2^\dagger\, d_3\, d_4 \\ &+ \sum_{123} d_2^\dagger\, d_3\, (-V_{1231} + V_{1213}) \\ &+ \frac{1}{2}\sum_{12} (V_{1221} - V_{1212})\,, \end{aligned} \tag{B.30}$$

where for simplicity a change of notation has been made $1 \equiv (k_1, y_1, \xi, s, m)$, and so forth. The first term above is identical in form to the original interaction Hamiltonian in terms of c operators. However, there are terms quadratic in d, the *single hole terms*, that were not present in the original Hamiltonian. Note that the terms on the third row are constant. The terms on the second row, on the other hand, turn out to be k_x-dependent and thus impose a single hole potential; this is the origin of the particle hole asymmetry between the fillings ±3, as was discussed in the main text. Note that unlike this situation, in the usual Hubbard model with a single band, nearest neighbor hopping and constant on-site interaction for example, the analogue of this term is just a redefinition of the chemical potential.

The single hole potential introduced above has the following explicit form:

$$\begin{aligned} &\sum_{k_2 y_2 y_3} \sum_{m_2 \xi_2 s_2} d^\dagger_{k_2,y_2,m_2,\xi_2,s_2}\, d_{k_2,y_3,m_2,\xi_2,s_2} \\ &\qquad \sum_{k_1 y_1; m_1 \xi_1} \Bigg[-2V_{k_1 y_1 \xi_1 m_1;\, k_2 y_2 \xi_2 m_2;\, k_2 y_3 \xi_2 m_2;\, k_1 y_1 \xi_1 m_1} \\ &\qquad\qquad + \delta_{\xi_2 \xi_1} \delta_{m_2 m_1}\ V_{k_1 y_1 \xi_1 m_1;\, k_2 y_2 \xi_1 m_1;\, k_1 y_1 \xi_1 m_1;\, k_2 y_3 \xi_1 m_1} \Bigg], \end{aligned} \tag{B.31}$$

This single hole potential has been calculated numerically for a special case and its eigenvalues are formed, see Fig.B.1. One can observe that hole states with k_x closer to 0 are preferred.

We briefly mention here what form of a particle hole transformation should be used, instead of (B.28), when $\eta \neq 0$ which mean that there is no chiral symmetry in the model. Generically and regardless of the value of Δ, the following transformation could be used:

$$\tilde{c}^{\dagger}_{\boldsymbol{k},1,\xi} = \tilde{d}_{-\tilde{\boldsymbol{k}},2,\bar{\xi}}, \quad \tilde{c}^{\dagger}_{\boldsymbol{k},2,\xi} = -\tilde{d}_{-\tilde{\boldsymbol{k}},1,\bar{\xi}}, \tag{B.32}$$

where for $\boldsymbol{k} = (k_x, k_y)$, we define $\tilde{\boldsymbol{k}} = (-k_x, k_y)$. Note that for the sake of clarity we have expressed the particle hole transformation for creation and annihilation operators in the parallel transport basis, i.e. before the hybrid Wannier transformation is performed. It is straightforward to re peat the manipulations detailed above also with this transformation. If $\Delta = 0$, the $C_2\mathcal{T}$ is present and one can use a particle hole transformation that works within each valley:

$$\tilde{c}^{\dagger}_{\boldsymbol{k},1,\xi} = \tilde{d}_{\tilde{\boldsymbol{k}},2,\xi}, \quad \tilde{c}^{\dagger}_{\boldsymbol{k},2,\xi} = -\tilde{d}_{\tilde{\boldsymbol{k}},1,\xi}. \tag{B.33}$$

It is worthwhile to note that (B.32) preserves the Chern number of the band, while (B.33) takes it to the opposite value. In Fig. 3.4a of the main text we have used the latter transformation since $C_2\mathcal{T}$ is present.

It is simple now to see how one could obtain a model with its HF zero point at $\nu = +4$; by requiring the second row in Eq. (B.30) to be cancelled by the terms in $H_{\mathrm{MF},0}$. Note that this will result in a Hamiltonian which is identical to the one we used in our first study, except that the electrons are replaced by holes. It is also easy at this point to check that the model with its zero point at the CNP is particle hole symmetric. This happens due to the particular form that $H_{\mathrm{MF},0}$ takes for this choice, i.e. Eq. (3.7); it is straightforward to check that the sum of $H_{\mathrm{MF},0}$ with the terms on the second row of Eq. (B.30) takes the form of $H_{\mathrm{MF},0}$ again but particle hole transformed.

B.5 Comparison with other Hartree Fock studies

In this Appendix, we compare our approach and results on the HF stability of QAHE with other recent HF studies, namely Refs. [77, 75, 133, 21]. We first summarize our results: our numerical analysis shows that with the physical choice of $\eta \approx 0.8$, we observe a robust QAHE for $\nu = -3$ and $\nu = +3$, if we set the zero point of our HF approach to be at $\nu = -4$ and $\nu = +4$ respectively. This QAHE is a consequence of valley, spin and band (in the HWF basis) polarization in the HF solutions. On the contrary, if the HF zero point is taken at the CNP, there is a particle hole symmetry between the many body states found at $\nu = \pm 3$; we only observe QAHE in small windows of parameters in either of these two filling factors for the choice of $\eta = 0.8$. Based on these observations and following a phenomenological argument, we expect the model with the HF zero point set at $\nu = +4$ to be most relevant to physics seen in TBG samples exhibiting QAHE. In the following, we compare the results of this model with those presented in some of the recent related HF studies.

We start with Ref. [133], where a HF study is carried out keeping the remote bands as dynamical in the analysis. Furthermore, the zero point of the HF Hamiltonian is taken at the CNP of decoupled monolayer graphene sheets. These authors have considered several filling factors, for example at CNP, they observe an interaction induced gap corresponding to a $C_2\mathcal{T}$ broken phase for large enough interaction. On the other hand, in the insulators they obtain at the fillings $\nu = \pm 1$ and $\nu = \pm 3$, $C_2\mathcal{T}$ is not necessarily broken and thus the many body states at these fillings do not automatically show QAHE. This is in contrast to our findings outlined above where an insulator exhibiting QAHE could be observed at one of these two fillings depending on the choice of the HF zero point.

We next turn to Ref. [77], where a HF study has been implemented taking only the active bands as dynamical. The zero point of their HF is set at the CNP of the active bands, and this makes their model similar to the one in one of our studies. The focus of this work is on the CNP and they report observing a variety of different symmetry broken insulating states in their numerical results, including $C_2\mathcal{T}$ broken, spin/valley polarized, etc. Ref. [21], on the other hand, deals with the full set of moiré bands in the HF analysis, but with the main focus on the CNP also. Interestingly, the $U(4) \times U(4)$ symmetry of the chiral model ($\eta = 0$) discussed in this work can also be seen in the HWF basis (and also the parallel transport basis) as discussed in the capter 3; for general η, when $C_2\mathcal{T}$ is present, an interaction-only model consisting of active bands only displays a $U(4) \times U(4)$ symmetry (see Appendix B.3).

Finally, we consider Ref. [75], where a HF study taking all bands into account has been presented. The authors consider several filling factors, and in particular, they are able to see a QAHE at $\nu = \pm 3$; the presence of a significant sublattice potential is crucial for the QAHE to materialize. This is in contrast to the present work, where the presence of a sublattice potential can make the QAHE stronger, but it is not necessary for the occurrence of the required flavor polarization. Within our study, we observed that a larger interaction strength could compensate for the absence of the sublattice potential.

Appendix C

Appendix for Chapter 4

C.1 Linear wave analysis with anisotropy

In this section, we present the magnon spectrum when the anisotropy is present, and separately discuss the cases of Ising anisotropy ($\beta > 0$) and XY anisotropy ($\beta < 0$).

C.1.1 Ising Anisotropy

Following the parametrization in equation (15), The Hamiltonian near the saddle point $\mathbf{N}_l^{\mathrm{cl}}$ is

$$\begin{aligned}\mathsf{H} =&(\nabla_{\mathsf{x}}\phi_1)^2 + (\nabla_{\mathsf{x}}\phi_2)^2 - \alpha\hat{\Phi}(\mathsf{x})\cos(\phi_1 - \phi_2) - \beta(\cos^2\phi_1 + \cos^2\phi_2)\\ &+(\nabla_{\mathsf{x}}u_1)^2 + (\nabla_{\mathsf{x}}u_2)^2 + (\nabla_{\mathsf{x}}v_1)^2 + (\nabla_{\mathsf{x}}v_2)^2 - v_1^2(\nabla_{\mathsf{x}}\phi_1)^2 - v_2^2(\nabla_{\mathsf{x}}\phi_2)^2\\ &-\frac{1}{2}\alpha\hat{\Phi}(\mathsf{x})\left[2v_1v_2 + \cos(\phi_1 - \phi_2)(2u_1u_2 - u_1^2 - u_2^2 - v_1^2 - v_2^2)\right]\\ &+\beta(u_1^2\cos 2\phi_1 + u_2^2\cos 2\phi_2 + v_1^2\cos^2\phi_1 + v_2^2\cos^2\phi_2) + \dots,\end{aligned} \tag{C.1}$$

where the first line is the 0th order contribution, and the dots in the end represent higher-order terms in u and v. Switching to the symmetric and anti-symmetric basis, this becomes

$$
\begin{aligned}
\mathsf{H} =&\mathsf{H}_{cl} + \frac{1}{2}\left[(\nabla_{\mathsf{x}} u_s)^2 + (\nabla_{\mathsf{x}} u_a)^2 + (\nabla_{\mathsf{x}} v_s)^2 + (\nabla_{\mathsf{x}} v_a)^2\right] \\
&- \frac{1}{8}\left\{(v_a^2 + v_s^2)[(\nabla_{\mathsf{x}}\phi_a)^2 + (\nabla_{\mathsf{x}}\phi_s)^2] + 4 v_s v_a \nabla_{\mathsf{x}}\phi_a \nabla_{\mathsf{x}}\phi_s\right\} \\
&+ \frac{\alpha}{4}\hat{\Phi}(\mathsf{x})\left[-v_s^2(1-\cos\phi_a) + v_a^2(1+\cos\phi_a) + 2u_a^2\cos\phi_a\right] \\
&+ \frac{\beta}{4}\left[(v_s^2+v_a^2) + (2u_s^2 + 2u_a^2 + v_s^2 + v_a^2)\cos\phi_s\cos\phi_a - (4u_s u_a + 2 v_s v_a)\sin\phi_s\sin\phi_a\right]
\end{aligned}
\tag{C.2}
$$

where H_{cl} is defined in equation (10) of the main text.

For the second order terms of the Hamiltonian, we go to the Lagrangian by

$$
\mathsf{L}_2 = \frac{1}{2v^2}\left(|\partial_t u_s|^2 + |\partial_t u_a|^2 + |\partial_t v_s|^2 + |\partial_t v_a|^2\right) - \mathsf{H}_2, \tag{C.3}
$$

which leads to the following coupled linear wave equations for u, v's:

$$
\begin{aligned}
\partial_t^2 u_s &= v^2 q_m^2\left[\nabla_{\mathsf{x}}^2 u_s - \beta(\cos\phi_s\cos\phi_a u_s - \sin\phi_s\sin\phi_a u_a)\right], \\
\partial_t^2 u_a &= v^2 q_m^2\left[\nabla_{\mathsf{x}}^2 u_a - \alpha\hat{\Phi}(\mathsf{x})\cos\phi_a u_a - \beta(\cos\phi_s\cos\phi_a u_a - \sin\phi_s\sin\phi_a u_s)\right], \\
\partial_t^2 v_s &= v^2 q_m^2[\nabla_{\mathsf{x}}^2 v_s + \frac{1}{4}\left(v_s(\nabla_{\mathsf{x}}\phi_s)^2 + v_s(\nabla_{\mathsf{x}}\phi_a)^2 + 2v_a\nabla_{\mathsf{x}}\phi_s\nabla_{\mathsf{x}}\phi_a\right) + \frac{\alpha}{2}\hat{\Phi}(\mathsf{x})(1-\cos\phi_a)v_s \\
&\qquad - \frac{\beta}{2}(v_s + v_s\cos\phi_s\cos\phi_a - v_a\sin\phi_s\sin\phi_a)], \\
\partial_t^2 v_a &= v^2 q_m^2[\nabla_{\mathsf{x}}^2 v_a + \frac{1}{4}\left(v_a(\nabla_{\mathsf{x}}\phi_s)^2 + v_a(\nabla_{\mathsf{x}}\phi_a)^2 + 2v_s\nabla_{\mathsf{x}}\phi_s\nabla_{\mathsf{x}}\phi_a\right) - \frac{\alpha}{2}\hat{\Phi}(\mathsf{x})(1+\cos\phi_a)v_s \\
&\qquad - \frac{\beta}{2}(v_a + v_a\cos\phi_s\cos\phi_a - v_s\sin\phi_s\sin\phi_a)].
\end{aligned}
\tag{C.4}
$$

Taking $u_{s/a}(\mathsf{x}, t) = e^{i\omega t}u_{s/a}(\mathsf{x})$ and using the Bloch ansatz (with $\mathsf{k} = \mathbf{k}/q_m$ being the dimensionless quasi-momentum vector),

$$u_{s/a}(\mathsf{x}) = \hat{u}_{s/a}(\mathsf{x})e^{i\mathsf{k}\cdot\mathsf{x}}, \quad v_{s/a}(\mathsf{x}) = \hat{v}_{s/a}(\mathsf{x})e^{i\mathsf{k}\cdot\mathsf{x}}, \tag{C.5}$$

we obtain

$$\begin{aligned}
\omega^2\hat{u}_s &= -v^2q_m^2\left[(\nabla_{\mathsf{x}} + i\mathsf{k})^2\hat{u}_s - \beta(\cos\phi_s\cos\phi_a\hat{u}_s - \sin\phi_s\sin\phi_a\hat{u}_a)\right], \\
\omega^2\hat{u}_a &= -v^2q_m^2\left[(\nabla_{\mathsf{x}} + i\mathsf{k})^2\hat{u}_a - \alpha\hat{\Phi}(\mathsf{x})\cos\phi_a\hat{u}_a - \beta(\cos\phi_s\cos\phi_a\hat{u}_a - \sin\phi_s\sin\phi_a\hat{u}_s)\right], \\
\omega^2\hat{v}_s &= -v^2q_m^2[(\nabla_{\mathsf{x}} + i\mathsf{k})^2\hat{v}_s + \frac{1}{4}\left(\hat{v}_s(\nabla_{\mathsf{x}}\phi_s)^2 + \hat{v}_s(\nabla_{\mathsf{x}}\phi_a)^2 + 2\hat{v}_a\nabla_{\mathsf{x}}\phi_s\nabla_{\mathsf{x}}\phi_a\right) \\
&\qquad + \frac{\alpha}{2}\hat{\Phi}(\mathsf{x})(1-\cos\phi_a)\hat{v}_s - \frac{\beta}{2}(\hat{v}_s + \hat{v}_s\cos\phi_s\cos\phi_a - \hat{v}_a\sin\phi_s\sin\phi_a)], \\
\omega^2\hat{v}_a &= -v^2q_m^2[(\nabla_{\mathsf{x}} + i\mathsf{k})^2\hat{v}_a + \frac{1}{4}\left(\hat{v}_a(\nabla_{\mathsf{x}}\phi_s)^2 + \hat{v}_a(\nabla_{\mathsf{x}}\phi_a)^2 + 2\hat{v}_s\nabla_{\mathsf{x}}\phi_s\nabla_{\mathsf{x}}\phi_a\right) \\
&\qquad - \frac{\alpha}{2}\hat{\Phi}(\mathsf{x})(1+\cos\phi_a)\hat{v}_a - \frac{\beta}{2}(\hat{v}_a + \hat{v}_a\cos\phi_s\cos\phi_a - \hat{v}_s\sin\phi_s\sin\phi_a)].
\end{aligned} \tag{C.6}$$

In the collinear phase, the Neel vectors in the two layers are uniform and point either to the $+\hat{z}$ or the $-\hat{z}$ direction. Namely, there are four possible combinations that are degenerate in energy: $(\phi_s, \phi_a) = (0, 0)$, $(2\pi, 0)$, and (π, π), $(\pi, -\pi)$. The last two of them satisfying $\cos\phi_s = \cos\phi_a = -1$ have the same discrete symmetry as that of the twisted-s phase, i.e. a simultaneous spin reflection $N_z \to -N_z$ and layer exchange. For this type of solutions, (C.6) reduces to a pair of degenerate equations for (u_s, v_a) and (u_a, v_s):

$$\begin{aligned}
\omega^2\hat{u}_s &= -v^2q_m^2[(\nabla_{\mathsf{x}} + i\mathsf{k})^2 - \beta]\hat{u}_s, \\
\omega^2\hat{u}_a &= -v^2q_m^2[(\nabla_{\mathsf{x}} + i\mathsf{k})^2 + \alpha\hat{\Phi}(\mathsf{x}) - \beta]\hat{u}_a.
\end{aligned} \tag{C.7}$$

For the other two solutions with $\cos\phi_s = \cos\phi_a = 1$, (C.6) reduces to a pair of degenerate equations for (u_s, v_s) and (u_a, v_a) instead. The u_s and u_a modes satisfy the same set of equations as in (C.7) upon substituting $\alpha \to -\alpha$. We will choose the $\cos\phi_s = \cos\phi_a = -1$ case below for concreteness.

The twisted-a phase is the only one that involves the interplay between the symmetric and anti-symmetric modes. As can be observed from (C.6), the $u_s,\ u_a$ modes are mixed, so are v_s and v_a; the four branches thus combine into two, which we will simply label as u and v. There is one Goldstone mode in the v-branch.

In the twisted-s phase, the four equations decouple, and there is again one Goldstone mode corresponding to the out-of-plane rotation v_s.

$$\begin{aligned}
\omega^2\hat{u}_s &= -v^2 q_m^2\left[(\nabla_{\mathsf{x}} + i\mathsf{k})^2 + \beta\cos\phi_a\right]\hat{u}_s,\\
\omega^2\hat{u}_a &= -v^2 q_m^2\left[(\nabla_{\mathsf{x}} + i\mathsf{k})^2 - \alpha\hat{\Phi}(\mathsf{x})\cos\phi_a + \beta\cos\phi_a\right]\hat{u}_a,\\
\omega^2\hat{v}_s &= -v^2 q_m^2[(\nabla_{\mathsf{x}} + i\mathsf{k})^2 + \frac{1}{4}(\nabla_{\mathsf{x}}\phi_a)^2 + \frac{\alpha}{2}\hat{\Phi}(\mathsf{x})(1-\cos\phi_a) - \frac{\beta}{2}(1-\cos\phi_a)]\hat{v}_s,\\
\omega^2\hat{v}_a &= -v^2 q_m^2[(\nabla_{\mathsf{x}} + i\mathsf{k})^2 + \frac{1}{4}(\nabla_{\mathsf{x}}\phi_a)^2 - \frac{\alpha}{2}\hat{\Phi}(\mathsf{x})(1+\cos\phi_a) - \frac{\beta}{2}(1-\cos\phi_a)]\hat{v}_a.
\end{aligned} \tag{C.8}$$

The magnon bands in the three phases are shown in figure C.1.

Similar to the isotropic case, the magnon bands flatten at large α due to their confinement in the disconnected domains in a large potential. Below we show an example $\alpha = 19,\ \beta = 9$ in the twisted-a phase.

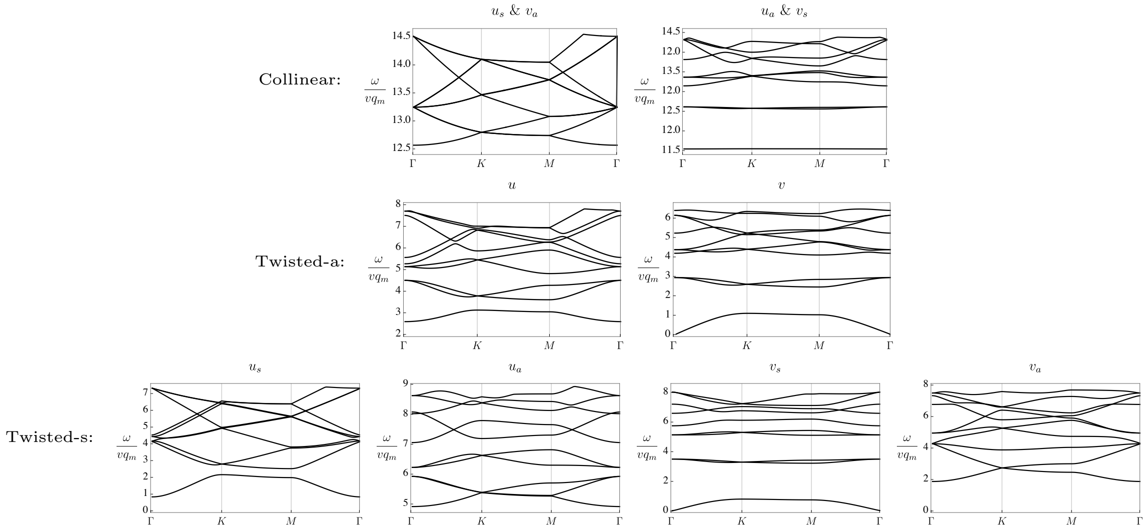

Figure C.1: Top row: The ten lowest magnon bands in the collinear phase for the four branches, where we have chosen $\cos\phi_s = \cos\phi_a = -1$. The dimensionless parameters are $\alpha = 1$, $\beta = 9$. Middle: Magnon bands for the two branches u, v in the twisted-a phase at $\alpha = 9$, $\beta = 1$. Bottom: Twisted-s phase for the four decoupled branches at $\alpha = 2$, $\beta = 0.2$.

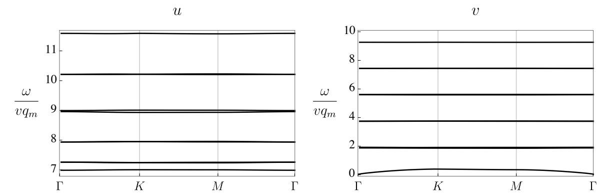

Figure C.2: Flattening of magnon bands in the twisted-a phase at $\alpha = 19$, $\beta = 9$.

C.1.2 XY Anisotropy

Now we turn to the case $d < 0$, where the Neel vectors tend to lie in the XY plane. We thereby choose the following ansatz:

$$\begin{aligned} \mathbf{N}_l &= \sqrt{1 - u_l^2 - v_l^2}\,\mathbf{N}_l^{cl}(\mathsf{x}) + u_l \mathbf{u}_l(\mathsf{x}) + v_l \mathbf{v}_l(\mathsf{x}), \\ \mathbf{N}_l^{cl} &= \sin\phi_l \hat{\mathbf{x}} + \cos\phi_l \hat{\mathbf{y}}, \quad \mathbf{u}_l = \cos\phi_l \hat{\mathbf{x}} - \sin\phi_l \hat{\mathbf{y}}, \quad \mathbf{v}_l = \hat{\mathbf{z}}. \end{aligned} \tag{C.9}$$

The Hamiltonian at the saddle point $\mathbf{N}_l^{cl}$ is $\mathsf{H}_{cl} = \frac{1}{2}\left[(\nabla_{\mathsf{x}}\phi_s)^2 + (\nabla_{\mathsf{x}}\phi_a)^2\right] - \alpha\hat{\Phi}(\mathsf{x})\cos\phi_a$. Classically, the system behaves as if there is no anisotropy, and ϕ_s is uniform everywhere. Near the saddle point, following the same procedure as the section above, we obtain in the symmetric/anti-symmetric basis:

$$\begin{aligned}\mathsf{H}_2 =& \frac{1}{2}\left[(\nabla_{\mathsf{x}} u_s)^2 + (\nabla_{\mathsf{x}} u_a)^2 + (\nabla_{\mathsf{x}} v_s)^2 + (\nabla_{\mathsf{x}} v_a)^2\right] - \frac{1}{8}(v_a^2 + v_s^2)(\nabla_{\mathsf{x}}\phi_a)^2 \\ &+ \frac{\alpha}{4}\hat{\Phi}(\mathsf{x})\left[-v_s^2(1-\cos\phi_a) + v_a^2(1+\cos\phi_a) + 2u_a^2\cos\phi_a\right] + \frac{\beta}{2}\left[(v_s^2 + v_a^2)\right],\end{aligned} \tag{C.10}$$

where the parametrization $\beta = 2|d|/\rho q_m^2$ has been used in the last line, which is slightly modified from that in the main text (where $\beta = 2d/\rho q_m^2$). The corresponding Lagrangian then leads to the following linear wave equations:

$$\begin{aligned}&\partial_t^2 u_s = v^2 q_m^2 \nabla_{\mathsf{x}}^2 u_s, \quad \partial_t^2 u_a = v^2 q_m^2\left[\nabla_{\mathsf{x}}^2 u_a - \alpha\hat{\Phi}(\mathsf{x})\cos\phi_a u_a\right], \\ &\partial_t^2 v_s = v^2 q_m^2[\nabla_{\mathsf{x}}^2 v_s + \frac{1}{4}v_s(\nabla_{\mathsf{x}}\phi_a)^2 + \frac{\alpha}{2}\hat{\Phi}(\mathsf{x})(1-\cos\phi_a)v_s - \beta v_s], \\ &\partial_t^2 v_a = v^2 q_m^2[\nabla_{\mathsf{x}}^2 v_a + \frac{1}{4}v_a(\nabla_{\mathsf{x}}\phi_a)^2 - \frac{\alpha}{2}\hat{\Phi}(\mathsf{x})(1+\cos\phi_a)v_s - \beta v_a].\end{aligned} \tag{C.11}$$

All the four branches decouple and almost reduce to the the isotropic form as in the main text, up to the constant shift of β in the v-branches. With the Bloch ansatz, the above equations become

$$\begin{aligned}&\omega^2\hat{u}_s = -v^2 q_m^2\left[(\nabla_{\mathsf{x}} + i\mathsf{k})^2\hat{u}_s\right], \\ &\omega^2\hat{u}_a = -v^2 q_m^2\left[(\nabla_{\mathsf{x}} + i\mathsf{k})^2\hat{u}_a - \alpha\hat{\Phi}(\mathsf{x})\cos\phi_a\hat{u}_a\right], \\ &\omega^2\hat{v}_s = -v^2 q_m^2[(\nabla_{\mathsf{x}} + i\mathsf{k})^2\hat{v}_s + \frac{1}{4}\hat{v}_s(\nabla_{\mathsf{x}}\phi_a)^2 + \frac{\alpha}{2}\hat{\Phi}(\mathsf{x})(1-\cos\phi_a)\hat{v}_s - \beta\hat{v}_s], \\ &\omega^2\hat{v}_a = -v^2 q_m^2[(\nabla_{\mathsf{x}} + i\mathsf{k})^2\hat{v}_a + \frac{1}{4}\hat{v}_a(\nabla_{\mathsf{x}}\phi_a)^2 - \frac{\alpha}{2}\hat{\Phi}(\mathsf{x})(1+\cos\phi_a)\hat{v}_a - \beta\hat{v}_a].\end{aligned} \tag{C.12}$$

There is one Goldstone mode in the $\hat{u}_s$ branch, corresponding to the rotation in the XY plane. As α increases, we will again observe the flattening of u_a and v_s bands. We plot an example in the twisted phase in the figure C.3 below.

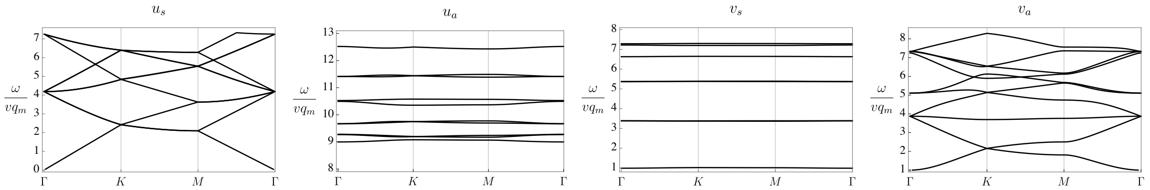

Figure C.3: The ten lowest magnon bands for the four branches at $\alpha = 9$, $\beta = 1$ in the XY-anisotropy case.

C.2 General perturbative solution of the Euler Lagrange equations

We will encounter the following energy functional and the subsequent partial differential equation in different situations in this work and thus we will first present a general study here. One needs to minimize an energy density functional of the following form:

$$\mathsf{H}_{\text{cl}} = \frac{1}{2}\left|\boldsymbol{\nabla}_{\mathsf{x}}\phi\right|^2 - \alpha\left(\xi(\mathsf{x}) + \xi_0\right)\cos\phi. \tag{C.13}$$

$\xi(\mathsf{x})$ is a periodic function defining a triangular lattice, and it has zero mean

$$\int_{\text{unit cell}} d^2\mathsf{x}\,\xi(\mathsf{x}) = 0,$$

over one unit cell. One can write a Fourier expansion for $\xi(\mathsf{x})$ in terms of the reciprocal lattice vectors $\hat{\boldsymbol{q}}$ of the above traingular lattice:

$$\xi(\mathsf{x}) = \sum_{\hat{\boldsymbol{q}}\neq 0} \xi_{\hat{\boldsymbol{q}}}\, e^{i\hat{\boldsymbol{q}}\cdot\mathsf{x}}, \tag{C.14}$$

We will be seeking solutions for ϕ that minimize the energy functional above and are periodic with the same period as that given by $\xi(\mathsf{x})$. There is always a trivial solution $\phi = 0$, with an average energy per unit cell equal to $-\xi_0\alpha$. Here we present a perturbative calculation of a nontrivial solution when α and ξ_0 are small; these two parameters are taken to be small with their ratio $\frac{\xi_0}{\alpha}$ kept a constant.

In order to find the function ϕ that minimizes the above energy functional, we will use the following Euler-Lagrange equation:

$$\nabla_{\mathsf{x}}^2 \phi = \alpha \left(\xi(\mathsf{x}) + \xi_0 \right) \sin \phi, \tag{C.15}$$

which should be solved with periodic boundary conditions. Since we are interested in the specific limit of both α and ξ_0 being small, while keeping their ratio $\delta = \frac{\xi_0}{\alpha}$ a constant, we will add a bookkeeping parameter ε to keep track of orders in our perturbation; we will ultimately set $\varepsilon = 1$. The equation thus takes the form:

$$\nabla_{\mathsf{x}}^2 \phi = \varepsilon \; \alpha \left(\xi(\mathsf{x}) + \varepsilon \xi_0 \right) \sin \phi. \tag{C.16}$$

We will find a nontrivial solution as a power series in ε:

$$\phi = \phi^{(0)} + \varepsilon \, \phi^{(1)} + \varepsilon^2 \, \phi^{(2)} + \dots \tag{C.17}$$

To zeroth order in ε, one needs ϕ to be a constant, this constant will be determined in higher orders:

$$\phi^{(0)} = \text{const.}. \tag{C.18}$$

To first order in ε, the differential equation takes the form:

$$O(\varepsilon): \qquad \sum_{\hat{\boldsymbol{q}} \neq 0} \left(-\left|\hat{\boldsymbol{q}}\right|^2 \right) \phi^{(1)}_{\hat{\boldsymbol{q}}} e^{i \hat{\boldsymbol{q}} \cdot \mathsf{x}} = \alpha \sin \phi^{(0)} \sum_{\hat{\boldsymbol{q}} \neq 0} \xi_{\hat{\boldsymbol{q}}} e^{i \hat{\boldsymbol{q}} \cdot \mathsf{x}}. \tag{C.19}$$

It could be satisfied if $\phi^{(1)}$ takes the form:

$$\phi^{(1)} = -\alpha \sin \phi^{(0)} \left(\sum_{\hat{\boldsymbol{q}} \neq 0} \frac{1}{|\hat{\boldsymbol{q}}|^2} \, \xi_{\hat{\boldsymbol{q}}} \; e^{i \hat{\boldsymbol{q}} \cdot \mathsf{x}} \right) \; + \; \phi^{(1)[\hat{\boldsymbol{q}}=0]}, \tag{C.20}$$

where $\phi^{(1)[\hat{\boldsymbol{q}}=0]}$ denotes a constant needed in the first order solution, this constant should also be fixed using higher orders of the equation. The second order in ε of the differential equation now reads:

$$O(\varepsilon^2): \qquad \sum_{\hat{\boldsymbol{q}} \neq 0} \left(- |\hat{\boldsymbol{q}}|^2 \right) \phi^{(2)}_{\hat{\boldsymbol{q}}} e^{i \hat{\boldsymbol{q}} \cdot \mathsf{x}} = \alpha \cos \phi^{(0)} \left(\sum_{\hat{\boldsymbol{q}}_1, \hat{\boldsymbol{q}}_2 \neq 0} \xi_{\hat{\boldsymbol{q}}_1} \phi^{(1)}_{\hat{\boldsymbol{q}}_2} \; e^{i (\hat{\boldsymbol{q}}_1 + \hat{\boldsymbol{q}}_2) \cdot \mathsf{x}} \right) + \alpha \xi_0 \sin \phi^{(0)}. \tag{C.21}$$

The left hand side of the above equation does not contain a $\hat{\boldsymbol{q}} = 0$ component while the right hand side does:

$$-\alpha^2 \cos \phi^{(0)} \sin \phi^{(0)} \sum_{\hat{\boldsymbol{q}} \neq 0} \frac{1}{|\hat{\boldsymbol{q}}|^2} \; |\xi_{\hat{\boldsymbol{q}}}|^2 + \alpha \xi_0 \sin \phi^{(0)}. \tag{C.22}$$

This needs to vanish so that the second order differential equation holds, and this fixes the value of $\phi^{(0)}$:

$$\cos \phi^{(0)} = \frac{\xi_0}{\alpha} \frac{1}{\sum \frac{1}{|\hat{\boldsymbol{q}}|^2} \; |\xi_{\hat{\boldsymbol{q}}}|^2} = \delta \; \frac{1}{\sum \frac{1}{|\hat{\boldsymbol{q}}|^2} \; |\xi_{\hat{\boldsymbol{q}}}|^2}. \tag{C.23}$$

This result shows that for values of δ smaller than $\sum \frac{1}{|\hat{\boldsymbol{q}}|^2} \; |\xi_{\hat{\boldsymbol{q}}}|^2$, a nontrivial solution could exist. Furthermore, the second order part of ϕ could be found also using (C.21):

$$\begin{aligned} \phi^{(2)} = {} & \alpha^2 \sin \phi^{(0)} \cos \phi^{(0)} \left(\sum_{\hat{\boldsymbol{q}}_1 \neq -\hat{\boldsymbol{q}}_2} \xi_{\hat{\boldsymbol{q}}_1} \xi_{\hat{\boldsymbol{q}}_2} \frac{e^{i (\hat{\boldsymbol{q}}_1 + \hat{\boldsymbol{q}}_2) \cdot \mathsf{x}}}{|\hat{\boldsymbol{q}}_1|^2 \; |\hat{\boldsymbol{q}}_1 + \hat{\boldsymbol{q}}_2|^2} \right) \\ & - \alpha \cos \phi^{(0)} \left(\sum_{\hat{\boldsymbol{q}} \neq 0} \frac{1}{|\hat{\boldsymbol{q}}|^2} \, \xi_{\hat{\boldsymbol{q}}} \; e^{i \hat{\boldsymbol{q}} \cdot \mathsf{x}} \right) \; \phi^{(1)[\hat{\boldsymbol{q}}=0]} \; + \; \phi^{(2)[\hat{\boldsymbol{q}}=0]}, \end{aligned} \tag{C.24}$$

with the constant $\phi^{(2)[\hat{\boldsymbol{q}}=0]}$ determined again by higher orders of the differential equation.

This procedure can be carried out order by order, we will just state the result for $\phi^{(1)[\hat{\boldsymbol{q}}=0]}$, which could be derived from the $\hat{\boldsymbol{q}} = 0$ component of the ε^3 order of the differential equation:

$$\phi^{(1)[\hat{\boldsymbol{q}}=0]} = \frac{\alpha}{2} \, \frac{\left(1 - 3\cos^2\phi^{(0)}\right)}{\sin\phi^{(0)}} \frac{\sum_{\hat{\boldsymbol{q}}_1,\hat{\boldsymbol{q}}_3,\hat{\boldsymbol{q}}_3} \frac{1}{|\hat{\boldsymbol{q}}_1|^2\,|\hat{\boldsymbol{q}}_2|^2} \, \xi_{\hat{\boldsymbol{q}}_1}\xi_{\hat{\boldsymbol{q}}_2}\xi_{\hat{\boldsymbol{q}}_3} \, \delta_{\hat{\boldsymbol{q}}_1+\hat{\boldsymbol{q}}_2+\hat{\boldsymbol{q}}_3,0}}{\sum_{\hat{\boldsymbol{q}}} \frac{1}{|\hat{\boldsymbol{q}}|^2} \left|\xi_{\hat{\boldsymbol{q}}}\right|^2}. \tag{C.25}$$

Also, the average energy density per unit cell can be found to be:

$$\overline{\mathsf{H}_{\text{cl}}} = -\frac{\alpha^2}{2}\left(\sum_{\hat{\boldsymbol{q}}\neq 0} \frac{1}{|\hat{\boldsymbol{q}}|^2} \left|\xi_{\hat{\boldsymbol{q}}}\right|^2\right)\left(1 + \cos^2\phi^{(0)}\right) + O\left(\alpha^3\right), \tag{C.26}$$

where $O\left(\alpha^3\right)$ denotes any cubic power of α and ξ_0. This should be compared with the trivial solution energy density, i.e. $-\xi_0\alpha$; the twisted solution, when it exists, has lower energy to this order and thus it is the true ground state for $\delta < \sum \frac{1}{|\hat{\boldsymbol{q}}|^2} \left|\xi_{\hat{\boldsymbol{q}}}\right|^2$. At $\delta = \sum \frac{1}{|\hat{\boldsymbol{q}}|^2} \left|\xi_{\hat{\boldsymbol{q}}}\right|^2$, interestingly, the two solutions coincide and thus this transition is continuous.

Finally we would like to emphasize that the above perturbative expansion works when both α and ξ_0 are small with their ratio $\delta = \frac{\xi_0}{\alpha}$ kept constant; δ could be small or order one but the perturbation breaks down for large δ. Below, we will elaborate on the three cases that the above perturbative calculation has been used in this work.

C.3 Twisted antiferromagnets

One should consider solving the following Euler-Lagrange equations for a twisted antiferromagnet as discussed in the main text:

$$\nabla^2_{\mathsf{x}}\phi_s = \beta\cos\phi_a \sin\phi_s, \tag{C.27}$$

$$\nabla^2_{\mathsf{x}}\phi_a = \Big(\beta\cos\phi_s + \alpha\hat{\Phi}(\mathsf{x})\Big)\sin\phi_a, \tag{C.28}$$

with $\hat{\Phi}(\mathsf{x}) = \sum_{a=1}^{3}\cos(\hat{\boldsymbol{q}}_a \cdot \mathsf{x})$ and $|\hat{\boldsymbol{q}}_a| = 1$. One can find a nontrivial twisted solution (which we call twisted-s in the main text) by setting $\phi_s = 0$ or π; it will be shown below that the $\phi_s = \pi$ solution has lower energy. Starting from the twsited-s solution, increasing β at small α results in a transtion to the collinear phase, while on the other hand for large α, with increasing β, one encounters a transition to the twisted-a phase. We will discuss these two cases separately below.

C.3.1 Transtion from the twisted-s phase to the collinear phase, large angles

At large angles, both α and β are small and we will treat the Euler-Lagrange equations perturbatively. With choosing $\beta = 0$ or π, the equations read:

$$\nabla^2_{\mathsf{x}}\phi_a = \alpha\left(\hat{\Phi}(\mathsf{x}) \pm \alpha\,\delta\right)\sin\phi_a, \tag{C.29}$$

where $+$ corresponds to $\phi_s = 0$ and $-$ corresponds to $\phi_s = \pi$, and we will be considering the limit where the ratio $\delta = \frac{\beta}{\alpha^2}$ is kept constant, so that we can use the perturbation series developed above; $\hat{\Phi}(\mathsf{x})$ plays the role of $\xi(\mathsf{x})$, and $\alpha\ \delta$ plays the role of ξ_0. The ϕ_a solution can be found order by order as discussed above:

$$\phi_a = \cos^{-1}\left(\pm\frac{2}{3}\delta\right) - \alpha \sin\phi^{(0)}\left(\hat{\Phi}(\mathsf{x}) - \left[\frac{1}{2} - \cot^2\phi^{(0)}\right]\right) + O(\alpha^2, \beta). \qquad \text{(C.30)}$$

The energy density can also be calculated which leads to:

$$\overline{\mathsf{H}_{\text{cl}}} = -\frac{3}{4}\alpha^2\left(1 + \frac{4}{9}\delta^2\right) \quad \pm\frac{1}{6}\alpha^3\delta\left(1 + 4\delta^2\right) \quad + O\left(\alpha^4\right). \qquad \text{(C.31)}$$

This result is kept to one higher order than the previous section; it is this higher order which shows that $\phi_s = \pi$ is preferred energetically and so the $-$ sign should be chosen throughout.

Also, it is worthwhile to note that the limit of $\delta \to 0$, corresponds to $\cos\phi_a^{(0)} = 0$, which simply means that $\boldsymbol{N}_1 \cdot \boldsymbol{N}_2 = 0$ to lowest order in α.

C.3.2 Transition from twisted-s phase to the twisted-a phase, small angles

At small angles, where α is large but β is kept still small, one can take the configuration of ϕ_a to be completely determined by satisfying the $-\alpha\hat{\Phi}(\mathsf{x})\cos\phi_a$ term in the Hamiltonian: $\cos\phi_a$ can be taken equal to sign $\left[\hat{\Phi}(\mathsf{x})\right]$. This forms domains of constant ϕ_a, with narrow domain walls between them. On the other hand, ϕ_s should be found using the Euler-Lagrange equations, which reduce to:

$$\nabla_{\mathsf{x}}^2\phi_s = \beta\cos\phi_a \sin\phi_s. \qquad \text{(C.32)}$$

For small β, we can use the perturbation theory developed above, with β, and $\cos\phi_a = \text{sign}\left[\hat{\Phi}(\mathsf{x})\right]$ (remember that ϕ_a is not dynamical in the above equation) playing the roles of α, and $\xi(\mathsf{x})+\xi_0$ respectively in (C.15). One can see that a twisted solution with $\cos\phi_s^{(0)} = \frac{\xi_0}{\sum\frac{1}{|\hat{\boldsymbol{q}}|^2}\left|\xi_{\hat{\boldsymbol{q}}}\right|^2}\frac{1}{\beta}$ exists, if β is large enough. It is found numerically that

$$\xi_0 = \frac{1}{A_{\text{u.c.}}}\int_{\text{unit cell}} \text{sign}\left[\hat{\Phi}(\mathsf{x})\right] = -0.21,$$

which means that domains with antiferromagnetic interlayer exchange have larger area than those with ferromagnetic interlayer coupling. Furthermore, one can also find numerically that

$$\sum\frac{1}{|\hat{\boldsymbol{q}}|^2}\left|\xi_{\hat{\boldsymbol{q}}}\right|^2 = 0.71.$$

These two values show that a twisted solution for ϕ_s could appear if $\beta > 0.29$; this should correpsond to the β value for which the transition between twisted-s and twisted-a phases occurs at large α, and it is indeed very close, with a few percent error actually, to the value found numerically at large α in the phase diagram presented in the main text.

C.4 Twisted ferromagnetic CrI_3 bilayer

For the properties of the interlayer exchange parameter in a bilayer CrI_3 system, we will be following the numerical results presented in Ref. [112], where first-principles calculations are carried out: it is shown that the interlayer exchange can vary considerably if the bilayer stacking is altered, and in fact it can change its sign; the pristine CrI_3 bilayer exhibits antiferromagnetic interlayer exchange, but the above statement implies that this can be modified if the stacking is varied. Remarkably in a twisted bilayer, the displacement between the layers is modulated periodically with a unit cell given by the moiré length and so all the different kinds of displaced bilayer stacking are realized. With this in mind, one can use the energy functional discussed in the main text

$$\mathcal{H}_{\rm cl} = \sum_{l} \left[\frac{\rho}{2}\left(\nabla \boldsymbol{M}_l\right)^2 - d\left(N_l^z\right)^2\right] - J'\,\Phi\left(\boldsymbol{u}_1(\boldsymbol{x}) - \boldsymbol{u}_2(\boldsymbol{x})\right)\boldsymbol{M}_1 \cdot \boldsymbol{M}_2, \tag{C.33}$$

where, as discussed in the main text, the stacking dependence of interlayer exchange, i.e. the function $\Phi(\boldsymbol{u}_1 - \boldsymbol{u}_2)$, could be extracted from some first principle calculations, for example those carried out in Ref. [112].

We have used the plots presented in Ref. [112], to find the Fourier components of the interlayer exchange which is indeed a periodic function of the interlayer displacement. It turns out that unlike the antiferromagnetic case initially studied in the main text, i.e. $\Phi(\boldsymbol{x}) = \sum_{a=1}^{3} \cos(\boldsymbol{q}_a \cdot \boldsymbol{x})$, the present $\Phi\left(\boldsymbol{u}_1(\boldsymbol{x}) - \boldsymbol{u}_2(\boldsymbol{x})\right)$ function needs several harmonics along with a constant term to be reproduced (see Fig. C.4). We will ultimately work with a rescaled Hamiltonian that has a form that is identical to that in the antiferromagnetic case:

$$\mathsf{H}_{\rm cl} = \frac{1}{2}\left(|\boldsymbol{\nabla}_{\mathsf{x}}\phi_s|^2 + |\boldsymbol{\nabla}_{\mathsf{x}}\phi_a|^2\right) - \left(\alpha\hat{\Phi}(\mathsf{x}) + \beta\cos\phi_{\mathsf{s}}\right)\cos\phi_{\mathsf{a}}. \tag{C.34}$$

α and β are defined as before and $\hat{\Phi}(\mathsf{x}) = \hat{\Phi}_0 + \sum_{\hat{\boldsymbol{q}} \neq 0} \hat{\Phi}_{\hat{\boldsymbol{q}}}\, e^{i\hat{\boldsymbol{q}}\cdot\mathsf{x}}$, where $\hat{\boldsymbol{q}}$'s are the rescaled

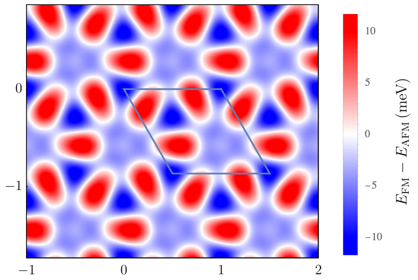

Figure C.4: A reproduced plot of interlayer exchange energy per unit cell of bilayer CrI$_3$ as a function of the displacement between the two layers. The data is extracted from figures in Ref. [112]. The two axes show displacement in the two directions in the units of a real space unit cell length; the interlayer exchange is indeed a periodic function. The blue and red regions show ferromagnetic and antiferromagnetc interlayer exchange.

moiré reciprocal lattice vectors. We have kept the lowest five harmonics along with the constant term here. Furthermore, $\hat{\Phi}$ is normalized in a way that $\sum_{\hat{\boldsymbol{q}}\neq 0} \frac{1}{|\hat{\boldsymbol{q}}|^2} \left|\hat{\Phi}_{\hat{\boldsymbol{q}}}\right|^2 = 1$. Variation of this energy functional leads to the same set of equations

$$\nabla^2_{\mathsf{x}}\phi_s = \beta \cos\phi_a \sin\phi_s, \tag{C.35}$$

$$\nabla^2_{\mathsf{x}}\phi_a = \left(\beta\cos\phi_s + \alpha\hat{\Phi}(\mathsf{x})\right)\sin\phi_a, \tag{C.36}$$

which should be solved to minimize the energy here also. We will only discuss the case of a positive infinitesimal β here, the case of general positive β should be similar to the antiferromagnetic case. The effect of a positive infinitesimal β is to fix a value for ϕ_s, and in this case it turns out that $\phi_s = 0$ is energetically favored; this will be justified below.

The only functionality that needs to be determined now is that of ϕ_a, and the only parameter is α; this time $\hat{\Phi}(\mathsf{x})$ has a nonzero constant term $\hat{\Phi}_0$ as well, and thus at small α the ϕ_a configuration is totally controlled by this constant term; we have derived $\hat{\Phi}_0 = 0.026 > 0$ which means that this constant imposes ferromagetic interlayer exchange, and thus the solution at small α turns out to be $\phi_a = 0$, with an energy density $\overline{\mathsf{H}_{\rm cl}} = -\alpha\hat{\Phi}_0$. One expects this trivial state to give way to a twisted solution with lower energy at some value of α; since $\hat{\Phi}_0$ is small itself, the transition to a twisted phase happens at a small α and thus one can set up a perturbative calculation for the twisted solution of ϕ_a at small α; this perburbative calculation, which is discussed in Sec. C.2 of the SM, yields

$$\phi_a = \phi_a^{(0)} + \alpha \left(-\sin\phi_a^{(0)} \sum_{\hat{\boldsymbol{q}}\neq 0} \frac{\hat{\Phi}_{\hat{\boldsymbol{q}}}}{|\hat{\boldsymbol{q}}|^2} e^{i\hat{\boldsymbol{q}}\cdot\mathsf{x}} + \phi_a^{(1)[\hat{\boldsymbol{q}}=0]} \right) + O(\alpha^2, \alpha\,\hat{\Phi}_0), \tag{C.37}$$

with $\cos\phi_a^{(0)} = \frac{1}{\alpha}\hat{\Phi}_0$. This means that the twisted solution exists for α above $\alpha_0 = \hat{\Phi}_0 = 0.026$ to leading order. The energy density for this state turns out to be $\overline{\mathsf{H}_{\rm cl}} = -\frac{1}{2}\left(\alpha^2 + \hat{\Phi}_0^2\right)$ to leading order; this shows that indeed a continuous transition to the twisted phase happens at $\alpha = \alpha_0$.

For very large values of α similar to what happens in the twisted antiferromagnets discussed in the main text, the twisted solution implies that ϕ_a is either 0 or π almost everywhere, so that $\cos\phi_a = \text{sign}[\hat{\Phi}(\mathsf{x})]$ except for narrow domain wall regions where $\hat{\Phi}(\mathsf{x}) = 0$.

Here we can see why $\phi_s = 0$ is chosen for an infinitesimal positive β in two different limits: at small α, the constant term $\hat{\Phi}_0$ is ferromagnetic and thus the energy will decrease by setting $\phi_s = 0$; for large α on the other hand, since one is in the extreme twisted phase, one should note that the area with ferromagnetic interlayer coupling is larger than that with antiferromagnetic coupling, or in other words

$$\frac{1}{A_{\text{u.c.}}}\int_{\text{unit cell}} \text{sign}\left[\hat{\Phi}(\mathsf{x})\right] > 0,$$

and thus $\phi_s = 0$ is again energetically favored. It is worthwhile to mention that this is a coincidence in CrI_3, that both small and large α limits prefer interlayer ferromagnetism; this could well not be the case in other materials in which cases it is reasonable to expect a transition at intermediate α from $\phi_s = 0$ to $\phi_s = \pi$.

Appendix D

Appendix for Chapter 5

D.1 Details on weak-coupling analysis

We describe a complete weak-coupling analysis in this section. Using a polar parametrization for the magnetization vector $\boldsymbol{M} = (\sin\theta\cos\phi, \sin\theta\sin\phi, \cos\theta)$, the Hamiltonian density takes the form:

$$\begin{aligned}\mathcal{H} =& \frac{1}{2}\left(\nabla\theta\right)^2 + \frac{1}{2}\sin^2\theta\ \left(\nabla\phi\right)^2 + \alpha\cos\theta\,\Phi(\boldsymbol{x}) \\ &\qquad + 2\,\beta\ \cos\theta\left[\cos\theta\left(\sin\phi\,\partial_x\theta - \cos\phi\,\partial_y\theta\right) + \sin\theta\left(\cos\phi\,\partial_x\phi + \sin\phi\,\partial_y\phi\right)\right],\end{aligned} \tag{D.1}$$

where $\Phi(\boldsymbol{x}) = \sum_\alpha \sin(\hat{\boldsymbol{d}}_\alpha \cdot \boldsymbol{x})$, and $\boldsymbol{x} = (x, y)$. The Euler-Lagrange equations read:

$$\begin{aligned}&\nabla^2\theta - \sin\theta\cos\theta\left(\nabla\phi\right)^2 + \alpha\sin\theta\,\Phi(\boldsymbol{x}) + 2\,\beta\sin^2\theta\left(\cos\phi\,\partial_x\phi + \sin\phi\,\partial_y\phi\right) = 0, \\ &\sin\theta\ \nabla^2\phi + 2\cos\theta\left(\nabla\phi\cdot\nabla\theta\right) - 2\,\beta\sin\theta\left(\cos\phi\,\partial_x\theta + \sin\phi\,\partial_y\theta\right) = 0.\end{aligned} \tag{D.2}$$

First, we seek a commensurate solution for θ and ϕ; the perturbation expansion to lowest orders in β and α read:

$$\begin{aligned}
\theta &= \frac{\pi}{2} + \alpha\,\Phi(\boldsymbol{x}) + O(\alpha^3) \\
&\qquad + 4\beta^2\alpha\left[\cos^2\phi^{(0)}\,\partial_x^2\Phi(\boldsymbol{x}) + 2\sin\phi^{(0)}\cos\phi^{(0)}\,\partial_x\partial_y\Phi(\boldsymbol{x}) + \sin^2\phi^{(0)}\,\partial_y^2\Phi(\boldsymbol{x})\right] + \ldots, \\
\phi &= \phi^{(0)} - 2\beta\alpha\left(\cos\phi^{(0)}\partial_x\Phi(\boldsymbol{x}) + \sin\phi^{(0)}\partial_y\Phi(\boldsymbol{x})\right) + \ldots\ .
\end{aligned} \tag{D.3}$$

The energy per unit cell taking the solutions up to this order into account reads:

$$\begin{aligned}
\mathcal{E} = &-\frac{3}{4}\alpha^2 + \ldots \\
&- 2\beta^2\alpha^2\sum_a\left(\hat{\boldsymbol{m}}_\parallel^{(0)}.\hat{\boldsymbol{d}}_a\right)^2 + \ldots,
\end{aligned} \tag{D.4}$$

where $\hat{\boldsymbol{m}}_\parallel$ is a unit vector in the direction of the in-plane component of the magnetization vector $\boldsymbol{M}$. The $\ldots$ on the first row stands for terms higher order in α and zeroth order in β, while the $\ldots$ on the second row represents higher orders in both α and β. The above form can be further simplified using $\sum_a\left(\hat{\boldsymbol{m}}_\parallel^{(0)}\cdot\hat{\boldsymbol{d}}_a\right)^2 = \frac{3}{2}$, this means that to this order there is no preferred direction for $\hat{\boldsymbol{m}}_\parallel^{(0)}$ or equivalently that $\phi^{(0)}$ is not determined to this order. We expect higher order corrections to break this rotational symmetry and give $\phi^{(0)}$ the three preferred values (that are C_3 equivalent) we found numerically.

Now we turn to a perturbative study of incommensurate configurations close to the commensurate-incommensurate transition line. Such configurations can show slow variations of the magnetization over a large *incommensurate length scale* on top of the fluctuations on the moiré scale. Additionally, one can see that the above form for the average energy per unit cell (D.4) contains no linear-in-β contribution; however such a linear term can arise in an incommensurate configuration where the angle θ acquires some accumulated winding over a long length. In the following, we will study this contribution and how it can lead to the commensurate-incommensurate transition.

In this limit, the following approximation is made: we take the incommensurate configuration to look locally like a commensurate one for which we found the perturbative solution above. In the above solution, the mean value of θ in moiré unit cells has to take the value $\pi/2$ in order for the energy to be minimized. However, in order to allow for large scale variations in θ, we let its mean value to change slowly as one moves in the moiré lattice; this will bring in some energy penalty due to the fact that in some unit cells the mean value of θ is different from its preferred value. The requirement for this energy penalty to be compensated by the linear-in-β term (arising from large-scale variations of θ also) allows us to find the point where the commensurate-incommensurate transition occurs.

To this end, we modify the above solution to accommodate an arbitrary mean for θ in each unit cell. This can be done by adding a Lagrange multiplier term to the Hamiltonian that is minimized. To zeroth order in β, $\phi = \text{const.} + O(\beta)$, and thus an equation of the form $\nabla^2\theta + \alpha \sin\theta\, \hat{\Phi}(x) = \lambda$ is obtained. λ is the Lagrange multiplier and is found order by order to ensure that $\bar{\theta}$ is the mean of θ to all orders. Solving with a definite $\bar{\theta}$:

$$\theta(\boldsymbol{x}) = \bar{\theta} + \alpha \sin\bar{\theta}\, \Phi(\boldsymbol{x}). \tag{D.5}$$

The energy per moiré unit cell is derived using the Hamiltonian density given by

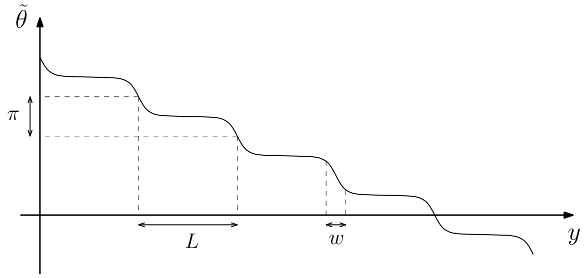

Figure D.1: A possible configuration for the variable $\tilde{\theta} = \pi/2 - \bar{\theta}$ in the incommensurate phase close to the CI transition, where $\bar{\theta}$ is the local mean value of the θ angle in unit cells. An incommensurate configuration consists of large regions with $\bar{\theta}$ close to $\frac{\pi}{2}$ which minimizes the energy in a commensurate configuration, however these regions are separated by narrow discommensurations (or solitons) where $\bar{\theta}$ varies by π. The width of the discommensurations is shown by w and their relative distance with L. As one gets closer to the transition line L diverges. This plot is inspired by a figure in Ref. [28].

$\frac{1}{2}\left(\nabla\theta\right)^2 + \alpha\cos\theta\,\Phi(\boldsymbol{x})$:

$$\mathcal{E} = -\frac{3}{4}\alpha^2\sin^2\bar{\theta}. \tag{D.6}$$

$\bar{\theta} = \pi/2$ minimizes this energy density and thus we expect that in the twisted solution fluctuations of θ happen around $\bar{\theta} = \pi/2$ as shown in (D.3).

Now one can let $\bar{\theta}$ to fluctuate slowly from a unit cell to another one that has an appreciable distance, such fluctuations will be controlled by an effective Hamiltonian of the form $\mathcal{H}^{\text{eff}}_{\text{kin+pot}} = \frac{1}{2}\left(\nabla\bar{\theta}\right)^2 - \frac{3}{4}\alpha^2\sin^2\bar{\theta}$, where the gradient is discretized and $\bar{\theta}$ takes values in moiré unit cells and varies slowly with position. One also needs to add the effect of the DM interaction, to first order in β, the Hamiltonian density reads $\mathcal{H}^{\text{eff}}_{\text{DM}} = 2\beta\cos^2\bar{\theta}(\sin\phi\,\partial_x\bar{\theta} - \cos\phi\,\partial_y\bar{\theta})$, where we have used the fact that ϕ is a constant to zeroth order in β. Any choice of ϕ determines a preferred direction for $\bar{\theta}$ variations. For example $\phi = 0$ corresponds to having variations of $\bar{\theta}$ in the y direction only. To this order in perturbation theory, there is no preferred direction for the incommensurate wavevector. Proceeding with this choice of ϕ, an effective one-dimensional Hamiltonian, taking all the above points into account, can be achieved:

$$\mathcal{H}^{\text{eff}} = \frac{1}{2}\left(\partial_y \bar{\theta}\right)^2 - \frac{3}{4}\alpha^2 \sin^2 \bar{\theta} - \beta\, \partial_y \bar{\theta}, \tag{D.7}$$

the Hamiltonian is defined on a dicretized lattice but we use a continuum limit approximation, which is most justified in the simultaneous limits of small α and β and large incommensurate periodicity. With a transformation $\tilde{\theta} = \pi/2 - \bar{\theta}$, the potential term in the effective Hamiltonian takes a positive definite form and one arrives at $\mathcal{H}^{\text{eff}} = \frac{1}{2}\left(\partial_y \tilde{\theta}\right)^2 + \frac{3}{4}\alpha^2 \sin^2 \tilde{\theta} + \beta\, \partial_y \tilde{\theta}$. Such Hamiltonians and their commensurate-incommensurate transitions are studied extensively in Ref. [28]. In particular, it is shown that a profile like the one shown in Fig. D.1 is expected for the variable $\tilde{\theta}$ in the incommensurate phase; the transition happens at a β value equal to $\beta_c = \frac{\sqrt{6}}{\pi}\alpha$, and above this β value, creation of the solitons shown in Fig. D.1 becomes energetically favored; in fact their relative distance is also found to have a form like $L = \frac{2}{\sqrt{3}\alpha} \log\left(\alpha^2 \frac{1}{\beta - \beta_c}\right)$. Notice that in reality, the value of L is bounded by the sample size from above, and the transition will happen at a larger $\beta > \beta_c$.

A plot of an incommensurate solution with a dominant β term is presented in Fig. D.2, where the numerical simulation is initialized with a spiral configuration assuming $\alpha = 0$, and the effect of the moiré potential with $\alpha \neq 0$ is implemented in the numerical minimization of the energy, which will result in intracell modulations of the spiral configuration. The period of the incommenurate solution is taken to be given only in terms of β, i.e. having the value $2\pi/\beta$; one expects the period to also have corrections due to the nonzero value of α, but since α is chosen to be small, we expect

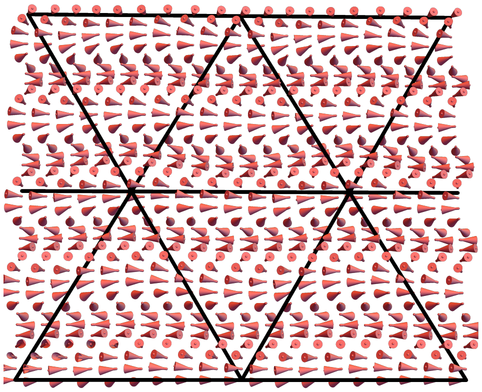

Figure D.2: The incommensurate relaxed spiral configuration at $\alpha = 0.3$ and $\beta = 2.2$ with incommensurate periodicity of $4\pi/\beta$ in the y-direction. To make explicit the incommensuration, we draw the moiré triangular lattices in black lines for comparison.

this correction to be perturbative and also expect the general properties of the solution to be unaltered. Such solution is far from the transition line between commensurate and incommensurate solutions, and thus not resembling the perturbative solution of the incommensurate phase as discussed above. However, notice that both of these solutions lie on the incommensurate side of the transition line.

One can approach the transition line by considering relaxed spirals in larger systems, and also letting their period vary. In figure D.3, we provide a comparison between the theoretically predicted CI transition line of $\beta_c = \frac{\sqrt{6}}{\pi}\alpha$ and the numerically found transition lines at various sample sizes. As the system size increases, for small enough α (but not too small, see below), the numerical line approaches the theoretical prediction which is based on infinite sample size and found perturbatively for small α and β. Note that for very small α, the numerically found β values for the transition show a saturation which is due to the finite size of the numerics. Furthermore, the saturation value decreases as the sample size increases.

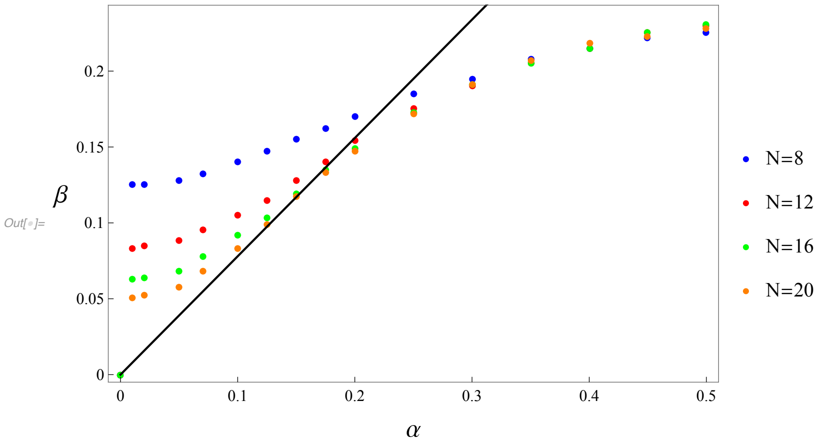

Figure D.3: Comparison between the theoretically predicted and the numerically found CI transition lines. The numerical results are based on periodic boundary conditions with N moire unit cells. The system is chosen to consist of 2 unit cells in one direction, and as a result $N/2$ unit cells in the other direction. The solution in each case accommodates only a winding equal to 1 in the larger direction of the system. As the system size increases from $N = 8$ moiré unit cells to 20 moiré unit cells, the numerical result approach the theoretical prediction. The numerical lines deviate from theory at larger values of α and β because the effects of higher-order terms begin kicking in in that region. The deviations at near the origin result from the fact that at tiny β, the relaxed spirals have huge periodicity, while the sample size is kept finite.

D.2 Details on numerics

In this section, we give more details on the Landau-Lifshitz-Gilbert simulation and the numerical phase diagram presented in figure 4. In the LLG equations $\frac{d\boldsymbol{M}}{dt} = -g\boldsymbol{M} \times \boldsymbol{B}^{\text{eff}} + \eta \boldsymbol{M} \times \frac{d\boldsymbol{M}}{dt}$, can be rewritten as

$$\frac{d\boldsymbol{M}}{dt} = -\frac{g}{1+\eta^2}\boldsymbol{M} \times \boldsymbol{B} - \frac{\eta g}{1+\eta^2}\boldsymbol{M} \times (\boldsymbol{M} \times \boldsymbol{B}).$$

For faster convergence, we ignore the torque term $\boldsymbol{M} \times \boldsymbol{B}$ and the simulation evolves towards the equilibrium along a steepest descent path. Our boundary conditions include commensurate periodic boundary conditions $\boldsymbol{M}(x, y) = \boldsymbol{M}(x + L_x, y) = \boldsymbol{M}(x, y + L_y)$ with several different choices of (L_x, L_y): such that the sample consists of 2×2, 2×1 and 1×1 moiré unit cells in the orthogonal basis $\tilde{\boldsymbol{a}}_1 = (4\pi/\sqrt{3}, 0)$, $\tilde{\boldsymbol{a}}_2 = (0, 4\pi)$ respectively (or 2×4, 2×2 and 1×2 unit cells in the non-orthogonal basis defined in figure 1). Since we are mainly interested in the configurations commensurate with the moiré potential, a large number of moiré unit cells is not necessary. In general, the states with larger sample sizes typically have higher averaged energy densities because of minor breakings of the moiré translation symmetries $\boldsymbol{M}(\boldsymbol{x}) = \boldsymbol{M}(\boldsymbol{x} + \boldsymbol{a}_1) = \boldsymbol{M}(\boldsymbol{x} + \boldsymbol{a}_2)$ allowed by the boundary conditions of larger periods.

The initial conditions we take are the following:

(1) Uniform magnetization in the $\hat{\boldsymbol{x}}$-direction, $\boldsymbol{M}(\boldsymbol{x}) = \hat{\boldsymbol{x}}$.

(2) Uniform magnetization in the $\hat{\boldsymbol{z}}$-direction, $\boldsymbol{M}(\boldsymbol{x}) = \hat{\boldsymbol{z}}$. The uniform configurations are ground states when there is no DM interaction or moiré potential, i.e., $\alpha = 0 = \beta$.

(3) Twisted configuration along the $\pm\hat{\boldsymbol{z}}$ directions, $\boldsymbol{M}(\boldsymbol{x}) = -\text{sign}[\Phi(\boldsymbol{x})]$, where $\Phi(\boldsymbol{x})$ is the moiré potential. This state has the lowest energy when $\beta = 0$ and α is finite.

(4) Spiral configuration propagating along the $\hat{\boldsymbol{y}}$-direction, $\boldsymbol{M}(\boldsymbol{x}) = \sin(\beta y)\hat{\boldsymbol{x}} + \cos(\beta y)\hat{\boldsymbol{z}}$, which is the ground state when $\alpha = 0$ and $\beta > 0$.

(5) The skyrmion lattice configuration with the scale characterized by β. It is generated from summation of three spirals propagating in three different directions.

(6) The commensurate twisted state which breaks the $SO(2)$ symmetry down to C_3, with the vertex configuration of the type (b)(c)(d) in figure 2. The configuration pattern is the same as that in figure 3 (left).

(7) The commensurate stripy Ising state with the vertex configuration (e)(f) in figure 2. The configuration pattern is the same as that in figure 3 (right).

(8) The commensurate moiré skyrmion lattice with the vertex configuration (e)(f) in figure 2. The configuration pattern is the same as that in figure 3 (middle).

The LLG equations are then solved with *OOMMF* using the *ubermag* framework. The maximal step size is $L_i/200$ in the two directions away from the phase boundaries and $L_i/300$ near the phase boundaries. After the final configurations are obtained, we compute the corresponding skyrmion numbers and averaged energy densities and plot the phase diagram. The phase diagram is generated using 668 data points with more points distributed near the phase boundaries. Figure D.4 shows the distribution of parameters that we choose.

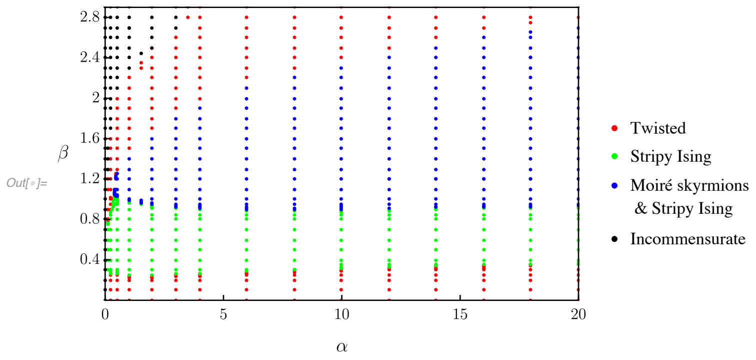

Figure D.4: The set of all parameters we choose for the phase diagram.

Below we show the energy (density) differences between the twisted state and the

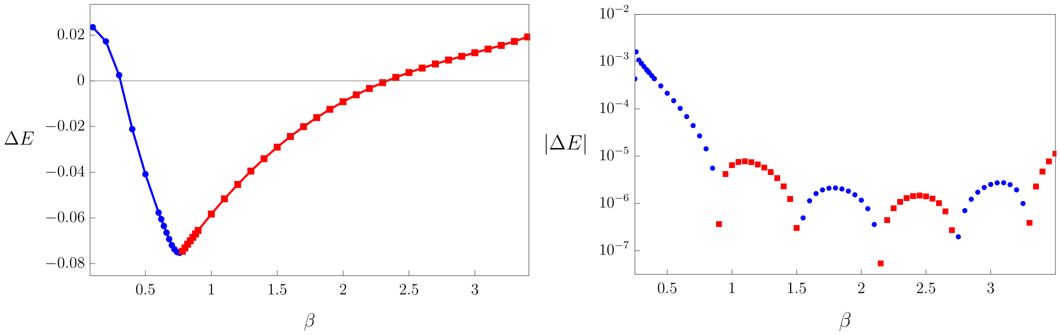

Figure D.5: Energy density differences of the commensurate phases at $\alpha = 10$ and various β. Left: $E_{\text{stripy}} - E_{\text{twisted}}$. The blue dots correspond to the twisted-0 solution at lower β, while the red dots correspond to the twisted-1 solution at higher β. Right: $|E_{\text{skyrmion}} - E_{\text{stripy}}|$. Red/blue dots correspond to the cases where E_{skyrmion} is larger/smaller than E_{stripy}, respectively. We view the two states as degenerate when the magnitude of the energy density difference between the two states is smaller than 10^{-5}. At smaller β, the stripy Ising state is preferred, while at larger β they become degenerate.

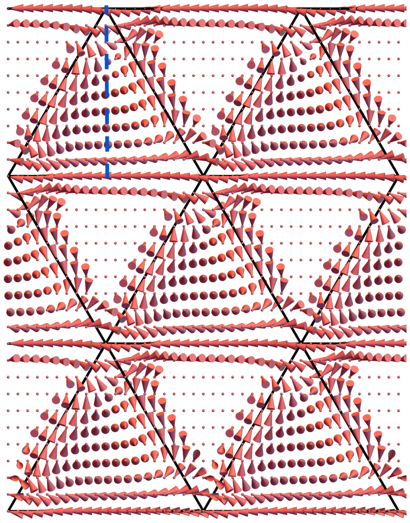

Figure D.6: The twisted-0 solution at the strong coupling ($\alpha = 10, \beta = 0.6$), it harbors a trivial configuration at all its vertices. The fact that all the vertices are trivial makes the winding number along the high symmetry line specified with the dashed line vanish. This is in contrast with the twisted-1 phase where the corresponding winding number is 1.

stripy Ising state, and between the stripy Ising state and the moiré skyrmion state, respectively. The phase transitions are thus clearly first-order.

Finally, we comment on the incommensurate configurations. In the top left region of the phase diagram of large β and small α, the configuration with the lowest energy (generated from the initial conditions listed above) is that of the relaxed spiral configuration. The rigid spiral configuration was described in the main text above the "weak-coupling analysis" section, with magnetization vectors rotating in one plane as the spiral propagates. The relaxed spiral configuration is roughly the same as the rigid spiral configuration, but with small modifications due to the moiré potential. The fact that such relaxed spiral configuration has lower energy than the other commensurate configurations, means that the effect of β is dominant over that of α. Therefore, potentially there could be other configurations with different periodicities that are incommensurate with the moiré potential and have even lower energies. This periodicity is expected to change smoothly with α and β. Since numerically one can only implement boundary conditions with a finite set of different periodicities, the lowest-energy configuration obtained from these boundary conditions is likely not the true ground state of the system. In particular, the region occupied by the incommensurate phases is underestimated. We thus focus only on the commensurate phases in the main phase diagram that are more predictable. We also perform a numerical analysis in the weak-coupling regime with large sample size and the results show a nice match with the theoretical prediction, see section D.1 of this supplemental material for details.

D.3 Symmetries of the commensurate solutions

In this section, we discuss the symmetries of the three different commensurate solutions discussed in the main text. The fact that they possess different symmetries means that they belong to different phases. We focus on strong coupling realizations below for clarity:

- **Twisted phases:** The twisted-0 and the twisted-1 phases have the same symmetries. Consider for example a twisted-1 solution with e.g. the 3-state clock vertex configuration named as (b) in the main text Fig. 1 (center). Suppose such configuration is realized at all of the vertices, its symmetries include: translation symmetries of the moiré triangular lattice $T_{\boldsymbol{a}_1}$, $T_{\boldsymbol{a}_2}$ (the basis vectors are also shown in Fig. 1 (left)), reflection symmetry with respect to the $y = 0$ line, i.e. a simultaneous action of $y \to -y$ and $M_z \to -M_z$.

- **Skyrmions phase:** Symmetries of this phase include again the transnational ones $T_{\boldsymbol{a}_1}$, $T_{\boldsymbol{a}_2}$, and there is an additional C_3 rotation symmetry.

- **Stripy Ising phase:** The symmetries are: $T_{\boldsymbol{a}_1}$, $T_{2\boldsymbol{a}_2}$, and a simultaneous action of $y \to -y$, $M_z \to -M_z$, $\boldsymbol{x} \to \boldsymbol{x} + \boldsymbol{a}_2$.

In addition, for all these commensurate phases, there is another reflection symmetry tied to the topological invariance of the winding number along the $x = 0$ line, that comprises a simultaneous action of $(x, y, z) \to (-x, y, z)$ and $(M_x, M_y, M_z) \to (M_x, -M_y, M_z)$; this symmetry dictates that the magnetization should lie in the $x - z$

plane on the $x = 0$ line.

D.4 The type of the Dzyaloshinskii-Moriya interaction

We have considered Bloch-type DM interaction in this work and utilized a term as $\boldsymbol{M} \cdot (\nabla \times \boldsymbol{M})$ in the continuum Hamiltonian. However, we argue in this section that if the DM interaction is of Néel-type, our analysis and results stay valid; in particular, should we use a form like $\boldsymbol{M} \cdot [\nabla \times (\hat{\boldsymbol{z}} \times \boldsymbol{M})]$ in the Hamiltonian, which represents a Néel type DM interaction, it is straightforward to see that solutions could be obtained by rotating those discussed in the main text by 90° around the $\hat{\boldsymbol{z}}$ axis. In other words, if a solution for the Bloch-type DM interaction is represented by $\boldsymbol{M}(\boldsymbol{r})$, a solution for the Néel-type DM interaction can be constructed by $\hat{\boldsymbol{z}} \times \boldsymbol{M}(\boldsymbol{r})$.

Appendix E

Appendix for Chapter 6

E.1 Efficient evaluation of wavelet basis

Here we elaborate how the basis elements can be evaluated on dyadic rational points; we start with the scaling equation for the scaling function $\phi(x)$, i.e. Eq. (6.1). If we consider all integer values of x for which $\phi(x)$ is nonzero in (6.1), we get $2K-2$ equations and $2K-2$ variables, i.e. $\phi(x)$ for integer values of x (because $\phi(x)$ is only nonzero for integer values that lie within the support of $\phi(x)$). As a result of this, one can take the right hand side of Eq. (6.1), as a matrix relation and the whole equation as an eigenvalue equation, such as follows:

$$\Phi = A\,\Phi, \tag{E.1}$$

where

$$\Phi = \begin{bmatrix} \phi(1) \\ \phi(2) \\ \vdots \\ \phi(2K-2) \end{bmatrix}, \tag{E.2}$$

is an eigenvector of the matrix A with eigenvalue 1 and A is defined as $A_{nm} = 2a_{2n-m}$ so that (6.1) and (E.3) are equivalent. This, as a result, gives a way to evaluate $\phi(x)$ for integer values of x; one just needs to find the eigenvector in Eq. (E.3) with eigenvalue 1.

Then, using equation Eq. (6.1) and having $\phi(x)$ for integer x values, it is straightforward to calculate $\phi(x)$ recursively for dyadic points $\frac{m}{2^r}$, starting with $r = 1$ and terminating at some positive integer r that is large enough.

In order to calculate derivatives, we note that taking a derivative of both sides of Eq. (6.1) and considering integer x values, results in the matrix equation:

$$\Phi' = 2A\,\Phi', \tag{E.3}$$

with

$$\Phi' = \begin{bmatrix} \phi'(1) \\ \phi'(2) \\ \vdots \\ \phi'(2K-2) \end{bmatrix}. \tag{E.4}$$

This means that in order to find the derivative of ϕ at integer points the same eigenvalue problem as before should be solved; however, this time the eigenvector with the eigenvalue $\frac{1}{2}$ corresponds to the vector of the first derivative at integer points. It is simple at this point to calculate the derivative an dyadic points such as $\frac{m}{2^r}$ recursively.

In general if for some Daubechies wavelet basis (specified by its order K), the nth derivative of the scaling function exists, the matrix A has an eigenvalue $\frac{1}{2^n}$; its corresponding eigenvector can be used to evaluate the nth derivative of the scaling function at dyadic points.

Having the scaling function evaluated at dyadic points, the mother wavelet function and its derivatives can also be evaluated at dyadic points using Eq. (6.7).

E.2 Benchmarking the DMRG

In this appendix, we discuss how the DMRG approach is benchmarked. For benchmarking, we do not use the fine graining circuit discussed in the main text. We use the Gaudin-Yang model, a model of 1 dimensional fermions with a δ function interaction which is exactly solvable by means of a nested Bethe ansatz[136, 43, 44]; the Hamiltonian of the model is given by $H = \sum_i \frac{p_i^2}{2} + c\sum_{i<j} \delta\left(x_i - x_j\right)$. There is one dimensionless parameter in the many body problem that is $\gamma = \frac{c}{n}$, where n is the fermion density. We focus on the thermodynamic limit exact solution of the *attractive* model here, which is discussed below. The ground state of the attractive Gaudin-Yang model is described effectively as a Luther-Emery liquid[80] where BCS-like pairs are formed and the spin sector is gapped.

In the thermodynamic limit, the Bethe ansatz equations can be written as integral equations to be solved self-consistently. We focus on the attractive model here, where the ground state equations exhibit a simple form. According to the theorem by Lieb and Mattis, the ground state belongs to the total spin 0 sector[73]; the ground state can be viewed as a collection of bound pairs of fermions with opposite spins. The integral equations that need to be satisfied read:

$$\begin{aligned} \pi\ \rho(k) &= 1 + \int_{-Q}^{+Q} \frac{dq}{n}\ \frac{\gamma\ \rho(q)}{\gamma^2 + \left(\frac{k-q}{n}\right)^2}, \\ \frac{E_0}{N} &= n^2 \left[-\frac{\gamma^2}{8} + 2 \int_{-Q}^{+Q} \frac{dq}{n}\ \rho(q)\ \left(\frac{q^2}{2n^2}\right) \right], \end{aligned} \tag{E.5}$$

and the cutoff wavenumber Q is defined through $\int_{-Q}^{+Q} \frac{dq}{n} \rho(q) = \frac{1}{2}$ [41]. In the above equations $\rho(k)$ is an auxiliary function that needs to be found self-consistently, γ is the dimensionless interaction stregth, n is the density, N is the total particle number, and E_0 is the ground state energy. These equations are solved iteratively numerically and their solution is compared with the wavelet DMRG solution.

We perform DMRG to find the ground state of δ-function interacting fermions in a box with length $L = 5$ with a high binding potential $V_b = 1000$ beyond its limits. A plot of the ground state spin up/down density of a system with a total number of 12 particles for an attractive and a repulsive interaction is shown in Fig. E.1 (top left). A quantitative comparison with the exact solution is also carried out by calculating the quantity $\delta E = \frac{1}{2}\left(E_{N=12} - E_{N=10}\right)$, which shows the energy difference between a system with 12 particles and a system with 10 particles in the numerics and comparing it with the similar quantity in the exact solution [1]. A plot of this quantity is show in Fig. E.1 (right); note that the thermodynamic limit result is recovered by an order 10 total number of particles. Furthermore, as is expected, a higher resolution basis is

---

[1] Since the density of the system with 12 particles is different from that with 10 particles, the interaction parameter c is also modified to keep the dimensionless parameter γ constant.

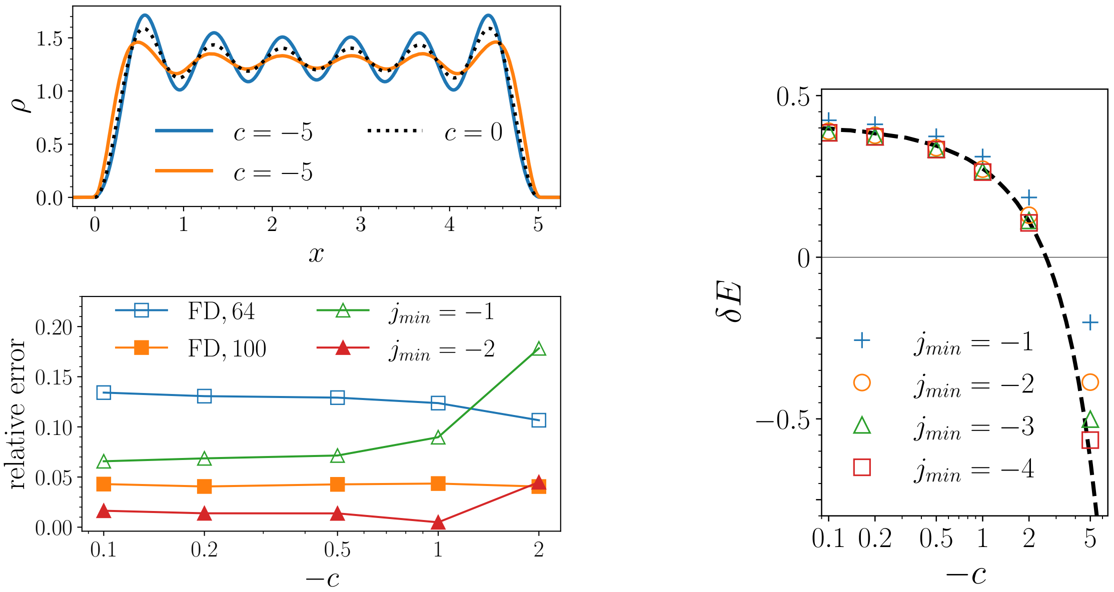

Figure E.1: The solution of the Gaudin Yang model. Top left: up/down spin density of the ground state for repulsive ($j_0 = -2, j_{min} = -3$) and attractive ($j_0 = -3, j_{min} = -4$) interactions. Right: the quantity δE defined in the main text and computed for the attractive Gaudin-Yang model; the exact result is shown with the dashed line. For every resolution, $j_0 = j_{min} + 1$ is used except for $j_{min=-4}$, were $j_0 = -4$ is used. Bottom left: the relative error defined as $\frac{(\delta E_{\text{wavelet/FD}} - \delta E_{\text{exact}})}{\delta E_{\text{exact},U_0=0}}$ is plotted for two different wavelets and two different FD resolutions. The effective lattice sizes for the two wavelet calculations with $j_{min} = -1$ and $j_{min} = -2$ are $M = 44$ and $M = 64$ respectively. All the solutions showed convergence with bond dimension equal to 100.

needed for more accurate results with stronger attractive interactions.

DMRG has also been performed for the same problem using a finite differences (FD) lattice basis (see the SM for details of the FD calculations). The same quantity δE introduced above is calculated with this approach. For a comparison between the wavelet and FD approaches, the quantity $\frac{(\delta E_{\text{wavelet/FD}} - \delta E_{\text{exact}})}{\delta E_{\text{exact},U_0=0}}$ is calculated as a measure of relative error and plotted in Fig. E.1 (left). It could be seen in the plot that the wavelets basis works better than the FD one even with smaller numbers of lattice points. We have also observed that for stronger attractive interaction the FD basis works better than the wavelets; the reason is the maximal locality of the FD basis that allows bound pairs to occupy the same spatial position and thus decrease the energy to a large extent.

E.3 Details of the Givens circuit

In this appendix, we present details of the Givens rotations circuit that was discussed in the main text. We will be following the notation and approach in [64] in presenting the general derivations.

First, we would like to find out what the effect of acting with the operator

$$U(u) = \exp\left[\sum_{ab} \log(u)_{ba}\ c_b^\dagger c_a\right] \tag{E.6}$$

on a state given by $\prod_i c_i^\dagger |0\rangle$ is. u is a real unitary matrix in our case. To this end, we define the operator $\kappa = \sum_{ab} \log(u)_{ba}\ c_b^\dagger c_a$ and note that the following relation holds:

$$\begin{aligned} U(u)\, c_i^\dagger\, U(u) &= e^{\kappa}\, c_i^\dagger\, e^{-\kappa} \\ &= c_i^\dagger + \left[\kappa, c_i^\dagger\right] + \frac{1}{2}\left[\kappa, \left[\kappa, c_i^\dagger\right]\right] + \dots\ . \end{aligned} \tag{E.7}$$

The nested commutator of κ and $c_i^\dagger$ with n commutators can be shown to satisfy:

$$\sum_b \left[\log(u)^n\right]_{bi} c_b^\dagger, \tag{E.8}$$

where $\log(u)^n$ represents the n matrix power of the matrix $\log(u)$. Taking all values of n into account, it is now obvious that:

$$U(u)\, c_i^\dagger\, U(u) = \sum_b u_{bi}\, c_b^\dagger. \tag{E.9}$$

This means that acting with the operator $U(u)$ has the effect of performing the above basis transformation which is what we were after in the main text.

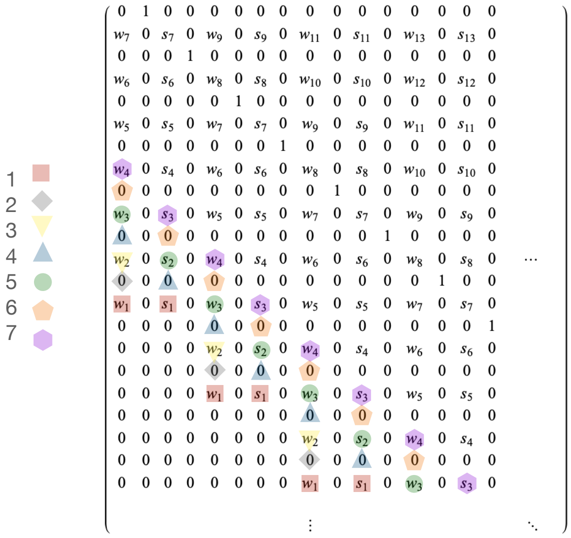

Figure E.2: A schematic view of a spinless $\tilde{u}$ matrix as defined in the main text, its elements are schematically shown as s_i and w_i. The order in which Givens rotations should be implemented is shown. This order ensures that the whole Givens circuit is shallow.

The above relation also shows that the operator U defines a homomorphism:

$$U(u_1)\,U(u_2) = U(u_1\ u_2). \tag{E.10}$$

As a result of this, a Givens rotation $r_pq(\theta)$, shown in Eq. (6.24) can act on a generic matrix u and change the operator U in the following way:

$$R_{pq}(\theta)U(u) = U(r_{pq(\theta)}u), \tag{E.11}$$

with R_{pq} defined in Eq. (6.22). We act with a series of Givens rotations as in Eq.(6.25) on our u matrix of interest to obtain a upper triangular matrix; since our u of interest is real and unitary, the identity matrix results. This means that we can reproduce $U(u)$ as shown in Eq. (6.23)

We now turn to our own case of interest, i.e. finding the Givens rotations for constructing the fine graining circuit. We consider the spinless case below. The spinful case is very similar. As discussed in the main text, we form a nonunitary matrix $\tilde{u}$ and find the set of required Givens rotations to make it upper triangular. Following the prescription discussed in the main text, the form that the matrix $\tilde{u}$ takes is schematically shown in Fig. E.2. The sequence in which the elements are made to vanish are also shown in the same figure. It is used that once two adjacent elements in a column are zero a Givens rotation does not alter the matrix.

One can check that in all steps, except possibly the first few, there are elements that need to be zeroed but have a zero right above them. Such a situation requires a Givens rotation by the angle $\pi/2$. Interestingly, the $\pi/2$ Givens rotations are required in an alternating order for wavelet and scaling functions of order $j+1$ (the solution from the previous step). The circuit shown in Fig. 6.3 is obtained in this way. Rotation angles that are not equal to $\pi/2$ are determined at each step based on the elements of the column in consideration.

Bibliography

[1] A. Agazzi, J.-P. Eckmann, and G. M. Graf. The colored hofstadter butterfly for the honeycomb lattice. *Journal of Statistical Physics*, 156(3):417–426, Aug 2014.

[2] Junyeong Ahn, Sungjoon Park, and Bohm-Jung Yang. Failure of nielsen-ninomiya theorem and fragile topology in two-dimensional systems with space-time inversion symmetry: application to twisted bilayer graphene at magic angle. *Physical Review X*, 9(2):021013, 2019.

[3] Monika Aidelsburger. *Square Lattice with Magnetic Field*, pages 9–26. Springer International Publishing, Cham, 2016.

[4] Muhammad Akram and Onur Erten. Skyrmions in twisted van der waals magnets. *Physical Review B*, 103(14):L140406, 2021.

[5] Yahya Alavirad and Jay Sau. Ferromagnetism and its stability from the one-magnon spectrum in twisted bilayer graphene. *Physical Review B*, 102(23):235123, 2020.

[6] A Alexandradinata and Leonid Glazman. Semiclassical theory of landau levels and magnetic breakdown in topological metals. *Physical Review B*, 97(14):144422, 2018.

[7] Per Bak. Commensurate phases, incommensurate phases and the devil's staircase. *Reports on Progress in Physics*, 45(6):587, 1982.

[8] Leon Balents. General continuum model for twisted bilayer graphene and arbitrary smooth deformations. *SciPost Phys.*, 7:48, 2019.

[9] Jens H Bardarson, J Tworzydło, PW Brouwer, and CWJ Beenakker. One-parameter scaling at the dirac point in graphene. *Physical review letters*, 99(10):106801, 2007.

[10] Federico Becca and Sandro Sorella. *Quantum Monte Carlo approaches for correlated systems*. Cambridge University Press, 2017.

[11] M. Beg, R. A. Pepper, and H. Fangohr. User interfaces for computational science: A domain specific language for oommf embedded in python. *AIP Advances*, 7(5):56025, 2017.

[12] M Beg, R A Pepper, T Kluyver, J Mulkers, J Leliaert, and H Fangohr. Ubermag: Meta package for ubermag project. *DOI: 10.5281/zenodo.3539496*, 2021.

[13] Aroop K Behera, Sugata Chowdhury, and Suprem R Das. Magnetic skyrmions in atomic thin $\mathrm{CrI_3}$ monolayer. *Applied Physics Letters*, 114(23):232402, 2019.

[14] R Bistritzer and AH MacDonald. Moiré butterflies in twisted bilayer graphene. *Physical Review B*, 84(3):035440, 2011.

[15] Rafi Bistritzer and Allan H MacDonald. Moiré bands in twisted double-layer graphene. *Proceedings of the National Academy of Sciences*, 108(30):12233–12237, 2011.

[16] A Bogdanov and A Hubert. Thermodynamically stable magnetic vortex states in magnetic crystals. *Journal of magnetism and magnetic materials*, 138(3):255–269, 1994.

[17] Alexei N Bogdanov and DA Yablonskii. Thermodynamically stable "vortices" in magnetically ordered crystals. the mixed state of magnets. *Zh. Eksp. Teor. Fiz*, 95(1):178, 1989.

[18] R. Brec. Review on structural and chemical properties of transition metal phosphorous trisulfides mps3. *Solid State Ionics*, 22(3), 1986.

[19] Christian Brouder, Gianluca Panati, Matteo Calandra, Christophe Mourougane, and Nicola Marzari. Exponential localization of wannier functions in insulators. *Physical review letters*, 98(4):046402, 2007.

[20] Nick Bultinck, Shubhayu Chatterjee, and Michael P Zaletel. Anomalous hall ferromagnetism in twisted bilayer graphene. *arXiv preprint arXiv:1901.08110*, 2019.

[21] Nick Bultinck, Eslam Khalaf, Shang Liu, Shubhayu Chatterjee, Ashvin Vishwanath, and Michael P. Zaletel. Ground state and hidden symmetry of magic angle graphene at even integer filling, 2019.

[22] Kenneth S. Burch, Daivd Mandrus, and Je-Geun Park. Magnetism in two-dimensional van der waals materials. *Nature*, 563:47–52, 2018.

[23] Kenneth S Burch, David Mandrus, and Je-Geun Park. Magnetism in two-dimensional van der Waals materials. *Nature*, 563(7729):47–52, 2018.

[24] Y Cao, JY Luo, V Fatemi, S Fang, JD Sanchez-Yamagishi, K Watanabe, T Taniguchi, E Kaxiras, and P Jarillo-Herrero. Superlattice-induced insulating states and valley-protected orbits in twisted bilayer graphene. *Physical review letters*, 117(11):116804, 2016.

[25] Yuan Cao, Valla Fatemi, Ahmet Demir, Shiang Fang, Spencer L Tomarken, Jason Y Luo, Javier D Sanchez-Yamagishi, Kenji Watanabe, Takashi Taniguchi, Efthimios Kaxiras, et al. Correlated insulator behaviour at half-filling in magic-angle graphene superlattices. *Nature*, 556(7699):80, 2018.

[26] Yuan Cao, Valla Fatemi, Shiang Fang, Kenji Watanabe, Takashi Taniguchi, Efthimios Kaxiras, and Pablo Jarillo-Herrero. Unconventional superconductivity in magic-angle graphene superlattices. *Nature*, 556(7699):43, 2018.

[27] Yuan Cao, Daniel Rodan-Legrain, Oriol Rubies-Bigordà, Jeong Min Park, Kenji Watanabe, Takashi Taniguchi, and Pablo Jarillo-Herrero. Electric field tunable correlated states and magnetic phase transitions in twisted bilayer-bilayer graphene. *arXiv preprint arXiv:1903.08596*, 2019.

[28] Paul M Chaikin and Tom C Lubensky. *Principles of condensed matter physics*. Cambridge university press, Cambridge, 1995.

[29] Ming-Che Chang and Qian Niu. Berry phase, hyperorbits, and the hofstadter spectrum: Semiclassical dynamics in magnetic bloch bands. *Physical Review B*, 53(11):7010, 1996.

[30] Guorui Chen, Aaron L Sharpe, Patrick Gallagher, Ilan T Rosen, Eli Fox, Lili Jiang, Bosai Lyu, Hongyuan Li, Kenji Watanabe, Takashi Taniguchi, et al. Signatures of gate-tunable superconductivity in trilayer graphene/boron nitride moir\'e superlattice. *arXiv preprint arXiv:1901.04621*, 2019.

[31] Lebing Chen, Jae-Ho Chung, Bin Gao, Tong Chen, Matthew B Stone, Alexander I Kolesnikov, Qingzhen Huang, and Pengcheng Dai. Topological spin excitations in honeycomb ferromagnet cri3. *Physical Review X*, 8(4):041028, 2018.

[32] Ingrid Daubechies. *Ten lectures on wavelets*. SIAM, 1992.

[33] Bei Ding, Zefang Li, Guizhou Xu, Hang Li, Zhipeng Hou, Enke Liu, Xuekui Xi, Feng Xu, Yuan Yao, and Wenhong Wang. Observation of magnetic skyrmion bubbles in a van der Waals ferromagnet Fe_3GeTe_2. *Nano Letters*, 20(2):868–873, 2019.

[34] John F Dodaro, Steven A Kivelson, Yoni Schattner, Xiao-Qi Sun, and Chao Wang. Phases of a phenomenological model of twisted bilayer graphene. *Physical Review B*, 98(7):075154, 2018.

[35] Michele Dolfi, Bela Bauer, Matthias Troyer, and Zoran Ristivojevic. Multigrid algorithms for tensor network states. *Physical review letters*, 109(2):020604, 2012.

[36] M. J. Donahue and D. G. Porter. *OOMMF User's Guide, Version 1.0*. National Institute of Standards and Technology, Gaithersburg, MD, 1999.

[37] JMB Lopes Dos Santos, NMR Peres, and AH Castro Neto. Graphene bilayer with a twist: electronic structure. *Physical review letters*, 99(25):256802, 2007.

[38] Igor Dzyaloshinsky. A thermodynamic theory of "weak" ferromagnetism of antiferromagnetics. *Journal of Physics and Chemistry of Solids*, 4(4):241–255, 1958.

[39] Glen Evenbly and Steven R White. Entanglement renormalization and wavelets. *Physical review letters*, 116(14):140403, 2016.

[40] Matthew Fishman, Steven R. White, and E. Miles Stoudenmire. The ITensor software library for tensor network calculations, 2020.

[41] JN Fuchs, A Recati, and W Zwerger. Exactly solvable model of the bcs-bec crossover. *Physical review letters*, 93(9):090408, 2004.

[42] Takahiro Fukui, Yasuhiro Hatsugai, and Hiroshi Suzuki. Chern numbers in discretized brillouin zone: Efficient method of computing (spin) hall conductances. *Journal of the Physical Society of Japan*, 74(6):1674–1677, 2005.

[43] M Gaudin. Un systeme a une dimension de fermions en interaction. *Physics Letters A*, 24(1):55–56, 1967.

[44] Michel Gaudin. *The Bethe Wavefunction*. Cambridge University Press, 2014.

[45] Thomas L Gilbert. A phenomenological theory of damping in ferromagnetic materials. *IEEE transactions on magnetics*, 40(6):3443–3449, 2004.

[46] Reza Haghshenas, Zhi-Hao Cui, and Garnet Kin-Lic Chan. Numerical continuum tensor networks in two dimensions. *Physical Review Research*, 3(2):023057, 2021.

[47] Jung Hoon Han, Jiadong Zang, Zhihua Yang, Jin-Hong Park, and Naoto Nagaosa. Skyrmion lattice in a two-dimensional chiral magnet. *Physical Review B*, 82(9):094429, 2010.

[48] Yasuhiro Hatsugai, Takahiro Fukui, and Hideo Aoki. Topological analysis of the quantum hall effect in graphene: Dirac-fermi transition across van hove singularities and edge versus bulk quantum numbers. *Physical review B*, 74(20):205414, 2006.

[49] Kasra Hejazi and Bela Bauer. Many-body physics in the continuum using wavelets. Manuscript in prepration.

[50] Kasra Hejazi, Xiao Chen, and Leon Balents. Hybrid wannier chern bands in magic angle twisted bilayer graphene and the quantized anomalous hall effect. *Physical Review Research*, 3(1):013242, 2021.

[51] Kasra Hejazi, Chunxiao Liu, and Leon Balents. Landau levels in twisted bilayer graphene and semiclassical orbits. *Physical Review B*, 100(3):035115, 2019.

[52] Kasra Hejazi, Chunxiao Liu, Hassan Shapourian, Xiao Chen, and Leon Balents. Multiple topological transitions in twisted bilayer graphene near the first magic angle. *Physical Review B*, 99(3):035111, 2019.

[53] Kasra Hejazi, Zhu-Xi Luo, and Leon Balents. Noncollinear phases in moiré magnets. *Proceedings of the National Academy of Sciences*, 117(20):10721–10726, 2020.

[54] Kasra Hejazi, Zhu-Xi Luo, and Leon Balents. Heterobilayer moiré magnets: Moiré skyrmions and commensurate-incommensurate transitions. *Physical Review B*, 104(10):L100406, 2021.

[55] Bevin Huang, Genevieve Clark, Dahlia R Klein, David MacNeill, Efrén Navarro-Moratalla, Kyle L Seyler, Nathan Wilson, Michael A McGuire, David H Cobden, Di Xiao, et al. Electrical control of 2d magnetism in bilayer cri3. *Nature nanotechnology*, 13(7):544, 2018.

[56] Bevin Huang, Genevieve Clark, Efrén Navarro-Moratalla, Dahlia R. Klein, Ran Cheng, Kyle L. Seyler, Ding Zhong, Emma Schmidgall, Michael A. McGuire, David H. Cobden, Wang Yao, Di Xiao, Jarillo-Herrero Pablo, and Xiaodong Xu. Layer-dependent ferromagnetism in a van der waals crystal down to the monolayer limit. *Nature*, 546:270–273, 2017.

[57] Hiroki Isobe, Noah FQ Yuan, and Liang Fu. Unconventional superconductivity and density waves in twisted bilayer graphene. *Physical Review X*, 8(4):041041, 2018.

[58] Peiheng Jiang, Cong Wang, Dachuan Chen, Zhicheng Zhong, Zhe Yuan, Zhong-Yi Lu, and Wei Ji. Stacking tunable interlayer magnetism in bilayer cri3. *Physical Review B*, 99(14):144401, 2019.

[59] P A Joy and S Vasudevan. Magnetism in the layered transition-metal thiophosphates MPS_3 (M= Mn, Fe, and Ni). *Physical Review B*, 46(9):5425, 1992.

[60] Jian Kang and Oskar Vafek. Symmetry, maximally localized wannier states, and a low-energy model for twisted bilayer graphene narrow bands. *Physical Review X*, 8(3):031088, 2018.

[61] Jian Kang and Oskar Vafek. Non-abelian dirac node braiding and near-degeneracy of correlated phases at odd integer filling in magic angle twisted bilayer graphene. *arXiv preprint arXiv:2002.10360*, 2020.

[62] Y Kasahara, T Ohnishi, Y Mizukami, O Tanaka, Sixiao Ma, K Sugii, N Kurita, H Tanaka, J Nasu, Y Motome, et al. Majorana quantization and half-integer thermal quantum hall effect in a kitaev spin liquid. *Nature*, 559(7713):227–231, 2018.

[63] BM Kessler, GL Payne, and WN Polyzou. Wavelet notes. *arXiv preprint nucl-th/0305025*, 2003.

[64] Ian D Kivlichan, Jarrod McClean, Nathan Wiebe, Craig Gidney, Alán Aspuru-Guzik, Garnet Kin-Lic Chan, and Ryan Babbush. Quantum simulation of electronic structure with linear depth and connectivity. *Physical review letters*, 120(11):110501, 2018.

[65] Mikito Koshino, Noah FQ Yuan, Takashi Koretsune, Masayuki Ochi, Kazuhiko Kuroki, and Liang Fu. Maximally localized wannier orbitals and the extended hubbard model for twisted bilayer graphene. *Physical Review X*, 8(3):031087, 2018.

[66] K. Kurosawa, S. Saito, and Y. Yamaguchi. Neutron diffraction study on mnps3 and feps3. *J. Phys. Soc. Jpn.*, 52:3919, 1983.

[67] Ko Kurosawa, Shozo Saito, and Yasuo Yamaguchi. Neutron diffraction study on $MnPS_3$ and $FePS_3$. *Journal of the Physical Society of Japan*, 52(11):3919–3926, 1983.

[68] Lev Davidovich Landau and E Lifshitz. On the theory of the dispersion of magnetic permeability in ferromagnetic bodies. *Phys. Z. Sowjet.*, 8:153, 1935.

[69] G. Le Flem, R. Brec, G. Ouvard, A. Louisy, and P. Segransan. Magnetic interactions in the layer compounds mpx3 (m=mn, fe, ni; x=s, se). *J. Phys. Chem. Solids*, 43:455, 1982.

[70] You-Quan Li, Ye-Hua Liu, and Yi Zhou. General spin-order theory via gauge Landau-Lifshitz equation. *Physical Review B*, 84(20):205123, 2011.

[71] Biao Lian, Zhijun Wang, and B. Andrei Bernevig. Twisted Bilayer Graphene: A Phonon Driven Superconductor. *arXiv e-prints*, page arXiv:1807.04382, Jul 2018.

[72] Biao Lian, Fang Xie, and B Andrei Bernevig. The landau level of fragile topology. *arXiv preprint arXiv:1811.11786*, 2018.

[73] Elliott Lieb and Daniel Mattis. Theory of ferromagnetism and the ordering of electronic energy levels. *Physical Review*, 125(1):164, 1962.

[74] Wenbin Lin, Narayan Kovvali, and Lawrence Carin. Direct algorithm for computation of derivatives of the daubechies basis functions. *Applied mathematics and computation*, 170(2):1006–1013, 2005.

[75] Jianpeng Liu and Xi Dai. Correlated insulating states and the quantum anomalous hall phenomena at all integer fillings in twisted bilayer graphene. *arXiv preprint arXiv:1911.03760*, 2019.

[76] Jianpeng Liu, Junwei Liu, and Xi Dai. Pseudo landau level representation of twisted bilayer graphene: Band topology and implications on the correlated insulating phase. *Physical Review B*, 99(15):155415, 2019.

[77] Shang Liu, Eslam Khalaf, Jong Yeon Lee, and Ashvin Vishwanath. Nematic topological semimetal and insulator in magic angle bilayer graphene at charge neutrality, 2019.

[78] Xiaomeng Liu, Zeyu Hao, Eslam Khalaf, Jong Yeon Lee, Kenji Watanabe, Takashi Taniguchi, Ashvin Vishwanath, and Philip Kim. Spin-polarized correlated insulator and superconductor in twisted double bilayer graphene. *arXiv preprint arXiv:1903.08130*, 2019.

[79] Xiaobo Lu, Petr Stepanov, Wei Yang, Ming Xie, Mohammed Ali Aamir, Ipsita Das, Carles Urgell, Kenji Watanabe, Takashi Taniguchi, Guangyu Zhang, et al. Superconductors, orbital magnets and correlated states in magic-angle bilayer graphene. *Nature*, 574(7780):653–657, 2019.

[80] A Luther and VJ Emery. Backward scattering in the one-dimensional electron gas. *Physical Review Letters*, 33(10):589, 1974.

[81] Nicola Marzari, Arash A Mostofi, Jonathan R Yates, Ivo Souza, and David Vanderbilt. Maximally localized wannier functions: Theory and applications. *Reviews of Modern Physics*, 84(4):1419, 2012.

[82] Nicola Marzari and David Vanderbilt. Maximally localized generalized wannier functions for composite energy bands. *Physical review B*, 56(20):12847, 1997.

[83] Michael A McGuire, Hemant Dixit, Valentino R Cooper, and Brian C Sales. Coupling of crystal structure and magnetism in the layered, ferromagnetic insulator cri3. *Chemistry of Materials*, 27(2):612–620, 2015.

[84] N. D. Mermin and H. Wagner. Absence of ferromagnetism or antiferromagnetism in one- or two-dimensional isotropic heisenberg models. *Phys. Rev. Lett.*, 17(22):1133–1136, 1966.

[85] Stephan Mohr, Laura E Ratcliff, Paul Boulanger, Luigi Genovese, Damien Caliste, Thierry Deutsch, and Stefan Goedecker. Daubechies wavelets for linear scaling density functional theory. *The Journal of chemical physics*, 140(20):204110, 2014.

[86] Pilkyung Moon and Mikito Koshino. Energy spectrum and quantum hall effect in twisted bilayer graphene. *Physical Review B*, 85(19):195458, 2012.

[87] Tôru Moriya. Anisotropic superexchange interaction and weak ferromagnetism. *Physical review*, 120(1):91, 1960.

[88] Sebastian Mühlbauer, Benedikt Binz, F Jonietz, Christian Pfleiderer, Achim Rosch, Anja Neubauer, Robert Georgii, and Peter Böni. Skyrmion lattice in a chiral magnet. *Science*, 323(5916):915–919, 2009.

[89] W Münzer, A Neubauer, T Adams, S Mühlbauer, C Franz, F Jonietz, R Georgii, P Böni, B Pedersen, M Schmidt, A Rosch, and C Pfleiderer. Skyrmion lattice in the doped semiconductor $\mathrm{Fe}_{1-x}\mathrm{Co}_x\mathrm{Si}$. *Physical Review B*, 81(4):041203(R), 2010.

[90] N Nagaosa, X Z Yu, and Y Tokura. Gauge fields in real and momentum spaces in magnets: monopoles and skyrmions. *Philosophical Transactions of the Royal Society A: Mathematical, Physical and Engineering Sciences*, 370(1981):5806–5819, 2012.

[91] Naoto Nagaosa and Yoshinori Tokura. Emergent electromagnetism in solids. *Physica Scripta*, 2012(T146):014020, 2012.

[92] Richarad J Needs, Michael D Towler, Neil D Drummond, and P López Ríos. Continuum variational and diffusion quantum monte carlo calculations. *Journal of Physics: Condensed Matter*, 22(2):023201, 2009.

[93] AH Castro Neto, Francisco Guinea, Nuno MR Peres, Kostya S Novoselov, and Andre K Geim. The electronic properties of graphene. *Reviews of modern physics*, 81(1):109, 2009.

[94] Kentaro Nomura, Mikito Koshino, and Shinsei Ryu. Topological delocalization of two-dimensional massless dirac fermions. *Physical review letters*, 99(14):146806, 2007.

[95] K. S. Novoselov, A. Mishchenko, A Carvalho, and A. H. Castro Neto. 2d materials and van der waals heterostructures. *Science*, 353(6298), 2016.

[96] Kiichi Okuda, Ko Kurosawa, Shozo Saito, Makoto Honda, Zhihong Yu, and Muneyuki Date. Magnetic properties of layered compound $MnPS_3$. *Journal of the Physical Society of Japan*, 55(12):4456–4463, 1986.

[97] Neil S Ostlund and Attila Szabo. *Modern Quantum Chemistry: Introduction to advanced electronic structure theory*. Macmillan, 1982.

[98] G. Ouvrard. *Thesis*. PhD thesis, Nantes, France, 1980.

[99] G Ouvrard, R Brec, and J Rouxel. Synthesis and physical characterization of the lamellar compound cops3. *Chemischer Informationsdienst*, 13(35):no–no, 1982.

[100] Je-Geun Park. Opportunities and challenges of 2d magnetic van der waals materials: magnetic graphene? *Journal of Physics: Condensed Matter*, 28(30):301001, jun 2016.

[101] Tae-Eon Park, Licong Peng, Jinghua Liang, Ali Hallal, Fehmi Sami Yasin, Xichao Zhang, Kyung Mee Song, Sung Jong Kim, Kwangsu Kim, Markus Weigand, Gisela Schuetz, Simone Finizio, Joerg Raabe, Karin Garcia, Jing Xia, Yan Zhou, Motohiko Ezawa, Xiaoxi Liu, Joonyeon Chang, Hyun Cheol Koo, Young Duck Kim, Mairbek Chshiev, Albert Fert, Hongxin Yang, Xiuzhen Yu, and Seonghoon Woo. Néel-type skyrmions and their current-induced motion in van der Waals ferromagnet-based heterostructures. *Physical Review B*, 103(10):104410, 2021.

[102] Hoi Chun Po, Liujun Zou, Ashvin Vishwanath, and T Senthil. Origin of mott insulating behavior and superconductivity in twisted bilayer graphene. *Physical Review X*, 8(3):031089, 2018.

[103] Hryhoriy Polshyn, Matthew Yankowitz, Shaowen Chen, Yuxuan Zhang, K Watanabe, T Taniguchi, Cory R Dean, and Andrea F Young. Phonon scattering dominated electron transport in twisted bilayer graphene. *arXiv preprint arXiv:1902.00763*, 2019.

[104] R Rammal. Landau level spectrum of bloch electrons in a honeycomb lattice. *Journal de Physique*, 46(8):1345–1354, 1985.

[105] Cécile Repellin, Zhihuan Dong, Ya-Hui Zhang, and T Senthil. Ferromagnetism in narrow bands of moir\'e superlattices. *arXiv preprint arXiv:1907.11723*, 2019.

[106] Ulrich K Roessler, A N Bogdanov, and C Pfleiderer. Spontaneous skyrmion ground states in magnetic metals. *Nature*, 442(7104):797–801, 2006.

[107] Alistair CH Rowe and Paul C Abbott. Daubechies wavelets and mathematica. *Computers in Physics*, 9(6):635–648, 1995.

[108] Yu Saito, Jingyuan Ge, Kenji Watanabe, Takashi Taniguchi, and Andrea F Young. Independent superconductors and correlated insulators in twisted bilayer graphene. *Nature Physics*, 16(9):926–930, 2020.

[109] Lucile Savary and Leon Balents. Quantum spin liquids: a review. *Reports on Progress in Physics*, 80(1):016502, 2017.

[110] M Serlin, CL Tschirhart, H Polshyn, Y Zhang, J Zhu, K Watanabe, T Taniguchi, L Balents, and AF Young. Intrinsic quantized anomalous hall effect in a moiré heterostructure. *Science*, 367(6480):900–903, 2020.

[111] Aaron L. Sharpe, Eli J. Fox, Arthur W. Barnard, Joe Finney, Kenji Watanabe, Takashi Taniguchi, M. A. Kastner, and David Goldhaber-Gordon. Emergent ferromagnetism near three-quarters filling in twisted bilayer graphene. *Science*, 365(6453):605–608, 2019.

[112] Nikhil Sivadas, Satoshi Okamoto, Xiaodong Xu, Craig J Fennie, and Di Xiao. Stacking-dependent magnetism in bilayer cri3. *Nano letters*, 18(12):7658–7664, 2018.

[113] Tiancheng Song, Zaiyao Fei, Matthew Yankowitz, Zhong Lin, Qianni Jiang, Kyle Hwangbo, Qi Zhang, Bosong Sun, Takashi Taniguchi, Kenji Watanabe, Michael A. McGuire, David Graf, Ting Cao, Jiun-Haw Chu, David H. Cobden, Cory R. Dean, Di Xiao, and Xiaodong Xu. Switching 2d magnetic states via pressure tuning of layer stacking. *Nature Materials*, 18(12):1298–1302, 2019.

[114] Zhida Song, Zhijun Wang, Wujun Shi, Gang Li, Chen Fang, and B Andrei Bernevig. All magic angles in twisted bilayer graphene are topological. *Physical review letters*, 123(3):036401, 2019.

[115] D Soriano, C Cardoso, and J Fernández-Rossier. Interplay between interlayer exchange and stacking in cri3 bilayers. *Solid State Communications*, 299:113662, 2019.

[116] Petr Stepanov, Ipsita Das, Xiaobo Lu, Ali Fahimniya, Kenji Watanabe, Takashi Taniguchi, Frank HL Koppens, Johannes Lischner, Leonid Levitov, and Dmitri K Efetov. Untying the insulating and superconducting orders in magic-angle graphene. *Nature*, 583(7816):375–378, 2020.

[117] Grigory Tarnopolsky, Alex Jura Kruchkov, and Ashvin Vishwanath. Origin of magic angles in twisted bilayer graphene. *Physical review letters*, 122(10):106405, 2019.

[118] David J Thouless, Mahito Kohmoto, M Peter Nightingale, and Md den Nijs. Quantized hall conductance in a two-dimensional periodic potential. *Physical Review Letters*, 49(6):405, 1982.

[119] Antoine Tilloy and J Ignacio Cirac. Continuous tensor network states for quantum fields. *Physical Review X*, 9(2):021040, 2019.

[120] Qingjun Tong, Fei Liu, Jiang Xiao, and Wang Yao. Skyrmions in the moiré of van der waals 2d magnets. *Nano letters*, 18(11):7194–7199, 2018.

[121] Benoit Tuybens, Jacopo De Nardis, Jutho Haegeman, and Frank Verstraete. Variational optimization of continuous matrix product states. *arXiv preprint arXiv:2006.01801*, 2020.

[122] Frank Verstraete and J Ignacio Cirac. Continuous matrix product states for quantum fields. *Physical review letters*, 104(19):190405, 2010.

[123] Hong Wang, Cuixiang Wang, Yan Zhu, Zi-An Li, Hongbin Zhang, Huanfang Tian, Youguo Shi, Huaixin Yang, and Jianqi Li. Direct observations of chiral spin textures in van der Waals magnet Fe_3GeTe_2 nanolayers. *arXiv preprint arXiv:1907.08382*, 2019.

[124] Zhe Wang, Ignacio Gutiérrez-Lezama, Nicolas Ubrig, Martin Kroner, Marco Gibertini, Takashi Taniguchi, Kenji Watanabe, Ataç Imamoğlu, Enrico Giannini, and Alberto F Morpurgo. Very large tunneling magnetoresistance in layered magnetic semiconductor cri3. *Nature communications*, 9(1):2516, 2018.

[125] GH Wannier. A result not dependent on rationality for bloch electrons in a magnetic field. *physica status solidi (b)*, 88(2):757–765, 1978.

[126] Dave Wecker, Matthew B Hastings, Nathan Wiebe, Bryan K Clark, Chetan Nayak, and Matthias Troyer. Solving strongly correlated electron models on a quantum computer. *Physical Review A*, 92(6):062318, 2015.

[127] Steven R White. Hybrid grid/basis set discretizations of the schrödinger equation. *The Journal of chemical physics*, 147(24):244102, 2017.

[128] Steven R White and E Miles Stoudenmire. Multisliced gausslet basis sets for electronic structure. *Physical Review B*, 99(8):081110, 2019.

[129] A. R. Wildes, B. Roessli, B. Lebech, and K. W. Godfrey. Spin waves and the critical behaviour of the magnetization in mnps3. *J. Phys.: Condens. Matter*, 10:6417–6428, 1998.

[130] A R Wildes, V Simonet, E Ressouche, R Ballou, and G J McIntyre. The magnetic properties and structure of the quasi-two-dimensional antiferromagnet $CoPS_3$. *Journal of Physics: Condensed Matter*, 29(45):455801, 2017.

[131] AR Wildes, B Roessli, B Lebech, and K W Godfrey. Spin waves and the critical behaviour of the magnetization in $MnPS_3$. *Journal of Physics: Condensed Matter*, 10(28):6417, 1998.

[132] Fengcheng Wu, AH MacDonald, and Ivar Martin. Theory of phonon-mediated superconductivity in twisted bilayer graphene. *Physical review letters*, 121(25):257001, 2018.

[133] Ming Xie and Allan H MacDonald. Nature of the correlated insulator states in twisted bilayer graphene. *Physical Review Letters*, 124(9):097601, 2020.

[134] Cenke Xu and Leon Balents. Topological superconductivity in twisted multilayer graphene. *Physical review letters*, 121(8):087001, 2018.

[135] Yang Xu, Ariana Ray, Yu-Tsun Shao, Shengwei Jiang, Daniel Weber, Joshua E Goldberger, Kenji Watanabe, Takashi Taniguchi, David A Muller, Kin Fai Mak, et al. Emergence of a noncollinear magnetic state in twisted bilayer cri3. *arXiv preprint arXiv:2103.09850*, 2021.

[136] Chen-Ning Yang. Some exact results for the many-body problem in one dimension with repulsive delta-function interaction. *Physical Review Letters*, 19(23):1312, 1967.

[137] Matthew Yankowitz, Shaowen Chen, Hryhoriy Polshyn, Yuxuan Zhang, K Watanabe, T Taniguchi, David Graf, Andrea F Young, and Cory R Dean. Tuning superconductivity in twisted bilayer graphene. *Science*, 363(6431):1059–1064, 2019.

[138] Su Do Yi, Shigeki Onoda, Naoto Nagaosa, and Jung Hoon Han. Skyrmions and anomalous Hall effect in a Dzyaloshinskii-Moriya spiral magnet. *Physical Review B*, 80(5):054416, 2009.

[139] Yi-Zhuang You and Ashvin Vishwanath. Superconductivity from valley fluctuations and approximate so (4) symmetry in a weak coupling theory of twisted bilayer graphene. *arXiv preprint arXiv:1805.06867*, 2018.

[140] X Z Yu, Naoya Kanazawa, Yoshinori Onose, K Kimoto, W Z Zhang, Shintaro Ishiwata, Yoshio Matsui, and Yoshinori Tokura. Near room-temperature formation of a skyrmion crystal in thin-films of the helimagnet FeGe. *Nature materials*, 10(2):106–109, 2011.

[141] X Z Yu, Yoshinori Onose, Naoya Kanazawa, J H Park, J H Han, Yoshio Matsui, Naoto Nagaosa, and Yoshinori Tokura. Real-space observation of a two-dimensional skyrmion crystal. *Nature*, 465(7300):901–904, 2010.

[142] Jiaren Yuan, Yumeng Yang, Yongqing Cai, Yihong Wu, Yuanping Chen, Xiaohong Yan, and Lei Shen. Intrinsic skyrmions in monolayer Janus magnets. *Physical Review B*, 101(9):094420, 2020.

[143] Fang Zhang, Hui Zhang, Wenbo Mi, and Xiaocha Wang. Electronic structure, magnetic anisotropy and Dzyaloshinskii-Moriya interaction in Janus $Cr_2I_3X_3$ (X= Br, Cl) bilayers. *Physical Chemistry Chemical Physics*, 22(16):8647–8657, 2020.